Faculté des Sciences
Département de Géographie
Unité de recherches SPHERES
Laboratoire de Climatologie et Topoclimatologie

Present and future sensitivity of the Antarctic surface mass balance to oceanic and atmospheric forcings: insights with the regional climate model MAR

A thesis submitted for the partial fulfilment
of the requirements for the academic degree of

Philosophiae Doctor in Sciences
at the University of Liège (College of Geography)
by

Christoph Kittel

Academic year 2020–2021

Jury members:

Emmanuel Mahieu	President	Senior Research Associate FRS-FNRS, ULiège
Xavier Fettweis	Promoter	Research Associate FRS-FNRS, ULiège
Charles Amory	Co-promoter	Postdoctoral Researcher, Université Grenoble-Alpes
Aurélia Hubert	Secretary	Professor, ULiège
Cécile Agosta		Research Fellow, Laboratoire des Sciences du Climat et de l'Environnement
Hubert Gallée		Senior Researcher CNRS, Université Grenoble-Alpes
Thierry Fichefet		Professor, UCLouvain

This work was supported by the Fonds de la Recherche Scientifique – FNRS
under grant no. T.0002.16

Remerciements

Pour certains d'entre vous chers lecteurs, cette section sera la seule que vous lirez avec beaucoup d'intérêt. J'espère toutefois que cette thèse vous passionnera autant que moi pendant ces années consacrées à la rédiger. Chaque jour, je n'ai pu être qu'émerveillé par ce lointain continent Antarctique. Il y a évidemment eu des moments moins agréables, ce serait presque un euphémisme, mais *Je puis tout par celui qui me fortifie.* Si cette thèse est ce qu'elle est aujourd'hui, c'est également une somme de contributions, de partages et de discussions (et pas seulement scientifiques).

Une thèse est évidemment portée par des promoteurs. Xavier Fettweis et Charles Amory m'ont apporté un suivi de tout instant. Je ne mentirais pas en disant que ce suivi était presque 24h sur 24h. Xavier m'a fait confiance dès mon master, orientant les grandes décisions à prendre tout en me donnant une liberté dont peu de doctorants peuvent bénéficier. Bien plus important encore, il m'a toujours poussé à aller plus loin et notamment à comprendre comment le modèle fonctionne. Si Charles présente l'Antarctique comme le continent de la démesure, sachez que travailler avec lui l'est tout autant. Nous avons refait maintes fois le monde scientifique dans nos différents bureaux, redéfinis comment le modèle devrait fonctionner et soyons honnêtes, avons été parfois plus que rageux. J'ai pu trouver bien plus qu'un promoteur ou co-bureau (avec son bruit de ventilateur) et espère que nos carrières scientifiques permettront encore de nombreuses collaborations entre nous.

Le pilote n'est rien sans son bolide de course. J'ai pu hérité d'un modèle ultra-développé par de nombreux chercheurs. Je ne pourrai tous les citer, mais en plus de Xavier, je pense évidemment à Hubert Gallée (inventeur et grand développeur de MAR) et à l'ensemble de la MAR-Marvelous Antarctic Research Team en partie à Grenoble et depuis peu aussi à Paris. Si j'ai pu achever la course, je n'ai en réalité que repris le relai de Cécile Agosta. Elle avait assuré

tout le réglage et a continué à me suivre activement durant toute cette thèse. Je n'oublierai pas Thierry Fichefet qui pour poursuivre cette analogie fut en quelque sorte un co-sponsor.

Je ne pourrai pas vous dire aujourd'hui si être confiné pendant toute la rédaction finale ne m'a pas aidé à avancer un peu plus vite, mais je peux vous assurer que la présence de tous mes (anciens) collègues climatologues et/ou géographes fut plus que précieuse.

Chère famille, voici ce sur quoi je travaille ces dernières années. Vous avez su comprendre quand je ne voulais pas en parler mais avez été toujours été une source de soutien. J'ai également une pensée particulière pour vous les *gros tas*.

Enfin, Aurélie a fait bien plus que me supporter et m'encourager chaque jour de cette aventure. Je suis fier du chemin que nous parcourons et de ce que nous allons construire ensemble.

Ces quelques lignes et dire merci n'exprime pas mon infinie envers vous. reconnaissance

"Success isn't overnight. It's when everyday you get a little better than the day before. It all adds up." – **Dwayne Johnson**

Summary

Recent Global Warming has caused widespread ice losses from the Antarctic Ice Sheet (AIS) leading to an increase in mean sea level. By influencing the ice dynamics and the mass of water that accumulates on the continent, the surface mass balance (SMB, i.e, the difference between snow accumulation and ablation at the surface of the ice sheet) contributes to sea-level variations. A better knowledge of how present and future SMB will change is therefore needed to refine sea-level-rise estimates.

With the aim of identifying the driving processes from different components of the climate system (from the surface of the ocean to high-elevation clouds), we reconstruct and project the Antarctic SMB using the regional climate model MAR developed at ULiège, over 1980–2100. The results of MAR have been first compared to diverse observations to evaluate its performance. We gathered observations of several types (near-surface climate and snow accumulation) to guarantee the robustness of our results and conclusions based on our climate modeling. A first objective of this thesis was to determine to what extent the recent changes at the ocean surface can exert a direct feedback on the atmosphere and SMB. Our simulations with perturbed sea-ice concentration and sea-surface temperature around Antarctica reveal that strong and persistent katabatic winds prevent most atmospheric changes induced by the ocean to penetrate inland. This suggests a limited influence of the ocean surface on the Antarctic SMB. We focused afterwards on the sensitivity of the SMB to atmospheric warmings projected by global models using high-emission scenarios (RCP8.5 and ssp585). Higher temperatures are projected to increase SMB on the grounded ice as a result of stronger snowfall while the future SMB over the ice shelves should be dominated by higher meltwater-runoff values (compromising the stability of ice shelves) and is consequently projected to decrease. Leaving aside the role of the ocean on the thinning of ice shelves, increasing surface melt should however remain weak under

the Paris Agreement limiting potential ice-shelf collapses and accelerated Antarctic ice losses. However, our results suggest a large spread in melt increase over the ice shelves during the 21st century resulting in large uncertainties in their potential disappearance. Given the important role of ice shelves in limiting the acceleration of Antarctic ice losses (as they restrain the grounded ice to flow into the ocean), the third subject of this thesis has been devoted to the physical drivers explaining differences in increased summer melt over the Antarctic ice shelves. Although the melt increase results from higher greenhouse-gas concentrations, differences in projected melt increases arises from liquid-containing clouds. These clouds re-emits more longwave energy towards the surface, increasing melt over the ice shelves and later favouring absorption of solar energy again strengthening melt.

In conclusion, we investigate the sensitivity of the Antarctic SMB to different components of the climate system over 1981–2100. Uncertainties linked with the grounded Antarctic SMB essentially depend on the projected increased rates in snowfall associated with higher temperatures while uncertainties in the ice-shelf SMB decrease are related to cloud properties with more liquid-containing clouds leading to a stronger decrease of the ice-shelf SMB.

Résumé

Le réchauffement global ces dernières années a causé d'importantes pertes de masse de l'inlandsis Antarctique induisant une augmentation du niveau marin moyen. En influençant la dynamique glaciaire et la quantité d'eau qui s'accumule sur le continent, le bilan de masse en surface (BMS, soit la différence entre l'accumulation neigeuse et l'ablation à la surface de l'inlandsis) contribue aux variations du niveau moyen des océans. Une meilleure connaissance des variations passées du BMS et prédiction de celles à venir est ainsi nécessaire pour raffiner les estimations de la hausse du niveau marin.

Dans le but d'identifier les facteurs des variations du SMB parmis les différentes composantes du système climatique (de la surface des océans aux nuages des hautes altitudes), nous avons reconstruit et projeté le BMS de l'Antarctique en utilisant le modèle de climat régional MAR développé à l'ULiège, sur la période 1980–2100. Les résultats de MAR ont été également comparés à de nombreuses observations (de climat de proche surface et d'accumulation neigeuse) pour évaluer les performances du modèle permettant de garantir la robustesse de nos résultats et conclusions. Un premier objectif de cette thèse fut de déterminer à quel point les récents changements à la surface de l'océan autour de l'Antarctique peuvent influencer directement l'atmosphère et le BMS. Nos simulations où la concentration en glace de mer et température de surface de l'océan ont été modifiées révèlent que les vents catabatiques protègent l'inlandsis en repoussant au large les changements dans l'atmosphère engendrés par l'océan. Cela suggère une influence relativement limitée de la surface de l'océan sur le BMS de l'Antarctique. Nous nous sommes donc concentrés sur la sensibilité du BMS aux réchauffements atmosphériques projetés par les modèles globaux et les scénarios à très fortes émissions (RCP8.5 et ssp585). Les plus hautes températures devraient augmenter le BMS sur la partie posée de l'inlandsis en réponse à davantage de chutes de neige alors que le BMS des plateformes glaciaires devrait lui être dominé par une augmentation du

ruissellement de l'eau de fonte et ainsi diminuer. Si l'on ne considère pas le rôle de l'océan expliquant majoritairement l'amincissement des plateformes glaciaires, l'augmentation de fonte en surface restera faible si l'on respecte les Accords de Paris ce qui limiterait alors les risques d'effondrement de ces plateformes et l'accélération des pertes de masses de l'inlandsis Antarctique. Cependant, nos résultats suggèrent une grande gamme d'augmentation de fonte sur ces plateformes ce qui se traduirait par de grandes incertitudes sur leur disparition potentielle. Vu leur rôle très important pour limiter l'accélération des pertes de masse de l'inlandsis (elles retiennent la glace sur le continent et l'empêchent donc de couler dans l'océan), le troisième sujet de cette thèse est dédié aux facteurs physiques qui expliquent les différences d'augmentation de fonte sur les plateformes glaciaires en Antarctique. Bien que l'augmentation intrinsèque de fonte provient des concentrations de gaz à effet de serre qui sont plus importantes, les différences d'augmentation sont dues aux nuages contenant des particules liquides. Ces nuages ré-émettent plus d'énergie infrarouge vers la surface ce qui augmente la fonte et favorise d'autant plus l'absorption d'énergie solaire renforçant encore la fonte.

En conclusion, nous avons analysé la sensibilité du BMS de l'Antarctique à différentes composantes du système climatique sur la période 1980–2100. Les incertitudes pour la glace posée résultent essentiellement de l'augmentation prévue des précipitations neigeuses liée aux augmentations de température tandis que les incertitudes concernant les plateformes glaciaires dépendent des nuages et de leur contenu en particules liquides.

List of abbreviations

AIS	Antarctic Ice Sheet
ASL	Amundsen Sea Low
AWS	Automatic Weather Station
CC	Cloud Cover
COD	Cloud Optical Depth
CMIP5	5th phase of the Coupled Model Intercomparison Project
CMIP6	6th phase of the Coupled Model Intercomparison Project
CRMSE	Centered Root mean squared error
DJF	December-January-February (summer)
ENSO	El Niño Southern Oscillation
ESM	Earth-System Model
GCM	General Circulation Model
ISMIP6	Ice Sheet Model Intercomparison Project for CMIP6
IWP	Ice Water Path
JJA	June-July-August (winter
LHF	Latent heat flux
LIM	Louvain-la-Neuve sea Ice Model
LWD	Longwave downwelling radiation
LWN	Net Longwave radiation
LWP	Liquid Water Path
LWU	Longwave upwelling radiation
masl	meter above sea level
MAR	Modèle Atmosphérique Régional
MAR(ACCESS1.3)	MAR forced by ACCESS1.3
MAR(CESM2)	MAR forced by CESM2
MAR(CNRM-CM6-1)	MAR forced by CNRM-CM6-1
MAR(DS)	MAR with drifting snow
MAR(ERA5)	MAR forced by ERA5
MAR(NorESM1-M)	MAR forced by NorESM1-M
MAR(NDS)	MAR without drifting snow
MICI	Marine Ice-Cliff Instability
MISI	Marine Ice-Sheet Instability
ME	Surface Melt
NEMO	Nucleus for European Modelling of the Ocean
OSTIA	Operational SST and Sea Ice Analysis (OSTIA)
q_i	Cloud ice-crystal concentration
q_r	Cloud rain-drop concentration

q_s	Cloud snowflake concentation
q_v	Specific humidity concentration
q_w	Cloud water-droplet concentration
r	Correlation coefficient
$\mathbf{R}^2$	Determination coefficient
RF	Rainfall
RCM	Regional Climare Model
RCP	Representative Concentration Pathway
RMSE	Root mean squared error
RU	Meltwater Runoff
SAM	Southern Annular Mode
SEB	Surface Energy Budget
SHF	Sensible heat flux
SF	Snowfall
SIA	Sea-ice area
SIC	Sea-ice concentration
SIC ± x	Experiment with SIC changes
SIC(CMIP5)	Experiment with SIC CMIP5-based changes
SISVAT	Soil Ice Snow Vegetation Atmosphere Transfer
SLE	Sea-level equivalent
SLR	Sea-level rise
SMB	Surface Mass Balance
SSC	Sea-surface condition
ssp	Shared Socioeconomic Pathways
SST	Sea-surface temperature
SST/SIC(CMIP5)	Experiment with SST and SIC CMIP5-based changes
SST/SIC(GISS-E2-H)	Experiment with SST and SIC GISS-E2-H-based changes
SST/SIC(NorESM1-ME)	Experiment with SST and SIC NorESM1-ME-based changes
SST ± x / SIC ∓ x	Combined (SST and SIC) perturbed experiment
SST ± x	Experiment with SST changed by x °C
SU	Sublimation
SWD	Shortwave downwelling radiation
SWN	Net shortwave radiation
SWU	Shortwave upwelling radiation
z_{0m}	Roughness length for momentum

List of publications

Delhasse, A., **Kittel, C.**, Amory, C., Hofer, S., van As, D., S. Fausto, R., and Fettweis, X.: Brief communication: Evaluation of the near-surface climate in ERA5 over the Greenland Ice Sheet, The Cryosphere, 14, 957–965, 2020.

Delhasse, A., Hanna, E., **Kittel, C.**, and Fettweis, X.: Brief communication: CMIP6 does not suggest any atmospheric blocking increase in summer over Greenland by 2100, International Journal of Climatology, 2020

Donat-Magnin, M., Jourdain, N. C., Gallée, H., Amory, C., **Kittel, C.**, Fettweis, X., Wille, J. D., Favier, V., Drira, A., and Agosta, C.: Interannual Variability of Summer Surface Mass Balance and Surface Melting in the Amundsen Sector, West Antarctica, The Cryosphere, 2020.

Donat-Magnin, M., Jourdain, N. C., **Kittel, C.**, Agosta, C., Amory, C., Gallée, H., Krinner, G., and Chekki, M.: Future ice-sheet surface mass balance and melting in the Amundsen region, West Antarctica, The Cryosphere Discussions [accepted], 1–30, 2020.

Fettweis, X., Hofer, S., Krebs-Kanzow, U., Amory, C., Aoki, T., Berends, C. J., Born, A., Box, J. E., Delhasse, A., Fujita, K., Gierz, P., Goelzer, H., Hanna, E., Hashimoto, A., Huybrechts, P., Kapsch, M.-L., King, M. D., **Kittel, C.**, Lang, C., Langen, P. L., Lenaerts, J. T. M., Liston, G. E., Lohmann, G., Mernild, S. H., Mikolajewicz, U., Modali, K., Mottram, R. H., Niwano, M., Noël, B., Ryan, J. C., Smith, A., Streffing, J., Tedesco, M., van de Berg, W. J., van den Broeke, M., van de Wal, R. S. W., van Kampenhout, L., Wilton, D., Wouters, B., Ziemen, F., and Zolles, T.: GrSMBMIP: intercomparison of the modelled 1980–2012 surface mass balance over the Greenland Ice Sheet, The Cryosphere, 14, 3935–3958, 2020.

Hofer, S., Lang, C., Amory, C., **Kittel, C.**, Delhasse, A., Tedstone, A., and Fettweis, X.: Greater Greenland Ice Sheet contribution to global sea level rise in CMIP6, Nature communications, 11(1), 1-11, 2020.

Kittel, C., Amory, C., Agosta, C., Jourdain, N. C., Hofer, S., Delhasse, A., Doutreloup, S., Huot, P.-V., Lang, C., Fichefet, T., and Fettweis, X.: Diverging future surface mass balance between the Antarctic ice shelves and grounded ice sheet, The Cryosphere Discussions [accepted], pp. 1–29, 2020.

Mottram, R., Hansen, N., **Kittel, C.**, Wessem, M. v., Agosta, C., Amory, C., Boberg, F., Berg, W. J. v. d., Fettweis, X., Gossart, A., et al.: What is the Surface Mass Balance of Antarctica? An Intercomparison of Regional Climate Model Estimates, The Cryosphere Discussions [accepted], pp. 1–42, 2020.

Agosta, C., Amory, C., **Kittel, C.**, Orsi, A., Favier, V., Gallée, H., van den Broeke, M. R., Lenaerts, J. T. M., van Wessem, J. M., van de Berg, W. J., and Fettweis, X.: Estimation of the Antarctic surface mass balance using the regional climate model MAR (1979–2015) and identification of dominant processes, The Cryosphere, 13, 281–296, 2019.

Amory, C. and **Kittel, C.**: Brief communication: Rare ambient saturation during drifting snow occurrences at a coastal location of East Antarctica., The Cryosphere, 13, 2019.

Doutreloup, S., Wyard, C., Amory, C., **Kittel, C.**, Erpicum, M., and Fettweis, X.: Sensitivity to Convective Schemes on Precipitation Simulated by the Regional Climate Model MAR over Belgium (1987–2017), Atmosphere, 10, 34, 2019.

Doutreloup, S., **Kittel, C.**, Wyard, C., Belleflamme, A., Amory, C., Erpicum, M., and Fettweis, X.: Precipitation evolution over Belgium by 2100 and sensitivity to convective schemes using the regional climate model MAR, Atmosphere, 10(6), 321, 2019.

Lambert, M., **Kittel, C.**, Damseaux, A., and Fettweis, X.: Sensitivity of arctic surface temperatures to sea ice thickness changes using the regional climate model mar, BSGLg, 2019.

Lippl, S., Friedl, P., **Kittel, C.**, Marinsek, S., Seehaus, T. C., and Braun, M. H.: Spatial and Temporal Variability of Glacier Surface Velocities and Outlet Areas on James Ross Island, Northern Antarctic Peninsula, Geosciences, 9(9), 374, 2019.

Delhasse, A., Fettweis, X., **Kittel, C.**, Amory, C., and Agosta, C.: Brief communication: Impact of the recent atmospheric circulation change in summer on the future surface mass balance of the Greenland Ice Sheet, The Cryosphere, 12, 3409–3418, 2018.

Kittel, C., Amory, C., Agosta, C., Delhasse, A., Doutreloup, S., Huot, P.-V., Wyard, C., Fichefet, T., and Fettweis, X.: Sensitivity of the current Antarctic surface mass balance to sea surface conditions using MAR, The Cryosphere, 12, 3827–3839, 2018.

Fettweis, X., Box, J., Agosta, C., Amory, C., **Kittel, C.**, Lang, C., van As, D., Machguth, H., and Gallée, H.: Reconstructions of the 1900–2015 Greenland ice sheet surface mass balance using the regional climate MAR model, The Cryosphere, 11, 1015–1033, 2017.

Contents

CHAPTER 1

General introduction

Pervasive changes in Earth's climate have been already caused by human activities. Since the pre-industrial period (1850–1900), emission of greenhouse gases by these activities has increased the global temperature by 1 °C ± 0.2 °C (IPCC, 2018). Although this seems to be a relatively limited warming, consequences of this change have been already visible on ecosystems and organisms including human well-being (Hoegh-Guldberg et al., 2018). This is particularly true for the cryosphere where climate changes are amplified through positive feedbacks. Recent estimates reveal that the cryosphere has taken up 3.2 % of the global energy imbalance between 1994–2017 leading to the loss of 28 trillion tonnes of ice (Slater et al., 2021). Beyond the effects these changes may have on the water cycle, ocean currents and consequences for ecosystems, the melting of the (grounded) cryosphere will mainly increase the global sea level. Although the individual contributions to sea-level rise from melting Greenland and Antarctic ice sheets are currently less than the thermal expansion of the ocean, they are also the largest potential contributors to sea-level rise due to ice stored over these two ice sheets (Oppenheimer et al., 2019). Since ice-sheet losses have been tracking now the upper range of climate warming scenarios (Slater et al., 2020), a specific attention has to be paid to polar ice sheets and in particular the Antarctic Ice Sheet which is the largest one.

1.1 Antarctic

1.1.1 Geographical portrait

The Antarctic continent is almost entirely surrounded by the Antarctic Circle (66°33' S) and is fortuitously almost centered on the South Pole, making it the southernmost land mass on Earth. Although Antarctica (Fig. 1.1) is often considered as the driest place and thus the largest desert on Earth, the frozen accumulated water accounts for 70% of the total Earth's fresh water. 98% of Antarctica is covered by the Antarctic Ice Sheet (AIS) (King and Turner, 1997). If all the accumulated snow and ice on the continent were to melt, the sea level would rise by around 58 m (Fretwell et al., 2013; Morlighem et al., 2020). At 13.92 Mkm^2, the AIS is a little larger than Europe (10.18 Mkm^2) and corresponds to

453.5 times our small, dear, and beloved Belgium. The AIS is also 8 times larger than the Greenland Ice Sheet which is the second largest ice sheet on Earth and which by entirely melting could only raise the mean sea level by ∼7m (Bamber et al., 2013). The AIS is then the largest potential contributor to sea-level rise among the cryosphere.

From a geographical perspective, Antarctica can be divided into three main regions: the East Antarctic Ice Sheet , the West Antarctic Ice Sheet, and the Antarctic Peninsula (Fig. 1.1). The largest region is the East Antarctic Ice Sheet (10.4 Mkm^2) which is notably composed of a large plateau whose altitude varies between 2000 and 4000 mabovesealevel (masl). West and East regions are separated by the Transantarctic mountains. The West AIS measures 1.97 Mkm^2 and peaks at 4892 masl (Mount Vinson), the highest summit of the AIS. Finally, the Antarctic Peninsula, which is the geological extension of the West AIS and Andes Mountains, is the northernmost region crossing the Antarctic circle. This is a narrow (less than 300 km wide) range of mountains and frozen archipelagos about 1500 km long with summits higher than 3000 masl. These 3 regions respectively contain the equivalent of 53.3 m, 4.3 m and 0.2 m sea-level rise (SLR) (Fretwell et al., 2013).

The large mass of Antarctic ice leads to a deformation of the underlying bedrock, which sinks below sea level. Thus, 5.5 Mkm^2 (or 44.7% of the grounded ice) is at an altitude of less than 0 masl (Fretwell et al., 2013). The mean ice thickness of the AIS is 2166 unitm, with a maximum thickness around 4897 masl at the top of the Adelie Land sector. New measurements there suggest the existence of ice at the bottom of the ice sheet older than 1.5Myear (near Dome C) potentially revealing much older information on the past climate variations (Lilien et al., 2020).

Due to gravity, the ice mass grounded over the continent flows toward the ocean where basal friction essentially vanishes, forming flat floating extensions of the ice sheet. The largest ones are called ice shelves. For instance, the Ross and Filchner-Ronne ice shelves measure more than 420 000 km^2 (i.e, each more than 13 times the size of Belgium). Although only representing 7% of the AIS, the ice shelves play a crucial role in the dynamical stability of the AIS. As illustrated by Figure 1.2, they *buttress* (similarly to pillars supporting buildings) the ice over the grounded continent by acting against the ice-flow acceleration at the grounding ligne (line separating the ice shelves from the grounded ice). Since the ice shelves are floating on the ocean, they make only a very small contribution to sea-level

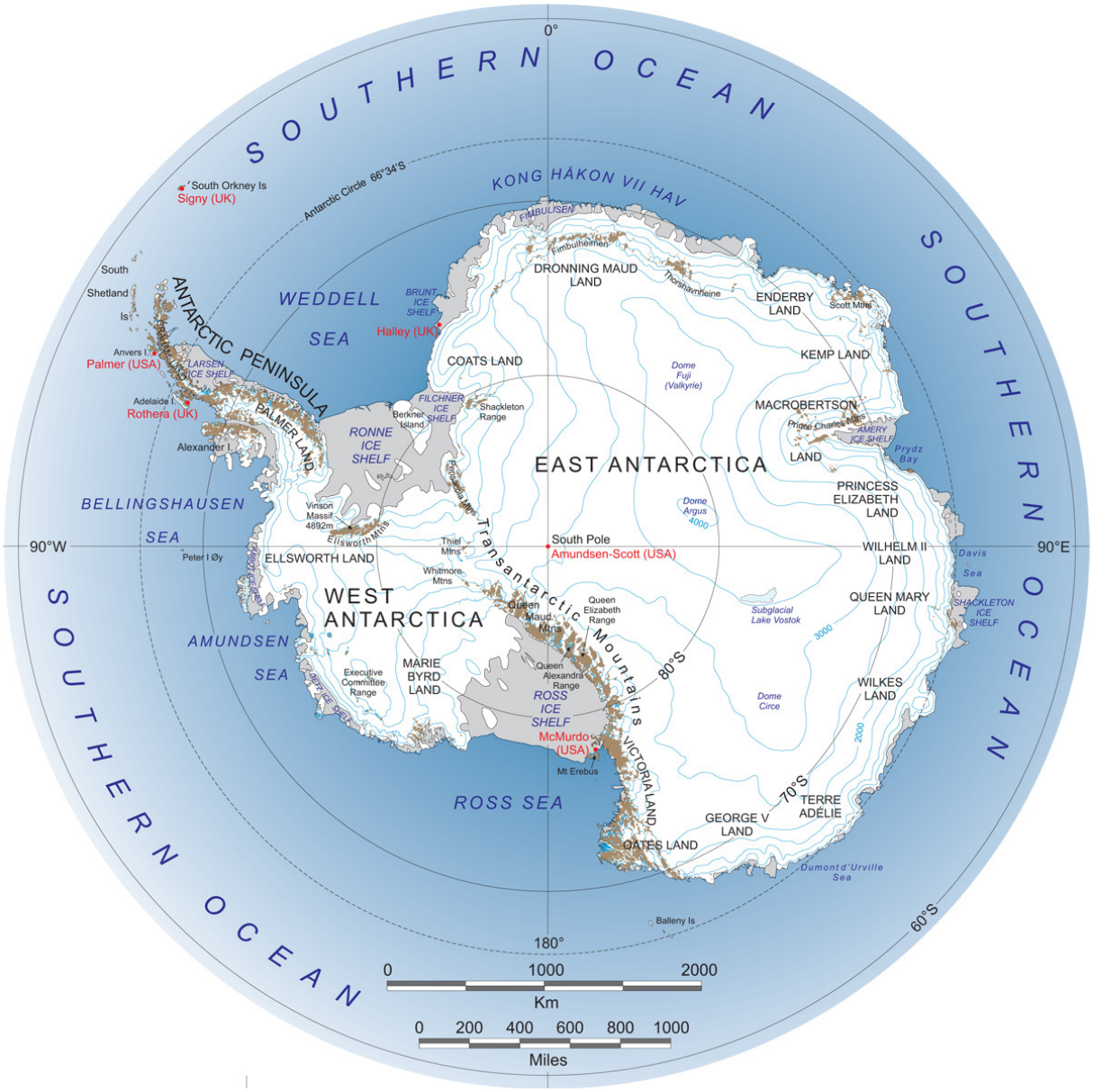

Figure 1.1: The Antarctic Ice Sheet with surface elevation and subregions of the continent and Southern Ocean Credit: NASA, retrieved from http://lima.nasa.gov/pdf/A3_overview.pdf (last accessed 01/12/2020)

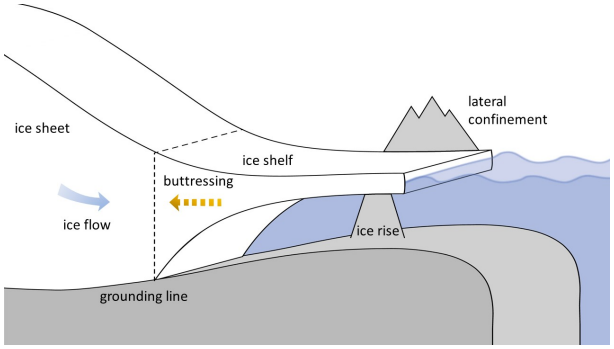

Figure 1.2: Schematic buttressing effect of the ice-sheet-shelf system. The buttressing acts against the ice gravity flow towards the ocean. It arises due to the lateral containment of an ice shelf in an embayment or at the grounds by pinning points. Credit: Ronja Reese & Maria Zeitz, retrieved from https://blogs.egu.eu/divisions/cr/2019/05/10/image-of-the-week-kicking-the-ices-buttressing/ (last acceessed 01/01/2021).

variations (Peter and Brower, 2007) but control the ice discharge to the ocean and then indirectly influence the sea level (e.g., Rignot et al., 2004; Dupont and Alley, 2005; Gudmundsson, 2013; Fürst et al., 2016).

1.1.2 Climatological portrait

1.1.2.1 Atmospheric circulation

The Southern Annular Mode (SAM or Antarctic Oscillation) and the El Niño Southern Oscillation (ENSO) are the main drivers of the atmospheric circulation variability in the Antarctic region (e.g., Turner, 2004; Marshall, 2007; Clem et al., 2016), with in addition the Amundsen Sea Low (ASL) in the Pacific sector (e.g., Raphael et al., 2016). The SAM is the dominant variability mode in the high-latitude Southern Hemisphere. It controls the strength of the westerlies as a result of the position of the low-pressure belt surrounding the AIS (Thompson and Wallace, 2000). The SAM then influences the position of low-pressure systems around the AIS leading to alternating moist/warm and dry/cold air advection (Kim et al., 2020). The two phases of ENSO (El Niño and La Niña) arise from interactions between the atmosphere and the ocean in the Pacific, generating Rossby waves that can influence the Antarctic climate (Latif et al., 1998; Wang et al., 2017). ENSO modulates heat and moisture transport onto the West AIS, affecting temperature and precipitation patterns (Lenaerts et al., 2019). The ASL is actually a set of low-pressure systems located in the Amundsen, Bellinghausen and Ross seas, whose position and magnitude influence the atmospheric circulation in this region, resulting in changes in winds, advections of warm and humid

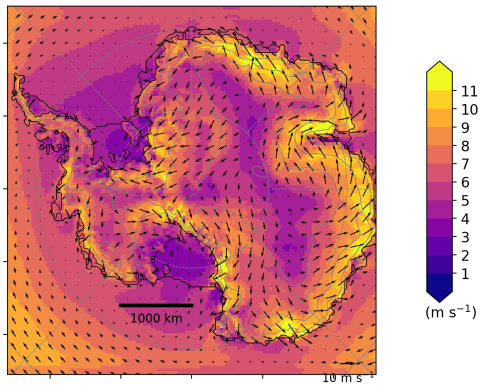

Figure 1.3: Mean annual 10-m wind speed and direction ($m\,s^{-1}$) as simulated by MAR over 1979–2019.

maritime air and precipitation (Raphael et al., 2016; Fyke et al., 2017; Scott et al., 2019). The SAM and ENSO are likely connected together and so inherently with the ASL (Fogt et al., 2011; Turner et al., 2013b; Scott et al., 2019; Fogt and Marshall, 2020).

1.1.2.2 Near-surface temperatures and winds

The temperatures over the AIS are mainly determined by the location and the elevation. The location southwards of the Antarctic circle results in the alternance of polar night (no sunshine during winter months) and midnight sun (sunshine during the summer months). Furthermore, the Antarctic surface strongly reflects the shortwave (solar) downwelling radiations and absorbs few direct energy from the summer sun as the albedo (i.e, ratio of shortwave reflected and downwelling energy) of the snow/ice surface is high. The surface energy budget (resultant of all energy fluxes at the surface) is then mostly negative inducing cooling of the air by the surface. Temperatures are also lower as altitude increases. For instance, mean annual temperatures are close to -10 °C in most margin locations (except over the Peninsula where mean annual temperatures are closer to -5 °C) and lower than -50 °C for the highest elevation (Turner et al., 2004).

The cooling of the air by the surface creates strong temperature inversions (up to 2.5 $°C\,m^{-1}$) on the Antarctic Plateau (Genthon et al., 2013) favouring the development of frequent and persistent katabatic winds. As the cooling of the air is stronger near the surface, the temperature increases with the altitude (i.e, inversion of the thermal lapse rate). Denser and colder air accumulates on the surface and flows from the center of the ice sheet towards the margins. The

flow strengthens as it accelerates along the slope and is enhanced by topographic channelings (e.g., Parish and Wendler, 1991) and generates intense near-surface downslope winds that are driven by gravity and called katabatic winds. These katabatic winds are deviated towards the West due to the Coriolis force (Fig. 1.3). Their annual mean speed can reach more than 20 $\mathrm{m\,s^{-1}}$ at the coastal margins (Parish and Bromwich, 1991) while gusts of 96 $\mathrm{m\,s^{-1}}$ have been measured at Dumont d'Urville (Adelie Land, East Antarctica) (Wendler et al., 1997).

1.1.2.3 Precipitation

The Antarctic climate is characterised by a strong contrast between inland and coastal regions. While the wind is weaker, the temperatures are lower at high-elevation locations. On the opposite, the wind is stronger and is associated with higher temperature over the margins. Furthermore, the climate at the margins is more strongly influenced by synoptic-scale meteorological systems from oscillations of the polar front (boundary between polar and temperate air masses). These systems bring a lot of moisture and precipitation but can hardly penetrate the continent because of the slopes of the ice sheet acting as an orographic barrier. The moisture contained in the air masses condensate as the air rises along the topography reducing the advection of humidity towards the plateau which can be considered as a desert. This results in much higher precipitation rates over the margins than in the interior (Fig. 1.4). Whereas the mean annual precipitation values are often larger than 700 $\mathrm{kg\,m^{-2}\,yr^{-1}}$ (or $\mathrm{mm\,w.e.\,yr^{-1}}$, the interior values are usually less than 50 $\mathrm{kg\,m^{-2}\,yr^{-1}}$. Figure 1.4) also highlights the importance of orographic barriers such as the Antarctic Peninsula that concentrate precipitation on their windward side while the lee side is much drier.

Precipitation is almost exclusively solid due to the low temperatures (e.g., Van Wessem et al., 2014b; Agosta et al., 2019). Liquid precipitation remains scarce and mainly occurs over the Antarctic Peninsula and to a lesser extent over other coastal regions mostly in summer. Solid precipitation then falls as snow or diamond dust (ie., ice crystal). This latter is often qualified as 'clear-sky' precipitation and was thought to deliver most of the precipitation budget over the cold continental interior (e.g., Bromwich, 1988; Ekaykin et al., 2004). However, recent studies (e.g., Schlosser et al., 2010; Turner et al., 2019) have also shown that episodic and extreme warm and wet events (called atmospheric rivers) can bring most of the annual precipitation budget. These events result from intrusions of sub-tropical and temperate maritime air into the Antarctic interior due to

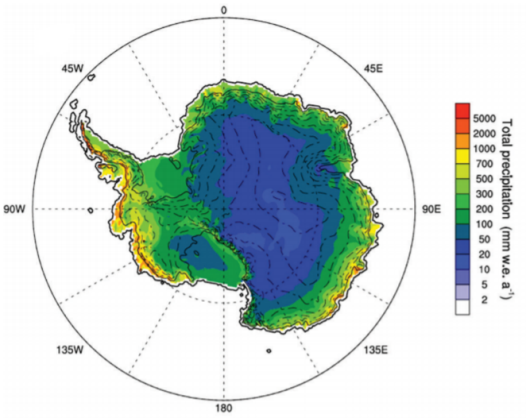

Figure 1.4: Mean total precipitation (mmw.e. yr^{-1}) as simulated by RACMO over 1979–2011 (from Van Wessem et al. (2014b)).

blocking ridges directing them directly towards the ice sheet (Naithani et al., 2002; Schlosser et al., 2010). While these air masses bring significant moisture over the ice sheet, the associated abundant clouds can induce intense melt events (Nicolas et al., 2017; Kuipers Munneke et al., 2018; Scott et al., 2019; Wille et al., 2019). Finally, air humidity can also directly condensate or deposit over the cold surface and slightly contributes to a local mass gain.

1.1.2.4 Drifting-snow processes

Once the snow precipitation has reached the ground, they are frequently remobilised by the wind. Strong winds can erode previously-deposited snow and redistribute it elsewhere. The transport of snow is organised in two main modes: saltation and suspension. Saltation consists in mobile snow particles periodically bouncing on the surface within heights of the order of 10 centimetres (Pomeroy, 1989). The suspension mode refers to snow particles entrained upward in the atmosphere without contact with the surface in stronger wind conditions. A further distinction in the suspension mode is made depending on the height of the snow particles: the term "drifting snow" is commonly used for snow transport below the human eyes (< 2 m) while "blowing snow" is used for the transport above that limit. The erosion and transport of snow by the wind, hereafter referred to as drifting snow without consideration of the height, is a common feature of the Antarctic climate (e.g., Lenaerts and Van den Broeke, 2012; Palm et al., 2017) that can be active up to 81% of the time in some locations (Amory, 2020). Drifting snow, when driven by katabatic winds, then redistributes snow towards the ice-sheet margins and can contribute to the export of large volumes of snow

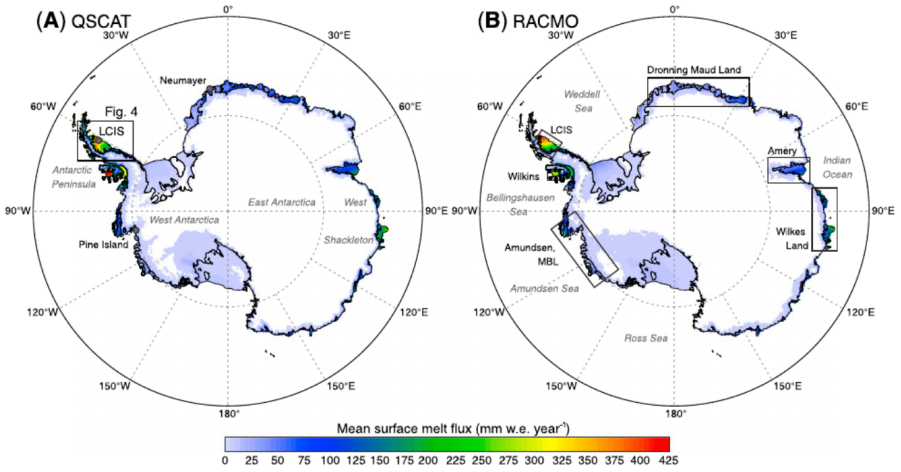

Figure 1.5: Mean (1992–2009) annual surface melt (mmw.e. yr^{-1}) A) derived from QSCAT satellite and B) simulated by RACMO (from Trusel et al. (2013)).

beyond the continental boundaries (Scarchilli et al., 2010; Palm et al., 2011).

Furthermore, drifting-snow particles interact with their surrounding atmosphere. By sublimating, they increase the relative humidity of the air by releasing water vapour (e.g., Bintanja, 2001; Amory and Kittel, 2019). This also decreases the air temperature as sublimation removes latent heat from the air. Note that similar moisture exchange also occurs between the snow-covered surface and the atmosphere. However, the greater exposed surface area and the ventilation of drifting-snow particles results in larger sublimation rates than surface sublimation (Schmidt, 1982; Lenaerts and Van den Broeke, 2012; Van Wessem et al., 2018). Hereafter in this manuscript, drifting-snow processes refer to the transport, erosion, deposition and concurrent sublimation.

1.1.2.5 Surface melt

Surface melt is currently limited to the ice-sheet margins with higher values over the southernmost ice shelves (Picard et al., 2007; Kuipers Munneke et al., 2012; Trusel et al., 2013). The stronger meltwater fluxes over the eastern or lee side of the Peninsula result from the Foehn effect (Fig. 1.5). As the moist air masses rises with elevation, humidity condensates which generates heavy precipitation (known as orographic precipitation) on the windward (western) side of the Peninsula. The drier air descending down the leeside of the mountain range, heats up due to the adiabatic compression (Foehn effect). This induces strong surface melting over the Peninsula and the Larsen ice shelves even outside of the usual summer melt season (e.g., Kuipers Munneke et al., 2018; Datta et al., 2019). Adiabatic

compression associated with drifting-snow processes can also increase melt at the surface (Lenaerts et al., 2017a). The stronger sensible heat exchange (generated by adiabatic compression and related warm air advection) and enhanced solar radiation absorption (since drifting-snow tends to expose lower-albedo ice layers) favour surface melting. Finally, liquid-containing clouds can enhance melt by increasing longwave radiations emitted towards the surface (e.g., Nicolas et al., 2017; Scott et al., 2019; Wille et al., 2019).

1.1.2.6 Surface mass balance

The preceding paragraphs summarise the main snow accumulation and ablation processes occurring at the Antarctic surface. The difference between accumulation (snowfall (SF), rainfall (RF), and surface deposition and condensation (DE)) and ablation (erosion (ER), surface sublimation and evaporation (SU), and runoff (RU)) is called Surface Mass Balance (SMB, Eq. 1.1):

$$SMB = SF + RF + DE - ER - SU - RU, \tag{1.1}$$

Drifting-snow processes (redistribution of snow through erosion/deposition and concurrent atmospheric sublimation) are naturally included in the balance between SF (snow accumulation) and ER (snow erosion) even if they have often been wrongly considered to as separate processes (e.g., Van de Berg et al., 2006; Lenaerts and Van den Broeke, 2012; Thiery et al., 2012; Van Wessem et al., 2018; Lenaerts et al., 2019). Runoff occurs when the snowpack can no longer absorb any excess in liquid water (rainfall or melt) and when the slope favours the drainage of water accumulated at the surface.

The Antarctic SMB highly varies across multiple space-scale challenging its observation and representation in climate models (Lenaerts et al., 2019). In situ single-point observation of SMB can be performed using stakes (e.g., Frezzotti et al., 2005; Agosta et al., 2012), snow pits (e.g., Traversi et al., 2009), ice cores (e.g., Thomas et al., 2017) and ultrasonic radar (e.g., Souverijns et al., 2018) while ground-penetrating radar (e.g., Medley et al., 2014) can sample a larger area. However, these methods rely on the knowledge of the snow/ice density potentially leading to large uncertainties. We refer to (Eisen et al., 2008) for a detailed description of these methods and associated difficulties and uncertainties.

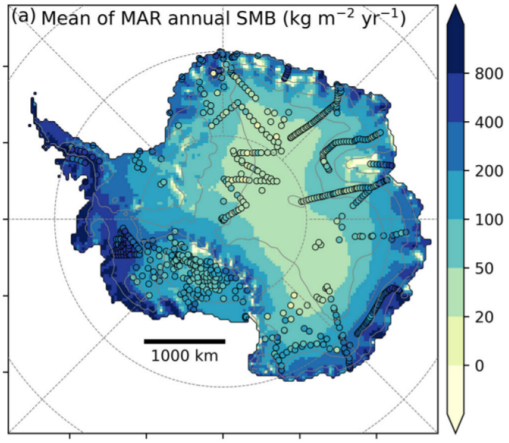

Figure 1.6: Mean annual SMB (kg m^{-2} yr^{-1}) simulated by MAR over 1979–2015. Circled dots represented the mean annual observed SMB (from Agosta et al. (2019)).

Climate modeling can also provide a continuous estimation of the SMB over all the AIS and over long temporal periods. In particular, two types of models are frequently used: General Circulation Models (GCMs) or following their level of complexity, Earth-System Models (ESMs) that simulate the Earth's climate (see Ch. 2) and polar-oriented Regional Climate models (RCMs) that only represent the climate of a specific area. GCM and ESM outputs are mainly used to study very-long term SMB variations (paleo-climate or projections of several centuries or even millennia projections), but often also for shorter scales (around one hundred years). These models have the advantages of 1) not requiring any meteorological forcing fields at their boundaries, and 2) taking into account more feedback mechanisms from the global climate system. However, using their outputs directly to study the evolution of the SMB often involves several compromises: 1) their spatial resolution remains too coarse to correctly represent the steep margins of the ice sheet or the peripheral ice shelves (Seroussi et al., 2020) and 2) they do not account properly for important physical processes of polar regions, in particular those related to the stable boundary layer and snow metamorphism, melt, albedo feedbacks, and refreezing in the snowpack (Lenaerts et al., 2016; Favier et al., 2017). Dynamical downscaling of these global models with polar-oriented RCMs (e.g., Van Wessem et al., 2018; Agosta et al., 2019) offers an alternative to address not only the issue of coarse spatial resolution, but also and more importantly to more robustly evaluate changes in mass and energy fluxes at the ice-sheet surface with a dedicated physics (e.g., Fyke et al., 2018; Lenaerts et al., 2019; Fettweis et al., 2020).

The spatial distribution of the mean SMB is strongly correlated with the

precipitation distribution as it largely dominates SMB gradients. SMB is then higher on the margins and progressively decreases inland with very low values over the Antarctic plateau (Fig 1.6). Blue-ice areas (negative SMB) are rare (approximately 1-2%, Hui et al., 2014) and scattered over all the AIS (e.g., Brown and Scambos, 2004; Favier et al., 2011; Spaulding et al., 2012). They results from locally strong drifting-snow processes (erosion and sublimation) and/or melt (e.g., Bintanja, 1999; Genthon et al., 2007; Lenaerts et al., 2017a).

While runoff (and precedent melt) fluxes are currently marginal compared to precipitation (and hence weakly influencing the SMB) over the AIS (e.g., Agosta et al., 2019), meltwater ponds and lakes often form over the Antarctic ice shelves in topographic depression (Bell et al., 2017; Arthur et al., 2020). This can have a major influence on the ice-sheet dynamics following three actions (Arthur et al., 2020). They can 1) intensify melt by their lower albedo (Hubbard et al., 2016), 2) increase the ice velocity and ice discharge after a rapid percolation (Tuckett et al., 2019) 3) be an important precursor for ice-shelf collapse by inducing ice-shelf flexure and/or triggering widespread (hydro)fracturation both leading to disintegration (Rott et al., 1996; Scambos et al., 2003; van den Broeke, 2005; Glasser and Scambos, 2008; Scambos et al., 2009; Banwell et al., 2013, 2014, 2019)).

1.1.2.7 Mass balance

The mass balance (MB, Eq. 1.2) is the difference between accumulation and ablation processes occurring at the top, bottom, and boundaries of the ice sheet. It determines the SLR contribution of the AIS through:

$$MB = SMB - D - M_{basal}, \tag{1.2}$$

The AIS currently loses mass mainly by ice discharge (D) and basal melting (M_{basal}, including the balance between melt at the bottom of the ice sheet and refreezing at the interface with the ocean), while SMB is the only significant positive accumulation process. Ice discharge represents the export of ice beyond the grounded line. Mass variations over the ice shelves do not directly contribute to the mass balance of the Antarctic Ice Sheet. Furthermore, their contribution to sea-level variations is insignificant since the sea level already accounts for the

floating fresh-water ice (Peter and Brower, 2007). However, disintegration and ice-shelf collapse result in a reduction in the buttressing effect which accelerates the ice discharge (Scambos et al., 2004; Fürst et al., 2016; Glasser et al., 2011) highlighting the major role of ice shelves for the stability of the ice sheet and their indirect contribution to sea-level variations.

1.1.2.8 Surrounding ocean

The AIS is in direct contact with the surrounding ocean. Due to the low temperature and strong wind chill resulting from katabatic winds, the ocean is often covered by sea ice in winter while it is more open in summer except near the margins (Fig. 1.7). The ice extent ranged from approximately 3 10^6 km^2 in February to a maximum of 18.5 10^6 km^2 in September between 1979–2010 (Parkinson and Cavalieri, 2012). While sea-ice extent has a strong seasonal cycle, the interannual variability is relatively small (Parkinson and Cavalieri, 2012).

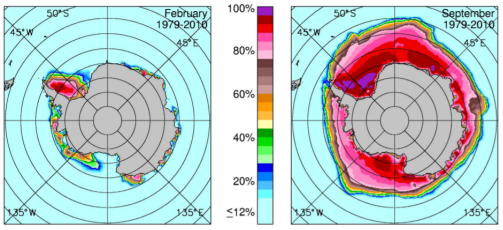

Figure 1.7: Mean sea-ice concentration in February (left) and September (right) over 1979-2010 (from Parkinson and Cavalieri (2012))

1.1.3 Recent climate trends

1.1.3.1 Ocean

The total Antarctic sea-ice cover exhibits no significant trend over 1979–2018 (Ludescher et al., 2019). While it has increased between 1979–2015 (e.g., Parkinson and Cavalieri, 2012; Comiso et al., 2017), the sea ice has retreated since 2016 (e.g., Meehl et al., 2019; Wang et al., 2019a). However, local strong discrepancies exist with ice gain in Ross and Weddel seas and ice loss in Amundsen and Bellingshausen seas (e.g., Parkinson and Cavalieri, 2012; Massonnet et al., 2013; Holland, 2014). Changes in atmospheric circulation likely explain the sea-ice increase before 2016 (e.g., Holland and Kwok, 2012).

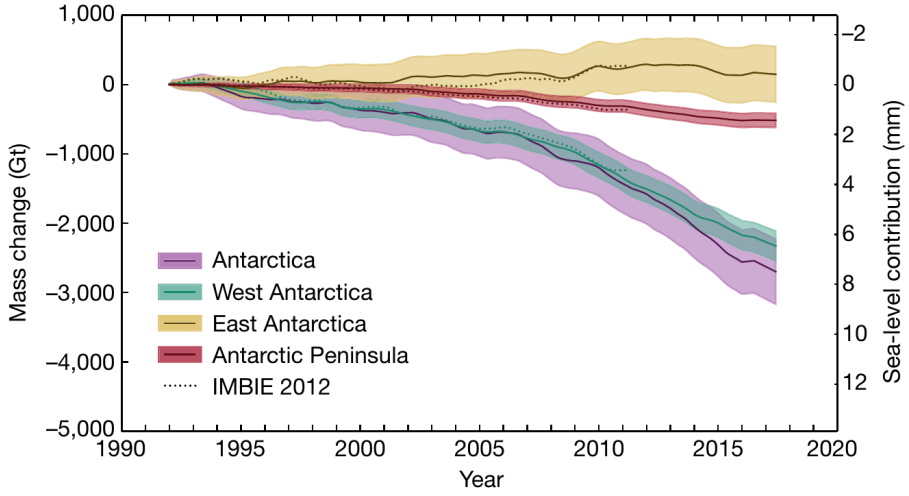

Figure 1.8: Cumulated mass change (Gt) since 1992 adapted from Shepherd et al. (2018). The uncertainties defined as one standard deviation are shaded, while dots illustrate the values from Shepherd et al. (2012).

Similarly, a large part of the changes at the ocean surface are conditioned by changes in the atmosphere. Temperatures of the surface and subsurface (between 200 m and 700 m depth) ocean exhibit an opposite trend with a cooling of the surface (Fan et al., 2014; Spence et al., 2014; Jones et al., 2016; Armour et al., 2016) and warming of the subsurface (Schmidtko et al., 2014). These trends result from 1) water subsurface advection and surface heat export northwards (Spence et al., 2014, 2017) as a consequence of wind changes due to the combination of the SAM, ENSO and ASL 2) a likely strong decoupling between the surface and the subsurface of the ocean by the presence of fresh and cold water coming from the melting base of the ice shelves (Bintanja et al., 2013).

1.1.3.2 Antarctic mass balance

The AIS has been losing mass at an increasing rate in recent years (Shepherd et al., 2018; Rignot et al., 2019; Meredith et al., 2019). Following Rignot et al. (2019), the total mass loss was 40 ± 9 $\mathrm{Gt\,yr^{-1}}$ in 1979–1990 and reached 252 ± 26 $\mathrm{Gt\,yr^{-1}}$ in 2009–2017. If such an acceleration continues, the AIS could soon become a larger contributor to SLR than the Greenland Ice Sheet (Shepherd et al., 2018). The loss is mainly driven by the West Antarctic region with a smaller contribution of the Antarctic Peninsula to be put into perspective with its smaller size (Fig. 1.8). The East Antarctic region exhibits a non-significant positive trend with the largest uncertainties.

The recent higher mass loss is due to an increased ice discharge caused by

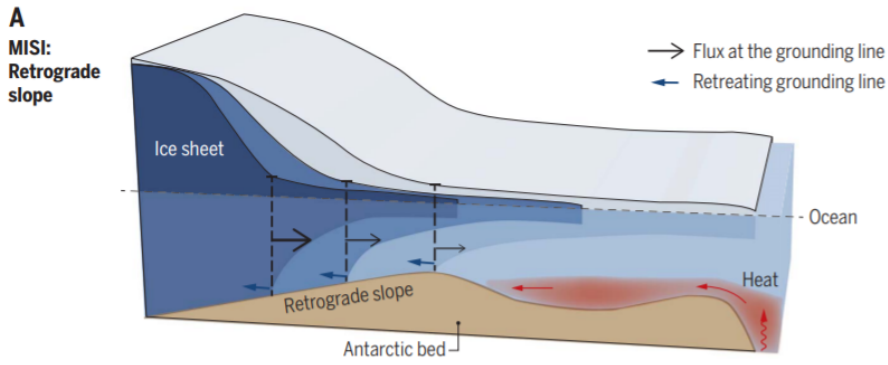

Figure 1.9: Marine Ice-Sheet Instability (MISI) (from Pattyn and Morlighem (2020), credit: N. Cary). Ocean-induced basal melt progressively induces a retreat of the grounded line which increases the melting zone and the flow

glacier flow acceleration occurring in West Antarctica and Antarctic Peninsula (Mouginot et al., 2014; Konrad et al., 2017; Gardner et al., 2018; Shepherd et al., 2018; Rignot et al., 2019). This mainly results from the reduction of ice-shelf buttressing as a response to basal ice-shelf melting enhanced by warmer sub-surface water (e.g., Paolo et al., 2015; Cook et al., 2016; Rintoul et al., 2016; Paolo et al., 2018; Gardner et al., 2018; Jenkins et al., 2018; Rignot et al., 2019). Furthermore, sudden and dramatic collapse of ice shelves in the northern Antarctic Peninsula has also led to enhanced ice discharge and thinning of the ice sheet in this region (Scambos et al., 2004, 2014).

Due to the reduced buttressing effect, the disparition of the surrounding ice shelves can have severe consequences for the AIS equilibrium. The buttressing effect is supposed to be much more pronounced for the Amundsen and Bellingshausen sectors in the West Antarctic region than other regions (Fürst et al., 2016). This explains why ice-shelf thinning in the West Antarctic region has resulted in stronger glacier flow acceleration. Furthermore, this region is characterised by a bedrock below sea level and a retrograde slope (i.e., upward slope in the direction of flow) which is a precondition of the Marine Ice-Sheet Instability (MISI, Fig. 1.9. This hypothesis suggests that the ice flow is a direct function of the ice thickness at the grounded line (Weertman, 1974; Schoof, 2007). A backward movement of the grounded line associated with a retrograde slope could then result in a larger ice flow and also larger melting surface in contact with the ocean. This then thins the ice sheet inducing more backward movement in a positive-feedback mechanism. Although the retrograde slope does not systematically lead to MISI (Gudmundsson, 2013), it is likely that some glaciers in West Antarctica (Pine Island and Thwaites Glaciers) may already be undergoing MISI (Joughin et al.,

2014; Christianson et al., 2016; Seroussi et al., 2017; Pattyn and Morlighem, 2020).

1.1.3.3 Surface mass balance

There is strong regional variability in recent SMB changes on the AIS. More generally, increasing air temperatures and associated moisture content leads to more surface gain. For instance, Frieler et al. (2015) suggested an increase in accumulation linked to air temperature of $\sim 6\%\,\mathrm{C}^{-1}$. This is confirmed by long-term trend over the two last centuries (e.g., Thomas et al., 2017; Medley et al., 2018; Medley and Thomas, 2019). Snow accumulation then mitigated the twentieth-century SLR with an increasing rate. Diverging trends and disagreements are found for more recent periods. Somes studies (e.g., Bromwich et al., 2004; Monaghan et al., 2008; Lenaerts et al., 2016; Palerme et al., 2017; Medley and Thomas, 2019) reveal a positive non-significant trend after 1950 while others suggest no changes (Monaghan et al., 2006). Furthermore, precipitation (and related accumulation) since 1979 are thought to have either decreased (Monaghan et al., 2006; Medley and Thomas, 2019) or increased before decreasing (Kim et al., 2020; Mottram et al., 2020) suggesting more uncertainties in the recent years. The internal climate variability (including SAM) determining precipitation amounts and patterns compared to the recent (too short) SMB reconstructions might explain the apparent disagreement (Previdi and Polvani, 2016; Medley and Thomas, 2019). SAM-induced changes have likely hidden an increase in accumulation due to the temperature increase expected over the Antarctic Peninsula where climate warming is stronger (Thomas et al., 2017; Medley and Thomas, 2019). The important effects of the SAM, ENSO (and ASL) on accumulation resulted in locally bi-polar diverging trends with an increase in western Antarctic Peninsula, Queen Maud Land, Wilkes Land and a decrease in eastern Antarctic Peninsula, Amundsen region and Adelie Land (Lenaerts et al., 2012b; Velicogna et al., 2014; Raphael et al., 2016; Marshall et al., 2017; Medley and Thomas, 2019; Kim et al., 2020).

The SMB also contributes to the Antarctic mass balance variations. While it is commonly accepted that ocean changes have driven the Antarctic contribution to SLR (e.g., Meredith et al., 2019; Pattyn and Morlighem, 2020), the recent acceleration in mass loss could also be directly attributed to SMB variations instead of enhanced basal melt (Seo et al., 2015; Kim et al., 2020). Following these studies, the apparent abrupt change in mass balance (including in West Antarctic) since 2007 could be mainly explained by a decrease in SMB (and precipitation) which was added to the losses caused by the dynamic ice discharge. This was

also partly highlighted by Velicogna et al. (2014) who found a strong correlation between mass changes and SMB variations except over the Amundsen and the Antarctic Peninsula; yet suggesting a stronger contribution of the ice dynamics in these regions. This highlights the importance of the influence of the SMB, its variability, and atmospheric-induced consequences on the Antarctic mass balance. The Antarctic SMB has a direct and an indirect effect on the sea-level variation: it directly influences sea level by determining snow accumulation over grounded lands and indirectly controls the mass discharge into the ocean by modifying the thickness of both grounded ice and ice shelves (thus indirectly contributing to sea-level variations). However, recent Antarctic SMB trends remain relatively poorly understood as illustrated by the several different and sometimes diverging trends in previous studies. The reasons behind SMB changes (thermodynamics and/or atmospheric dynamics) remain unclear (Lenaerts et al., 2019). Given the global warming context and the important roles of SMB, the present thesis aims to better understand factors influencing the recent and future SMB evolution over the AIS.

1.2 Objectives of this thesis

1.2.1 Sensitivity of the Antarctic SMB to sea surface conditions

The precedent section highlights the recent major influence of ocean changes on the Antarctic mass balance while underlining the SMB contribution to mass balance variations. Furthermore, changes in the ocean are determined by local atmospheric changes. A starting objective of this thesis was then **to determine to what extent the ocean surrounding the AIS can exert a direct influence on the atmosphere and SMB**.

Still little is known about feedbacks forced by the ocean on the atmosphere, their influences on the Antarctic SMB, and potential related uncertainties in SMB estimations. For instance, sea ice affects the exchanges of gases, momentum and heat between the atmosphere and the ocean. It also changes the thermodynamic and radiative properties of the ocean surface due to its high albedo and its thermal insulation power while the temperature at the ocean surface can either warm or cool the atmosphere. Furthermore, the most reliable tool we currently have to perform projections of the SMB, i.e, RCMs especially dedicated to represent the

climate of Antarctica, require the prescriptions of forcing fields at their domain boundaries including sea surface conditions (SSCs, namely sea-ice concentration, SIC, and sea-surface temperature, SST). Since the recent variability of SSCs in the Southern Hemisphere is not reproduced by most models used to force RCMs (Turner et al., 2013a; Mahlstein et al., 2013; Agosta et al., 2015; Shu et al., 2015; Roach et al., 2018) and since the future Antarctic climate could strongly depends on present SSCs (Agosta et al., 2015), projections of the future SMB could be strongly biased.

Moreover, the original aim of the thesis was to study the influence of the coupled ocean-atmosphere system in Adelie Land requiring to couple the atmospheric RCM Modèle Atmosphérique Régional (MAR, Gallée and Schayes, 1994) to the ocean and sea-ice model Nucleus for European Modelling of the Ocean (NEMO, Madec, 2016) - Louvain-la-Neuve sea Ice Model (LIM, Rousset et al., 2015). This coupling should also enable improved representations of interactions between the ocean, the sea ice and the atmosphere. MAR, mainly developed at ULiège, is known as a reference atmospheric model for representing polar climates (Fettweis et al., 2020; Mottram et al., 2020) and is therefore used in this study. Evaluating the sensitivity of the atmosphere and SMB to SSC changes can also be seen as a first evaluation of the interest of coupling these models together (from an atmospheric point of view) compared to other direct developments in the atmospheric model.

1.2.2 Future Antarctic SMB

Future SMB changes will influence the contribution of the AIS to SLR with a direct effect on the grounded ice accumulation and an indirect effect on the ice dynamics. More surface mass gain is expected over the AIS as a result of the temperature-induced snowfall increase (Palerme et al., 2017; Gorte et al., 2020).

The most recent projections of the Antarctic (surface) mass balance (e.g., Seroussi et al., 2020) are directly based on GCMs and ESMs of the 5th and recent 6th phases of the Coupled Model Intercomparison Project (CMIP5 Taylor et al., 2012) and (CMIP6 O'Neill et al., 2016). However, using the outputs of these models to project the evolution of the SMB involves several compromises related to their coarse resolution, their poorer inclusion of typical processes in the polar regions influencing SMB and the neglection of surface runoff and drifting snow (Lenaerts et al., 2016; Favier et al., 2017; Lenaerts et al., 2019; Seroussi

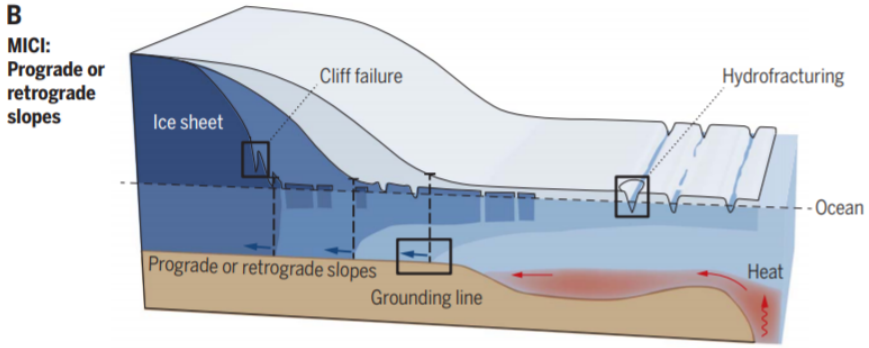

Figure 1.10: Marine Ice-Cliff Instability (MICI) (from Pattyn and Morlighem (2020), credit: N. Cary). Surface meltwater percolates into ice shelves resulting in hydrofracturing which leads to a retreat of the grounded line with potential unstable cliffs.

et al., 2020). This stresses **the need of 1) SMB projections relying on improved and adapted models in the context of global warming and 2) assessing the uncertainties related to using direct outputs from CMIP5 and CMIP6 models** to better understand the sensitivity of the Antarctic SMB to higher temperatures and finally better constrain mass balance projections and Antarctic contribution to SLR.

1.2.3 Physical drivers behind future ice-shelf melt

Ice shelves whose buttressing effect maintains the equilibrium of the AIS, can also collapse due to interactions with the atmosphere. Percolation of surface melt into the ice can lead to hydro-fracturation (Fig. 1.10) which can occur when pressure increases after filling of crevasses by liquid and refrozen water (Scambos et al., 2000; van den Broeke, 2005). Furthermore, the meltwater accumulated on ice shelves can cause bending potentially breaking ice shelves (Banwell et al., 2019). Both these processes reduce the buttressing effect and increase the contribution of the AIS to SLR. Finally, repeated hydrofracturing and ice-shelf breaking could induce the Marine Ice-Cliff Instability (MICI) where high newly-created cliffs located near the grounded line would become unstable and could collapse (Fig. 1.10). DeConto and Pollard (2016) have even suggested that this process could significantly increase the Antarctic contribution to SLR. However, their conclusions rely on unreached melting rates over the AIS while MICI is not needed to reconstruct the past and recent sea-level variations due to ice sheets questioning the actual importance of this process (Edwards et al., 2019).

Although there was non-significant change in melt volume either continent-

wide or locally since 1979 and by extension in runoff (e.g., Kuipers Munneke et al., 2012; Van Wessem et al., 2018; Agosta et al., 2019), several ice-shelf collapses have occured over the Antarctic Peninsula during the late 1990s/early 2000s resulting in an enhanced ice discharge (e.g., Scambos et al., 2004, 2014). In the same way, ice-shelf collapse is projected to increase SLR when taken into account in mass balance projections (Seroussi et al., 2020). However, projected melt increases over the ice shelves significantly diverge under different emission scenarios and models by 2100 (Trusel et al., 2015). The large uncertainties in melt projections could then contribute significantly to the overall mass balance uncertainties. Even if melt and ice-shelf collapses do not directly contribute to the SLR, this also shows **the importance of relying on better constrained projections of ice-shelf melt and of a better understanding of uncertainty sources in melt projections**.

1.2.4 Objectives

This PhD thesis is organised around 3 scientific objectives :

1. investigate the sensitivity of the Antarctic SMB to SSCs and more specifically to CMIP5 SSC anomalies for the period 1979–2015.
2. quantify the surface response of the AIS to warmer climates, and more specifically the different responses of the grounded ice and ice shelves for several climate scenarios.
3. study the factors resulting in differences in projected melting on the Antarctic ice shelves.

1.3 Thesis outline

The manuscript consists of eight chapters summarized in Fig. 1.11.

Chapter 2 provides a description of MAR, the regional climate model used all along this thesis, and its large-scale forcings. It also presents a new database gathering near-surface climate and SMB observations, melt estimates as well as the development of a robust comparison method that enables a comprehensive evaluation of MAR.

Chapter 3 evaluates MAR with near-surface climate and SMB observations and melt estimates. It is also the opportunity to prove the consistency of the

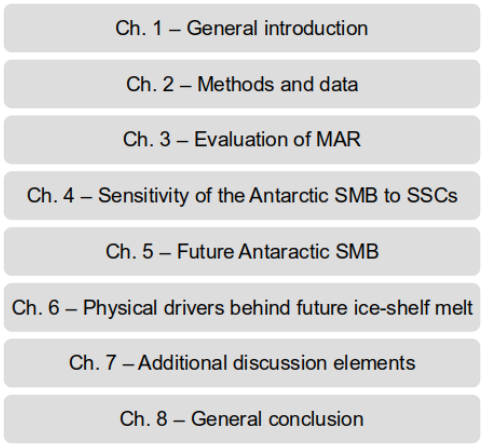

Figure 1.11: Thesis outline

results with changing model versions, resolutions, and forcings throughout these 4 years of research.

Chapters 4 to 6 present the main results obtained during this thesis. These chapters correspond to papers that have been published (/accepted) or will be submitted to international peer-reviewed journals. Each introduction to these chapters presents the concepts needed (re)place them in their respective contexts. Consequently, there may be some redundancy with the introduction of these different chapters, which is however necessary for each chapter to be self-sufficient.

Chapter 4 is based on **Kittel, C.**, Amory, C., Agosta, C., Delhasse, A., Doutreloup, S., Huot, P.-V., Wyard, C., Fichefet, T., and Fettweis, X.: Sensitivity of the current Antarctic surface mass balance to sea surface conditions using MAR, The Cryosphere, 12, 3827–3839, 2018. It investigates the direct effect of changes in SSCs on the Antarctic SMB (objective 1).

Chapter 5 follows **Kittel, C.**, Amory, C., Agosta, C., Jourdain, N. C., Hofer, S., Delhasse, A., Doutreloup, S., Huot, P.-V., Lang, C., Fichefet, T., and Fettweis, X.: Diverging future surface mass balance between the Antarctic ice shelves and grounded ice sheet, The Cryosphere Discuss. [preprint], accepted, 2020. It highlights the contrasting effect of global warming on the future grounded and ice-shelf SMB in addition to reconstructing the SMB for different scenarios and global models (objective 2).

Chapter 6 is a draft of a publication that will be submitted shortly: **Kittel, C.**, Amory, C., Hofer, S., Agosta, C., Jourdain, N. C., Gilbert, E., Gallée, H., Fettweis, X.: Cloud phase drives differences in future surface melt over Antarctic

ice shelves, in preparation. This chapter studies the physical drivers of the future melt over the Antarctic ice shelves and attributes to differences in cloud properties the projected spread in melt increase (objective 3).

Chapter 7 introduces additional experiments that were made in parallel with the overarching structure of the thesis and discusses several elements of perspectives covered in the different chapters, notably the influence of blowing snow processes, the resolution used for our simulations and the interest of a coupling with an ocean model over Adelie Land.

Finally, Chapter 8 summarizes the main results of the PhD thesis and presents perspectives for further research.

CHAPTER 2

Methods and data

This chapter provides a description of MAR which is the regional climate model used in the thesis (Sect. 2.1). It also describes the large-scale forcings over the present and future periods (Sect. 2.2). This chapter also presents a new database that gathers near-surface climate (Sect. 2.3.1) and SMB observations (Sect. 2.3.2). This set of observations is based on pre-existing databases that were gathered together for the first time and also includes updates from more recent data. Finally, melt estimates used to evaluate MAR are also described (Sect. 2.3.3).

2.1 The regional climate model MAR

The "Modèle Atmosphérique Régional" (MAR) is a polar-oriented RCM firstly developed for representing katabatic winds over Terra Nova Bay (located in Victoria Land, East Antarctic; see Fig. C.2) in 1994 (Gallée and Schayes, 1994). The model has then also been used over the Greenland Ice Sheet (Gallée et al., 1995) before being adapted to temperate (De Ridder and Gallée, 1998; Brasseur et al., 1998) and tropical climate (Massager et al., 2004). Since those first studies, MAR has evolved to represent more physical processes and include many more parameterisations. The model is now recognised as a reference for simulating the climate and SMB of the two ice sheets (see Fettweis et al. (2020); Mottram et al. (2020)) and is also a member of several model intercomparison projects for instance over Belgium (e.g., Termonia et al., 2018) or the Arctic (e.g., Akperov et al., 2018; Inoue et al., 2021). The very first version of MAR only represented the atmosphere and after its interactions with the surface. This original atmosphere-land component has been recently coupled to both ocean and ice-sheet models leading MAR to rather an earth system model able to simulate interactions between atmosphere, ocean, and ice dynamics.

This section does not aim to retrace the history of the developpement of MAR or the parameterisations that have been included along with model developpements before being depreciated (we refer to the list of publications involving MAR available on https://mar.cnrs.fr/, last accessed 22/01/2021), but to present the model in its current state (MARv3.11) and undocumented changes. Moreover, the description of MAR in the next sections would be more exhaustive

than frequently needed for ensuring a general comprehension of how the model works. They have therefore been constructed with several levels of readings for each aspect of the model from summary to in-depth descriptions.

MAR, as most current atmospheric models (whether for climatological or meteorological applications), is composed of 1) a dynamical core that solves the primitive and known equations of the atmosphere and 2) a physical heuristic core for all the processes not represented by the dynamical core. Although the primitive physical equations representing the conservation of mass, momentum, and (heat) energy) are shared by the different models, their mathematical expression mainly depends on approximations and numerical methods used by each model. The dynamical core is the part of the model code that simulates the large-scale and horizontal movements. The physical core and the included parameterisations of a model aim to represent the effects of processes not resolved by the dynamical core on the energy source terms in the primitive equations within the 1D atmospheric column through heat exchanges by radiation, water-phase changes, interactions with the surface, or subgrid-scale movements (turbulence, convection). This second part is based in particular on a combination of physical equations and conservation laws, theories, empirical and semi-empirical parameterisations. This is a strong source of spread between models and can be regarded as the main strength of a regional model like MAR that seeks to represent in detail the processes specific to a given area. The chapter is thus organised as follows: a brief presentation of the dynamic core of MAR and the numerical methods used (Sect. 2.1.1), the nudging methods (Sect. 2.1.2) and a more exhaustive presentation of the physics of MAR (Sect. 2.1.3).

2.1.1 Dynamical core

MAR is a hydrostatic model that solves the primitive equations as described in Gallée and Schayes (1994). The mass conversion equation is expressed in its full continuity form without approximation. In order to better represent topography-induced variations in the atmosphere, the vertical coordinate (σ_{level}) is normalized by the presure (Eq. 2.1):

$$\sigma_{level} = (p - p_{top})/(p_s - p_{top}) \tag{2.1}$$

where p, p_{top}, and p_{top} are respectively the level pressure, the surface pressure and a constant pressure at the top of the atmosphere (p_{top}= 0.1 hPa in most current

MAR configurations).

The model also takes into account the air loading (Eq. 2.2, adapted from Gallée (1995)) due to hydrometeor particles (see subsect. 2.1.3.1 for the descriptions of hydrometeors in MAR) in the air specific mass (air density) by changing the virtual temperature and the hydrostatic equation.

$$Loading = 0.85 \times (q_v - 1.64 \times (q_w + q_i + q_r + q_s)) \tag{2.2}$$

where q_v, q_w, q_i, q_r, q_s are the specific humidity concentration ($\mathrm{kg\,kg^{-1}}$), and the concentrations ($\mathrm{kg\,kg^{-1}}$) of cloud droplets, ice crystals, rain droplets, and snow particles.

The numerical scheme relies on a spatial discretisation based on Arakawa A grid (Arakawa and Lamb, 1977). It solves differential equations of horizontal momentum and conservation using finite differences and more especially a numerical centered scheme, second-order-accurate (leap-frog) in time and fourth-order accurate in space (Gallée and Schayes, 1994). This scheme computes the new values at distinct interleaved time steps using different levels of precision for time and space. The advection is handled by a semi-Lagrangian scheme adapted from Pielke (1984) and improved by Seibert and Morariu (1991) that represents a compromise between the Eulerian fixed frame and the Lagrangian parcel frame of reference. Wind-components (u,v), specific humidity and potential temperature are filtered using a two-dimension low-pass filter (Raymond and Garder, 1988). In the same way, the mass conservation equation is corrected following the relaxation term defined by Yan and Anthes (1987) to limit mass changes in open-boundary conditions. Finally, MAR is parallelised using the application programming interface Open-MP (Fettweis et al., 2017).

2.1.2 Nudging and boundaries

As MAR only simulates atmospheric processes and their interactions with the surface over a regional area, the model has to be constrained at its boundaries by large-scale forcing fields. These forcings mainly come from two different kinds of models: reanalyses and GCMs or ESMs. A reanalysis is a climate model that associates a dynamical core and physical-process representations (as does MAR) with different levels of complexity of data (observation) assimilation. GCMs and ESMs are also climate models representing the Earth's climate but without

assimilation methods, mainly used to study past and future climate variations. We refer to Sect. 2.2 for a more detailed description of the large-scale forcings used in this manuscript.

The boundary conditions enable to take into account the contribution of larger (global) meteorological processes and climate variability. The integration domain is divided in 3 areas (Fig. 2.1). At the lateral boundaries, the MAR results are prescribed by the large-scale forcing field values, while inside the domain it does not assimilate any observations or values from the large-scale forcing to drive its results. The 7-pixel transition between these two areas (the relaxation zone) aims to progressively make the model solution independent of the large-scale forcing. MAR is forced by 6-hourly lateral conditions and a linear interpolation is made at each model time step to ensure a smooth temporal transition from the current forcing to the next one.

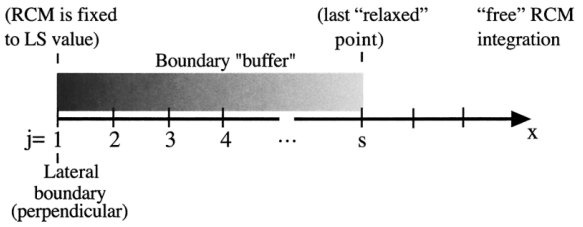

Figure 2.1: Schematic view of the boundary treatment reproduced from Marbaix et al. (2003)

The dynamic relation includes a Newtonian term (following Davies (1976)) and a diffusion term (Davies, 1983; Anthes et al., 1989). The Newtonian term removes a part of the difference between the MAR results and its forcing while the second term diffuses the differences horizontally. We refer to Marbaix et al. (2003) for more details about the lateral nudging of MAR.

The relaxation method described above is only applied at the lateral boundaries where MAR is constrained by the surface pressure (influencing the vertical discretisation), temperature, specific humidity, and both u-v wind components from the large-scale model. It then does not directly assimilate neither clouds nor precipitation. Since MAR does not represent the ocean (except in coupling experiments such as in Jourdain et al. (2011), it is also forced by SCCs: SST and SIC. For these two variables, there is no buffer zone as above and MAR is entirely forced by SST and SIC from the large-scale fields.

MAR has firstly been developed to simulate the climate of local areas. It then adds small-scale values in its results while the general circulation is supposed

to remain the one prescribed by the large-scale forcing. For larger domains (such as over the AIS or the Arctic), MAR has a greater degree of freedom due to a larger modelled area. To prevent it from creating its own atmospheric circulation and better constraining the climate variability by the large-scale forcing, an additional nudging was added at the top of the atmosphere following van de Berg and Medley (2016). This nudging is qualified to be an indiscriminate forcing as it adjusts MAR results to the large-scale fields without considering spatial scales or structures (as opposite to spectral nudging). Although this one removes a fraction of MAR small-scale patterns not represented in the coarser-resolution large-scale forcing, it combines both the added value from the RCM and the interannual variability from its forcing in the upper layers of troposphere ($\geq$ 200hPa) and stratosphere. The upper air relaxation used in MAR (Agosta et al., 2019) is only applied on temperature and u-v wind components in the higher atmospheric levels. The upper specific humidity is not nudged to prevent any impact on the cloud microphysics of the model. Furthermore, the upper air relaxation is stronger at the top of the model while gradually decreasing for underneath layers. Due to the sigma coordinates, the relaxation never directly changes the near-surface fields even in case of strong topography variations (van de Berg and Medley, 2016).

2.1.3 Model physics

2.1.3.1 Cloud-microphysical scheme

The model includes a cloud-microphysical scheme solving conservation equations for the concentration of five water species (cloud droplets (q_w), ice crystal (q_i), rain drops (q_r), snow particles (q_s), and specific humidity (q_v) firstly described by Gallée (1995)) and the ice crystal number(n_i) (Massager et al., 2004). MAR solves the conservative equation 2.3 for every horizontal pixel and vertical-σ layer.

$$\frac{\delta q_\alpha}{\delta t} = -u \cdot \frac{\delta q_\alpha}{\delta x} - v \cdot \frac{\delta q_\alpha}{\delta y} + \dot{\sigma} \cdot \frac{\delta q_\alpha}{\delta \sigma} + F_{q\alpha} + P_{q\alpha}(+P_{sed}) \tag{2.3}$$

where the three first terms represent the 3D advection by the wind following the x, y and σ directions, $F_{q\alpha}$ the turbulent flux divergence of the hydrometeor specie, and P_{sed} a source term. P_{sed} is an additional term that describes the sedimentation of precipitating hydrometeors (rain drops, snow particles, and ice crystals) depending on their specific falling velocities. The source term in Eq. 2.3 represents the 21 microphysical processes detailed in Table 2.1 originally based

on Kessler (1969) parameterisations in addition to the sedimentation towards the surface of the three precipitating hydrometeors. Since graupels are not (fully yet) included in the model, all accretion processes that should result in graupel following Lin et al. (1983) lead to snowflake formation assuming a Marshall-Palmer size distribution (Gallée, 1995).

Table 2.1: Microphyscal processes represented in MAR and associated references as firstly described by Gallée (1995) and modified afterwards

Nucleation by cloud droplet solidification (q_w to q_i, if $TT \leq -35$ °C)	Emde and Kahlig (1989); Levkov et al. (1992)
Deposition and condenstation-freezing nucleation (q_w to q_i, if $TT \leq -35$ °C)	Meyers et al. (1992); Levkov et al. (1992)
Contact-freezing nucleation or depositional growth of cloud ice (q_w to q_i)	Meyers et al. (1992); Prenni et al. (2007); Levkov et al. (1992)
Ice crystal sublimation (q_i to q_v)	Emde and Kahlig (1989); Levkov et al. (1992)
Ice crystal melting (q_i to q_w, if $TT \geq 0$ °C)	Levkov et al. (1992)
Water vapor condensation (q_v to q_w, if $TT \geq -35$ °C)	Emde and Kahlig (1989)
Cloud droplet evaporation (q_w to q_v)	Emde and Kahlig (1989)
Cloud droplet autoconversation (q_w to q_r)	Lin et al. (1983); Sundqvist (1988)
Depositional growth of snow (q_i to q_s)	Levkov et al. (1992)
Ice crystal aggregation (q_i to q_s)	Levkov et al. (1992)
Accretion of cloud droplet by rain (q_w to q_r)	Lin et al. (1983); Emde and Kahlig (1989)
Accretion of cloud droplet by snow (q_w to q_s)	Lin et al. (1983); Locatelli and Hobbs (1974)
Accretion of ice crystal by snow (q_i to q_s)	Lin et al. (1983); Levkov et al. (1992)
Accretion of ice crystal by rain (since no graupel, q_i to q_s, if $TT \leq 0$ °C)	Lin et al. (1983); Levkov et al. (1992)
Accretion of rain by ice crystal (since no graupel, q_r to q_s, if $TT \leq 0$ °C)	Lin et al. (1983)
Accretion of rain by snow (since no graupel, q_r to q_s, if $TT \leq 0$ °C)	Lin et al. (1983); Emde and Kahlig (1989)
Accretion of snow by rain (since no graupel, q_s to q_r, if $TT \geq 0$ °C)	Lin et al. (1983); Emde and Kahlig (1989)
Rain freezing (since no graupel, q_r to q_s, if $TT \leq 0$ °C)	Lin et al. (1983); Emde and Kahlig (1989)
Rain evaporation (q_r to q_v)	Lin et al. (1983)
Deposition on snow (q_v to q_s) or sublimation (q_s to q_v)	Lin et al. (1983)
Snow melting (q_s to q_r, if $TT \geq 0$ °C)	Lin et al. (1983)
Rain sedimentation	Emde and Kahlig (1989)
Snow sedimentation	Emde and Kahlig (1989); Levkov et al. (1992); Locatelli and Hobbs (1974); Fettweis et al. (2017)
Ice crystal sedimention	Levkov et al. (1992)

Table 2.1 also lists the parameterisations that have been recently included in MAR since the original description by Gallée (1995). In particular, the ice crystal nucleation used by Lin et al. (1983) (and based on Fletcher (1962) overestimates ice crystal concentration leading to the model underestimation of the downwelling solar radiation towards the surface, the convective available potential energy (CAPE), and rain (Massager et al., 2004). It has thus been replaced by Meyers et al. (1992)'s parametrization later improved by Prenni et al. (2007). Ice crystal sedimentation is not neglected anymore by adding a prognostic equation for ice crystal number according to Levkov et al. (1992). Furthermore, the conversion rate of cloud droplets to rain particles takes into account an adapted parameterisation from Sundqvist (1988). It relies on two parameters: a critical cloud water mixing ratio (qwo) enabling the rainfall formation and a characteristic time scale for auto-conversion processes (CO). Note that a low fraction of cloud droplets can be converted to rain even if q_w is lower than qwo (Delobbe and Gallée, 1998). In MARv3.11, qwo and Co values are respectively fixed to $1{\cdot}10^{-3}$ ($\mathrm{kg\,kg^{-1}}$) and $1{\cdot}10^{-4}$. Finally, other subtle adjustments such as an increase in snowfall sedimentation velocity or cloud lifetime (Fettweis et al., 2017, 2020) have been made to tune the model in order to more accurately reproduce clouds over the polar ice sheets.

2.1.3.2 Radiative scheme

The radiative scheme is composed of two individual shortwave and infrared schemes as detailed in Morcrette (2002). MAR uses the radiative scheme from the ECMWF ERA40 reanalyses Uppala et al. (2005).

The shortwave radiation scheme (Fouquart and Bonnel, 1980) has been updated by Morcrette (1993). It solves the shortwave transfer equation by using a two-stream method that accounts for the scattering (due to clouds and aerosols) following a Delta-Eddington approximation (Joseph et al., 1976). For each atmospheric layer, the transmission and reflectivity depends on 1) scatterings by molecules (Rayleigh scattering), aerosols, and clouds; 2) absorptions by gases, aerosols and clouds; 3) reflection by the surface (Morcrette, 2003). Water vapour, uniformly-mixed gases (CO_2, O_2 in the original version and CH_4, N_20, CO as updated by Morcrette (1993)), and ozone (with a function of the effective zenith angle) are taken into account, as well as the temperature and the pressure. Following Morcrette (1993), the shortwave downwelling radiation (SWD) reaching the surface is particularly dependent on the aerosol concentration. Finally, the Fouquart and Bonnel's scheme determines the transmission and reflectivity for clear-sky and cloudy conditions separately assuming maximum-random cloud overlap. The scheme assumes that all cloud layers maximise their vertical overlap and that each cloud layer is treated independently (See Morcrette and Fouquart (1986) for the sensitivity of the radiative scheme to this assumption).

For the longwave radiation scheme, MAR uses an improved version (Morcrette et al., 2003) of the Rapid Radiation Transfer Model (Mlawer et al., 1997) based on the correlated-k method. This method is an approximate technique that enables fast computations of radiative fluxes and cooling rates for non-homogeneous atmospheres using limited approximations. The continuous infra-red spectrum is divided in several discrete bands. Each band corresponds to a small spectrum window where a limited number of gases (2 in this scheme) could strongly absorb the energy. The absorption due to these gases is modelled with a high precision, while the other gases (considered to be minor absorbers) are less rigorously taken into account. Represented species are water vapour, CO_2, O_3, CH_4, N_2O and the main halocarbons (CFC-11, CFC-12, CFC-22, CCl-4) (Mlawer et al., 1997). Similarly to the shortwave scheme, the longwave scheme includes a maximum-random overlap assumption (Morcrette, 2002).

Both improved shortwave and longwave radiation schemes represent the in-

teractions (absorption, attenuation, scattering, and reflection) between hydrometeors computed by the cloud-microphysical scheme and radiations. The radiative scheme uses q_i, q_w, and q_v concentrations from each atmospheric layer to determine the cloud optical properties. The latests depend on the region of the solar spectrum and on the particle phase contained in the cloud. Since properties of mixed phase clouds (containing both liquid and ice particles) are the summed contribution of both phases (Morcrette, 1993), the two next paragraphs will describe the individual contribution of ice and water particles on shortwave and longwave cloud optical properties.

For shortwave radiations, the scheme uses the microphysical properties defined by Slingo (1989) for water clouds and by Fu (1996) for ice clouds. Slingo's parameterisation links water cloud properties with the cloud liquid water path (vertically-integrated water content between the cloud base and top) and equivalent droplet-radius size distribution neglecting the effect of water vapour. In the same way, the shortwave optical properties for ice clouds are defined on the ice water content and the generalised effective size that represents the ice-crystal size distribution. In a few words, smaller ice particles have a higher radiative effect resulting notably in more scattering and absorption than larger ice particles (Morcrette, 1993).

Similarly, the water cloud properties for longwave is a function of the liquid water content vertically-integrated over the layer (liquid water path) and the effective radius based on the droplet size distribution as described by Lindner and Li (2000). This parameterisation neglects scattering interactions which makes absorption the dominant processes for longwave radiation. Optical properties for ice particles in the longwave spectrum are functions of the cloud ice water content and generalised effective size that accounts for different ice crystal distributions (Fu et al., 1998). Furthermore, the radiative scheme used by MAR also enables the use of different parameterisations to compute the cloud optical properties. Morcrette (2002) suggested a relatively low effect on longwave but a higher effect (up to 10 unitW m^{-2}) on the shortwave in cloudy conditions.

The radiative transfer relies on the effective radius which is a factor describing the distributions of the mass and volume of the particles. The ice effective radius is computed using Sun and Rikus (1999) parametrization and is a function of the ice-water content and cloud temperature. It has been adapted to Antarctic conditions using a value of 15 µm as the minimum diameter for ice particles (Walden et al., 2003). The liquid effective radius is a linear function of the

liquid water content and the droplet water concentration contained in the cloud depending on the continental or oceanic origin of the air masses (Martin et al., 1994) which in MAR is simply depending on the land-sea mask.

As highlighted above, radiative cloud properties do not directly depend on q_s concentration. The q_s concentration is implicitly taken into account by being partially included in the q_i concentration from each layer treated by the radiative scheme. The contribution of q_s is expressed as an additional mass for q_i by assuming that the total ratio of q_s and q_i is similar to the ratio of effective radii, i.e only 30% of q_s is added in q_i seen by the radiative scheme (Gallée and Gorodetskaya, 2010). The effect of rain droplets on radiations is neglected. This assumption is reasonable knowing that the fall velocity of rain droplets used in MAR (Emde and Kahlig, 1989) induces that most of them reach the surface within one time-step of the radiative scheme.

Gas concentration are provided by historical concentration, in particular the MAR radiative scheme uses the Fortuin and Langematz (1995)'s ozone climatology. Future concentration are specified by the selected emission pathway, i.e the Representative Concentration Pathway (RCP) (Moss et al., 2010) used for the latest IPCC report or the more recent Shared Socioeconomic Pathways (ssp) (O'Neill et al., 2016) that represents future emissions for different socio-economic trajectories. Note that while the cloud mycrophisical scheme uses a constant aerosol value (Meyers et al., 1992), the aerosols inputs of the radiative scheme are time-varying loads based on a monthly climatology of tropospheric aerosols (soil dust, sulfate, sea salt, black carbon, and organic) defined by Tegen et al. (1997) and daily volcanic aerosols from the Goddard Institute for Space Studies. Only the present observed aerosol-radiation interactions till 2002 are taken into account in MAR since cloud-aerosols interactions are neglected (Wyard et al., 2018).

2.1.3.3 Convective scheme

The hydrostatic approximation used by MAR implies that other vertical forces are negligible compared to pressure forces (Archimede) and weight. This means that only relatively small vertical movements due to small (smoothed) topography variations are permitted. In other words, vertical movements are negligible compared to horizontal movements. This is suitable for representing the large-scale katabatic flow. This limits the horizontal resolution over complex-topography areas such as the Antarctic Peninsula where strong vertical topographic

gradients at very high resolution could induce strong vertical updrafts and make the approximation invalid; but also requests an implicit representation of large vertical movements that occurs during convective events. Cold conditions in Antarctica prevent the development of strong convective movements, but yet enables convection to occur (Van Den Broeke et al., 2006; Van Wessem et al., 2014a; Kuipers Munneke et al., 2018). Furthemore, a low amount of precipitation over coastal areas can be generated by convective clouds (Van Wessem et al., 2014b).

The convection in MAR is based on an updated version of the convective scheme from Bechtold et al. (2001) used in MESO-NHv5.3.1 (Lac et al., 2018). The parameterisation is a bulk mass-flux that represents the deep and shallow convections. It represents moist thermodynamics and convective downdraughts as well as dry thermals. If the temperature of at least one atmospheric layer is higher than -3°C, or if there is no temperature inversion in the near-surface levels and the near-surface temperature exceeds 10°C at night, the convective scheme determines whether the atmospheric profile is unstable. If the profile is considered as unstable, the convective scheme tries to restore an equilibrium by implicitly representing vertical mouvements and by inducing hydrometeor concentration and temperature changes. In the case of the scheme used by MAR, the equilibrium is assumed to be restored when 90% of the convective available potential energy has been removed (Bechtold et al., 2001). Two types of different convections are explicitly represented: shallow and deep convections that differ in the size of the clouds (>500 m and >3000 m) and the characteristic time-scale (shallow between 1h and 3h and deep between 30 min and 1h). The deep convection scheme is based on Kain and Fritsch (1990) that also represent the convective clouds (Lac et al., 2018). The scheme predicts the temporal evolution of atmosphere quantities (notably momentum, temperature, and hydrometeor concentrations) as well as liquid and solid precipitation engendered by the convective adjustments.

Since convective precipitation is assumed to instantaneously reach the surface, their interactions with the surrounding atmosphere is only accounted for in the convective scheme. This means that rain and snowfall computed by the convective scheme follow different processes than the ones described in Sect. 2.1.3.1. In the same way, they are not included in the quantities seen by the radiative scheme. Doutreloup et al. (2019a,b) evaluated the effect of using different convective schemes in MAR to represent present and future rainfall in Belgium and found significant differences in modelled precipitation although no scheme resulted in a

better representation of precipitation than another one.

2.1.3.4 Turbulence scheme

Similarly to convective movements, subgrid-scale and high-frequency turbulent movements cannot be directly represented by the model. This means that parameterisations are needed to represent heat, momentum, and hydrometeor transfers. Subgrid-scale fluxes are parameterised differently in the surface boundary layer and above it. The turbulence in MAR has been particularly developed to represent very stable conditions that can be found over the ice sheets (Duynkerke, 1991; Duynkerke and Van den Broeke, 1994).

The turbulence above the surface boundary layer is modelled using the one-and-half order closure $E - \epsilon$ model by Duynkerke (1988) and updated by Bintanja (2000) for taking into account the sedimentation of snow particles. It includes prognostic equations for turbulent kinetic energy production (E) and turbulent kinetic energy dissipation (ϵ). The turbulent mixing length then depends on the local flow characteristics which is important for representing the katabatic winds (Gallée et al., 2001). The turbulence also depends on water phase changes (Duynkerke and Driedonks, 1987).

In the surface boundary layer, the parametrization of subgrid-scale fluxes is based on Monin-Obukhov similarity theory using stability functions described in (Duynkerke and Van den Broeke, 1994). MAR also represents the increase in air density due to the presence of snow by changing the virtual potential temperature used in the turbulent scheme.

Furthermore, MAR represents the small-scale exchanges between sea sprays and the near-surface atmosphere. The projected water enhances evaporation acting as a moisture source over the ocean and decreasing the air potential temperature. These exchanges are parameterised as a function depending on the fraction of open ocean and the near-surface wind speed (Andreas, 1990, 1995; Andreas and Emanuel, 2001; Andreas and Decosmo, 2002; Andreas, 2004).

2.1.3.5 Surface module

One of the MAR strengths is its ability to represent the interactions between the atmosphere and the surface, but also the evolution of the properties of the soil, the vegetation, and especially the snowpack. The transfer of mass and energy

between the surface and the atmosphere is simulated by the 1-D surface scheme SISVAT (Soil Ice Snow Vegetation Atmosphere Transfer) module, which consists of soil and vegetation (De Ridder and Schayes, 1997; De Ridder, 1997), snow (Gallée and Duynkerke, 1997; Gallée et al., 2001) and ice (Lefebre et al., 2003) sub-modules.

For MAR and SISVAT, each surface pixel is either fully oceanic or continental (including the floating Antarctic ice shelves). However, the surface pixel in SISVAT includes a tilling that divides the surface pixel in several sub-pixels in order to better represent the heterogeneity of surface conditions. Oceanic pixels can then be open-ocean, ice-covered, or any combination of both conditions (Gallée, 1996). Similarly, continental pixels are divided into three subpixels representing several types of vegetations (De Ridder and Gallée, 1998) for temperate and tropical climate configurations of MAR, or in two surface subpixels for the permanent ice and tundra (Fettweis et al., 2013) in polar configurations, excepted over the AIS where the surface is composed of permanent ice and exposed rocks called Nunataks (Kittel et al., 2020). SISVAT is called for each subpixel and MAR averages momentum and energy fluxes using weighting coefficients according to the sub-pixel fraction (De Ridder and Gallée, 1998). SISVAT is forced by atmospheric variables from the nearest surface level (wind speed, temperature, humidity, precipitation, and both downwelling shortwave and longwave fluxes) to compute turbulent (latent and sensible) fluxes, reflected shortwave and emitted longwave radiations.

Soil and vegetation

The soil and vegetation modules (De Ridder and Schayes, 1997) describe the properties of 7 soil vertical layers and one vegetation layer, and resulting transfers with the atmosphere. There are 12 types of vegetation (and a 13th that represents urban area) which have different properties of albedo, emissivity, and evaporation capacity. Although the "vegetation" classes are not used in the Antarctic configuration of MAR, the vegetation module will be described for the sake of completeness in the next paragraphs and because it is closely related to the soil module.

The modules solve the energy and water balances separately for the soil and vegetation. In SISVAT, both the vegetation and soil are considered to be directly ventilated by the turbulence which means that direct exchanges between the ground and the canopy are neglected (De Ridder and Schayes, 1997). The sensible heat flux is then computed as the sum of the ground and vegetation

contributions, while the latent heat flux is also the sum of both these contributions (evapotranspiration and ground depending on the soil humidity potential) and the direct contribution of evaporation in case of wet leaves.

The vegetation is described with several properties which facilitate or mitigate the canopy transpiration and which absorb or reflect more radiations. The transpiration depends on differences in water potential between the soil and the leaves that regulate the flow from the ground to the atmosphere through the canopy. It takes into account the soil-root resistance and the number of roots fraction in the upper soil (De Ridder and Schayes, 1997). Each vegetation type has its own stomatal resistance to represent leaf properties and resulting resistance compared to radiation, water stress, temperature or humidity saturation deficit. Monthly climatology of the Leaf area index (LAI) from the MERRA-2 reanalysis (Gelaro et al., 2017) are used to determine the stomatal resistance and inherent transpiration, the heat vegetation capacity (Gallée and Duynkerke, 1997) and interactions with solar radiations (De Ridder, 1997). In addition to LAI, the canopy surface energy budget takes into account zenith and azimuth angles, and reflective/absorptive properties of the different vegetation classes. SISVAT also represents multiple shortwave scattering due to multiple leaf-interactions and the longwave emission trapping inside the canopy that result in a higher canopy emissivity than the emissivity of a single leaf (De Ridder, 1997). Furthermore, the canopy layer acts as a supplementary layer above the ground for radiations (De Ridder, 1997).

In the soil and vegetation modules in SISVAT, the liquid water can either be pumped towards the surface by the evapotranspiration of the ground and the canopy, or percolate into the ground. The diffusion-gravitation equation that represents the transport of liquid water into the soil is based on the soil water content that determines the soil water potential and hydraulic conductivity following (Clapp and Hornberger, 1978) and the soil hydraulic diffusivity (Hillel, 1971). When the liquid water (rain and snow melting) amount exceeds the maximum infiltration rate, the extra water is assumed to runoff and is considered to be lost for the soil water balance in the absence of a river scheme.

Rocks (nunataks or non-snow-covered ground) and surface open-ocean are considered as two different soil classes in SISVAT. The soil heat capacity depends on the soil substrates and water content. Ocean is considered permanently saturated in water. Exposed rocks have a low albedo (0.17) contrasting with the prevailing high albedo of the snow over the AIS. The open-ocean albedo is fixed at

0.11. Open-ocean roughness length for momentum and heat follows Wang (2001) while the soil roughness length for rocks is a fixed value (0.01).

Ice and snow

The dynamical snow and ice components represent snow properties and metamorphism across 30 snow/firn/ice layers resolving the 20 first meters of snow/ice over the ice-sheet pixels. In SISVAT, sea ice potentially covered by snow is represented with the same processes as the snow/ice on the ice sheet. While the snow/ice height is kept fixed over the AIS, the sea-snow/ice thickness is constrained by th e presence of sea ice in the large-scale forcing. For each surface pixel with a SIC value greater than 0%, the MAR sea-ice thickness is initially fixed at 55 cm and sea ice can be covered by snow. The sea-ice thickness can then evolve as a function of accumulated snowfall or surface melt, with a minimum thickness of 10 cm as long as the forcing SIC is positive. Similarly, the snowpack height over rocks changes according to snow accumulation or erosion without any minimal thickness.

The snow and ice module consists of the physical snowpack model of (Gallée and Duynkerke, 1997) and a former version of CROCUS (Brun et al., 1989) with snow metamorphism laws (Brun et al., 1992). The metamorphism laws describe the snow grains in terms of dendricity, sphericity, and descriptive size. The fresh-fallen snow has a dendricity around 1 and decreases to 0 representing the part of original crystal shapes that are still in a snow layer. Sphericity (0-1) represents the ratio of rounded shapes compared to angular and evolves according to temperature gradients between the snow layers. Large (small) gradients result in decreased (increased) sphericity.

The snowpack is also described through other physical parameters: temperature, liquid water content, and density. Over the AIS, the density of the fresh falling snow (Eq. 2.4) is a function of the 10 m wind speed ws_{10} ($\mathrm{m\,s^{-1}}$) (adapted from Agosta et al. (2019) in Kittel et al. (2020) to fit density observations over the upper 50 cm (Agosta et al., 2019, Table S2):

$$\rho_\mathrm{s} = 200 + 32 \cdot \mathrm{ws}_{10}, \tag{2.4}$$

with minimum and maximum values fixed to 300 and 400 $\mathrm{kg\,m^{-3}}$. The dry snow settling is parameterised as a function of the weight of overlying layers and effect of metamorphism (described in Gallée and Duynkerke (1997) following Navarre (1975)). Densification also occurs as a consequence of melt and refreezing into

the snowpack that promotes grain cohesion and decreases the firn air content. In MAR, the snow is assumed to have density values between $300\,\mathrm{kg\,m^{-3}}$ and $450\ \mathrm{kg\,m^{-3}}$ while ice has a minimal density of $830\,\mathrm{kg\,m^{-3}}$. Between these two types is the firn ($450\,\mathrm{kg\,m^{-3}}$ – $830\,\mathrm{kg\,m^{-3}}$).

Sea-ice and ice-sheet surfaces have the same thermal and texture properties. The snow-conduction coefficient is a function of the density Yen (1981) while the snow-heat capacity is fixed at $2105\,\mathrm{J\,kg^{-1}\,K^{-1}}$ (Loth et al., 1993) and emissivity of the snow is 0.99. In MARv3.11, the roughness length for momentum z_{0m} is fixed at 1 mm but can also be a function of the air temperature as in the previous model version (Agosta et al., 2019) and used for Ch. 4. The contribution of the subgrid orography can be included in the roughness length computation (Jourdain and Gallée, 2011) but is deactivated as it requires a resolution-dependant tuning. Finally, melt (through increase in snow/ice density) influence is not taken into account in contrast to the Greenland configuration (Greuell and Konzelmann, 1994; Lefebre et al., 2003). The roughness length for heat z_{0t} is often derived from z_{0m} using a scaling factor ranging from 1-100 (Garratt, 1992). In MAR, z_{0t} equals z_{0m} scaled by 7.4 linking the two properties with the Reynolds number (Andreas, 1987) although no universal relation has proved yet to be efficient over the AIS (see Vignon et al. (2017) and references therein).

SISVAT resolves the energy and water budget for each layer of the snowpack that leads to changes in temperature and humidity content. The snow-covered surface energy budget (SEB, Eq. 2.5) is defined as:

$$SEB = SWN + LWN + SHF + LHF + G, \tag{2.5}$$

$$SWN = SWD - SWU, \tag{2.6}$$

$$SWU = \alpha \times SWD, \tag{2.7}$$

$$LWN = LWD - LWU, \tag{2.8}$$

$$LWU = \varepsilon \times \sigma \times ST^4, \tag{2.9}$$

with SEB the surface energy budget, SWN and LWN the net shortwave and longwave fluxes, SHF and LHF the sensible and latent heat fluxes, G the heat transfer through the snow. SWN (Eq. 2.6) and LWN (Eq. 2.8) are computed as the difference between downelling (SWD or LWD) fluxes from the radiative scheme and the upwelling fluxes (SWU and LWU). SWU (Eq. 2.7) is defined as

SWD energy reflected by the surface albedo (α), while LWU (Eq. 2.9) is defined by the Stefan-Bosman Law (surface emissitivy (ε) times Stefan-Bosman constant (σ) times the fourth power of the surface temperature (ST)).

Since MAR does not represent the penetration of radiative fluxes into the snowpack, the energy budget for inner layers only depends on G that represents heat transfer with adjacent (above and below) layers, or for the deepest layer with the ground or SST below the sea-ice. The sub-grid SST beneath sea ice is fixed at -2 °C while the sea-ice surface temperature is free to evolve according to its surface energy balance. Snow-covered surface temperature is limited at 0 °C and any excess of energy ($SEB > 0$) is used to melt snow (Lefebre et al., 2003). On the opposite, any deficit in surface energy ($SEB < 0$) is compensated by (re)freezing liquid water (melt and rain). Liquid water can percolate through the snowpack depending on its permeability (Colbeck, 1972). In the Antarctic configuration, each snow/firn layer has a maximum water retention of 5%. The liquid water saturates each successive vertical layer as long as the underlying layer is permeable ($\rho < 830\,\mathrm{kg\,m^{-3}}$). Remaining liquid water beyond the snowpack saturation is converted into surface runoff. In the absence of a water-routing hydrological scheme and as Zuo and Oerlemans (1996) runoff delay is not activated over the AIS (unlike Greenland), all surface water that could potentially form melt ponds is considered as runoff, i.e., is instantaneously lost by the ice sheet.

The albedo of the ice sheet depends on the optical properties of snow, the thickness of the snow cover, the presence of blue ice, meltwater and clouds. The penetration of solar radiations in the snow strongly differs according to the spectral wavelength. The snow albedo (α_s) is therefore computed in three spectral bands (0.3-0.8 µm, 0.8-1.5 µm and 1.5-2.8 µm) to represent different solar absorption (Brun et al., 1989). However, since the radiative scheme outputs are broadband radiations, the snow albedo (Eq. 2.10) is a weighted average of the albedo in the three spectral bands:

$$\alpha_s = 0.6 \cdot \alpha_{0.3-0.8\mu m} + 0.3 \cdot \alpha_{0.8-1.5\mu m} + 0.1 \cdot \alpha_{1.5-2.8\mu m}, \tag{2.10}$$

where α_s is the broadband snow albedo, and $\alpha_{0.3-0.8\mu m}$ (Eq. 2.11), $\alpha_{0.8-1.5\mu m}$ (Eq. 2.12), $\alpha_{1.5-2.8\mu m}$ (Eq. 2.13) are a function of the optical grain size (Brun et al., 1992) and successively modified in Lefebre et al. (2003) and Alexander et al. (2014):

$$\alpha_{0.3-0.8\mu m} = max(0.94, 0.96 - 1.58 \cdot \sqrt{d}), \tag{2.11}$$

$$\alpha_{0.8-1.5\mu m} = 0.95 - 15.4 \cdot \sqrt{d}, \tag{2.12}$$

$$\alpha_{1.5-2.8\mu m} = 346 \cdot min(d, 0.0023) - 32.1 \cdot \sqrt{d} + 0.88, \tag{2.13}$$

The optical grain size d (m) is a function of snow grain properties (Brun et al., 1992). While faceted crystals have a lower optical grain size than spherical snow grains, larger snow grains notably induced by melt decrease the albedo (Lefebre et al., 2003). However, the snow albedo cannot be lower than 0.7. This value represents the albedo of snow that has previously melted. The minimum firn albedo (Eq. 2.14) during the transition from snow to ice is a function of the firn density (ρ) (Tedesco et al., 2016) and is comprised between 0.55 and 0.7:

$$\alpha_{firn} = 0.55 + (0.7 - 0.55) \times (\rho - 920)/(450 - 920), \tag{2.14}$$

Over the AIS, the albedo of blue-ice areas in MAR can vary between a minimum ($\alpha_{icemin} = 0.5$) and a maximum value ($\alpha_{icemax} = 0.55$) depending on the presence of meltwater at the surface (Eq. 2.15):

$$\alpha_{ice} = \alpha_{icemin} - (\alpha_{icemin} - \alpha_{icemax}) \times e^{-\sqrt{(RU/K)}}, \tag{2.15}$$

with RU the amounts of accumulated melt water that will runoff (unit: $kg\,m^{-2}$), and K a scale factor set to 60 ($kg\,m^{-2}$). However, as the delay of runoff is switched off, $\alpha_{ice} = \alpha_{icemax}$ in our configuration.

In case of a snow cover thickness (h_{snow} in m) thinner than 0.1 m, the albedo reflects the contribution of both snow (α_s) and ice (α_{ice}) albedos (Lefebre et al., 2003) (Eq. 2.16) while the albedo is the snow albedo for thicker snow cover. Furthemore, SISVAT takes into account the effect of solar zenith angle on the snow albedo as formulated by Segal et al. (1991) and the increase in albedo due to clouds that absorbs solar radiation in the same near-infrared spectrum than snow following Greuell and Konzelmann (1994).

$$\alpha = (\alpha_s \times h_{snow}) + (\alpha_{ice} \times (0.1 - h_{snow}))/0.1, \tag{2.16}$$

SISVAT only simulates a limited number of snow layers and therefore uses a sophisticated aggregation scheme to discretise the snowpack in several (maximum

fixed) layers. An aggregation scheme (described in Brun et al. (1989, 1992) manages the stratification of the snowpack due to snow accumulation, ablation, settling, and metamorphism enabling the dynamical evolution of the physical properties of the different layers though time. It merges layers having similar properties (metamorphism state, temperature, density, and water content) to conserve a maximum of 30 snow/ice layers in case of accumulation (snowfall and deposition). In the same way, the scheme splits the snowpack to ensure a minimal number of 10 layers over permanent-ice areas. Furthermore, the maximum layer thickness of the 4 uppermost layers is fixed (0.02, 0.05, 0.1, and 0.3 m) warranting a fine discretisation to represent surface-atmosphere interactions and sub-surface processes such as heat transfer. Ablated snow mass is removed from the uppermost layer. Finally, the internal snow layers cannot be thinner than 2 mm, and the fresh fallen snow mass is only added into the snowpack if the snowfall amount is larger than 1 mm for numerical stability reasons. Note that properties (such as metamorphism and inherent albedo) of the uppermost layer already take into account the fresh snowfall characteristics while the snow mass is added in the next precipitation event (Lefebre et al., 2003).

Drifting snow

Finally, another important climate feature of polar ice sheets is the wind-driven erosion of snow particles, subsequent transport and redeposition. Drifting snow can change local accumulation (Eisen et al., 2008), but also near-surface atmospheric properties (Le Toumelin et al., 2020). MAR includes a drifting-snow scheme that simulates wind-driven erosion based on Gallée et al. (2001) but did not accurately represent both SMB and drifting-snow events simultaneously at that time (Gallée et al., 2001; Gallée et al., 2005, 2013; Amory et al., 2015). The drifting-snow scheme has therefore been deactivated in many studies (e.g., Fettweis et al., 2017; Agosta et al., 2019; Fettweis et al., 2020; Mottram et al., 2020) including this work (and related publications (Kittel et al., 2018, 2020)). However, recents developments have enabled the reconciliation of the representation of both SMB and drifting-snow events (Amory et al., 2020). Although not used in the main part of this manuscript, the new drifting-snow scheme will be presented hereafter to complete the MAR presentation but also because part of the thesis was devoted to participating in the development and evaluation of this scheme on Adelie land, and then also over the AIS. This section is a summary of the exhaustive description of the new drifting-snow scheme developments that has been submitted to the *Geoscientific Model Development* Journal:

Amory, C., **Kittel, C.**, Le Toumelin, L., Agosta, C., Delhasse, A., Favier, V., and Fettweis, X.: Performance of MAR (v3.11) in simulating the drifting-snow climate and surface mass balance of Adelie Land, East Antarctica, *Geosci. Model Dev. Discuss.* [preprint], in review, 2020.

Snow erosion is assumed to occur when the wind shear stress (the friction velocity) exceeds the cohesive and gravitational forces of the surface (the threshold friction velocity) represented in MAR as a function of the surface snow density only (Amory et al., 2020). The scheme computes the concentration of snow particles that are assumed to become mobile and bounce on the surface. This concentration represents the particle mass transported in saltation ($qsalt$) and is directly related to the difference between the friction velocity and the threshold friction velocity following Bintanja (2000), i.e, to what extent the shear stress overcomes the resistives forces maintaining the snow particles on the surface. The saltating particle concentration $qsalt$ is only theoretical and is used as a boundary condition for the diffusion of snow particles towards the suspension layer. This transport mode refers to the transport of snow particles without periodic contact with the surface, which is in MAR the snow advection occuring at the lowest atmospheric level. The diffusion of snow particles from the saltation layer (ie, theoretical level located at the surface in MAR) to the suspension layer (lowest atmospheric level) is a function of the difference between q_s (snow concentration at the lowest atmospheric level including both drifting and precipitation snow particles) and $qsalt$ (Gallée et al., 2001; Gallée et al., 2005; Amory et al., 2020). The drifting-snow model aims to represent the turbulent diffusion of eroded snow particles from the surface towards the atmosphere (Gallée et al., 2001).

Since the current version MAR does not distinguish drifting snow originated from the surface and snow resulting from cloud precipitation, q_s represents both types of snow. Snow is then drag vertically and horizontally by the turbulent, cloud-microphysical and advection schemes where snow can interact with solar radiations and the surrounding atmosphere especially by sublimating, which in turns modify the humidity and energetic bilan of atmospheric layers as described above.

Drifting-snow particles also induce modifications in surface properties. Repetition of erosion and deposition events increase the snowpack cohesion (Vionnet et al., 2013) and changes grain properties from dendritic to rounded shapes (Sato et al., 2008). Furthermore, erosion and deposition creates microrelief (sastrugis) determining the roughness of snow surfaces (e.g., Amory et al., 2017). When

the drifting-snow scheme is switched on, MAR takes into account these processes by prescribing different surface properties (fallen-snow density, metamorphism and roughness length) than the parameterisations used in the version without drifting-snow. For instance, the increase in snowpack cohesion is represented by a progressive increase in density of the fresh snow reaching the surface replacing the density equation (Eq. 2.4 presented above (Amory, 2020) while the parameterisation of surface roughness depends on the temperature as proposed by Amory et al. (2017).

An important limit of the current drifting-snow scheme implemented in MAR is the non-distinction of the snow particles source between the surface and the clouds. This means that MAR outputs with drifting snow prevent analysis of changes resulting from separate trends in drifting-snow or cloud-created precipitation. Furthermore, the drifting-snow contribution to surface properties (density, grain sizes and shapes) is only assessed through an assumption of its relative importance compared to cloud-created precipitation. Finally, MAR assumes the same sedimentation velocity for both drifting and cloud-created snow particles, while due to their smaller size, drifting-snow particles should have a lower sedimentation velocity (Gallée et al., 2005) potentially underestimating their residence time in the atmosphere and the related interactions. Future developments of the drifting-snow scheme should therefore focus on this aspect. This requests a radical modification of the previously described scheme to add an additional hydrometeor, as already done in the future MAR version (Gallée, 2020).

2.1.4 Common set-up and versions

In this manuscript, two different versions of MAR adapted to the AIS are used: the version 3.6.4 (described in Agosta et al. (2019)) for Ch. 4 and the version 3.11 (presented in Kittel et al. (2020)) for Ch. 5 and Ch. 6. Furthermore, Chapter 4 relies on a coarse resolution (50km) as a consequence of the large number of simulations that were carried out while MAR simulations were performed at a 35km resolution for Ch. 5 and Ch. 6. A comparison of the results from these two different versions (and resolutions) is presented in Ch. 3 and shows that the MAR performances are similar across this manuscript despite using different resolutions and versions.

The Antarctic topography, and ice/rock fractions are computed from the 1 km resolution digital elevation model Bedmap2 (Fretwell et al., 2013). The ice

mask is fixed and cannot evolve, meaning that changes in ice extent following for instance an ice-shelf collapse are not represented. The same is true for surface elevation that is assumed to remain constant in the absence of ice dynamics and evolving topography. Therefore, feedbacks between the ice sheet geometry and the atmosphere are not taken into account in our simulations. Finally, as the drifting-snow scheme (Amory et al., 2020) was still under development when we performed our simulations, it was not activated.

2.2 Large-scale forcings

Since MAR only represents a limited area, it has to be driven at its boundaries by large-scale forcing fields to take into account the climate variability outside of its integration domain. The model is forced by 6-hourly large-scale forcing fields only at its atmospheric lateral boundaries (pressure, wind, specific humidity, and temperature). The SSC are prescribed (SIC and SST) over the whole integration domain, as well as wind and temperature) at the top of the troposphere and in the stratosphere. A linear interpolation is made at each model time step from the current forcing to the next one. In this manuscript, we used two kinds of large-scale forcings: the reanalyses for hindcast (recent past and present) simulations and GCMs or following their level of complexity, ESMs, for projections. ESMs represent more climate processes than GCMs and especially the carbon cycle. In the following, GCMs and ESMs will not be distinguished and will be commonly designated as ESMs. While both reanalyses and ESMs are used to force MAR over 1979 – present, ESMs only simulate meteorological conditions representative of their corresponding climate at that time. This means that a particular year from an ESM cannot be directly compared to the same year in a reanalysis. The same applies to the study of inter-annual variability when using the ESMs to study the climate before the availability of accurate reanalysis forcings (i.e, in 1979 with the start of the satellite era).

2.2.1 Reanalyses

Reanalyses are produced through assimilation of observations into a general circulation model to improve their representation of the actual Earth's climate. These observations include near-surface and vertical measurements and satellite measurements revolutionising the observation system since 1979 (Bengtsson et al.,

2004). However, the coverage of the AIS remains poor, even with satellites, partly because of the harshness and remoteness of the environment, which makes it difficult to install and maintain many observation stations, but also because of the solar conditions (polar night) and the difficulty of differentiating clouds from a snow-covered surface (Andersson, 2007; Bouchard et al., 2010). This results in lower amounts of assimilated data compared to the Greenland Ice Sheet, which, combined with the climatic isolation of Antarctica, introduces many uncertainties into the reanalyses. They were therefore considered too uncertain before 1979 (Bromwich et al., 2007, 2011).

For simulating the recent past and present climate of the AIS, we used two reanalyses of the European Centre for Medium-Range Weather Forecasts (ECMWF): ERA-Interim and its successor ERA5.

The ERA-Interim reanalysis (Dee et al., 2011) has a horizontal resolution 0.75° (i.e. ∼30km × ∼88km km at 70°S) and 60 vertical levels from the surface to 0.01 hPa. It is available from 1979 to 31 August 2019. ERA-Interim is often considered as a reference reanalysis (e.g., Agosta et al., 2015; Barthel et al., 2020) as it correctly represents the Antarctic climate (e.g., Bromwich et al., 2011; Huai et al., 2019) and especially atmospheric circulation and moisture advection (Dufour et al., 2019; Gossart et al., 2019) that are essential to force MAR. ERA-Interim displays large biases in its representation of surface temperature (Fréville et al., 2014) or interior precipitation (Bromwich et al., 2011). This however does not influence MAR that produces its own independent results over the ice sheet interior and generally below 500 hPa.

The ERA5 reanalysis (Hersbach et al., 2020), which is the latest generation of ECMWF reanalyses, has replaced ERA-Interim in late 2019. It has higher spatial ∼0.3° (i.e., ∼9 km x ∼27 km at 70°S) and vertical (137 levels versus 60) resolutions than ERA-Interim. The outputs are also available at a higher temporal resolution. ERA5 is available from 1950 to near-real time, although 6-hourly forcing fields needed for MAR are only currently available starting from 1979 and initial results suggest that the reanalysis is not reliable before (Hersbach et al., 2020). It uses an improved 4D-VAR assimilation as well as many more observations than ERA-Interim. ERA5 has been shown to better represent the average climate over the AIS than ERA-Interim (Gossart et al., 2019; Vignon et al., 2019), even if this is not true for all climate parameters, especially on the peninsula (Hillebrand et al., 2020).

ERA-Interim is used to force MAR in Ch. 4 over 1979–2015, while ERA-

5 is used in Ch. 5 and Ch. 6 as a reference over 1979–2019. This however has no influence on our results as highlighted in Ch. 3. (Agosta et al., 2019) showed that forcing MAR with other reanalyses (JRA-55 (Kobayashi et al., 2015), MERRA (Gelaro et al., 2017)) leads to similar results albeit regional and temporal differences exist.

2.2.2 Earth-System Models

ESMs are complex climate models representing the Earth's climate. They consist of atmosphere and ocean general circulation models coupled together, and for the most advanced ones, an additional biogeochemical component that enables the representation of the carbon cycle. ESMs are mainly used to study the past (before the observation/reanalysis/satellite era) and future climates.

In this thesis, we used ESM outputs from CMIP5 (Taylor et al., 2012) and the ongoing 6th Phase (CMIP6, Eyring et al., 2016). Among others, CMIP6 relies on new emission scenarios and more sophisticated models. The CMIP6 models often have a higher resolution thanks to the increasing performance computing resources (Haarsma et al., 2016) and the coupling between the different components of the Earth-System has been improved (Eyring et al., 2016). We only chose the scenarios of the largest increase in greenhouse-gas emissions from CMIP5 (RCP8.5) and its updated version in CMIP6 (ssp585) in order to assess the sensitivity of the Antarctic surface and overlying low atmosphere to the strongest warming signals. These two scenarios have an equivalent global radiative forcing of $+8.5\,\mathrm{W\,m^{-2}}$ by 2100, but differ in the prescription of the different anthropogenic gas concentrations. Notable differences between CMIP5 RCP8.5 and CMIP6 ssp585 are the projected land use changes and concentrations of individual long-lived-greenhouse-gas species, potentially resulting in local differences in 21st century warming, despite a similar global radiative forcing (O'Neill et al., 2016). First analyses of the CMIP6 results revealed higher equilibrium climate sensitivity (ECS, the steady-state global temperature increase for a doubling of CO2) (Mauritsen et al., 2019; Voldoire et al., 2019; Meehl et al., 2020) likely due to cloud feedbacks and cloud-aerosol interactions (Zelinka et al., 2020; Wyser et al., 2020), suggesting warmer future climates. However, this higher climate sensitivity is potentially not supported by paleo-climate records (Zhu et al., 2020). While CMIP6 models seem to be more developed, the future climates they simulate are therefore not more likely than CMIP5 climates. This highlights the need of using

several forcing ESMs coming from both CMIP5 and CMIP6 experiments to study the future Antarctic climate and capture the range of current uncertainties from both extremes.

The selection of ESMs that were dynamically downscaled by MAR was based on their ability to 1) represent the current climate (air temperature and humidity, sea surface conditions, and large-scale circulation) around the AIS and 2) diversify the projected changes during the 21st century. These criteria ensure on one hand, that the ESM biases will not have a prejudicial effect on the projections since the present state determines future biases (Agosta et al., 2015; Krinner and Flanner, 2018) and on the other hand that we assess the AIS response to a wide range of projected temperature increases for a better quantification of the future uncertainties. We therefore selected ESMs by comparing them to the ECMWF reanalysis ERA5 (Hersbach et al., 2020) over the recent "historical" period (1980–2004) following the method defined in Agosta et al. (2015) and Barthel et al. (2020) for CMIP5, extended here to CMIP6 and applied only to the Antarctic atmosphere. Large-scale forcing models were chosen among the CMIP5 and CMIP6 ESMs with available 6-hourly outputs as needed by MAR.

We selected two models in each of the two CMIP5 and CMIP6 ensembles:

- The Australian Community Climate and Earth-System Simulator (ACCESS1.3, Bi et al., 2013; Dix et al., 2013) (CMIP5). ACCESS1.3 has an atmospheric horizontal resolution of 1.25° in latitude and 1.875° in longitude, using 38 vertical hybrid levels. The ocean component is run on a 1° tri-polar grid that has a higher resolution south of 30°S (0.33° for the latitude). This provides a better representation of the Southern Ocean (important in particular for representing the climate of Australia).

- The Community Earth System Model 2 (CESM2, Danabasoglu et al., 2020) (CMIP6). CESM2 uses a regular atmospheric grid (0.9° in latitude and 1.25° in longitude) with 32 vertical levels. The horizontal resolution in latitude is 1.125° while the resolution varies in longitude. Contrary to ACESS1.3, the resolution is coarser in the Southern Hemisphere (∼0.53°) while it is highest over the equator (0.27°).

- CNRM-CM6-1 (Voldoire et al., 2019) (CMIP6) is conjointly developed by CNRM-GAME (Centre National de Recherches Météorologiques—Groupe d'études de l'Atmosphère Météorologique) and Cerfacs (Centre Européen de Recherche et de Formation Avancé). At the equator, the atmospheric resolution is ∼1.4° and has 91 vertical levels. The ocean model (NEMO) benefits of an extended grid

south of 67°S. This enables a better representation of the Antarctic coast and interactions between the ocean and the ice shelves. The nominal resolution is 1° with refinement in the tropics (∼0.33°).

- The Norwegian Earth System Model (NorESM1-M, Bentsen et al., 2013; Iversen et al., 2013) (CMIP5). The atmospheric component resolution (1.9° in latitude and 2.5° in longitude) has 26 atmospheric levels while the ocean has a 1.125° resolution grid at the equator.

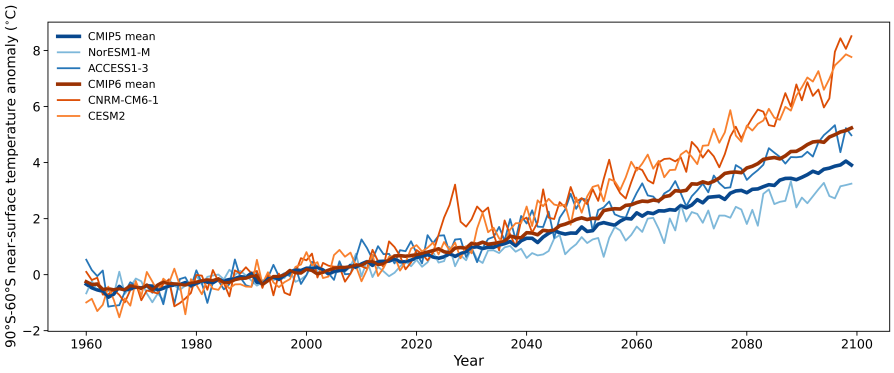

Figure 2.2: Time series of the 90°S–60°S annual near-surface temperature anomaly (°C) between 1960 and 2100 compared to the present reference period (1981–2010) from both the extreme high-emission scenarios RCP8.5 and ssp585. The thick blue and red lines represent the mean annual warming from 28 CMIP5 and 34 CMIP6 ESMs. Thinner orange and blue lines are for ESMs selected as boundary conditions for our regional climate model MAR: CNRM-CM6-1 and CESM2 (CMIP6, ssp585) and NorESM1-M and ACCESS1-3 (CMIP5, RCP85).

The Antarctic (90°S–60°S) near-surface warming they produce for RCP8.5 (CMIP5) and ssp585 (CMIP6) is shown in Fig. 2.2. ACCESS1.3 is the model that best represents the present Antarctic climate compared to ERA-Interim (Agosta et al., 2015), and is also among the best models when compared to ERA5 (Agosta et al., in preparation). This ESM has a near-surface Antarctic warming close to the CMIP6 multi-model mean (+5 °C). NorESM1-M projects a weaker Antarctic atmospheric warming (+3.2 °C), Fig. 2.2) but a stronger ocean warming (Barthel et al., 2020). CNRM-CM6-1 correctly represents the present Antarctic climate and was among the first CMIP6 models available. This model also enables to assess the AIS response to an extreme Antarctic warming (+8.5 °C) since it is the warmest model over the AIS among the CMIP5 and CMIP6 ensembles at the end of the 21st century. CESM2 has a lower score than half of the CMIP5 and CMIP6 models compared to ERA5 (Agosta et al., in preparation). Despite its modest ranking, it was chosen due to its relatively detailed representation of polar-oriented processes, early availability, and the frequent use of this model and its earlier version to study

the AIS (e.g., Lenaerts et al., 2016; Fyke et al., 2017; Medley et al., 2018; Nowicki et al., 2020). Its projected warming (+7.7 °C) is close to the mean warming projected by CNRM-CM6-1. From this perspective, selecting both CESM2 and CNRM-CM6-1 does not maximise the diversity of projected warmings at the end of the 21st century preventing our selected ESM ensemble to be representative of the mean CMIP5 and CMIP6 warming. However, selecting more ESMs with a high ECS enables a better quantification of the sensitivity of the AIS in warmer climates as significant changes were only projected to occur for strong warmings. In that way, selecting CESM2 and CNRM-CM6-1 maximises the diversity in atmospheric forcings (such as circulation and advection in humidity) associated with future climates warmer than 7.5°C that are only projected by a few ESMs. This then helps to better estimate the projected SMB changes and uncertainties for large warmings.

2.3 Evaluation datasets

The harsh climate conditions and the remoteness of the AIS explain why observations are only available recently, often discontinuous and for scarce locations and limited periods of time. While few research bases were established around 1950, the first International Geophysical Year (also known as the Third International Polar Year) in 1957 marked the development of many permanent bases and thus increased the number of available atmospheric measures. Accumulation measurements using ice-coring techniques provide a large temporal coverage (up to 1 million years), but are only representative of one point and cannot necessarily be used to study the recent or short-period variability (Eisen et al., 2008; Favier et al., 2013). Annual stake networks (e.g., Agosta et al., 2013; Wang et al., 2017) and extensive observation campaigns (e.g., Amory, 2020) have significantly increased the measurement coverage of the ice sheet over the recent years.

Two main databases are used over the AIS to evaluate climate models: Favier et al. (2013) which is a quality controlled SMB observation compilation and the READER climate database Turner (2004) that gather monthly near-surface climate observations. The latest only enables to evaluate mean climatic conditions simulated by the models. However determining climate processes such as intense sporadic episodes of snow accumulation and erosion (Souverijns et al., 2018; Amory, 2020), or short-lived melt events (Kuipers Munneke et al., 2018; Wille et al., 2019) occur on a much finer time scale. This highlights the necessity

to assess the model ability to represent near-surface (meteorological) conditions at least on a daily basis. For the moment, most model evaluations have not reconciled high-temporal resolution near-surface (meteorological) conditions and SMB aspects focusing exclusively on SMB (e.g., Agosta et al., 2013) or relying only on a few high-temporal near-surface observations in additions to SMB observations (e.g., Lenaerts and Van den Broeke, 2012; Van Wessem et al., 2018).

2.3.1 Near-surface observation database

As there was no reliable near-surface observation database at a high temporal resolution, we have compiled observations of surface pressure, near-surface temperature and wind speed from 303 (automatic) weather stations (AWS) notably collected by the Alfred-Wegner-Institut (AWI), the Antarctic Meteorological Research Center (AMRC), the Australian Antarctic Division Glaciology Program (AAD), the British Antarctic Survey (BAS), the International Polar Foundation, the Institute for Marine and Atmospheric research Utrecht (IMAU, (Van Wessem et al., 2014a; Jakobs et al., 2020), the Institut des Géosciences de l'Environnement (IGE) and Institut Polaire Français Institut Paul-Emile Victor (IPEV) (Amory, 2020), the Italian Antarctic Research Programme (ITA), and the POLENET program (http://polenet.org, last accessed: 02/12/2020). Furthermore, some weather stations also record radiative flux and relative humidity observations. Part of this data was used in the READER database (Turner, 2004).

The original data were sampled at different time steps (sub-hourly, hourly or 3-hourly) and were then averaged into daily values. We discarded daily averages computed from less than 75% of the original sub-daily values that were considered as not representative of the entire measurement day (UTC). Although the original data were often subjected to quality checks, we found remaining suspicious measurements (sudden discontinuity in pressure and temperature, temperature values capped to the lower bound of the measurement range during the whole winter season, null mean wind speed, etc) resulting from icing or more generally instrument malfunction. In that case, all observations from these AWS were removed from the database (Table A.1 lists the spurious parameters for each AWS) leading to 267 checked AWS including 27 AWS recording radiative flux and/or accurate relative humidity (Table A.2, Table A.3, Table A.4,Table A.5). Furthermore, wind-speed observations of 0 $\mathrm{m\,s^{-1}}$ for day-long periods were occasionally recorded, likely due to sensor riming and were then considered as no data for these days. We also

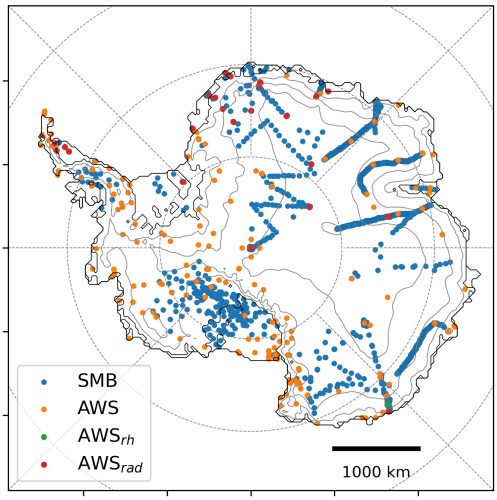

Figure 2.3: Location of SMB (blue) and AWS observations used in this thesis. AWS that measure only measure near-surface pressure, temperature and wind speed are represented by orange dots while the AWS that also contained relative humidity and radiative fluxes data are in red. Note D47 (green) that also measures relative humidity but not the radiative fluxes.

discarded episodic values of longwave radiation following van den Broeke et al. (2004). In particular, this homogenous and quality-control database has already been used in Donat-Magnin et al. (2020b); Mottram et al. (2020); Kittel et al. (2020) and several other submitted papers. Note that the dataset might still contain biased measurements due to undetected failures such as burial of instruments by snow, battery failure or tilting, highlighting the difficulties involved in collecting data in extreme Antarctic conditions.

Since we aim at comparing simulations using two resolutions (50 km and 35 km), we only retained for the evaluation stations belonging to the common ice mask (ie., that correspond to an ice-sheet pixel in both simulations) and having a difference in elevation lower than 500 m with the model in each simulation, leading to the use of 215 AWS presented on Fig. 2.3 and indicated with $*$ in Table A.2, Table A.3, Table A.4, Table A.5. The modelled surface pressure, near-surface, temperature, wind speed and relative humidity, and radiative fluxes, as well as the model elevation, are computed using a four-nearest inverse-distance-weighted method that interpolates model values to the AWS location. Finally, the vertical model level closest to the surface (2 m in our simulations) is used for all comparisons with the near-surface observations, since the measurement height of the observations is not always known.

2.3.2 Surface mass balance observation database

For evaluating the SMB simulated by MAR, we used the GLACIO-CLIM SAMBA database (Favier et al., 2013) which contains three levels of quality-controlled data: full data-base (5548 observations), "A"-rated observations (3539) and model-evaluation (3243). This highest confidence level that is used here discards observations whose altitude is too far away from a digital elevation reference model. In addition, the database has been updated in an attempt to maintain the same level of control with transect observations presented in Wang et al. (2016) and yearly values of ice cores used in Thomas et al. (2017). The radar measurements published by Medley et al. (2014) are not included as they are indirect measurements of SMB (see Favier et al. (2013)). We then compare the SMB simulated by MAR to an original dataset of around 7136 observations representing various time periods and covering a wide range of locations across the ice sheet.

In the same way as for the AWS comparison, we do not directly compare MAR-modelled SMB values to the observations. The method was developed in Agosta et al. (2019) and improved for the SMB model intercomparison from several RCMs over the AIS in Mottram et al. (2020). The modelled and observed SMB values are computed in 4 steps. The observations are firstly selected if they correspond to an ice-sheet pixel in the reference ice mask. Furthermore, we only selected SMB observations between 1950 to 2019. These conditions reduced the total number of observations used in the comparison to 3049. Observations between 1950 and 1981, or 2015 and 2019 not fully included in the common modelling period (ie., 1981 to 2015), were used for evaluation only if they covered more than 5 years. These 1643 SMB observations are compared to modelled values averaged over the common modelling period in order to compute a climatological mean while we averaged modelled SMB values over the exact same period for the observations between 1981 to 2015 (1406 observations). Secondly, the original modelled SMB values are interpolated to the observation location using a four-nearest inverse-distance-weighted method (as for AWS). Thirdly, all the interpolated SMB values contained in a same grid cell from the reference mask grid are averaged, as well as the observations for finally creating 780 comparison pairs. These steps ensure a fair comparison for each simulation taking into account the benefit of using a higher resolution, but also reducing the very high spatial variability ($<$1km and even smaller than 10 m with the presence of sastrugis (Eisen et al., 2008; Agosta et al., 2012)) of the observed SMB that cannot be represented by MAR.

As SMB observations are not evenly distributed over the ice sheet, the comparison statistics may be artificially influenced by over- and/or under-sampled regions. In this evaluation, we used the MAR grid at 35km as a reference mask.

2.3.3 Melt estimates

The amount of surface melt water is relatively low over the present climate, but is expected to increase in the (near) future and may therefore become an important surface process. Furthermore, it has been considered as a major source of model discrepancies over the Greenland Ice Sheet (Fettweis et al., 2020) highlighting the needs of evaluating the melt simulated by MAR despite relatively low present values. However, melt production cannot be directly measured so that we rely on different indirect products such as satellite-based or AWS-forced estimates. Using surface brightness temperatures (Picard and Fily, 2006) or multi-spectral combinaisons (Moussavi et al., 2020), satellites can detect whether the surface is melting while radar backscatter signal can be used to determine the melt intensity or more exactly the quantity of liquid water at the surface (Trusel et al., 2012). Trusel et al. (2013) have then derived melt volume estimates by linking radar backscatter attenuations with an energy balance model. Nevertheless, this kind of products rely on several hypotheses related to the satellite signal treatment or the energy balance model. Rather than satellite, we therefore used the AWS-forced energy-balance-model melt estimates presented in Jakobs et al. (2020). Even if they might be of local significance, they are at least affected by a lower level of uncertainty than satellite-derived products.

By inducing temperature biases, elevation differences between the AWS and MAR can have a strong prejudicial influence on the melt evaluation. Since applying a criterion on common modeling periods and elevation differences between all the grids would result in a too drastic reduction of the number of comparisons, we carry out individual comparisons for each simulation by selectionning AWS-derived estimates with a difference in elevation lower than 250 m.

CHAPTER 3

Evaluation

This chapter presents an exhaustive evaluation of MAR results over the AIS against a set of near-surface meteorological observations as well as SMB and melt data. While MAR results have been compared to both AWS and SMB measurements along with the development of the latest version over the last few years, most available comparisons in the literature primarily focused on one of these aspects at the expense of the other (see for instance Gallée et al. (2013); Amory et al. (2015) for comparaisons against AWS observations only and Kittel et al. (2018); Agosta et al. (2019) for comparaisons against SMB observations only). For this reason, the evaluation proposed here simultaneously focuses on each of these aspects for the results of MARv3.11 forced by the most recent ECMWF reanalysis (ERA5), which are currently the new (MAR) reference over the AIS. Furthermore, this evaluation is at least, if not more, equally comprehensive as recent evaluations of other RCMs such as RACMO (Van Wessem et al., 2018) or COSMO (Souverijns et al., 2019). The dataset that was gathered during this thesis consists of daily (instead of commonly-used monthly), quality-(re)controlled AWS data (up to 267 locations scattered over the AIS), including new observations recently made available (radiative fluxes, relative humidity, melt rates). It has been partly used in the recent comparisons of Mottram et al. (2020) which is based on the evaluation method reported here, i.e. a combined evaluation of the (near)-surface climate, surface melt and SMB simulated by the model that enable a robust characterisation of RCM results and possible regional variability in its performance.

Finally, this is also an opportunity to prove the consistency of our results with changing model versions (v3.6.4 vs 3.11), resolutions (50 km vs 35 km), and forcings (ERA-Interim vs ERA5) throughout these 4 years of research. In order to enable a more direct comparison and the understanding of the effect of each factor, the results from Agosta et al. (2019), who used MARv3.6.4 at 35 km resolution and forced by ERA-Interim, are added in the comparison. In the same way, we forced MARv3.11 at 35 km by ERA-Interim. The chapter is divided into 3 parts: the model results are first evaluated against near-surface climate observations (near-surface pressure, air temperature, wind speed, air relative humidity, and surface radiative fluxes), then against SMB data, and finally against melt estimates.

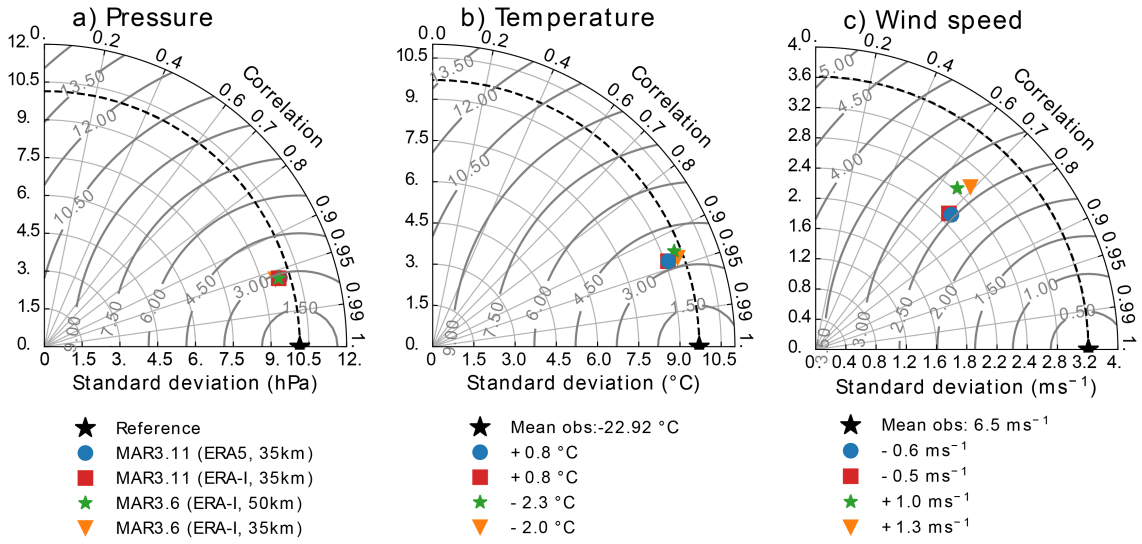

Figure 3.1: Taylor diagrams illustrating the model performances compared to daily observations of surface pressure (a), near-surface temperature (b), and near-surface wind speeds (c) over the AIS. The horizontal and vertical axes represent the observed and modelled standard deviations, the dashed line in bold shows the standard deviation of the observations. The correlation between the models and the observations is measured by the angle with the x-axis while the CRMSE is represented by the curved lines in light grey. Finally, the centered Root Mean Squared Error (CRMSE) is represented by the curved lines in light grey. The units of standard deviation, CRMSE, mean bias and mean of the observations are the same (hPa for near-surface pressure, °C for near-surface temperature, and $\mathrm{m\,s^{-1}}$ for near-sirface wind speed). The closer a model is to the observations (black star) the better it is.

3.1 Near-surface climate

3.1.1 Near-surface pressure

All the MAR configurations correctly reproduce the near-surface pressure over the ice sheet ($r > 0.96$, Fig. 3.1). While local mean biases can differ according to differences in elevation, the evaluation reveals an overall similar model performance for the different simulations thanks to the use of the same nudging method adapted to each domain size and configuration. Despite this nudging, MAR struggles to represent near-surface pressure over the Ross Ice Shelf and the sector of McMurdo as the correlations drop between 0.89 and 0.94 for each configuration (not shown).

Table 3.1: Mean bias, Root Mean Squared Error (RMSE), Centered Root Mean Squared Error (CRMSE), and correlation between daily observations and MARv3.11$_{\mathrm{ERA5}}$, MARv3.11$_{\mathrm{ERAI}}$, MARv3.6$_{35\mathrm{km-ERAI}}$, and MARv3.6$_{50\mathrm{km-ERAI}}$. Annual, summer (DJF), and winter (JJA) statistics are given for the near-surface temperature (°C), the near-surface wind speed ($\mathrm{m\,s^{-1}}$), the shortwave downward and upward radiative flux (SWD and SWU) ($\mathrm{W\,m^{-2}}$) , and the longwave downward and upward radiative flux (LWD and LWU) ($\mathrm{W\,m^{-2}}$) over 1980–2015, i.e the common modelled period.

		Annual				Summer				Winter			
		Mean bias	RMSE	CRMSE	Correlation	Mean bias	RMSE	CRMSE	Correlation	Mean bias	RMSE	CRMSE	Correlation
Temperature (°C)	MARv3.11$_{\mathrm{ERA5}}$	0.80	4.30	3.28	0.94	0.27	2.99	2.21	0.84	1.26	4.92	3.55	0.86
	MARv3.11$_{\mathrm{ERAI}}$	0.79	4.31	3.30	0.94	0.28	2.99	2.21	0.84	1.24	4.92	3.57	0.86
	MARv3.6$_{35\mathrm{km-ERAI}}$	-1.97	4.56	3.37	0.94	-2.05	3.53	2.18	0.85	-1.77	5.08	3.72	
	MARv3.6$_{50\mathrm{km-ERAI}}$	-2.35	4.91	3.51	0.93	-2.40	3.65	2.22	0.85	-2.10	5.47	3.94	0.83
Mean obs 1980–2015			-22.92				-11.72				-30.75		
Standard obs 1980–2015			9.70				4.34				7.00		
Wind speed ($\mathrm{m\,s^{-1}}$)	MARv3.11$_{\mathrm{ERA5}}$	-0.55	3.06	2.58	0.71	-0.70	2.50	2.09	0.68	-0.34	3.43	2.84	0.70
	MARv3.11$_{\mathrm{ERAI}}$	-0.57	3.07	2.59	0.70	-0.70	2.52	2.10	0.68	-0.36	3.44	2.84	0.70
	MARv3.6$_{35\mathrm{km-ERAI}}$	1.31	3.39	2.68	0.69	0.44	2.47	2.07	0.70	2.06	2.47	2.07	0.69
	MARv3.6$_{50\mathrm{km-ERAI}}$	1.03	3.37	2.80	0.66	0.29	2.52	2.15	0.66	1.71	3.98	3.07	0.65
Mean obs 1980–2015			6.40				5.35				7.01		
Standard obs 1980–2015			3.61				2.86				3.94		
Relative Humidity (%)	MARv3.11$_{\mathrm{ERA5}}$	9.40	14.93	9.38	0.23	5.81	10.74	7.73	0.37	11.38	16.78	8.45	0.22
	MARv3.11$_{\mathrm{ERAI}}$	9.54	14.97	9.33	0.23	6.04	10.79	7.80	0.37	11.46	16.80	8.42	0.21
	MARv3.6$_{35\mathrm{km-ERAI}}$	9.03	15.23	9.34	0.22	11.21	7.73	7.47	0.32	10.51	17.01	8.65	0.32
	MARv3.6$_{50\mathrm{km-ERAI}}$	8.09	15.03	9.35	0.26	5.94	11.22	7.68	0.38	9.32	16.93	8.93	0.22
Mean obs 1980–2015			81.41				82.09				81.38		
Standard obs 1980–2015			8.70				7.47				8.35		
SWD ($\mathrm{W\,m^{-2}}$)	MARv3.11$_{\mathrm{ERA5}}$	-10.70	36.16	32.02	0.98	-6.88	48.83	39.63	0.88	/	/	/	/
	MARv3.11$_{\mathrm{ERAI}}$	-11.68	36.81	32.30	0.98	-8.64	49.46	39.77	0.88	/	/	/	/
	MARv3.6$_{35\mathrm{km-ERAI}}$	2.41	33.21	29.97	0.98	2.41	47.69	36.82	0.90	/	/	/	/
	MARv3.6$_{50\mathrm{km-ERAI}}$	2.31	33.36	30.18	0.98	11.95	47.94	37.37	0.89	/	/	/	/
Mean obs 1980–2015			168.08				320.81				/		
Standard obs 1980–2015			147.64				88.96				/		
SWU ($\mathrm{W\,m^{-2}}$)	MARv3.11$_{\mathrm{ERA5}}$	-12.44	26.61	22.52	0.98	-12.98	34.34	27.38	0.91	/	/	/	/
	MARv3.11$_{\mathrm{ERAI}}$	-13.12	27.28	22.90	0.98	-14.34	35.13	27.59	0.90	/	/	/	/
	MARv3.6$_{35\mathrm{km-ERAI}}$	-4.42	21.20	19.39	0.99	-1.97	29.49	24.87	0.92	/	/	/	/
	MARv3.6$_{50\mathrm{km-ERAI}}$	-3.91	21.26	19.56	0.98	-1.10	47.94	37.37	0.89	/	/	/	/
Mean obs 1980–2015			134.96				266.16				/		
Standard obs 1980–2015			121.40				68.94				/		
LWD ($\mathrm{W\,m^{-2}}$)	MARv3.11$_{\mathrm{ERA5}}$	-9.93	26.54	22.49	0.78	-15.06	29.03	22.82	0.62	-8.17	24.70	20.62	0.78
	MARv3.11$_{\mathrm{ERAI}}$	-9.41	26.41	22.53	0.78	-14.14	28.46	22.77	0.62	-7.78	24.93	20.81	0.77
	MARv3.6$_{35\mathrm{km-ERAI}}$	-25.58	36.21	21.48	0.79	-28.82	34.21	21.48	0.68	-23.68	32.04	19.75	0.77
	MARv3.6$_{50\mathrm{km-ERAI}}$	-25.34	34.47	22.11	0.78	-28.22	36.14	20.89	0.66	-24.01	33.06	20.89	0.75
Mean obs 1980–2015			182.89				206.15				162.20		
Standard obs 1980–2015			35.46				28.09				29.79		
LWU ($\mathrm{W\,m^{-2}}$)	MARv3.11$_{\mathrm{ERA5}}$	-40.94	49.74	26.97	0.70	-61.39	65.12	20.99	0.48	-28.71	37.36	22.33	0.70
	MARv3.11$_{\mathrm{ERAI}}$	-40.39	49.14	26.75	0.70	-60.39	64.01	20.61	0.50	-28.32	37.15	22.40	0.72
	MARv3.6$_{35\mathrm{km-ERAI}}$	-56.86	62.62	24.96	0.73	-75.40	78.07	19.73	0.60	-44.36	49.44	20.38	0.73
	MARv3.6$_{50\mathrm{km-ERAI}}$	-56.66	62.44	25.05	0.73	-74.58	77.46	19.50	0.57	-44.71	49.96	21.12	0.71
Mean obs 1980–2015			216.41				255.59				190.24		
Standard obs 1980–2015			35.35				17.47				23.18		

3.1.2 Near-surface temperature

The mean near-surface temperature simulated by MARv3.11 forced by ERA5 is 0.8 °C higher than the observation (Table 3.1). This mean bias masks a seasonal contrast in the model behavior. The overestimation is more pronounced in winter (+1.3 °C) than in summer (+0.3 °C) and in the same way, the centered root mean squared error (CRMSE) is higher in winter (3.5 °C) than in summer (2.2 °C). Beyond seasonal differences, MARv3.11 overestimates low mean temperatures (especially in winter or over the plateau in East Antarctica) while it slightly underestimates the high temperatures close to 0 °C notably over the Peninsula where the comparison reveals a negative bias (Figs. 3.2 and B.1).

MAR performs less well over the Peninsula and over the Ross Ice Shelf. The 35 km resolution used in this configuration is too coarse to correctly represent the sharp topography variations and their inherent influence on the atmospheric

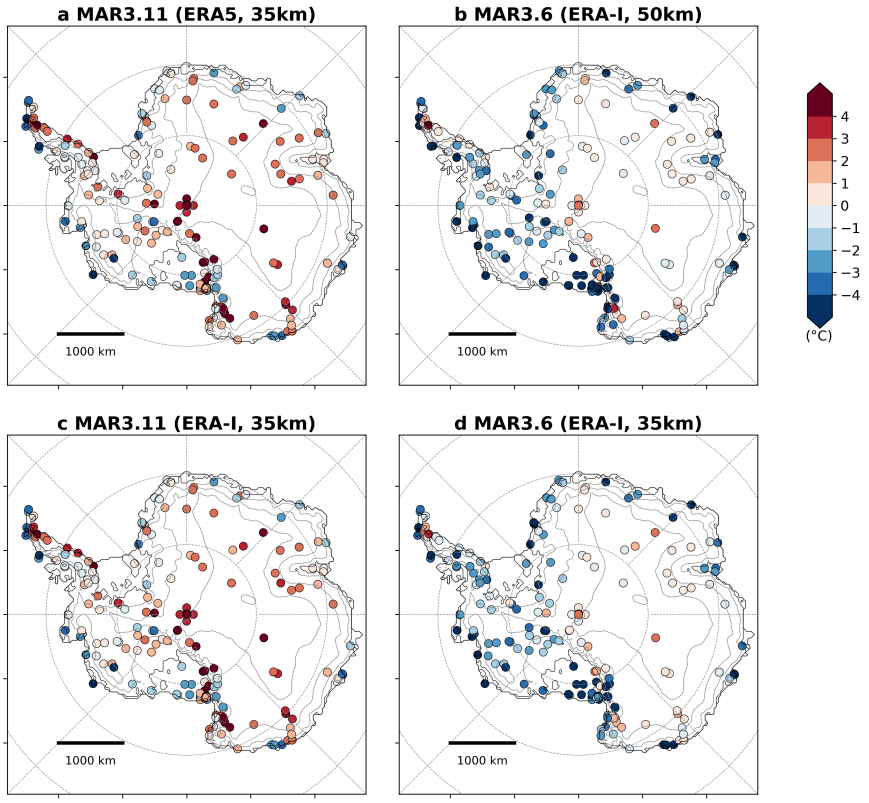

Figure 3.2: Mean annual near-surface temperature biases for MARv3.11 forced by ERA5 (a) and ERA-Interim (b) at 35 km, MARv3.6 forced by ERA-Interim at 50 km(b) and 35 km (d) for each AWS (Units: °C). The subplots a and b are the configurations used in this manuscript while c and d enables a comparison between the different resolutions, forcings and model versions.

dynamics (as the Foehn effect). While MARv3.11 does not correctly represent the pressure variation in summer over the Ross Ice Shelf, the near-surface temperatures are better modelled in summer than in winter, when they are too high (Fig. B.1). This feature could be linked to the proximity of the Transantarctic Mountains and valleys where the katabatic flow is topographically channeled and affects the climate of the Ross Ice Shelf and the McMurdo sector. The coarse resolution does not properly account for the orographic roughness potentially leading to temperature biases (Jourdain and Gallée, 2011). These authors have developed a parameterisation in MAR representing the subgrid orographic roughness improving the comparison with the near-surface observations. It was however not activated in our configurations as this parameterisation requests a special tuning for each resolution and domain extension (Jourdain and Gallée, 2011).

While MARv3.11 simulates too high near-surface temperature with both ERA-Interim and ERA-5 forcings (mean bias of +0.8 °C for both simulation), MARv3.6 at 50 km forced by ERA-Interim has a negative bias of -2.3 °C. This is specific to the version as MARv3.6 at 35 km reveals a similar bias (-2.0 °C). MARv3.6 simulates a lower positive bias over the plateau compared to MARv3.11 in winter but simulates lower temperature over the ice-sheet margins (Fig. 3.2). CRMSE is only slightly reduced in MARv3.11. The most significant differences occur on the Ross Ice Shelf where MARv3.11 forced by ERA5 overestimates the near-surface temperature by +1.6 °C while MARv3.6 underestimates it by -2.8 °C. The dispersion of the temperatures biases in MARv3.6 is similar to MARv3.11 but is shifted towards low temperature while temperatures between -40 °C and -20 °C are still overestimated (Fig. B.2).

Apart from the biases mentioned above, the results over the whole ice sheet are similar for both simulations used in this manuscript. They are only slightly improved by using the more recent model version, forcing and higher resolution. Finally, the evaluation suggests that there is no influence of using ERA5 instead of ERA-Interim as MAR forcing to simulate the near-surface temperature.

3.1.3 Near-surface wind speed

Compared to the two previous variables, MARv3.11 simulates the near-surface wind speed with less accuracy, as the Root Mean Squared Error (RMSE) equals almost 70% of the observed variability and the correlation is 0.71, in agreement with Delhasse et al. (2019) that showed a worse comparison for the

wind over Greenland. On average, MARv3.11 underestimates observed wind speeds (-0.3 $\mathrm{m\,s^{-1}}$ in winter and -0.7 $\mathrm{m\,s^{-1}}$ in summer; Table 3.1) even it can locally overestimates the mean wind speed (Fig. 3.3). The negative bias results from the underestimation of high wind speeds, although low wind speeds are generally overestimated. MARv3.11 uses a constant value of z_{0m} (1 mm) that is more representative of aerodynamically rough surfaces generally encountered in coastal areas or when the wind direction and microrelief are of crosswise orientations (Amory et al., 2017). This is however not necessarily valid for the entirety of the continent as persistent katabatic winds generally create optimally streamlined shapes through erosion in the preferential directional range, consequently reducing the drag effect and z_{0m} (Amory et al., 2016). Overestimating z_{0m} results in a wind-retarding effect, which seems particularly pronounced at high wind speeds in MARv3.11, explaining the general negative wind-speed bias. As discussed by (Amory et al., 2020), the local turbulence scheme of MAR is adapted for stable atmospheric conditions in which small and short-lived eddies can develop. The model thus likely struggles to represent neutral atmospheric conditions in which large eddies of the height of the boundary layer can entrain momentum from higher atmospheric levels to the surface and generates near-surface wind gusts. The influence of a too low resolution through a coarse representation of the topography is also likely to be influential as it leads to a misrepresentation of the channeling of katabatic winds in topographic depressions where the near-surface flow can locally accelerate (Parish and Bromwich, 2007).

While MARv3.11 underestimates the mean near-surface wind speed, MARv3.6 overestimates it. This difference could be explained by the temperature and the surface roughness prescription. The fixed value of surface roughness in MARv3.11 corresponds to the higher bound of the parameterisation in MARv3.6 in which z_{0m} is computed as a function of air temperature (Agosta et al., 2019) slowing down the wind in MARv3.11 relative to the former model version. Finally, the underestimation of the near-surface temperature in MARv3.6 affects the representation of z_{0m} by artificially capping it to lower values.

3.1.4 Near-surface relative humidity

The evaluation reveals a poor representation of the near-surface relative humidity by MARv3.11 even though it has been slightly improved compared to MARv3.6 as a consequence of the reduction of the temperature bias (Table 3.1).

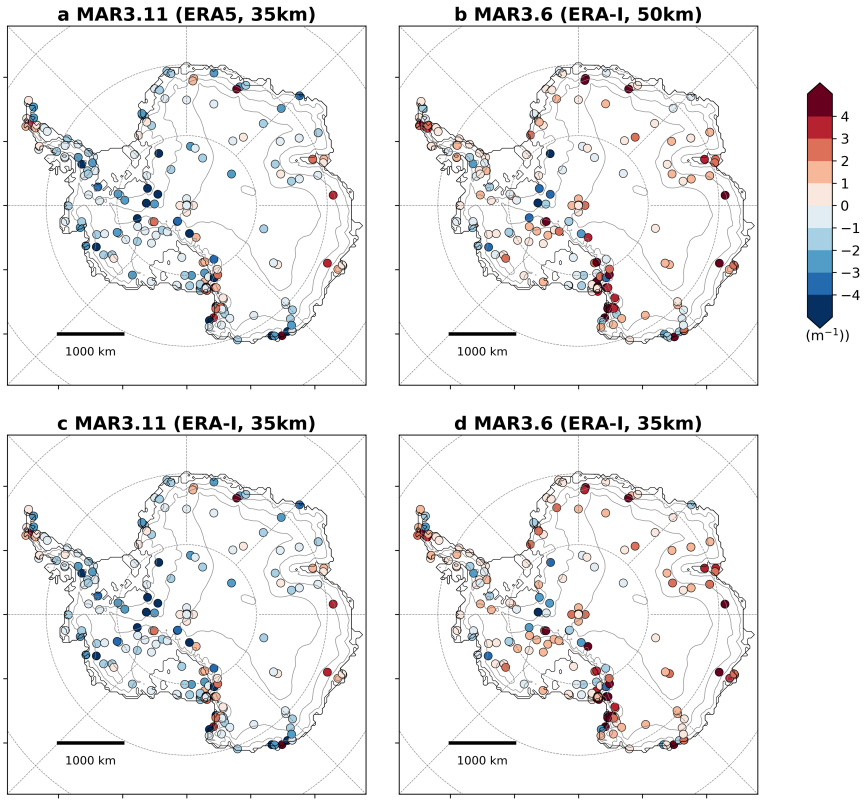

Figure 3.3: Mean annual near-surface wind-speed biases for MARv3.11 forced by ERA5 (a) and ERA-Interim (b) at 35 km, MARv3.6 forced by ERA-Interim at 50 km(b) and 35 km (d) for each AWS (Units: $\mathrm{m\,s^{-1}}$). The subplots a and b are the configurations used in this manuscript while c and d enables a comparison between the different resolutions, forcings and model versions.

The error is considered to be significant since the RMSE is larger than the observed variability. This is not surprising as all the MAR configurations evaluated here do not represent drifting snow knowing that the sublimation of drifting-snow particles strongly influences the humidity budget of the air (Amory and Kittel, 2019) and controls the seasonal cycle in relative humidity in drifting-snow areas (Le Toumelin et al., 2020).

3.1.5 Radiative fluxes

MARv3.11 underestimates SWD in summer and LWD throughout the year (Table 3.1). SWD is underestimated by -6.9 $\mathrm{W\,m^{-2}}$ with a mean RMSE reaching ∼44% of the observed variability (Table 3.1). As SWU are even more underestimated (-12.4 $\mathrm{m^{-2}}$), the model likely underestimates also the snow/ice albedo. Figure 3.4 illustrates the mean SWN bias (computed as the difference in mean SWD and SWU biases). Positive values represent situations where $Meanbias_{SWD} > Meanbias_{SWU}$, i.e the surface absorbs more shortwave energy suggesting an underestimation of the albedo. On the opposite, negative values in mean SWN biases ($Meanbias_{SWD} < Meanbias_{SWU}$) suggest an overestimation of the albedo as the surface reflects too much incoming energy. The albedo is underestimated over the ice shelves and most of low and middle elevations (below 3000 masl), except at Princess Elisabeth station, while it is overestimated at high-elevation locations. MARv3.11 also underestimates LWD by -9.9 $\mathrm{W\,m^{-2}}$, but the bias is stronger in summer (-15.1 $\mathrm{W\,m^{-2}}$) than in winter (-8.2 $\mathrm{W\,m^{-2}}$). The reproduction of the LWD variability is also less good in summer ($r = 0.62$) than in winter ($r = 0.78$). Note that MAR better reproduces the SWD variations compared to LWD, but this statistics is biased due to the natural cycle of SWD (null winter values) artificially increasing the ability of MAR to reproduce SWD variations. On the opposite, the LWD simulation involves more physical aspects of the code (atmosphere temperature, humidity content, and clouds). The comparison also reveals a negative bias in LWU for all the stations indicating that the modelled surface temperature is underestimated. The underestimation in LWD by MAR has also been highlighted over the Greenland Ice Sheet (e.g., Fettweis et al., 2017; Delhasse et al., 2019).

The underestimation of both SWD and LWD suggests biases in the cloud microphysics scheme (misrepresentation of the different atmospheric water species and related distribution) and/or in the radiative scheme itself (genesis and

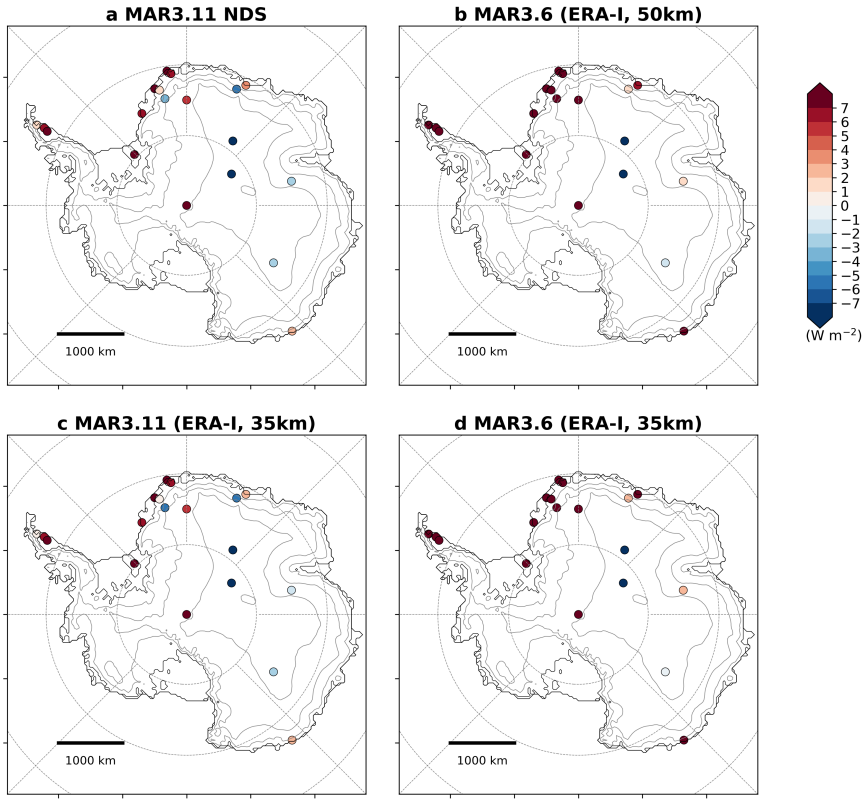

Figure 3.4: Mean annual shortwave net biases for MARv3.11 forced by ERA5 (a) and ERA-Interim (b) at 35 km, MARv3.6 forced by ERA-Interim at 50 km(b) and 35 km (d) for each AWS (Units: $\mathrm{W\,m^{-2}}$). The subplots a and b are the configurations used in this manuscript while c and d enables a comparison between the different resolutions, forcings and model versions.

interactions of radiation with the aerosols, greenhouse gases and cloud particles). As described in Ch. 2, MAR uses the same radiative scheme than the ERA-40 reanalysis (Uppala et al., 2005), which is now outdated (Morcrette et al., 2008; Hersbach et al., 2020) and is likely to be responsible for most biases (Delhasse et al., 2019). Furthermore, the cloud scheme in MAR relies on a one-moment scheme that represents the evolutions of the mixing ratio (and two moments for the ice crystal particles) involving a simplified parameterisation of the particle distributions. Using a two-moment scheme for all the hydrometeors would likely improve the model results (Morrison et al., 2005; Morrison and Pinto, 2005). Another potential aspect for the underestimation of the LWD is the drifting snow, neglected here, that has been proved to reduce the negative bias in MAR (Le Toumelin et al., 2020). Finally, it is worth mentioning that the measurements may be still biased in particular by riming on the radiometer despite the strict selection procedure following van den Broeke et al. (2004), or be only representative of too local conditions that the model could not represent due to its relative coarse resolution. The lower amount of measurements for the radiative fluxes compared to the other meteorological variables contributes to the uncertainty related to potential measurement errors and inferred model performance.

Since the near-surface air temperatures in winter and/or over the plateau simulated by MAR are too high despite too little incoming energy, MAR likely have compensating biases elsewhere in the model physics. The energy budget at the surface of the AIS essentially results from the equilibrium between the radiative and the turbulent (latent and sensible) fluxes. Although difficult to measure, it is likely that a misrepresentation of these turbulent fluxes compensates for errors in the radiative fluxes. As highlighted by Hofer et al. (2019); Mattingly et al. (2020), biases in the radiative scheme seem significant compared to the radiative forcing due to the present and future increase in greenhouse-gas concentration. Despite the good results of MAR for representing the near-surface temperature variability and trend, future developments of the model should focus on the improvement of the representation of radiative fluxes, including for instance the implementation of a more recent radiative scheme such as EcRad developed at the ECMWF and used to produce the ERA5 reanalysis (Hersbach et al., 2020).

MARv3.6 overestimates SWD in summer (+11.9 $\mathrm{W\,m^{-2}}$ for the configuration at 50 km forced by ERA-Interim) while strongly underestimates the mean annual LWD (-25.3 $\mathrm{W\,m^{-2}}$ for the same configuration). This underestimation of LWD, also occurring in winter, explains the negative biases in near-surface temperature

in MARv3.6 and differences with MARv3.11 (where the underestimation is weaker, see Table 3.1). The calibration of MARv3.11 over Antarctica revealed a small loss of water mass in MARv3.6 leading to the removal of clouds in the highest cloud layer. Differences in cloud representation partly explain the difference in simulated LWD between MARv3.6 and MARv3.11. Furthermore, major efforts between these two versions have been made to improve the cloud lifetime (Delhasse et al., 2019), which reduces the bias in LWD but also results in a reduction of the incoming SWD. However, remaining biases in LWD could be related to an underestimation of liquid-containing clouds in MAR (Hofer et al., 2019; Mattingly et al., 2020) likely due to a too fast conversion in the clouds of liquid into ice particles. The next stages of development and evaluation should therefore also address the microphysical properties of clouds in MAR.

3.2 Surface mass balance

The comparison between MARv3.11 forced by ERA5 and the observed SMB reveals a mean bias of -1 $\mathrm{kg\,m^{-2}\,yr^{-1}}$ corresponding to less than 1% of the mean observed SMB, and a RMSE of 79 $\mathrm{kg\,m^{-2}\,yr^{-1}}$ (Fig. 3.5). Figure 3.7 highlights that MAR does not present any systematic spatial bias but shows an alternance of negative and positive biases that has been related to the absence of drifting-snow and the curvature of the topography (Agosta et al., 2019). The comparison is further done using elevation classes to make the results clearer and to limit the influence of undersampled areas. Note that negative values were removed from the scatter plots shown by elevation classes (Fig. 3.6) and the statistical indicator using logarithmic value (*rlog*, the correlation computed on the logarithm of SMB values), but are retained in the other indicators using the original populations.

MAR tends to overestimate (underestimate) low (high) accumulation values in every elevation class. Over the ice shelves, MARv3.11 underestimates the SMB by 15 $\mathrm{kg\,m^{-2}\,yr^{-1}}$ (i.e, -8%) but this is mainly explained by one location (Fig. 3.6). The SMB simulated by MAR over the grounded margins (0-1200 masl) is too high (6 $\mathrm{kg\,m^{-2}\,yr^{-1}}$ or 3%). This is also the case for the 1200 masl – 2200 masl range (+14 $\mathrm{kg\,m^{-2}\,yr^{-1}}$ or 6%) where the RMSE nearly equals the variability of the observations (114 $\mathrm{kg\,m^{-2}\,yr^{-1}}$ vs 126 $\mathrm{kg\,m^{-2}\,yr^{-1}}$, i.e 90% of the observation variability) indicating a lower model performance. This overderestimation can be attributed to the absence of drifting-snow (including surface erosion and atmospheric sublimation) in these MAR simulations as this process mainly occurs

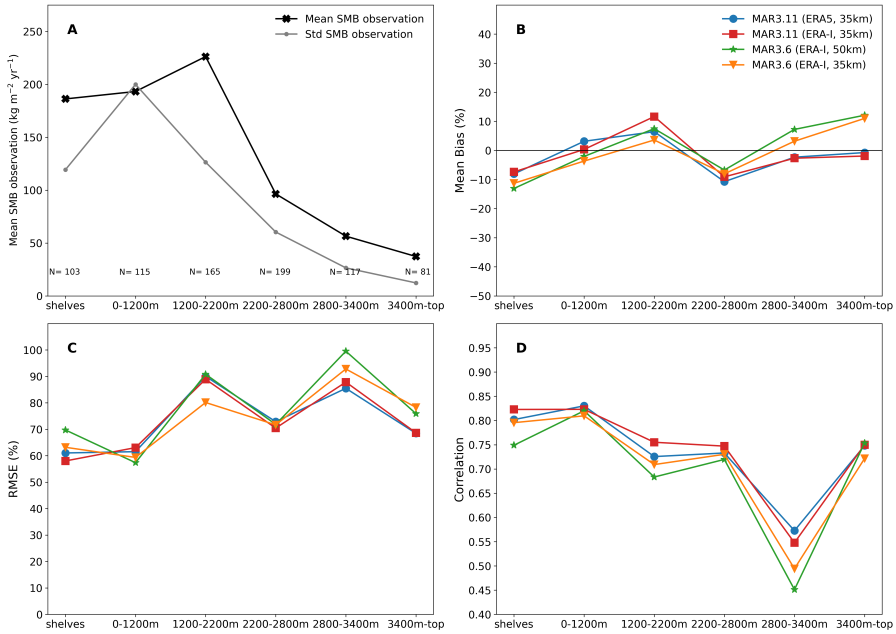

Figure 3.5: Comparison of the SMB modeled by MARv3.11 at 35 km forced by ERA5 (blue), ERA-Interim (red), MARv3.6 forced by ERA-Interim at 50 km (green) and at 35 km (orange) to SMB observations. A. Mean SMB observation value ($\mathrm{kg\,m^{-2}\,yr^{-1}}$) for each elevation class. Number of comparison pairs per class is also indicated. B. mean biases (% of the mean class-averaged SMB), C. RMSE (% of the class standard deviation SMB), and D. correlation for each elevation class

over the marginal slopes below 2000 masl (Lenaerts and Van den Broeke, 2012; Palm et al., 2017, 2018). Between 2200 masl and 2800 masl, MAR underestimates the accumulation (-10 $\mathrm{kg\,m^{-2}\,yr^{-1}}$ or -10%) but strongly overestimates the low values of SMB (Fig. 3.6). The MAR performance is worse for the elevation range between 2800 masl and 3400 masl with a high RMSE (23 $\mathrm{kg\,m^{-2}\,yr^{-1}}$ or 88%) and low correlations ($r = 0.57$ and $rlog = 0.55$). This could be related to local misrepresentations of latent heat fluxes (and associated deposition or sublimation) or snowfall advection and should be more investigated as the reason remains unclear. For the highest-elevation class, MARv3.11 correctly represents the mean accumulation (mean bias= 0 $\mathrm{kg\,m^{-2}\,yr^{-1}}$) and results are similar to lower-elevation classes, highlighting the singularity of the previous class. Despite the mentioned discrepancies, all the mean differences between MARv3.11 and the observation are not significant ($pvalue > 0.05$, Welch's t-test) illustrating the overall good ability of MAR to reproduce the mean SMB of each elevation class.

Figure 3.5 reveals that MARv3.6 at 50 km has less good results than the other configurations over the ice shelves. This is likely due to the coarse resolution that does not correctly represent these narrow areas and the processes occurring

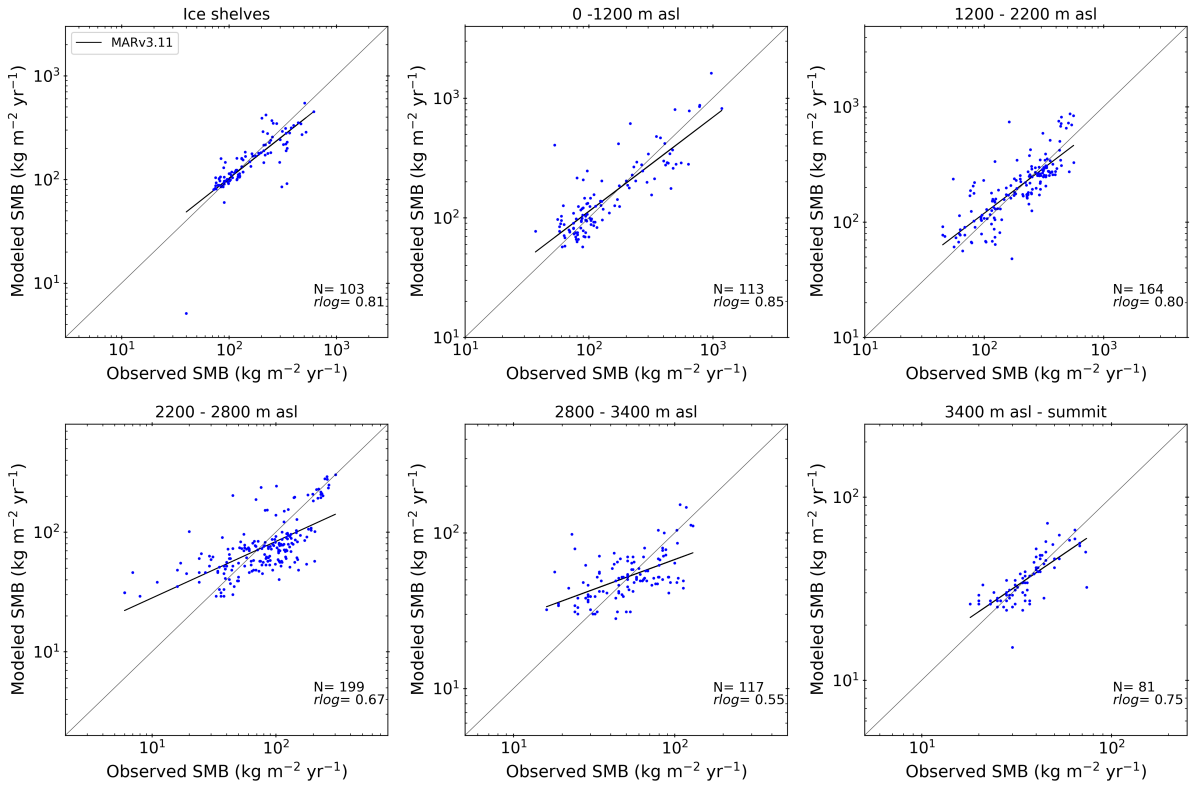

Figure 3.6: Comparison between MARv3.11 and observed SMB ($\mathrm{kg\,m^{-2}\,yr^{-1}}$) over the ice shelves and by elevation classes. Due to the use of logarithmic axes, only positive values for the observed and modelled SMB from all the MAR simulations are used (number for each bin N). Finally, the correlation coefficient based on logarithmic values is also shown (*rlog*).

there such as precipitations and interactions with katabatics winds or topography. Between 1200 masl and 2200 masl, MARv3.6 (35 km) forced by ERA-Interim has a lower RMSE and positive bias than MARv3.11 forced by ERA-5 despite the fact that using ERA-Interim seems to increase this bias as suggested by the higher bias when MARv3.11 is forced by these reanalyse. For higher-elevation classes (2800 masl–3400 masl and 3400 masl to the summit), MARv3.6 (both resolutions) results are less accurate. While MARv3.6 overestimates the SMB for these high elevations, the changes in the representation of the cloud-life time and sedimentation velocity of hydrometeors in more recent versions has reduced this bias. Snowfall in MARv3.11 is higher over the margins (explaining the positive bias up to 2200 masl) while it can intrude further inlands in MARv3.6 due to reduced sedimentation velocity. Note that the mean SMB modelled by MARv3.6 above 3400 masl significantly differs with the mean observed SMB ($pvalue = 0.01$ for MARv3.6 at 50 km and $pvalue = 0.02$ for MARv3.6 at 35 km) highlighting the improvements in MARv3.11.

3.3 Melt

MARv3.11 simulates more melt over the Peninsula, and less melt over the Queen Maud Land than the AWS-forced estimates from Jakobs et al. (2020) (Fig. 3.8). This could suggest that MAR overestimates melt at locations where melt is strong and underestimates it where it is weak. Due to the snow-melt albedo feedback, biases in melt are strengthened: if MAR overestimates the melting, stronger biases can be expected and conversely when MAR underestimates it. However, as the comparison is based on a small sample of data, no definitive conclusion can be drawn about a weak-strong melt contrast or whether it is only a regional bias. Furthermore, the data used for the comparison are partially obtained from a Surface Energy Balance model (i.e., dependent on a small amount of assumptions and parameterisations with its own biases), so this comparison must be regarded as an evaluation of the plausibility of the model results rather than the real model performance.

The excess of melt over the Peninsula is linked to the overestimation of SWN (Fig. 3.4) in summer (combinaison of higher SWD and too low albedo). It increases melt that is further enhanced by the snow-melt albedo feedback. Furthermore, the near-surface air temperatures simulated by MAR during summer are too high over the eastern side of the Peninsula (Fig. 3.2) which could also suggest stronger

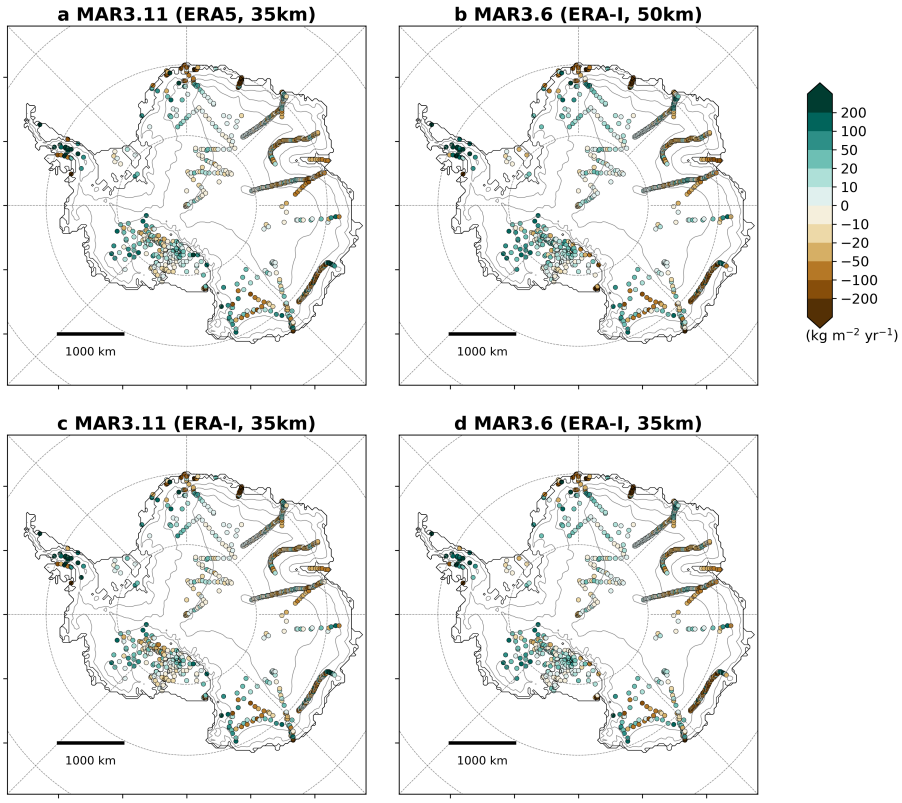

Figure 3.7: Mean annual SMB biases for MARv3.11 forced by ERA5 (a) and ERA-Interim (b) at 35 km, MARv3.6 forced by ERA-Interim at 50 km(b) and 35 km (d) (Units: $\mathrm{kg\,m^{-2}\,yr^{-1}}$). The subplots a and b are the configurations used in this manuscript while c and d enables a comparison between the different resolutions, forcings and model versions.

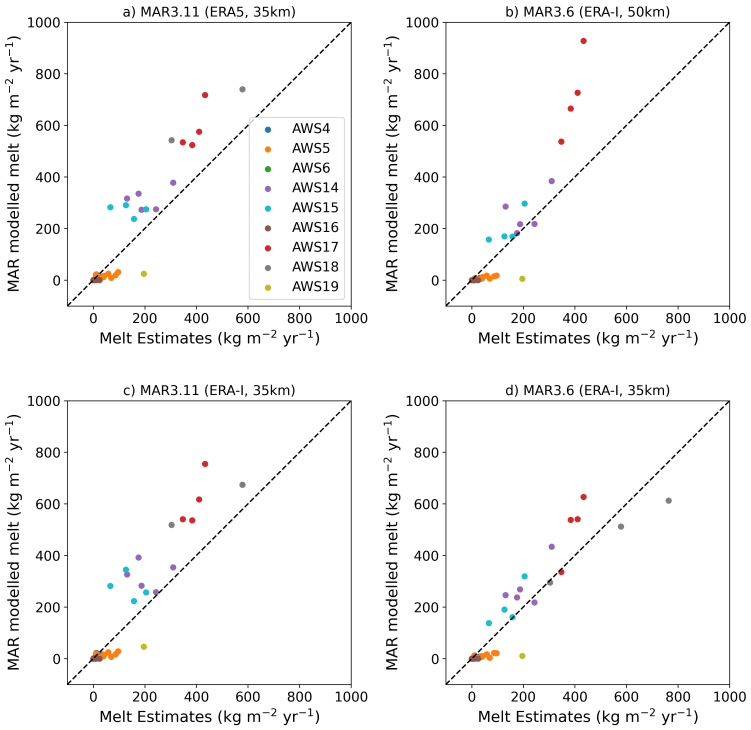

Figure 3.8: Comparison between MAR annual melt ($\mathrm{kg\,m^{-2}\,yr^{-1}}$) and AWS-forced melt estimates modelled by Jakobs et al. (2020) ($\mathrm{kg\,m^{-2}\,yr^{-1}}$) at 9 AWS locations for MARv3.11 forced by ERA5 (a) and ERA-Interim (b) at 35 km, MARv3.6 forced by ERA-Interim at 50 km (b) and 35 km (d). The subplots a and b are the configurations used in this manuscript while c and d enables a comparison between the different resolutions, forcings and configurations (see Fig. B.4 for the locations of the AWS).

sensible flux also increasing melt (and contributing to enhance the absorption of SWD). Foehn effects advect warm air and favour meltwater production due to the turbulent mixing and sensible heat exchanges (e.g., Datta et al., 2019) but also the dissipation of clouds increasing SWD. The overestimation of melt over the Peninsula could then be related to underestimation of albedo, overestimation of the Foehn effect reducing the cloud cover and/or other mechanisms such as the absence of drifting snow and its SWD reduction effect.

The misrepresentation of radiative fluxes and surface albedo, the neglection of drifting-snow processes, and the coarse resolutions are likely the main reasons explaining the underestimation of melt in Queen Maud Land (East Antarctica). The 35 km resolution of MARv3.11 is too coarse to accurately represent the conditions at AWS19 (the Roi Baudouin Ice Shelf) and the Princess Elisabeth Station (AWS16). While the model correctly simulates the katabatic winds at AWS16 (mean bias= $0.1\,\mathrm{m\,s^{-1}}$, $r = 0.93$) that warms the air and enhances melt, the elevation difference (+132 m) results in a negative bias in temperature (-1.1 °C) explaining the underestimation of melt despite a too low albedo. The Princess Elisabeth Station is located on a rocky escarpment where adiabatic compression of the descending flow warms the near-surface air. The low-albedo rocks absorb solar radiations and warms the snow surface by re-emitting longwave radiations leading to melt (Pattyn and Decleir, 1993; Pattyn et al., 2009). While MARv3.11 represents rocks and nunataks at the surface (Kittel et al., 2020), the coarse resolution precludes the representation of small rock areas leading to an underestimation of the surface albedo. The overestimation of the albedo, the underestimations of SWD and likely rock contributions lead to reduced meltwater production preventing the albedo from decreasing and further underestimating the meltwater production. Finally, MAR underestimates LWD over all the AWS in Queen Maud Land which contributes to a lack of incoming energy for melt production.

3.4 Chapter conclusion

MAR correctly reproduces the near-surface climate of the AIS and MARv3.11 reveals several improvements over MARv3.6. While the near-surface temperature of the new reference Antarctic configuration (MARv3.11 at 35 km forced by ERA5) is 0.8 °C higher than the observed average, the model tends to underestimate high temperatures but overestimate low temperatures inducing local different biases

according to the elevation. A particular attention should be paid to improve MAR results over the Peninsula and around the Ross Ice Shelf. MARv3.11 underestimates the summer SWD and LWD throughout the year. Despite a strong negative bias in temperature in MARv3.6 at 50 km (version and configuration of the model used in Ch. 4) due to an underestimation of LWD, the comparison over the whole ice sheet is similar to MARv3.11 at 35 km used in Ch. 5 and Ch. 6.

Regarding the representation of SMB, MAR exhibits no systematic biases and differs not statistically from the observations. However, the SMB simulated by MAR tends to be overestimated (underestimated) in low (high) accumulation areas. While the comparison reveals a correct agreement between MAR and the observations, accounting for drifting-snow processes should likely improve our results. MARv3.11 simulates more melt over the Peninsula where strong melt occurs, and less melt over the Queen Maud Land with observed weak surface melt rates. The misrepresentation of radiative fluxes and surface albedo, the neglection of drifting-snow processes, and the coarse resolutions are likely the main reasons explaining these melt biases, which are inherently amplified by the melt-albedo feedback.

Our comparison shows not significant differences between results at 35 km and 50 km resolution. This might suggest that a 35 km resolution is still too coarse to improve the representation of the Antarctic climate, or the opposite, i.e., that a 50 km resolution is already enough. We rather attribute these small differences to the absence of observations where a 35 km resolution could be an added value. Although this method enables a fair comparison between different grids and masks and smoothes out the small ($<$1 km) subgrid variability that a model could not represent, it also tends to not favour higher resolutions.

Future MAR developments over the AIS should be focused on a better representation of radiative fluxes by updating the radiative scheme itself and improving the interactions with the hydrometeors, but also including the penetration and diffusion of radiative fluxes (e.g., van Dalum et al., 2020) into the snowpack. Furthermore, updating the current broadband radiative scheme will also enable to fully use the three separate spectral bands pre-existing in the albedo scheme. Finally, the evaluation suggests biases in the surface albedo that could be directly related to the misrepresentation of radiative fluxes and the snow-melt albedo feedback, but also to the adaptations into the MAR albedo scheme that were (only) carried out for the Greenland Ice Sheet. The continuation of this work should therefore consist of an evaluation with satellite products to assess the MAR albedo

over the whole AIS before coming back to the evaluation of meltwater production.

CHAPTER 4

Sensitivity of the current Antarctic surface mass balance to sea-surface conditions using MAR

Following:

Kittel, C., Amory, C., Agosta, C., Delhasse, A., Doutreloup, S., Huot, P.-V., Wyard, C., Fichefet, T., and Fettweis, X.: Sensitivity of the current Antarctic surface mass balance to sea surface conditions using MAR, The Cryosphere, 12, 3827–3839, 2018.

Abstract Estimates for the recent period and projections of the Antarctic surface mass balance (SMB) often rely on high-resolution polar-oriented regional climate models (RCMs). However, RCMs require large-scale boundary forcing fields prescribed by reanalyses or global models (such as ESMs). Since the recent variability of sea-surface conditions (SSCs, namely sea-ice concentration, SIC, and sea-surface temperature, SST) over the Southern Ocean is not reproduced by most ESMs from the 5th phase of the Coupled Model Intercomparison Project (CMIP5), RCMs are then subject to potential biases. We investigate here the direct sensitivity of the Antarctic SMB to SSC perturbations around the Antarctic. With the RCM "Modèle Atmosphérique Régional" (MAR), different sensitivity experiments are performed over 1979–2015 by modifying the ERA-Interim SSCs with (i) homogeneous perturbations and (ii) mean anomalies estimated from all CMIP5 models and two extreme ones, while atmospheric lateral boundary conditions remained unchanged. Results show increased (decreased) precipitation due to perturbations inducing warmer, i.e. higher SST and lower SIC (colder, i.e. lower SST and higher SIC), SSCs than ERA-Interim, significantly affecting the SMB of coastal areas, as precipitation is mainly related to cyclones that do not penetrate far into the continent. At the continental scale, significant SMB anomalies (i.e greater than the interannual variability) are found for the largest combined SST/SIC perturbations. This is notably due to moisture anomalies above the ocean, reaching sufficiently high atmospheric levels to influence accumulation rates further inland. Sensitivity experiments with warmer SSCs based on the CMIP5 biases reveal integrated SMB anomalies (+5 % to +13 %) over the present climate (1979–2015) in the lower range of the SMB increase projected for the end of the 21st century.

4.1 Context

SIC and SST, hereafter referred to as SSCs, influence the exchange of gas, momentum, and heat at the air–sea interface at high latitudes. Due to its high albedo and thermal insulation, sea ice notably affects the thermodynamic and radiative properties of the ocean surface. Sea ice also prevents evaporation and inherent water vapour loading of air masses, potentially affecting precipitation at high latitudes. This is of particular importance for the AIS as its SMB is mainly controlled by precipitation (Van Wessem et al., 2018; Agosta et al., 2019).

Southern Ocean SSCs and especially sea-ice extent (generally defined as the area of all grid cells of satellite or model products with a SIC of at least 15 %) have experienced a significant increase since the 1970s (e.g. Parkinson and Cavalieri, 2012; Massonnet et al., 2013), highly contrasting with the dramatic decline reported in the Arctic Ocean (Cavalieri and Parkinson, 2012). Nonetheless, this general trend conceals major regional differences. For instance, the Amundsen–Bellingshausen seas showed a strong decrease in sea-ice extent, unlike other surrounding Antarctic seas (Turner et al., 2016). Despite the observed changes in the Antarctic SSCs and their large potential impacts on the climate system, the Antarctic SMB did not exhibit any significant trend at the continental scale over the last decades (Bromwich et al., 2011; Lenaerts et al., 2012b; Frezzotti et al., 2013; Favier et al., 2017; Agosta et al., 2019).

Several modelling studies have illustrated the influence of open-ocean areas on the AIS climate, for instance through a strong atmospheric heating (Simmonds and Budd, 1991; Gallée, 1995), an enhancement of cyclone activity (Simmonds and Wu, 1993; Gallée, 1996; Krinner et al., 2014), and intensified precipitation related to intensified evaporation (Wu et al., 1996; Bromwich et al., 1998; Weatherly, 2004). Conversely, the atmosphere has been shown to be less sensitive to SIC anomalies than SIC to atmosphere anomalies (Simmonds and Jacka, 1995; Bailey and Lynch, 2000) as anomalies induced by the ocean surface are often restricted to the lower atmospheric layers above the Southern Ocean (van Lipzig et al., 2002). However, these previous studies were based on coarse-resolution models (e.g. Weatherly, 2004), with simplified physics, resulting notably in biased surface sublimation (e.g. Noone and Simmonds, 2004), or on RCMs, forced by earlier and less reliable reanalyses and over short periods (e.g. van Lipzig et al., 2002).

High-resolution polar-oriented RCMs provide more reliable estimates of the Antarctic SMB components, but they depend on their forcing boundary conditions,

including SSCs. Using adequate SSCs in climate models could be as crucial as using a suitable downscaling model (Krinner et al., 2008; Beaumet et al., 2019b). This is of particular importance since most ESMs from CMIP5 (Taylor et al., 2012) have failed to reproduce the SSC temporal and spatial variability in the Southern Ocean area over the last decades (Mahlstein et al., 2013; Turner et al., 2013a; Shu et al., 2015; Agosta et al., 2015; Roach et al., 2018). As the projected Antarctic SMB could highly depend on the representation of the present sea-ice extent (Agosta et al., 2015), we investigate here the sensitivity of the Antarctic SMB to SSCs and more specifically to CMIP5 SSC anomalies with MAR for the period 1979–2015. This will help in the partitioning of the uncertainty in Antarctic SMB projections resulting from biased SSCs in ESMs from the uncertainty resulting from biased large-scale circulation patterns. Even though MAR is a well adapted tool to study the climate sensitivity to SSCs (Gallée, 1995, 1996; Massager et al., 2004; Noel et al., 2014), this study only discusses the direct and local impact of SSCs on the Antarctic SMB. This means that no feedbacks on the general circulation associated with sea-ice removal are considered (e.g. Bromwich et al., 1998; Krinner et al., 2014). Only direct impacts on air temperature, moisture, and SMB components are accounted for. Note that the general atmospheric circulation remains unchanged in our sensitivity experiments.

4.2 Additional methodological aspects

4.2.1 MAR and set-up

In this chapter, we use the version 3.6.4 of MAR adapted to Antarctica (Agosta et al., 2019). We refer to Agosta et al. (2019) and Ch. 2 (Sect. 2.1) for a detailed description of the model, its set-up and physics adaptations. MARv3.6.4 results have been evaluated in Ch. 3.

MAR is forced by ERA-Interim (Dee et al., 2011) every 6 h over 1979–2015 at its atmospheric lateral boundaries (pressure, wind, specific humidity, and temperature) and over the ocean surface (SIC and SST). It is worth noting that ERA-Interim uses the SST and SIC values from ERA-40, which are based on monthly and weekly ocean forcing fields (Fiorino, 2004), until January 2002. Afterwards, a switch was made with the daily operational NCEP product and since 2009 with the Operational SST and Sea Ice Analysis (OSTIA). The latter is a daily global SST analysis product at a 0.05° resolution (Stark et al., 2007; Donlon

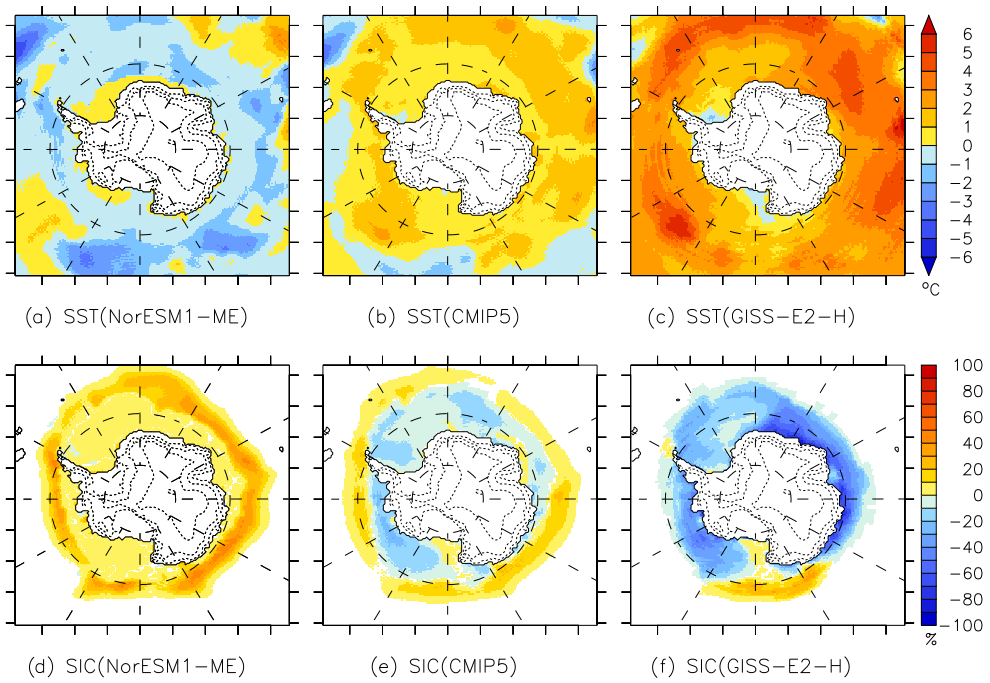

Figure 4.1: Top: SST anomalies (°C) of **(a)** NorESM1-ME, **(b)** CMIP5 average, and **(c)** GISS-E2 compared to ERA-Interim SST over 1979–2005. Bottom: SIC anomalies (%) for **(d)** NorESM1-ME, **(e)** CMIP5 average, and **(f)** GISS-E2 compared to ERA-Interim SIC over 1979–2005. These anomalies were introduced in the 6-hourly ERA-Interim SSCs.

et al., 2012). Finally, as for spin-up time, we start our simulations in March 1976 using ERA-40 reanalysis (Uppala et al., 2005) until 1979 with initial snowpack conditions interpolated from a previous reference simulation (Agosta et al., 2019).

Compared to Agosta et al. (2019), our integration domain (Fig. 4.1a) has been extended to include the maximum seasonal sea-ice extent as well as the major moisture source for precipitation over the AIS (Sodemann and Stohl, 2009). A resolution of 50 km has been selected to preserve a reasonable computational time. An upper-air relaxation extending from the top of the atmosphere to 6 km above the surface is used in order to constrain the MAR general atmospheric circulation (van de Berg and Medley, 2016; Agosta et al., 2019). This upper relaxation prevents potential feedbacks between the ocean state and the general atmospheric circulation. Similarly to Noel et al. (2014), the SMB sensitivity to SSC perturbations will thus be limited to the direct and local impacts of SST and SIC anomalies within the MAR integration domain.

4.2.2 Simulations

In this study, we consider MAR forced by ERA-Interim over 1979–2015 as the reference simulation. We perform two sets of sensitivity experiments in which SSCs from ERA-Interim are perturbed as described below. The first set follows the methods described in Noel et al. (2014), which are simplified and idealized scenarios, while in the second set, SSCs are modified according to SSC anomalies from CMIP5 models. In both cases, we analyse the direct impact of SSC anomalies on the Antarctic SMB.

4.2.2.1 SST sensitivity experiments

In these experiments, the 6-hourly ERA-Interim SST are decreased (increased) by 2 °C (SST ± 2) and 4 °C (SST ± 4) for ice-free grid cells. In cases of an SST reduction, ice-free oceanic grid cells are converted into full ice-covered grid cells if the SST drops below the assumed seawater freezing point (−2 °C). For an SST increase, the SST of any grid cell with a positive SIC value is set to the melting point (0 °C) to avoid positive SST and to prevent any SIC change.

4.2.2.2 SIC sensitivity experiments

To prevent changes at the interface between ice-covered and ice-free grid cells that are too strong, ERA-Interim SIC are reduced (increased) by the minimum (maximum) SIC value of the three and six ocean neighbours of each MAR grid cell. These experiments are called SIC ± 3 and SIC ± 6. Knowing that the resolution is 50 km, this means that the SIC is gradually decreased (increased) by a distance of 150 and 300 km. Following Noel et al. (2014), a SST correction is applied in order to prevent open-water temperature from dropping below −2 °C and maintain the SST of sea ice-covered grid cells below the melting point (0 °C).

4.2.2.3 Combined SST/SIC sensitivity experiments

Combined SST/SIC forcing fields are computed according to the two previous subsections. The added value of these experiments is the simultaneous representation of the increase (decrease) in sea-ice extent associated with the decrease (increase) in SST. They are named SST ± 2/SIC ∓ 3, SST ± 4/SIC ∓ 6.

Table 4.1: JJA and DJF sea-ice area (SIA) ($10^6\,km^2$) within the MAR domain over the period 1979–2015. SIA is defined as the sum of the products of the SIC and the area of all grid cells with a SIC value of at least 15 %. The DJF (JJA) seasonal mean SST is computed for the ocean free of ice in all experiments in DJF (JJA). We only considered grid cells remaining free of ice (SIC < 15 %) in all experiments in order to remove the influence of sea ice on surface temperature and numerical artefacts due to differences in open-ocean areas.

Experiment	JJA SIA ($10^6\,km^2$)		DJF SIA ($10^6\,km^2$)		JJA SST (°C)		DJF SST (°C)	
	Mean	Anomaly	Mean	Anomaly	Mean	Anomaly	Mean	Anomaly
Reference	13.31	–	4.49	–	5.55	–	6.36	–
SST −4/SIC +6	20.63	+7.32	10.83	+6.34	1.55	−4.00	2.36	−4.00
SST −2/SIC +3	17.04	+3.73	7.70	+3.21	3.55	−2.00	4.36	−2.00
SST +2/SIC −3	9.70	−3.61	2.08	−2.41	7.55	+2.00	8.36	+2.00
SST +4/SIC −6	6.77	−6.54	0.96	−3.53	9.55	+4.00	10.36	+4.00
SST/SIC(NorESM1-ME)	16.06	+2.75	8.63	+4.14	5.02	−0.33	5.78	−0.58
SST/SIC(CMIP5)	12.71	−0.60	4.05	−0.44	5.86	+0.31	6.77	+0.41
SST/SIC(GISS-E2-H)	9.66	−3.65	2.34	−2.15	8.30	+2.75	9.22	+2.86

4.2.2.4 CMIP5-based sensitivity experiments

In addition to the spatially homogeneous perturbations described above, we evaluate how SSC anomalies from CMIP5 models over the current climate can influence the present-day Antarctic SMB modelled by RCMs. For that purpose, we have determined a perturbation whose magnitude is representative of the CMIP5 ensemble bias. Firstly, monthly SSCs over 1979–2005 from all the CMIP5 models (using the historical scenario), as well as from ERA-Interim, were interpolated on the MAR grid (50 km × 50 km) using an inverse-distance weighted method based on the four CMIP5 models/ERA-Interim grid cells nearest to the current MAR one. We then computed the CMIP5 ensemble average from the interpolated CMIP5 monthly SSCs. Monthly SST anomalies between CMIP5 and ERA-Interim were computed only if the SICs from both the CMIP5 ensemble average and ERA-Interim were less than 50 % to avoid introducing additional temperature biases. Secondly, we averaged the monthly anomalies to obtain a mean anomaly, supposed to represent a constant bias over time.

New 6-hourly forcing SST are calculated as the sum of the 6-hourly ERA-Interim (i.e. for a specific day of a certain month) and the corresponding monthly anomaly in SST from the CMIP5 ensemble average (Fig. 4.1b), hereafter referred to as the SST(CMIP5) experiment. In the same way, we define SIC(CMIP5) experiments in which SIC anomalies (Fig. 4.1e) from the CMIP5 ensemble average are added to the 6-hourly ERA-Interim SIC. Introducing CMIP5 anomalies into the original ERA-Interim SSCs enables constant CMIP5 anomalies to be accounted for with the seasonal and interannual SSC variability represented in the ERA-Interim reanalysis. The combined SST/SIC anomaly experiment is performed by adding

CMIP5-averaged SST and SIC anomalies to ERA-Interim and is hereafter referred to as SST/SIC(CMIP5). Following the same method, we perform combined experiments for two selected CMIP5 models, namely NorESM1-ME (Bentsen et al., 2013) and GISS-E2-H (Schmidt et al., 2014), respectively representative of colder (i.e. lower SST and higher SIC) and warmer (i.e higher SST and lower SIC) SSCs than ERA-Interim as shown in Agosta et al. (2015). These experiments are hereafter called SST/SIC(NorESM1-ME) (Fig. 4.1a, d) and SST/SIC(GISS-E2-H) (Fig. 4.1c, f).

Table 4.1 compares SSC perturbations to the reference SSCs for June–July–August (JJA) and December–January–February (DJF) SST and sea ice area (SIA). The mean SST and SIC anomalies of the CMIP5 ensemble average, NorESM1-ME, and GISS-E2-H are also listed. The SIA is defined as the sum of the products of the SIC and the area of all grid cells with a SIC value of at least 15 %. SIA is preferred to sea-ice extent because it better accounts for SIC variations (Roach et al., 2018). Sensitivity experiments with perturbed SST by $\pm 2\,^{\circ}\mathrm{C}$ and SIC with the ± 3 neighbour grid cells are 1.5 times as large as CMIP5 mean anomalies over the current climate. However, it should be remembered that our sensitivity experiments are not based on climatologically consistent SIC (SST) perturbations related to SST (SIC) perturbations. For instance, the SIC prescribed in our experiments associated with $2\,^{\circ}\mathrm{C}$ warmer SST could be significantly different from the real SIC in a $2\,^{\circ}\mathrm{C}$ warmer climate since we do not use SIC projections from an ESM.

4.3 Results

In this section, we analyse the local and direct impact of SSC anomalies on the Antarctic SMB and its components modelled by MAR forced by ERA-Interim over 1979–2015 (maps of SMB components for all experiments can be found in Figs. C.1–C.5). Since liquid precipitation accounts for negligible mass gains compared to snowfall (Table C.1 in the Supplement), we do not distinctly analyse snowfall and rainfall over the AIS. As the large majority of surface meltwater and rainfall percolates and refreezes into the snowpack, runoff is a negligible component of the Antarctic SMB in both the reference and sensitivity experiments. However, some runoff events can occur on the Antarctic Peninsula and are enhanced in sensitivity experiments with warmer SSCs ($+2\,\mathrm{Gt\,yr^{-1}}$ in SST/SIC(GISS-E2-H) and $+6\,\mathrm{Gt\,yr^{-1}}$ in SST $+4$/SIC -6). The Antarctic Peninsula is characterised

Table 4.2: Top: annual mean integrated ($Gt\,yr^{-1}$) and standard deviation ($Gt\,yr^{-1}$) SMB, precipitation, water fluxes (sublimation and deposition processes), and surface meltwater production over the whole AIS (including grounded and floating ice) for the reference run (1979–2015). Positive water fluxes represent a mass loss through sublimation and evaporation while negative water fluxes are representative of deposition processes. Bottom: Difference of annual mean integrated SMB ($Gt\,yr^{-1}$ and %), its components, and meltwater ($Gt\,yr^{-1}$) between each sensitivity test and the reference simulation (1979–2015). Anomalies larger than the interannual variability are considered as significant and are displayed in bold.

Mean ($Gt\,yr^{-1}$)	SMB		Precipitation	Water fluxes	Meltwater
Reference	2569 ± 115		2678 ± 110	109 ± 10	97 ± 29
Anomaly ($Gt\,yr^{-1}$)	SMB	SMB%	Precipitation	Water fluxes	Meltwater
SST −4	−50	−1.9	−64	**−14**	−21
SST −2	−82	−3.2	−89	−7	−21
SST +2	+41	+1.6	+50	+9	**+39**
SST +4	**+143**	**+5.6**	**+162**	**+17**	**+117**
SIC +6	**−169**	**−6.6**	**−170**	0	−1
SIC +3	−108	−4.2	−107	+1	−1
SIC −3	+24	+0.9	+25	+2	−5
SIC −6	+90	+3.5	+91	+1	−5
SST −4/SIC +6	**−121**	−4.7	**−136**	**−15**	+1
SST −2/SIC +3	**−126**	−4.9	**−129**	−7	−11
SST +2/SIC −3	**+122**	+4.7	**+133**	+9	**+53**
SST +4/SIC −6	**+326**	**+12.7**	**+344**	**+13**	**+218**
SST/SIC(NorESM1-ME)	−104	−4.0	−105	0	+3
SIC(CMIP5)	+36	+1.4	+36	0	+7
SST(CMIP5)	+78	+3.0	+80	+1	+12
SST/SIC(CMIP5)	+103	+4.0	+105	+1	+18
SST/SIC(GISS-E2-H)	**+355**	**+13.8**	**+368**	**+11**	**+95**

by a sharp elevation gradient inadequately resolved at 50 km resolution, leading to a poor representation of specific climatic processes encountered in complex topography such as the Foehn effect. Elsewhere coastal runoff amounts stand for very low values. Due to the coarse model resolution limiting the representation of the atmosphere dynamics over the Antarctic Peninsula and the marginal contribution of runoff to surface mass loss compared to sublimation, surface meltwater production is discussed hereafter instead of runoff amounts. This allows possible areas to be located where the occurrence of surface melting could possibly affect the surface climate through an increase in snowpack cohesion inhibiting wind erosion (Li and Pomeroy, 1997), or the ice sheet dynamics through meltwater percolation and subsequent ice shelf destabilization (Bevan et al., 2017).

4.3.1 Sensitivity to SST perturbations

The higher evaporation and inherent increase in air moisture content in SST +2 and SST +4 experiments induce significantly stronger precipitation rates (i.e. greater than the interannual variability) in coastal areas. Figure 4.2a points out an opposite pattern between AIS coastal and central areas with a decrease in precipitation over the plateau and large ice shelves (Filchner-Ronne, Ross, and Amery, see Fig. C.6 for the location of these ice shelves). The warmer ocean leads to an increase in near-surface air temperature of the same magnitude as the increase in SST converts snowfall into rainfall over the ocean (Figs. C.2 a, m and C.3 a, m). Higher air temperature also causes a significant increase in surface melt, twice as large as for SST +4 relative to the reference simulation (Fig. C.5 a). However, melt and rainfall water can percolate into the snowpack, which remains unsaturated except in a few places. As a consequence, the surface albedo remains high and does not strengthen melting. Even if mass losses due to surface sublimation are larger in SST +4 (Fig. C.4 a and Table 4.2) because of higher air temperature, increased precipitation dominates and the SMB anomaly is significantly positive (Table 4.2 and Fig. 4.2a).

Conversely, a reduction of the SST leads to non-significant negative integrated SMB anomalies (Table 4.2). Lower SST weaken evaporation at the ocean surface and reduce the saturation water vapour pressure, resulting in smaller annual mean integrated precipitation over the whole AIS. This decrease in precipitation mainly explains local negative SMB anomalies in coastal areas (e.g. Victoria Land, Wilkes Land, Queen Maud Land, Ellsworth Land, and Marie Byrd Land; Fig. 4.2e, p; Fig. C.6 locates these coastal areas). However, precipitation over large ice shelves is slightly enhanced and is locally significantly larger. Over the plateau, stronger deposition processes combined with an increase in snowfall induce a higher SMB than the reference run. These features are discussed in more detail in Sect. 4.3.3. The total accumulation by deposition is the highest in SST −4 (Table 4.2). Moreover, a significant part of rainfall is converted into snowfall over the colder ocean as the near-surface air is also cooled by the decreased SST (Figs. C.2e, p and C.3e, p).

In the SST(CMIP5) experiment (Fig. 4.2i), SST are slightly higher (+0.3 °C in winter and +0.4 °C in summer), revealing similar patterns as in SST +2 (Fig. 4.2m), although non-significant for both integrated and local mean SMB values.

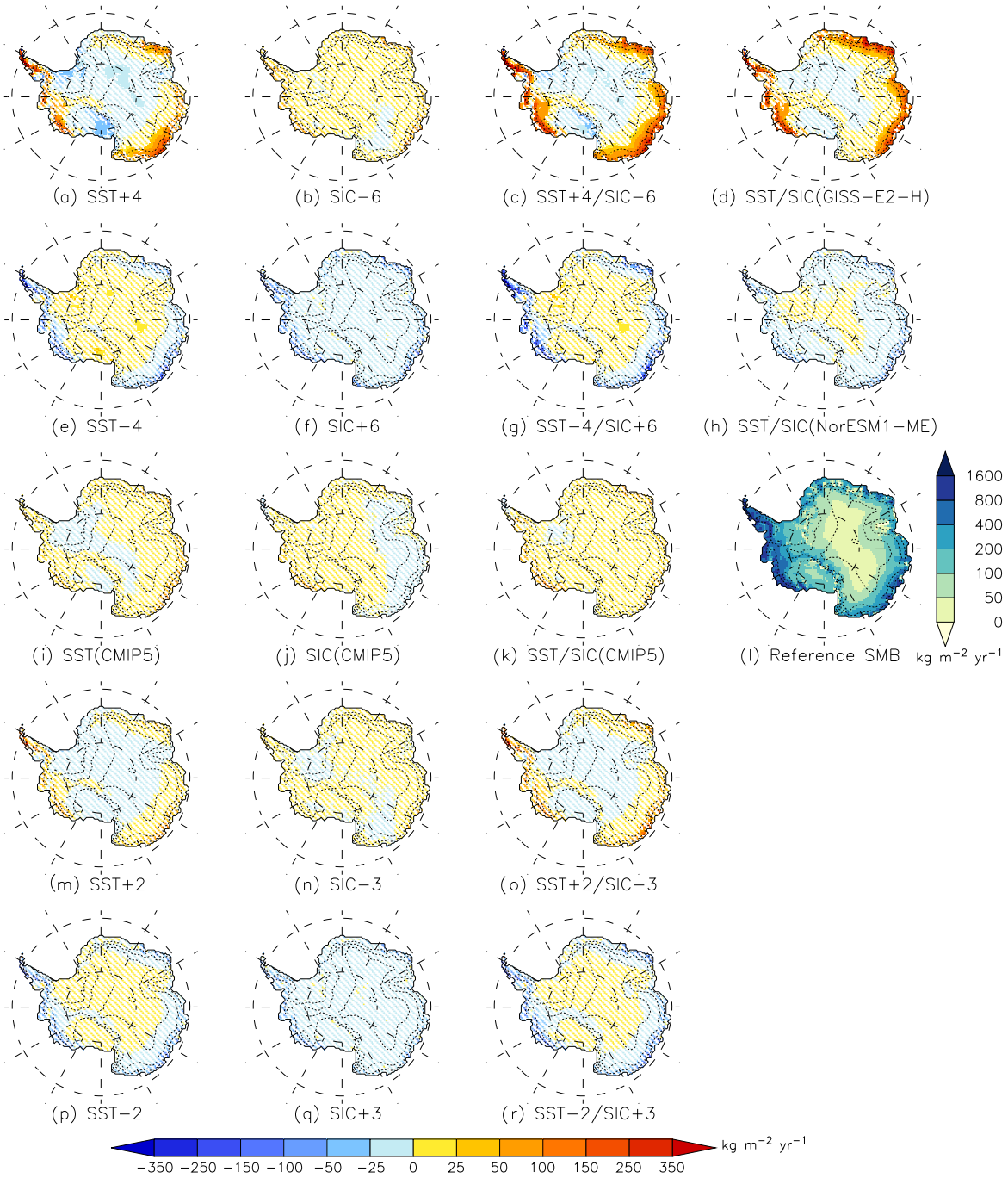

Figure 4.2: Difference in mean annual SMB ($\mathrm{kg\,m^{-2}\,yr^{-1}}$) between the reference simulation and **(a)** SST +4, **(b)** SIC −6, **(c)** SST +4/SIC −6, **(d)** SST/SIC(GISS-E2-H), **(e)** SST −4, **(f)** SIC +6, **(g)** SST −4/SIC +6, **(h)** SST/SIC(NorESM1-ME), **(i)** SST(CMIP5), **(j)** SIC(CMIP5), **(k)** SST/SIC(CMIP5), **(m)** SST +2, **(n)** SIC −3, **(o)** SST +2/SIC −3, **(p)** SST −2, **(q)** SIC +3, **(r)** SST −2/SIC+2 experiments. Differences less than the interannual variability are considered as non-significant and are shown by dashed lines. **(l)** Mean annual SMB ($\mathrm{kg\,m^{-2}\,yr^{-1}}$) simulated by MAR forced by ERA-Interim over 1979–2015.

4.3.2 Sensitivity to SIC perturbations

A sea-ice retreat induces a precipitation increase over the ice sheet, although most of the changes are smaller than the interannual variability (Fig. 4.2b, n) because it favours the advection of moister air masses towards the AIS, as already suggested by Gallée (1996). In contrast, a sea-ice increase produces a negative SMB anomaly driven by the reduction of precipitation over the whole AIS (Fig. 4.2f, q and Table 4.2). Similarly, a significant decrease in precipitation is observed over the new ice-covered ocean in SIC +6 (Fig. C.1f) because sea ice mainly acts as an isolator preventing evaporation at the ocean surface. Despite the decrease of the mean summer 2 m air temperature by 10 °C over new sea ice-covered areas in SIC +3 and SIC +6, surface melting does not exhibit a significant decrease over the ice sheet. The sensitivity of the Antarctic SMB to a decrease in SIC seems to be less pronounced than the sensitivity to an increase in SIC (+3.5 % in SIC −6 vs. −6.6 % in SIC +6). This is likely due to the smaller magnitude of the sea-ice retreat in SIC −6 and SIC −3 compared to the magnitude of the sea-ice extension in SIC +3 and SIC +6 (Table 4.1). Finally, the mean SMB from SIC(CMIP5) does not significantly differ from the reference SMB, both spatially (Fig. 4.2j) and integrated over the whole AIS (Table 4.2).

4.3.3 Sensitivity to combined SST/SIC perturbations

Higher SST associated with lower SIC reinforce anomalies found for individual perturbations. Evaporation at the ocean surface is stronger, while warmer air masses have a greater moisture content. Anomalies for integrated precipitation are significantly positive and account for +4.7 % and +12.7 % in the integrated Antarctic SMB for SST +2/SCI −3 and SST +4/SIC −6 respectively (Table 4.2). Similarly to SST +4 and SST +2, SST +4/SIC −6 and SST +2/SIC −3 show a large conversion of snowfall to rainfall over the ocean and enhanced precipitation rates over near-coastal regions, while the interior of the AIS exhibits lower accumulation rates (Fig. 4.2c, o). Moreover, snowfall significantly decreases over the Larsen C and George VI ice shelves (both located in the Antarctic Peninsula) but is largely compensated by rainfall refreezing into the snowpack. Finally, due to higher air temperatures, surface melting and sublimation are also significantly larger. On the contrary, colder SSCs (SST −4/SIC +6 and SST −2/SIC +3) prevent evaporation and result in lower precipitation over the AIS (Table 4.2, more particularly at the ice sheet margins (Fig. 4.2g, r). While SSC-combined sensitiv-

ity experiments over the Greenland Ice Sheet show similar anomalies to the SST sensitivity experiments (Noel et al., 2014), coupled perturbations act here together to induce larger anomalies over the AIS than the SST sensitivity experiments. Further, the sensitivity of the Antarctic SMB to SSCs is non-linear, illustrating the complexity of the interactions between the (sea ice-covered) ocean surface and the near-surface atmosphere.

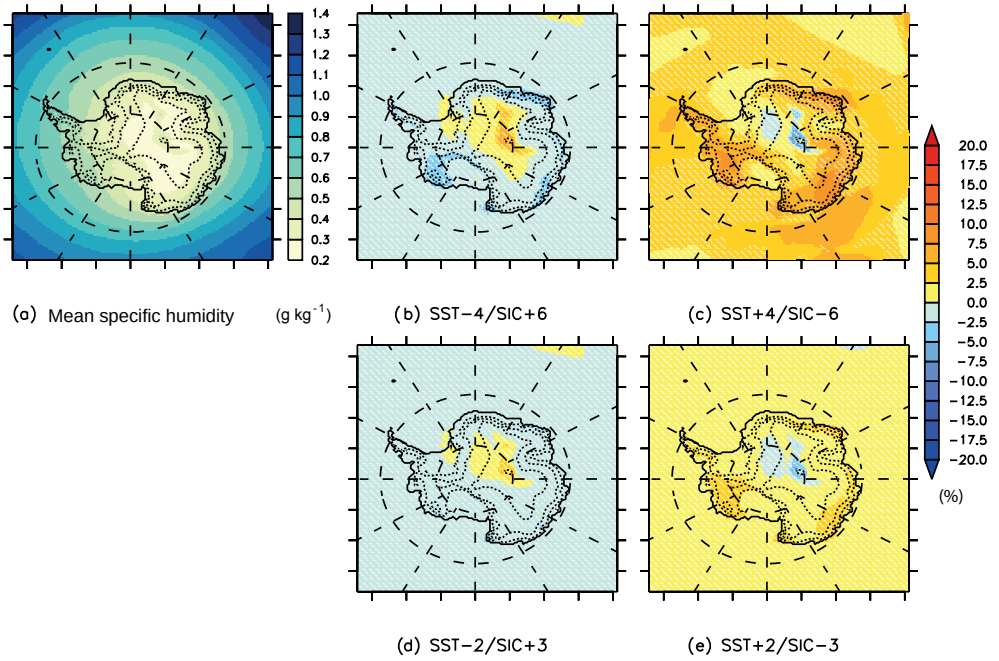

Figure 4.3: **(a)** Mean specific humidity modelled by MAR over 1979–2015 at 600 hPa (units: g kg^{-1}). Difference in mean specific humidity (%) between the reference simulation and **(b)** SST −4/SIC +6, **(c)** SST +4/SIC −6, **(d)** SST −2/SIC +3, **(e)** SST +2/SIC −3 experiments. Differences lower than the interannual variability are considered as non-significant and are shown by dashed lines.

As SSC anomalies in SST/SIC(GISS-E2-H) are close in magnitude to anomalies in SST +2/SCI −3 and SST +4/SIC −6, integrated values (Table 4.2) and spatial anomaly patterns (Fig. 4.2d) also illustrate the effect of warmer SSCs on the Antarctic SMB by a significant increase in precipitation, sublimation, and melt. However, the spatial pattern of precipitation is slightly different in comparison to SST +4/SIC −6. The precipitation anomaly in SST/SIC(GISS-E2-H) is reduced at the Adélie Land and George V Land margins in comparison to SST +4/SIC −6 due to the positive SIC anomalies in GISS-E2-H over the Ross and D'Urville seas (Fig. 4.1f). SST/SIC(CMIP5) displays a non-significant positive anomaly for both integrated and spatial SMB (Fig. 4.2k) as the mean SIC and SST anomalies in CMIP5 models do not significantly differ from the ERA-Interim SSCs (Figs. 4.1, 4.2b, e). CMIP5 model anomalies are more or less equally distributed (warm

or cold SSC anomalies) around the ERA-Interim SSCs, even if the mean CMIP5 SSCs are slightly warmer than ERA-Interim, explaining the non-significant positive SMB anomaly. Finally, for SST/SIC(NorESM1-ME), SSCs are representative of a colder ocean (lower SST and essentially higher SIC) resulting in a non-significant negative SMB anomaly with a precipitation decrease at the ice edge and over marginal areas of the plateau (Fig. 4.2h).

Since snowfall is the largest component of the Antarctic SMB, precipitation changes mainly explain the spatial anomaly patterns observed in our experiments. A warmer ocean with a smaller sea-ice cover tends to strongly enhance precipitation at the ice sheet margins, while decreased accumulation rates are modelled over the ice shelves and the central part of the ice sheet. These results suggest that precipitation can be formed further inland depending on the properties of air masses. In agreement with Gallée (1996), our hypothesis is that colder and drier air masses in cold ocean experiments are not sufficiently loaded with moisture to enable saturation and then snowfall over the margins. The decrease in moisture is likely to be larger than the decrease in saturation water vapour pressure associated with lower temperatures. This leads to a larger amount of remaining humidity that can be advected further inland (Figs. 4.3b, d and C.7b, d) where saturation occurs because of lower temperatures. On the contrary, the additional humidity in warm ocean experiments results in air masses that reach saturation faster (the increase in humidity overcompensates the increase in saturation water vapour pressure) and thus generate precipitation over the ice sheet slopes. MAR also simulates significantly higher upper-air temperature over the central part of the ice sheet (Figs. C.8c, e and C.9c, e) that, combined with the lower remaining humidity (Figs. 4.3c, e and C.7c, e), limits snowfall.

4.4 Discussion

Even if our sensitivity experiments rely on larger SSC perturbations than the interannual variability, mean integrated SMB anomalies are not systematically significant in comparison to our reference simulation. Similarly to van Lipzig et al. (2002), moisture and temperature anomalies remain confined below 700 hPa in the experiments with slightly perturbed SSCs (SST $\pm$ 2/SIC $\mp$ 3) (Figs. C.7d, e and C.9d, e). In contrast, moisture anomalies in the experiments with the largest SSC perturbations (SST $\pm$ 4/SIC $\mp$ 6) are not constrained to the boundary layer and reach upper atmospheric layers (600 hPa) (Fig. 4.3b, c). The blocking effect

due to the topographic barrier is likely to be reduced so that these large anomalies influence accumulation rates further inland (Fig. 4.2c, d, g). Furthermore, katabatic winds are enhanced when the SIC is decreased and the SST increased (Fig. C.10c) as already shown in Gallée (1996) and van Lipzig et al. (2002). Due to their offshore direction, they prevent the influence of warm ocean anomalies by precluding their propagation at the surface of the ice sheet and by advecting cold air from inland regions towards the margins.

In the context of global warming, it is important to note that the Antarctic SMB increases by 2 %–6 % for a SST increase alone and by 5 %–13 % for a SST increase coupled to a SIC drop (Table 4.2). Similar increases are found in sensitivity experiments based on CMIP5 SSC anomalies compared to ERA-Interim over the current climate (+4 % and +13 % respectively for SST/SIC(CMIP5) and SST/SIC(GISS-E2-H)). Knowing that the regional model RACMO2 projects an increase in SMB by 6 %–16 % in 2100 (Ligtenberg et al., 2013) and the global model LMDZ4 suggests a SMB increase of 17 % for the same horizon (Krinner et al., 2008), our sensitivity tests with warmer (CMIP5-based) oceans reveal SMB anomalies over the current climate in the lower range of the SMB increase projected for the end of the 21st century.

Sensitivity experiments are compared to SMB observations (Favier et al., 2013) from the GLACIOCLIM-SAMBA using an equivalent methods defined in Sect. 2.3.2, except that we averaged onto the MAR 50 km grid and only using grid cells containing more than one observation. This enables us to fairly compare the MAR 50 km simulations using 205 averaged comparison pairs. Correlation and RMSE do not vary significantly between the sensitivity experiments and the reference run (Table 4.3). Only mean biases vary, but the variations are by far smaller than the observed variability. Consequently, sensitivity experiments showing large local or integrated SMB anomalies do not significantly differ from the observed SMB. This is explained by the low number of available observations and highlights the importance of continuing to carry out field campaign measurements, as well as extending their spatial coverage to better evaluate model results.

4.5 Chapter Conclusion

Polar-oriented RCMs are suitable numerical tools to study the SMB of the AIS due to their high spatial resolution and adapted physics. Nonetheless, they are forced at their atmospheric and oceanic boundaries by reanalyses or ESM

Table 4.3: Comparison between modelled and observed SMB from the GLACIOCLIM-SAMBA database (Favier et al., 2013) over 1950–2015. Bias and RMSE units are $\mathrm{kg\,m^{-2}\,yr^{-1}}$. The observation mean is $65\,\mathrm{kg\,m^{-2}\,yr^{-1}}$, while the observation standard deviation is $119\,\mathrm{kg\,m^{-2}\,yr^{-1}}$.

Simulation acronym	SMB ($\mathrm{kg\,m^{-2}\,yr^{-1}}$)		
	r	BIAS	RMSE
Reference	0.93	−3	43
SST −4	0.93	−5	43
SST −2	0.93	−5	43
SST +2	0.93	−2	43
SST +4	0.93	+1	48
SIC +6	0.93	−8	42
SIC +3	0.94	−6	43
SIC −3	0.93	−3	43
SIC −6	0.93	0	43
SST −4/SIC +6	0.93	−6	44
SST −2/SIC +3	0.93	−7	44
SST +2/SIC −3	0.93	0	45
SST +4/SIC −6	0.92	+6	55
SST/SIC(NorESM1-ME)	0.93	−7	44
SIC(CMIP5)	0.93	−3	44
SST(CMIP5)	0.93	+3	47
SST/SIC(CMIP5)	0.93	0	43
SST/SIC(GISS-E2-H)	0.93	+8	52

products and are then influenced by their potential biases. These biases can be notably significant for SSCs (e.g. Agosta et al., 2015). With the RCM MAR, two sets of sensitivity experiments were carried out to assess the direct response of the Antarctic SMB to oceanic perturbations around Antarctica by perturbing the ERA-Interim SSCs over 1979–2015 while keeping the atmospheric conditions at the MAR lateral and upper boundaries unchanged. The first set consisted of spatially homogeneous SSC perturbations. The second set of experiments involved ERA-Interim SSC perturbations estimated from CMIP5 models anomalies over the current climate. We introduced mean anomalies from the historical run of CMIP5 models and two extreme models of CMIP5, namely NorESM1-ME and GISS-E2-H, respectively representative of warmer and colder SSCs than ERA-Interim.

Results mainly show increased (decreased) precipitation due to warmer (colder) SSCs affecting the SMB of the AIS. As precipitation is mainly caused by low-pressure systems that intrude into the continent and do not penetrate far inland, coastal areas are more sensitive to SSC perturbations with more significant anomalies compared to inland regions. Warmer SSCs significantly

enhance precipitation at the ice sheet margins since a greater moisture content of air masses leads to earlier saturation as they rise and adiabatically cool over the topography. On the contrary, colder SSCs reduce precipitation at the ice sheet margins and slightly increase it further inland as air masses have to rise up to higher elevations to reach saturation. Finally, the largest combined SST/SIC perturbations lead to significant (i.e., larger than the interannual variability) SMB anomalies integrated over the whole AIS due to moisture anomalies above the ocean reaching sufficiently high atmospheric levels to influence accumulation rates further inland. However, comparing modelled SMB from sensitivity experiments with observations shows no significant difference, suggesting that large integrated anomalies can remain unperceived when compared to the few field observations.

Our sensitivity tests with warmer (CMIP5-based) SSCs reveal that SMB anomalies over the current climate are in the lower range of the SMB increase projected for the end of the 21st century. Given the influence of SSC perturbations on the Antarctic SMB over the current climate, special attention should be paid to future SMB projections using potentially biased SSCs as forcing. This highlights the necessity of improving the representation of the current-climate SSCs in the context of downscaling the forthcoming CMIP6 model outputs to carry out future Antarctic SMB projections.

CHAPTER 5

Diverging future surface mass balance between the Antarctic ice shelves and grounded ice sheet

Following:

Kittel, C., Amory, C., Agosta, C., Jourdain, N. C., Hofer, S., Delhasse, A., Doutreloup, S., Huot, P.-V., Lang, C., Fichefet, T., and Fettweis, X.: Diverging future surface mass balance between the Antarctic ice shelves and grounded ice sheet, The Cryosphere Discuss. [preprint], accepted, 2020.

Abstract The future surface mass balance (SMB) will influence the ice dynamics and the contribution of the Antarctic Ice Sheet (AIS) to the sea-level rise. Most of recent Antarctic SMB projections were based on the 5th phase of the Coupled Model Intercomparison Project (CMIP5). However, new CMIP6 results have revealed a +1.3°C higher mean Antarctic near-surface temperature than in CMIP5 at the end of the 21st century enabling estimations of future SMB in warmer climates. Here, we investigate the AIS sensitivity to different warmings with an ensemble of four simulations performed with the polar regional climate model MAR forced by two CMIP5 and two CMIP6 models over 1981–2100. Statistical extrapolation allows us to expand our results to the whole CMIP5 and CMIP6 ensembles. Our results highlight a contrasting effect on the future grounded ice sheet and the ice shelves. The SMB over grounded ice is projected to increase as a response to stronger snowfall, only partly offset by enhanced meltwater runoff. This leads to a cumulated sea-level rise mitigation (i.e. an increase in surface mass) of the grounded Antarctic surface by 5.1 ± 1.9 cm sea-level equivalent (SLE) in CMIP5-RCP8.5 and 6.3 ± 2.0 cm SLE in CMIP6-ssp585. Additionally, the CMIP6 low-emission ssp126 and intermediate-emission ssp245 scenarios project a stabilised surface mass gain resulting in a lower mitigation to sea-level rise than in ssp585. Over the ice shelves, the strong runoff increase associated with higher temperature is projected to lower the SMB with a stronger decrease in CMIP6-ssp585 compared to CMIP5-RCP8.5. Ice shelves are however predict to have a close-to-present-equilibrium stable SMB under CMIP6 ssp126 and ssp245 scenarios. Future uncertainties are mainly due to the sensitivity to anthropogenic forcing and the timing of the projected warming. While ice shelves should remain at a close-to-equilibrium stable SMB under the Paris Agreements, MAR projects strong SMB decrease for an Antarctic near-surface warming above +2.5°C limiting the warming range before potential irreversible damages on the ice-shelves. Finally, our results reveal the existence of a potential threshold (+7.5°C) that leads to a lower grounded SMB increase. This however has to be

confirmed in following studies using more extreme or longer future scenarios.

5.1 Context

The Antarctic SMB is the resultant of accumulation through snowfall and ablation through surface erosion, sublimation and runoff. Positive (negative) SMB values reflect a mass gain (loss) at the surface of the ice sheet. The AIS currently loses mass mainly by ice discharge and basal melting. The difference between SMB and ice discharge determines the sea-level rise contribution of the AIS. Due to the large amount of grounded ice, the AIS is the largest potential contributor among the cryosphere (58 m SLE, Fretwell et al., 2013; Morlighem et al., 2020). Although not directly contributing to sea-level variations, relatively-flat and large ice shelves, i.e. the floating extensions of the ice sheet, nevertheless influence the ice dynamics by retaining the ice over the grounded continent that flows under the force of gravity toward the ocean. This buttressing effect first limits glacier-flow acceleration and then control ice discharge (e.g., Rignot et al., 2004; Dupont and Alley, 2005; Gudmundsson, 2013; Fürst et al., 2016).

Since the 2000s, the AIS has been losing mass at an accelerating rate mainly due to an increased ice discharge in the West AIS (Shepherd et al., 2018), itself caused by the acceleration of outlet glaciers in response to basal (ocean) melt thinning the ice shelves and reducing their buttressing effect (Paolo et al., 2015; Gardner et al., 2018; Rignot et al., 2019). Despite stable surface melt rates since 1979 (Kuipers Munneke et al., 2012), atmospheric conditions through intense melt events can lead to meltwater ponding at the surface of ice shelves, increasing their potential for hydrofracturing (Scambos et al., 2000; van den Broeke, 2005). The resulting ice-shelf collapses over the Antarctic Peninsula then caused enhanced ice discharge (Scambos et al., 2004, 2014), highlighting the important role of atmosphere-surface interactions in the AIS stability, likely to become even more important in the context of global warming.

With increasing temperatures, more surface mass gain is expected over the AIS as a result of an increase in precipitation (Palerme et al., 2017; Gorte et al., 2020). Frieler et al. (2015) suggested an increase in accumulation linked to air temperature of $\sim 6\%\,^{\circ}\mathrm{C}^{-1}$ that is confirmed by SMB reconstructions from ice cores over the 20th century (Medley et al., 2018; Medley and Thomas, 2019), but not retrieved in recent (too short) SMB reconstructions (Van Wessem et al., 2018; Agosta et al., 2019; Mottram et al., 2020) due to the internal climate variability

determining precipitation pattern (Previdi and Polvani, 2016). For moderate warming, increase in snowfall is likely to outpace increased losses through ablation and especially runoff making the Antarctic SMB the only future mitigating contributor to sea-level rise (Krinner et al., 2007; Agosta et al., 2013; Ligtenberg et al., 2013; Lenaerts et al., 2016; Garbe et al., 2020). Melt increase under the high emissions pathway by 2100 is however projected to be large enough to enhance ice-shelf collapses (Trusel et al., 2015; Donat-Magnin et al., 2020a). The future of ice shelves experiencing more snowfall that can enable the snowpack to absorb more liquid water, is still uncertain even if the firn air content should decrease (Ligtenberg et al., 2014; Donat-Magnin et al., 2020a), suggesting an increased risk of hydrofracturing and collapse (Kuipers Munneke et al., 2014).

The most recent projections of the Antarctic SMB are based on ESMs from CMIP5 (Taylor et al., 2012), whereas new climate projections are now available through CMIP6 (O'Neill et al., 2016). Under the highest emission scenario, projections for the AIS annual mean near-surface temperature in 2100 are $+1.3°C$ higher in CMIP6 models than in CMIP5 models (Fig. 2.2). However, using these climate models outputs directly to study the evolution of the SMB often involves several compromises: (i) their resolution remains too coarse to correctly represent the steep margins of the ice sheet or the peripheral ice shelves (Seroussi et al., 2020) and (ii) they do not account properly for important physical processes of polar regions, in particular those related to the stable boundary layer and snow metamorphism, snowmelt, albedo feedbacks, and refreezing in the snowpack (Lenaerts et al., 2016; Favier et al., 2017). This partly explains why the SMB derived from ESMs has often been roughly approximated as precipitation minus evaporation even for projections (e.g., Palerme et al., 2017; Favier et al., 2017; Gorte et al., 2020; Seroussi et al., 2020) or included a runoff computed from non-polar-oriented models (Golledge et al., 2015; Nowicki et al., 2020; Garbe et al., 2020), although a few exceptions exist (e.g., Lenaerts et al., 2016; Sellar et al., 2019).

Dynamical downscaling of ESMs (designating both global climate models and new-generation Earth System Models without any consideration of the model sophistication to represent the carbon cycle or cloud-aerosol interactions) with polar-oriented RCMs offers an alternative to address not only the issue of coarse spatial resolution, but also more importantly to more robustly evaluate changes in mass and energy fluxes at the ice-sheet surface (e.g., Fyke et al., 2018; Lenaerts et al., 2019; Fettweis et al., 2020). This is why we propose here to use the

polar-oriented RCM MAR, widely used over the AIS (e.g., Kittel et al., 2018; Agosta et al., 2019; Wille et al., 2019) to downscale an ensemble of 4 different ESMs from the CMIP5 and CMIP6 exercises, selected to cover a wide range of near-surface warming (+3.2°C to +8.5°C over the AIS during the 21st century and then statistically extrapolate our results to the full CMIP5 and CMIP6 ensembles. This study therefore aims to (1) quantify the surface response of the AIS to warmer climates, and more specifically the different responses of the grounded ice and ice shelves using both new scenarios and an adapted representation of polar processes, (2) discuss the evolution of individual SMB components including future runoff ablation that can significantly compensate for mass gained through snowfall, (3) assess the future contribution (and related uncertainties) of the grounded Antarctic SMB to sea-level rise and the future state of the peripheral ice shelves using all the CMIP5 and new CMIP6 models with different emissions scenarios by extrapolating RCM-derived SMB projections.

5.2 Additional methodological aspects

5.2.1 MAR and forcing ESMs

In this study, we used the latest MAR version (3.11), hereafter called MAR, that has been detailed (Ch. 2) and evaluated (Ch. 3) previously. The Antarctic topography, and ice/rock fraction are computed from the 1 km resolution digital elevation model Bedmap2 (Fretwell et al., 2013). The ice mask is fixed and cannot evolve, meaning that changes in ice extent following for instance an ice-shelf collapse are not represented. The same is true for surface elevation that is assumed to remain constant in the absence of ice dynamics and evolving topography. Therefore, feedbacks between the ice sheet geometry and the atmosphere are not taken into account in our simulations.

The selection of ESMs that were dynamically downscaled by MAR is presented Sect. 2.2.2; according to their ability to 1) represent the current climate around the AIS and 2) diversify the projected changes during the 21st century. We selected two models from the CMIP5 ensemble, ACCESS1.3 and NorESM-M, and two from CMIP6, CNRM-CM6-1 and CESM2.

5.2.1.1 Experiments

MAR is forced by 6-hourly large-scale forcing fields at its atmospheric lateral boundaries (pressure, wind, specific humidity, and temperature), at its sea surface (sea ice concentration and sea surface temperature), as well as at the top of the troposphere (wind and temperature). We forced MAR with the selected ESMs over 1976–2100, and the first five years (1976–1980) were discarded as spinup. The simulations are called MAR(ACCESS1.3), MAR(CESM2), MAR(CNRM-CM6-1), and MAR(NorESM1-M) hereafter. We used the same intermediate spatial resolution (35 km) as in Agosta et al. (2019) and Mottram et al. (2020) as a computation time compromise to run the model with multiple forcings over the 20th and the 21st centuries. In order to assess the quality of the downscaling over the present climate, we also forced MARv3.11 by the ERA5 reanalysis (MAR(ERA5) hereafter). The comparison between MAR forced by the different ESMs and by ERA5, is available as supplementary material (Sect. D.1).

We have chosen to define the reference period of the present climate as 1981–2010. This 30-year reference period coincides with the availability of reanalyses and is a compromise between the end of the historical scenarios, which last until 2004 for CMIP5 and 2014 for CMIP6. Furthermore, Mottram et al. (2020) showed that this period is characterised by a relatively stable SMB over Antarctica.

5.3 Results

Our ESMs-based experiments closely reproduce the SMB and near-surface climate of MAR(ERA5) over the historical period (Sect. D.1). The anomalies of the annual mean SMB modelled by MAR forced by each ESM compared to MAR(ERA5) are lower than the interannual variability (i.e, one standard deviation) of the SMB simulated by MAR(ERA5) over the historical period, suggesting that the biases are not significant. Overall, MAR(ACCESS1.3) has the best representation of the Antarctic SMB over the current climate (mean bias: -3 $\mathrm{Gt\,yr^{-1}}$, spatial rmse: 59 $\mathrm{kg\,m^{-2}\,yr^{-1}}$), while MAR(CESM2) is the least accurate (mean bias: -25 $\mathrm{Gt\,yr^{-1}}$, spatial rmse: 90 $\mathrm{kg\,m^{-2}\,yr^{-1}}$). We refer to Sect. D.1 to more details about the evaluation of our experiments. The results of our experiments over the current climate are consistent with the ranking of the ESMs given by Agosta et al. (2015), Barthel et al. (2020), and Agosta et al. (in preparation). This highlights the importance of selecting ESMs that correctly

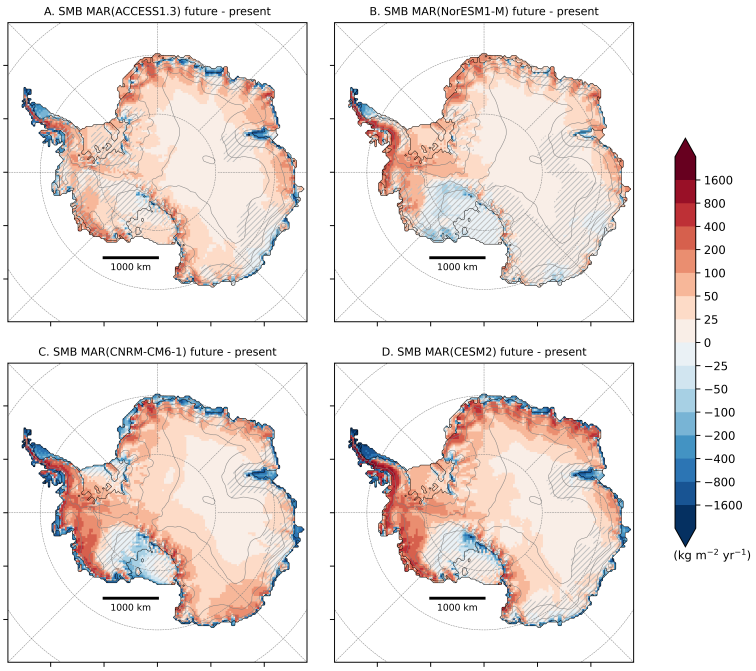

Figure 5.1: SMB changes ($\mathrm{kg\,m^{-2}\,yr^{-1}}$) between 2071–2100 and 1981–2010 as modelled by MAR forced by ACCESS1-3 (A), NorESM1-M (B), CNRM-CM6-1 (C), and CESM2 (D). Locations where future changes are smaller than the (natural) interannual variability over the present climate (interannual standard deviation) are hatched.

represent the historical climate around Antarctica as they strongly controls present biases independently of the capacity of the RCM to improve ESMs results.

Our projections of the Antarctic SMB show a trend towards surface mass gains by the end of the 21st century (Fig. D.4). MAR simulations forced by the high-emission scenarios ssp585 and RCP8.5 suggest a generally higher Antarctic SMB (including ice shelves) during 2071–2100 than for 1981–2010, with positive anomalies between $+257$ $\mathrm{Gt\,yr^{-1}}$ for MAR(CNRM-CM6-1) and $+505$ $\mathrm{Gt\,yr^{-1}}$ for MAR(CESM2). The projections reveal a spread of 248 $\mathrm{Gt\,yr^{-1}}$, i.e., almost a factor two between the lowest and the highest increase in SMB. Such a high amplitude highlights the importance of using multiple models for a better assessment of the uncertainties when discussing the future state of the Antarctic SMB throughout the 21st century.

5.3.1 Regional changes

Using Antarctic-integrated values however hides two distinct signals. The diverging trajectories of SMB over grounded versus floating ice (Fig. 5.1) suggest contrasted processes at play. In the rest of this manuscript, we will therefore

Table 5.1: Integrated anomalies ($Gt\,yr^{-1}$) of SMB, snowfall, rainfall, runoff, net sublimation (defined as surface sublimation minus surface deposition), and melt for the grounded ice sheet and the ice shelves over 2071–2100 compared to the present (1981–2010) from RCP8.5 and ssp585 simulations. All the anomalies are larger than the present interannual variability (i.e, standard deviation) of the same simulation and are therefore considered as significant.

	SMB	Snowfall	Rainfall	Runoff	Net sublimation	Melt
Grounded ice (11.94 $10^6\,km^2$)						
MAR(ACCESS1.3)	+382 ± 75	+501 ± 96	+36 ± 5	+151 ± 44	+4 ± 3	+277 ± 69
MAR(NorESM1-M)	+349 ± 61	+367 ± 64	+18 ± 5	+32 ± 11	+4 ± 3	+79 ± 25
MAR(CNRM-CM6-1)	+598 ± 67	+753 ± 120	+85 ± 29	+260 ± 124	-20 ± 12	+490 ± 17
MAR(CESM2)	+751 ± 60	+880 ± 111	+75 ± 24	+221 ± 89	-17 ± 8	+395 ± 135
Ice shelves (1.77 $10^6\,km^2$)						
MAR(ACCESS1.3)	-98 ± +44	+94 ± 17	+41 ± 9	+229 ± 62	+4 ± 1	+416 ± 93
MAR(NorESM1-M)	+30 ± 14	+83 ± 14	18 ± 15	+69 ± 23	+3 ± 1	+182 ± 51
MAR(CNRM-CM6-1)	-335 ± 190	+109 ± 12	+108 ± 34	+558 ± 227	-6 ± 4	+781 ± 220
MAR(CESM2)	-240 ± 127	+139 ± 8	+90 ± 28	+476 ± 162	-7 ± 3	+703 ± 179

discuss separately the ice shelves and the grounded ice sheet. This distinction is also justified by the direct equivalent between grounded-ice mass change and mean sea-level variations, whereas ice shelves do not directly contribute to sea-level variations even if their surface processes (such as hydrofracturing) are of crucial importance for the ice-sheet dynamics and therefore the Antarctic mass balance evolution. The locations mentioned hereafter are illustrated in Fig. D.5.

5.3.1.1 Grounded ice sheet

The grounded Antarctic SMB is projected to increase by +349 $Gt\,yr^{-1}$ (MAR(NorESM1-M)) to +751 $Gt\,yr^{-1}$ (MAR(CESM2)) from 1981–2010 to 2071–2100 (Table 5.1). Our simulations suggest large (up to more than twice the present - natural - interannual variability) positive SMB anomalies in West Antarctica (Marie Byrd and Ellsworth Land) and over the mountainous regions of the Antarctic Peninsula (Fig. 5.1). The situation in East Antarctica is more contrasted. The increase is significant (i.e, larger than the interannual variability over 1981–2010) in Queen Mary Land and high-elevation plateaus, while George V Land, Adelie Land and Wilkes Land are projected to have a weak increase in SMB for all the simulations, except MAR(CNRM-CM6-1) which suggests a strong increase there.

From 2015 onwards, the grounded SMB increases in all our MAR simulations (Fig. 5.3A). Large differences between projections appear around 2040–2050 when MAR(CESM2) and MAR(CNRM-CM6-1) suggest the strongest increase after 2050 and 2065 respectively while MAR(NorESM1-M) and MAR(ACCESS1.3) show a substantial increase at the end of the 21st century. Finally, only MAR(CNRM-

CM6-1) suggests a SMB decrease beyond 2095.

The grounded SMB trend is mainly dominated by an increase in snowfall (Fig. 5.3B). Increased air moisture content associated to higher air temperatures leads to a widespread increase in snowfall over the AIS, explaining most of the positive SMB anomalies. This increase is stronger where air masses saturate as they adiabatically cool when rising with the topography (Agosta et al., 2013; Ligtenberg et al., 2013). Figure 5.2 shows that the largest increase occurs in West Antarctica, where the accumulation by snowfall already is the highest over the present climate. Although more snowfall can be expected over most of the AIS in a warmer climate (Palerme et al., 2017), some parts of the Antarctic grounded ice sheet show negative anomalies. This decrease in snowfall affects areas such as inland of Marie Byrd where the SMB consequently decreases. This strong snowfall increase over the peripheral slopes associated afterwards with an inland reduction could result from enhanced condensation over the marginal slopes reducing moisture intrusion and snowfall formation inland (Kittel et al., 2018). Although this effect may be present in our projections, Figure D.4 also reveals a deepening of the ASL enhancing moisture advection towards the Antarctic peninsula in MAR(NorESM1-M). This deepening projected by NorESM-M especially occurs in winter (Raphael et al., 2016) and result from rising greenhouse-gas emissions (Hosking et al., 2016; Raphael et al., 2016).

Snowfall increase in response to higher air temperatures also competes with a subsequent increase in runoff over the grounded ice margins (Fig. 5.3E). Although runoff amounts are negligible in the present climate and the increase in runoff is lower than the increase in snowfall, the future runoff contribution could compensate up to 34% of the snowfall increase in MAR(CNRM-CM6-1) over 2071–2100, questionning the use of Precipitation-Evaporation in pace of SMB used in earlier studies (e.g., Palerme et al., 2017; Favier et al., 2017; Gorte et al., 2020). Other surface mass flux components such as rainfall (Fig. 5.3G), deposition and sublimation are not projected to contribute significantly to SMB changes.

From 1981 to 2100, our results suggest a grounded cumulative contribution of -3.7 cm, -5.8 cm, -8.1 cm and -10.6 cm SLE for MAR(NorESM1-M), MAR(ACCESS1.3), MAR(CNRM-CM6-1) and MAR(CESM2) respectively. Given that all these projections are obtained from similar anthropogenic forcing, this demonstrates the necessity of using several ESMs to evaluate the Antarctic contribution to the sea-level rise in high-emission scenarios at the end of the 21st century.

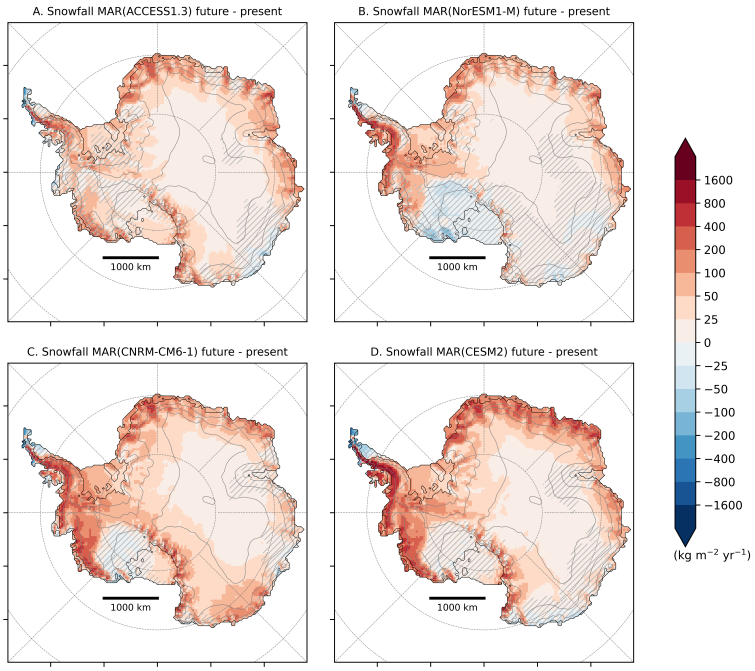

Figure 5.2: Snowfall changes (kg m^{-2} yr^{-1}) between 2071–2100 and 1981–2010 as modelled by MAR forced by ACCESS1-3 (A), NorESM1-M (B), CNRM-CM6-1 (C), and CESM2 (D), using ssp585 and RCP8.5. Locations where changes are smaller than the (natural) interannual variability of the present climate (interannual standard deviation) are hatched.

5.3.1.2 Ice shelves

The SMB evolution over the ice shelves shows more uncertainties depending on the forcing ESM. It remains close to the present-day values in MAR(NorESM1-M), while it strongly decreases after 2075 in the other simulations (Fig. 5.3B). All the MAR simulations agree on a significant SMB decrease over the ice shelves on the lee side (eastern) of the Northern Antarctic Peninsula and near Amery's grounding line (Fig. 5.1). With the exception of MAR(NorESM1-M), our projections also suggest a strong SMB decrease over the ice shelves on the windward side of the Northern Peninsula and over a majority of the ice shelves in Wilkes Land and in Queen Maud Land. Only MAR(CNRM-CM6-1) reveals widespread negative SMB anomalies over all the small Antarctic peripheral ice shelves. The Ronne-Filchner Ice Shelf is expected to have an increase in SMB, even in MAR(CNRM-CM6-1) except in the vicinity of the ocean. Our simulations suggest diverging responses over the Ross Ice Shelf, positive in MAR(ACCESS1.3) and MAR(CESM2), negative in MAR(CNRM-CM6-1) and MAR(NorESM1-M). The Ross Ice Shelf illustrates the large uncertainties related to the different model forcings on the future SMB over the Antarctic ice shelves until 2100.

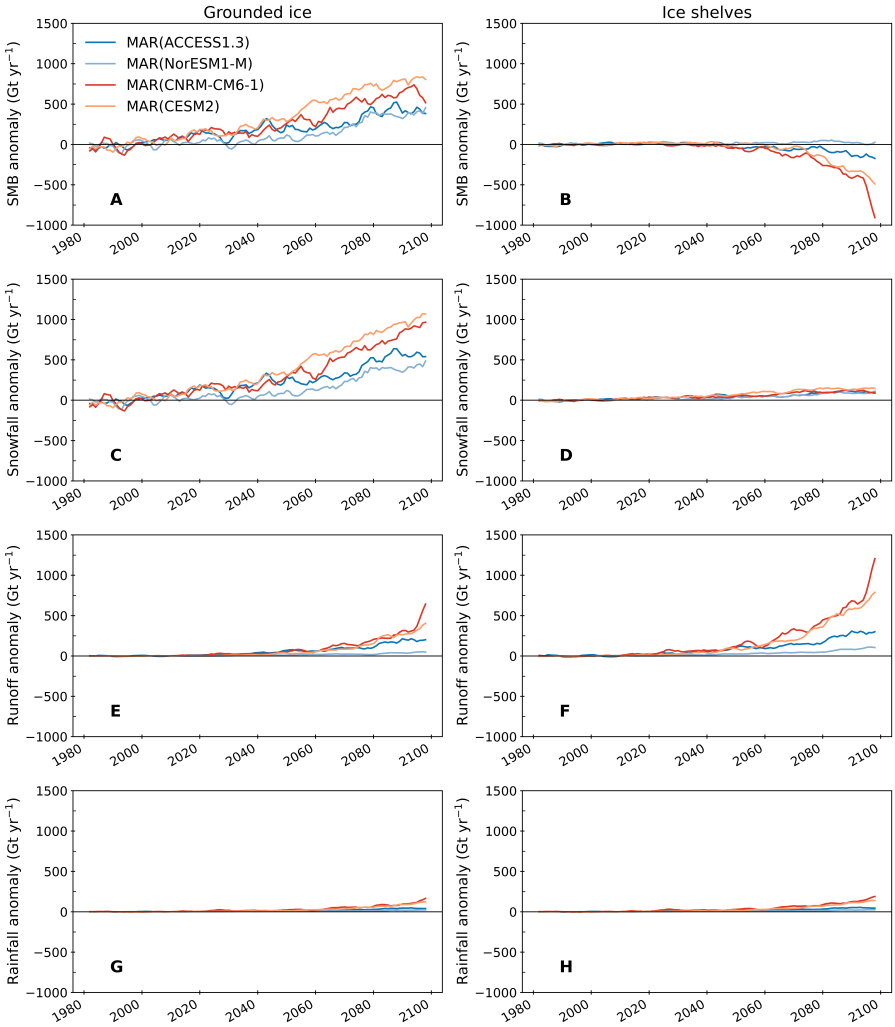

Figure 5.3: Time series of the integrated annual SMB (A, B), snowfall (C, D), runoff (E, F) and rainfall (G, H) anomalies (Gt yr^{-1}) over the Antarctic grounded ice (A, C, E, G) and the Antarctic ice shelves (B, D, F, H) from 1980 to 2100 simulated by MAR forced by RCP8.5 or ssp585 scenarios from ACCESS1-3 (blue), NorESM1-M (light blue), CNRM-CM6-1 (red), and CESM2 (orange) compared to the 1981–2010 reference period. A running average of 5 years was applied to the original time series for better readability. Sublimation and surface melt changes are shown in Fig. D.7.

MAR suggests an increase in snowfall over ice shelves (between +83 Gt yr^{-1} and +139 Gt yr^{-1}) regardless of the forcing ESM, but also a significant increase in rainfall (+18 Gt yr^{-1} to 108 Gt yr^{-1}) (Table 5.1). The increase in snowfall over the ice shelves is however weaker than the increase over the grounded margins, suggesting a stronger saturation of air masses when lifted over the ice-sheet slope (Fig. 5.2). Over the period 2071–2100, rainfall anomalies can be as large as snowfall anomalies on the ice shelves, or even outpace the increase in snowfall in MAR(CNRM-CM6-1), where snowfall is projected to decrease at the very end of the century (Fig. 5.3H). The warmer air also induces a conversion of snowfall into rainfall over the Antarctic Peninsula, where the total precipitation is projected to increase despite an increasing fraction falling as rain. Snowfall also decreases over the Ross Ice Shelf in MAR(NorESM1-M) due to a pronounced intensification of the ASL system bringing more moisture towards the Peninsula and less over the Ross Ice Shelf (Fig. D.6b), which reduces SMB over this area.

Higher air temperature also causes a significant increase in surface melt. Repeated years of intense melting, combined with increased rainfall, reduce the firn air content and weaken the snowpack capacity to retain liquid water. This results in large runoff production rates over the ice shelves, except over the Ronne-Filchner due to its more southern position, as displayed in Fig. 5.4. MAR(NorESM1-M) suggests the lowest increase in runoff (+18 Gt yr^{-1}), which is one order of magnitude lower than for MAR(CNRM-CM6-1) (+558 Gt yr^{-1}).

The amount of runoff projected at the end of the century explains the large changes in SMB over the ice shelves (Fig. 5.3F). The projected SMB decrease in MAR(CNRM-CM6-1) over the Ross Ice Shelf results from the larger increase in runoff than in snowfall while the decrease in SMB in the MAR(NorESM1-M) experiment is only attributed to reduced snowfall accumulation. Finally, the sharp runoff increase in MAR(CNRM-CM6-1) starting in 2090 reflects a widespread runoff over nearly all the ice shelves (Fig. 5.4).

5.3.2 Links with the ESM near-surface temperature

Our projections of the 21st century evolution of the Antarctic SMB yield large spread in SMB for both the Antarctic grounded ice and ice shelves. This spread can mostly be attributed to different warming rates in the forcing ESM, as they show a broad range of warming rates despite a similar radiative forcing due to anthropogenic emissions (Figure 2.2).

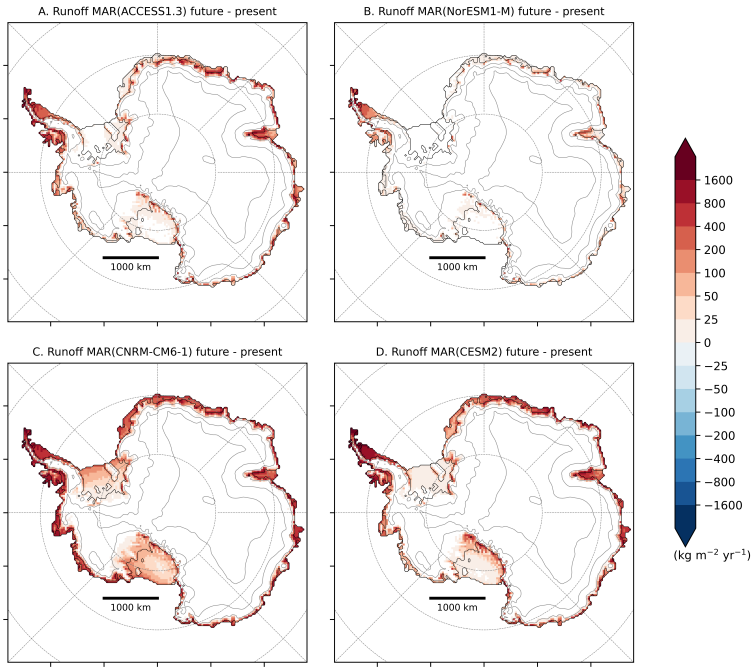

Figure 5.4: Changes in ruonff production ($\mathrm{kg\,m^{-2}\,yr^{-1}}$) between 2071–2100 and 1981–2010 as modelled by MAR forced by ACCESS1-3 (A), NorESM1-M (B), CNRM-CM6-1 (C), and CESM2 (D). Locations where changes are smaller than the (natural) interannual variability of the present climate (interannual standard deviation) are hatched.

We identify the 30-year periods (different for each ESM) characterised by an Antarctic (90°S–60°S) annual near-surface climate about +2.5 °C warmer on average than the climate over the historical period (1981–2010) to compare SMB anomalies resulting from an equivalent warming. This +2.5°C warming corresponds to the strongest 30-year averaged near-surface warming common to all our selected ESMs. The period selected for each ESM is listed in Table D.2. Mean SMB anomalies projected by MAR during these periods reveal a very similar spatial pattern between all our experiment. A +2.5 °C warming yields a mostly non-significant increase in SMB over the grounded ice sheet and a weak (negative) change over the surrounding ice shelves (Fig. D.8). This comparison at equivalent warming but different 30-year periods shows that the spread in the future SMB is mainly due to the timing and magnitude of the warming projected by the ESMs.

To remove the uncertainty associated to the different warming rates, we associate the future annual anomalies modelled by MAR to annual near-surface temperature anomalies over 90°S–60°S from the forcing ESM. Figure 5.5 reveals more consistent projections between all our experiments. Note that associating annual MAR anomalies with ESM temperature anomalies in the free atmosphere (700 or 850 hPa) does not change the comparison (not shown).

Precipitation increases following the Clausius-Clapeyron relation, a weak exponential form that can be approximated as a (nearly) linear relationship for moderate warming over the AIS (Agosta et al., 2013; Frieler et al., 2015; Palerme et al., 2017). The grounded (Fig. D.9A) increase is dominated by snowfall anomalies (Fig. 5.5A) with a weak contribution of rainfall (Fig. 5.5C). Over the ice shelves, snowfall is no longer increasing for strong warmings above +7.5°C. A the total increase in precipitation remains also approximately linear (Fig. D.9B), an increasing proportion of the potential additional precipitation falls as rain instead of snow for higher temperature over the ice shelves. Under increasing warming, more locations will experience rainfall, melting and runoff. We therefore link rainfall (Fig. 5.5C,D) and runoff (Fig. 5.5E,F) anomalies with near-surface temperature anomalies using a quadratic relation reflecting postive feedbacks (Fettweis et al., 2013). Our results suggest that the increase in rainfall will be stronger than the snowfall increase over the ice shelves for warming above 7.5°C. The integrated increase in runoff is stronger over ice shelves than over the grounded ice, despite the lower floating area compared to the grouded area. This is mainly explained by the low surface elevation of the ice shelves. Other studies (e.g., Kuipers Munneke et al., 2014; Trusel et al., 2015; Donat-Magnin et al., 2020a) also linked an exponential increase in melting with air temperature over the AIS.

Although the dominant signal explaining grounded SMB variations is the snowfall increase, the trend suggests a slowing or even a lower grounded SMB increase for warmings higher than +7.5°C (Fig. 5.6). This results from a strong increase in the grounded ice-sheet runoff. However, this grounded-SMB threshold is only supported by MAR(CNRM-CM6-1). Since this warming magnitude is not reached across all our other projections and as CNRM-CM6-1 is the warmest model in the entire CMIP5 and CMIP6 database, it would require longer projections to confirm the confidence of this threshold.

Over the ice shelves, a near-surface temperature increase by more than +2°C results in runoff anomalies larger than precipitation anomalies, hence leading to negative SMB anomalies (Fig. 5.6). While ice-shelf collapses could already occur due to hydrofracturing caused by enhanced surface melt, additional warming beyond this threshold will result in less surface accumulation, or even ice-shelf thinning for the warmings that result in a SMB decrease stronger than 478 $\mathrm{Gt\,yr^{-1}}$ (i.e., the present SMB simulated by MAR(ERA5)) over the ice shelves). This might induce MICI and/or enhancing positive feedbacks between ice dynamics and

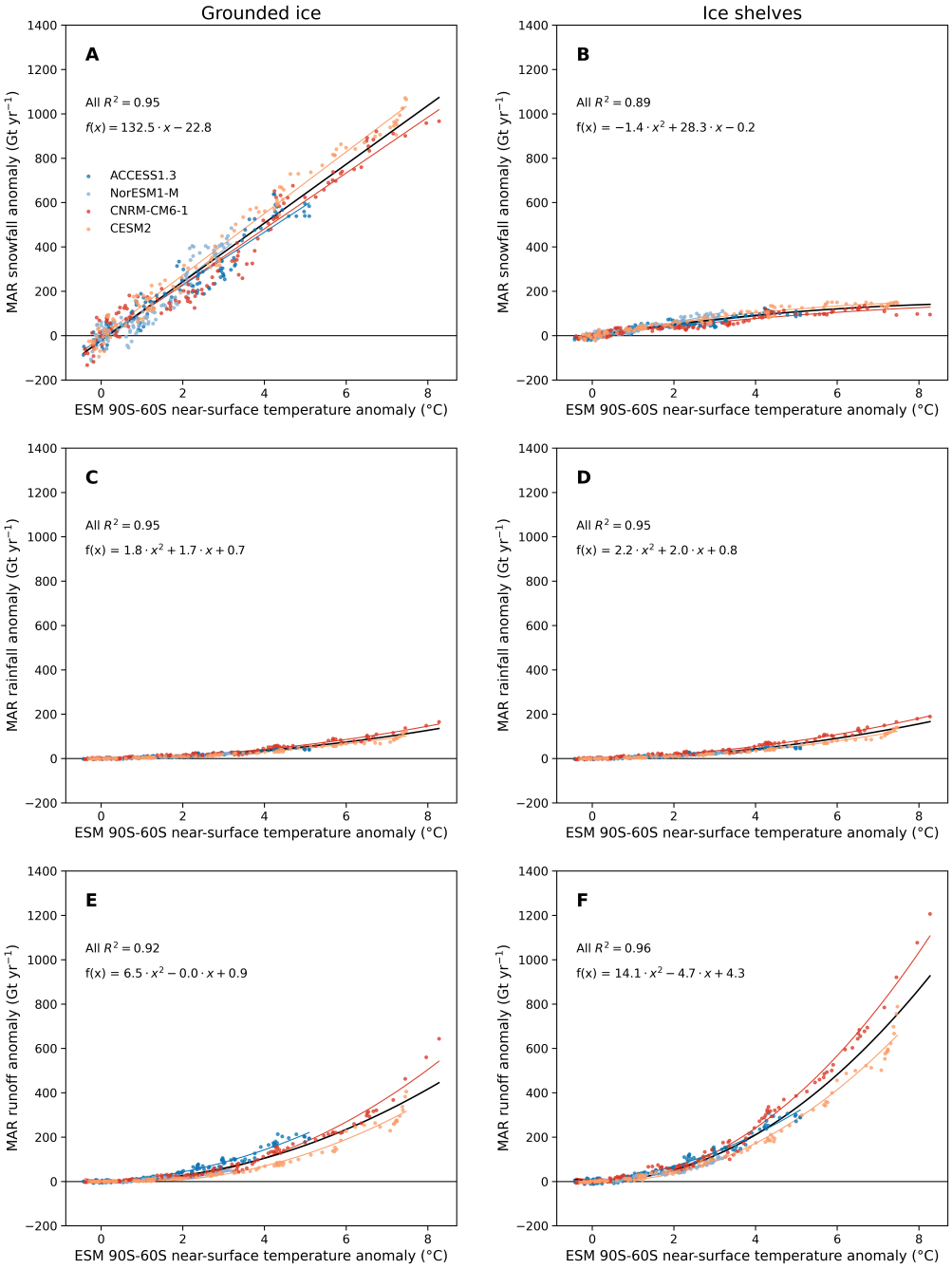

Figure 5.5: MAR snowfall (A, B), rainfall (C, D) and runoff (E, H) anomalies (Gt yr^{-1}) over the grounded ice (A, C, E) and ice shelves (B, D, H) compared to the annual near-surface temperature anomaly from the forcing ESM between 90°S-60°S (°C). The black regression was computed using all the MAR-ESM anomalies while individual regression are also represented (coloured lines). The regression equation and determination coefficient are mentioned for each scatter plot.

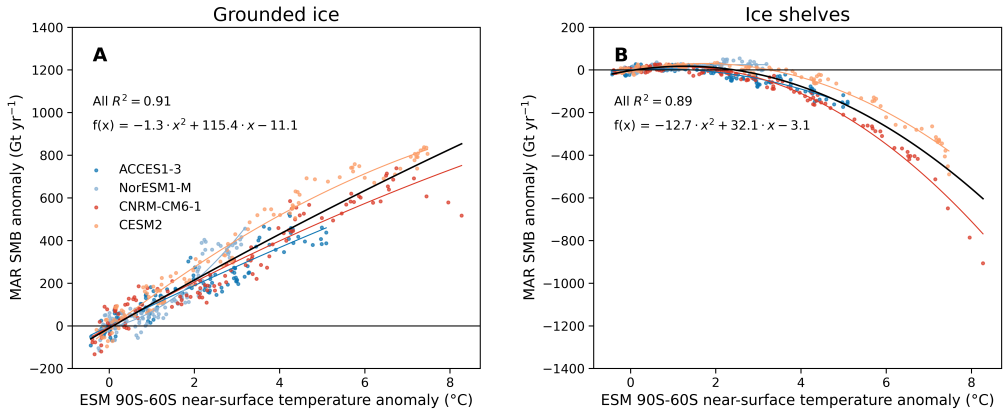

Figure 5.6: MAR SMB anomaly over the grounded ice (A) and ice shelves (B) compared to the annual near-surface temperature anomaly from the forcing ESM between 90°S-60°S (°C). The black regression was computed using all the MAR-ESM anomalies while individual regression are also represented (coloured lines).

new damage weakening the ice shelves (Lhermitte et al., 2020).

5.4 Discussion

5.4.1 Statistical projections for the CMIP5 and CMIP6 ensemble

Anomalies in Antarctic SMB and its driving components (precipitation and runoff) are strongly explained by near-surface ESM temperature anomalies between 90°S–60°S as discussed above (see Sect. 5.3.2). We therefore propose to reconstruct the SMB for both the Antarctic grounded ice (Eq. 5.1) and ice shelves (Eq. 5.2) using ESM near-surface temperature anomalies:

$$\Delta SMB_{grd} \approx -1.3\ \Delta TAS^2_{90-60S} + 115.4\ \Delta TAS_{90-60S} - 11.1, \tag{5.1}$$

$$\Delta SMB_{shf} \approx -12.7\ \Delta TAS^2_{90-60S} + 32.1\ \Delta TAS_{90-60S} - 3.1, \tag{5.2}$$

where ΔSMB_{grd}, ΔSMB_{shf}, and ΔTAS_{90-60S} represent the SMB anomalies over the grounded ice and ice shelves (in Gt yr^{-1}), and the ESM 90°S–60°S near-surface temperature anomaly (in °C) compared to their respective mean value over 1981–2010. A more detailed description of the ability of this regression to represent SMB anomalies is presented in Supplementary Material (Fig. D.10).

Since CNRM-CM6-1 has the strongest Antarctic near-surface warming among all CMIP5 and CMIP6 models, we can use this regression to predict the future SMB in 2100 without any extrapolation outside the warming range of our projections. However, this implies several hypotheses, such as the absence of strong atmospheric circulation changes (influencing humidity advection) or a fixed ice surface (topography).

Using Eq. (5.1) and Eq. (5.2), we reconstructed the annual Antarctic SMB for all the CMIP5 (RCP8.5) and CMIP6 (ssp126, ssp245, ssp585) models for which the annual near-surface temperature is available until 2100 (Figs. 5.7–5.8). The projected SMB anomalies remain similar until 2040–2050 in all the reconstructions. They then start to diverge and lead to a difference of -1.2cm SLE (-6.3 ± 2.0 cm SLE in CMIP6-ssp585 vs -5.1 ± 1.9 cm in CMIP5-RCP8.5 cumulated over the period 1981–2100). From the period 2045–2050, the SMB on the ice shelves starts decreasing in CMIP5-RCP8.5 models, and even more in CMIP6-ssp585 models, with a multi-model-mean difference of 65 $\mathrm{Gt\,yr^{-1}}$ over 2071–2100. A few models nonetheless suggest a steady-state ice-shelf SMB both in the CMIP5 and CMIP6 ensembles. It should also be noted that the CMIP6-ssp585 spread is much larger than in CMIP5-RCP8.5, as it ranges from strong negative anomalies (-600 $\mathrm{Gt\,yr^{-1}}$, i.e. lower than present ice-shelf SMB) to steady state or even slightly positive anomalies on the ice shelves. The CMIP6-ssp585 ensemble-mean value in 2100 is also nearly outside the spread range of CMIP5-RCP8.5 models highlighting the average stronger SMB decrease in CMIP6-ssp585. Similarly to what is projected for the Greenland ice sheet (Hofer et al., 2020), the higher equilibrium climate sensitivity of several CMIP6 models largely explains the differences between the CMIP5 and CMIP6 results. Both the CMIP6-ssp126 and CMIP6-ssp245 scenarios yield a stable SMB (increased over the grounded ice and close to steady state to slightly negative over the ice shelves) after 2050. In cumulative terms, our CMIP6 reconstructions cumulated over the 21st century indicate Antarctic grounded-surface contributions of -3.0 ±1.4 cm SLE for CMIP6-ssp126 and -4.2 ±1.6 cm SLE for CMIP6-ssp245, i.e a lower sea-level rise mitigation than for CMPIP6-ssp585. As described in Sect. 5.3, a high temperature increase induces higher precipitation rates but also higher runoff over the grounded ice sheet. Figure D.11 reveals large spreads in both integrated snowfall and runoff changes. However, as runoff increase partly compensates snowfall increase, the spread in SMB change is strongly reduced compared to the individual components.

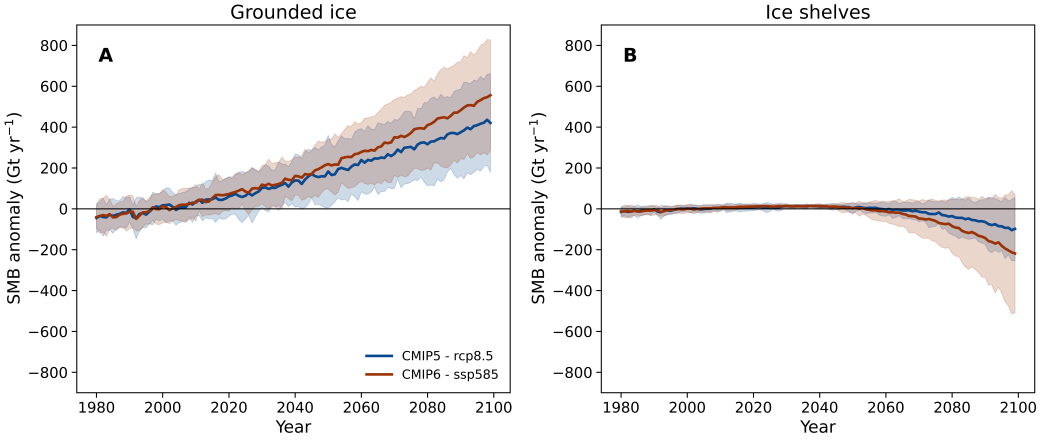

Figure 5.7: Reconstructed SMB anomaly Gt yr^{-1} using CMIP5-RCP8.5 (blue) and CMIP6-ssp585 models (red) over the Antarctic grounded ice (A) and ice shelves (B). Projections are shown using the multi-model mean (solid lines) and the 5 to 95% range, corresponding to ±1.64 standard deviation, across the distribution of individual models (shading).

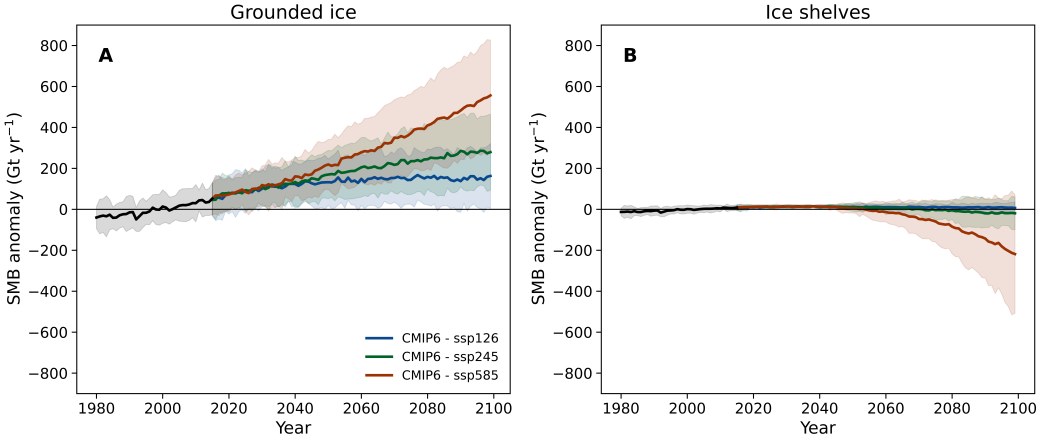

Figure 5.8: Reconstructed SMB anomaly Gt yr^{-1} for the CMIP6 models using the ssp126 (green), ssp245 (green) and ssp585 (red) scenarios over the Antarctic grounded ice (A) and ice shelves (B). Projections are shown using the multi-model mean (solid lines) and the 5 to 95% range, corresponding to ±1.64 standard deviation, across the distribution of individual models (shading).

5.4.2 Comparison with the ISMIP6-derived SMB

Due to time constraints and computational demands faced by the Ice Sheet Model Intercomparison Project (ISMIP6, Nowicki et al., 2016), future Antarctic projections for forcing ice-sheet models were derived directly from ESMs while, over the Greenland ice sheet MAR was used to downscale ESM projections (Nowicki et al., 2020). However, using ESMs to study the evolution of the SMB often involves several compromises related to their coarse resolution and their low sophistication to represent important physical processes of polar regions. Although RCMs have been believed to add uncertainties in the downscaling product (Nowicki et al., 2016), the significant (SMB) biases in ESMs over the current climate (e.g., Krinner et al., 2007; Agosta et al., 2015; Lenaerts et al., 2017b; Palerme et al., 2017; Krinner and Flanner, 2018) might be a larger source of uncertainties than the downscaling itself. Therefore, we compare our MAR projections forced by NorESM1-M (RCP8.5), CESM2 and CNRM-CM6-1 (ssp585) to the ISMIP6-derived SMB used to predict the future Antarctic sea-level contribution (Seroussi et al., 2020) by interpolating the 32 km SMB fields built by ISMIP6 on the 35 km MAR grid.

Figure 5.9 compares future SMB changes (2081–2100 versus 1995–2014 i.e., the ISMIP6 reference period) projected by MAR and the respective forcing ESMs. While the MAR projections are relatively insensitive to the forcing ESM for the same warming (see Sect. 5.3.2), the comparison between MAR and the forcing ESM reveals large differences, independently of the differences due to the higher resolution used in MAR that enables to distinguish high-elevation positives anomalies from low-elevation negative anomalies. For example, CNRM-CM6-1 projects a strong near-surface Antarctic warming (Fig. 2.2 and Nowicki et al. (Fig. 1a in 2020) but the related runoff increase is particularly weak (Figs. D.11 and D.8), leading to only very slightly negative anomalies, in contrast to MAR(CNRM-CM6-1), that simulates widespread negatives anomalies around nearly all the peripheral ice shelves consistent with a stronger warming Fig. 5.5. As highlighted by Fettweis et al. (2020), this suggests that the physics of the models and/or the biases over the current climate (in particular for the melt) could strongly influence the projected near-surface changes for identical changes in the free atmosphere. These MAR and ESM differences also highlight the importance of correctly representing the current climate and the need of additional projections relying on more models, including both RCMs and ESMs. As the integrated differences cumulated over 1995–2100 can be larger or as large as the

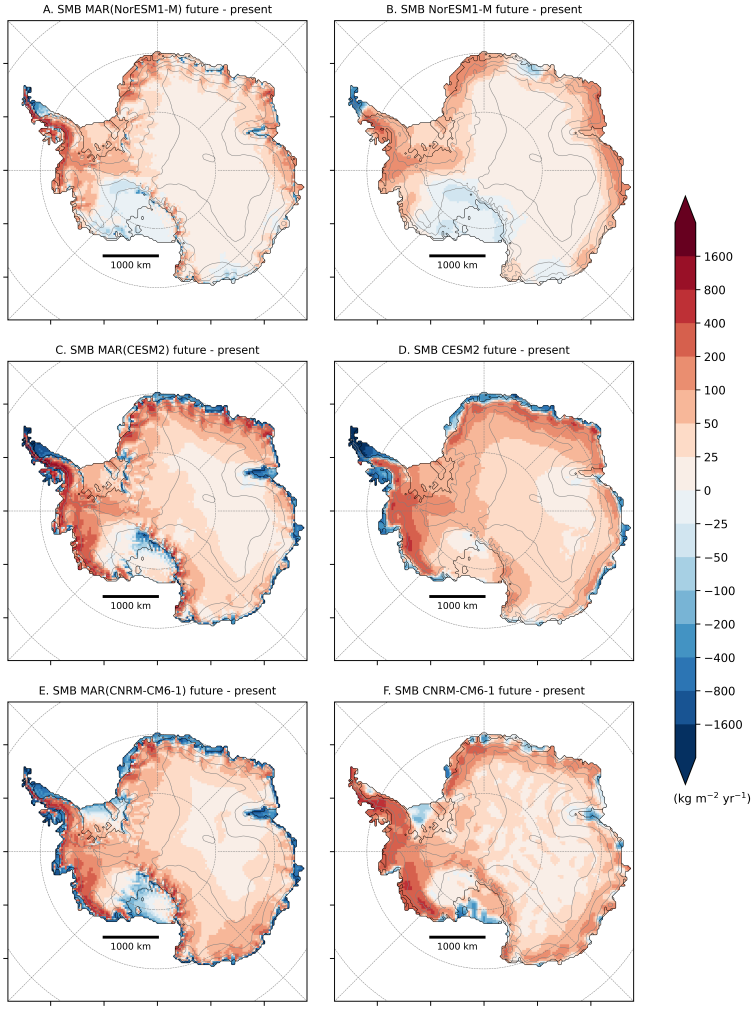

Figure 5.9: Comprison between SMB anomalies between 2081–2100 and 1995–2014 ($\mathrm{kg\,m^{-2}\,yr^{-1}}$) projected by MAR forced by NorESM1-M (A), CESM2(C), CNRM-CM6-1 (E), and the ISMIP6-SMB directly derived from NorESM1-M (B), CESM2 (D) and CNRM-CM6-1 (F).

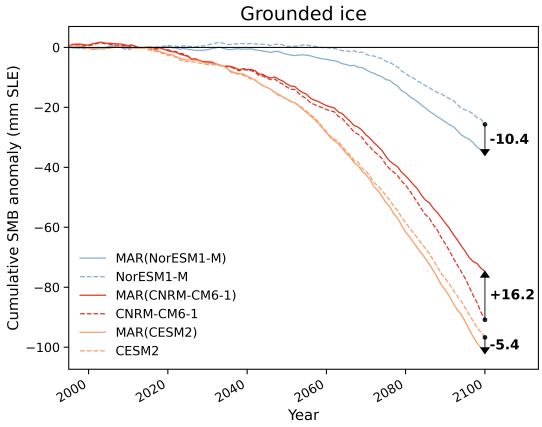

Figure 5.10: Cumulative contribution of the grounded Antarctic SMB (mmSLE) of MAR forced by NorESM1-M, CNRM-CM6-1, and CESM2 (solid ligne), and the ISMIP6-SMB directly computed from NorESM1-M, CNRM-CM6-1, and CESM2 (dashed lines) over 1995–2100. The differences between the cumulative contributions of the MAR experiments and their forcing ESM is also indicated in the figure.

differences between CMIP5-RCP8.5 and CMIP6-ssp585, or between CMIP6-ssp126 and CMIP6-ssp245 (Fig. 5.10), this also raises the question of the sensitivity to the forcing of ISMIP6 projections, where the SMB is used as an input for performing projections of the total AIS mass balance (Seroussi et al., 2020).

5.4.3 Limitations

Our projections suggest a significant ablation by runoff as the firn would not absorb all the additional liquid water, whereas almost all surface meltwater refreezes in the snowpack. MAR does not include a liquid-water routing scheme that could either create liquid-water flowing over the ice surface, or accumulate melted water into surface or sub-surface lakes, further away than the place of its production. The current view suggests that enhanced melt will be stored in crevasses or ponds that weaken ice shelves, potentially leading to their collapses by hydrofracturing (Scambos et al., 2000; Vieli et al., 2007; Pattyn et al., 2018). However, in some conditions, streams and rivers can transfer surface meltwater laterally and export it into the ocean (Kingslake et al., 2017; Pattyn et al., 2018; Dell et al., 2020; Arthur et al., 2020), which might eventually reduce the risk of hydrofracturing (Bell et al., 2017). Lake formation and meltwater runoff therefore represent a large uncertainty about the future of the ice shelves and the contribution of the AIS to sea level. These processes have yet to be implemented in the snowpack module of MAR.

MAR is not coupled to an ice-sheet model in these simulations and therefore has a static ice-sheet geometry (ie., fixed surface elevation and ice/ocean mask) that could lead to biases in the simulated SMB. For instance, melt-elevation feedback due to the lowering of the surface elevation by atmospheric and basal melt are not taken into account with a fixed geometry. Hence, we probably underestimate surface melt rates by overestimating the future surface elevation (Ritz et al., 2015). Since the ice/ocean mask is fixed over the whole simulation period (1975–2100), integrated anomalies could also be biased. The ice-shelf area and associated negative SMB value are potentially overestimated due to the absence of collapse processes. In the same way, the extent of grounded ice is reduced as grounding lines retreat, which should induce a negative contribution of the surface to sea-level rise. These two implicit consequences of using fixed ice mask and elevation could partly compensate each other. The elevation feedback has been shown to matter for 21st century Greenland projections (Le clec'h et al., 2019), but its importance for the AIS remains an open question.

Our simulations also do not include drifting snow, which can be active up to 81% of the time in some locations (Amory, 2020). Drifting snow has been simulated as the main present ablation component of the AIS (Lenaerts and Van den Broeke, 2012; Van Wessem et al., 2018) and can lead to exposure of low-albedo and blue-ice area (Lenaerts et al., 2017a). The sublimation of eroded particles also cools the atmosphere (Le Toumelin et al., 2020) and has a significant influence on the humidity budget of the near-surface atmosphere (Amory and Kittel, 2019). The drifting-snow scheme of MAR had not yet been evaluated at the scale of the ice sheet when we performed our simulations and was therefore deactivated. Projected runoff ablation is much higher than present wind-driven ablation suggesting that drifting snow would not remain the main ablation process by 2100. This highlights the importance of assessing the future Antarctic drifting-snow climate in the global warming context.

5.5 Chapter conclusion

In this study, we use the regional atmospheric model MAR, which includes determinant polar surface physics, forced by four carrefuly-selected ESMs (ACCESS1.3, NorESM1-M, CNRM-CM6-1, CESM2) to study the future evolution of the Antarctic SMB. These CMIP5 and CMIP6 models project a wide range of Antarctic near-surface warming (+3.2°C to +8.5°C) and enable us to investigate

the AIS sensitivity to different warmer climates in 2100.

Our results reveal an increase in grounded SMB (+349 Gt yr^{-1} to +751 Gt yr^{-1}) between 1981–2010 and 2071–2100 due to an increase in snowfall amounts, despite higher runoff values partly offsetting this increase (up to 34%). Higher surface meltwater production over the ice shelves at the end of the 21st century prevents a total absorption of additional liquid water by the snowpack, leading to high runoff values and mostly negative SMB anomalies. The spread over the ice shelves is however large, since our simulations project relatively stable SMB anomalies (+30 Gt yr^{-1}) to strong negative anomalies (-335 Gt yr^{-1}). Our results suggest significant differences at the end of the century at the scale of the entire ice sheet, whether we consider the grounded ice or ice shelves. However, future spatial and integrated changes for a same warming are similar, suggesting than uncertainties are mainly due to the sensitivity of ESMs to anthropogenic forcing and the timing of the projected warming.

Future changes modelled by MAR are strongly correlated with the near-surface warming of the forcing ESMs around the AIS. Using a statistical regression, we reconstruct integrated SMB anomalies over the grounded ice sheet as well as over the ice shelves for the whole CMIP5 (RCP8.5) and CMIP6 (ssp126, ssp245, ssp585) database. Over 2071–2100 compared to the present, this reconstructed grounded SMB suggests a higher increase for CMIP6-ssp585 (+447 ± 134 Gt yr^{-1}) than for CMIP5-RCP8.5 (+ 353 ± 114 Gt yr^{-1}) that respectively corresponds to a 2000-2100 cumulated sea-level contribution of -6.3 ±2.0 cm SLE and -5.1 ±1.9 cm SLE. Low (ssp126) and intermediate (ssp245) CMIP6 emission scenarios project a lower negative contribution to sea-level rise than ssp585 (-3.0 ±1.4 cm SLE using ssp126 and -4.2 ±1.6 cm SLE using ssp245. Conversely, CMIP6-ssp585 yield a stronger SMB decrease over the ice shelves (-119 ± 100 Gt yr^{-1}) than CMIP5-RCP8.5 (-54 ± 55 Gt yr^{-1}).

Future SMB estimates are also used as forcing for ice-sheet models, notably in the ISMIP6 project, where SMB estimates are directly derived from ESMs. Despite several improvements in the latest generation of CMIP6 ESMs, using these models to study the evolution of the SMB involves several compromises that could lead to large uncertainties in the future SMB. We therefore compare the MAR projected SMB to the ISMIP6-derived SMB, revealing large local and integrated differences between MAR and the respective forcing ESM. These MAR and ESM differences highlight the importance of correctly representing the current climate and the need of additional projections relying on more models including

both RCMs and ESMs.

Under the Paris Agreement (limiting global warming to +1.5°C compared to pre-industrial temperature, which is a colder target than the projected mean CMIP6-ssp126 warming), increased surface melt over the ice shelves should remain weak, limiting potential ice-shelf collapses due to hydrofracturing. This weak increase in melt amounts should also limit surface thinning and then positive feedbacks between surface damages and ice-shelf instability. However, large uncertainties remain in the influence of surface melt on the ice-shelf stability. Furthermore, our results highlight a warming threshold (+2.5°C) where the ice-shelf SMB could decrease, suggesting a low range of warming before potential irreversible damages on the ice-shelves. Finally, our simulations also suggest a stabilisation or even a decrease in grounded SMB with a +7.5°C near-surface warming, which would lead to a decrease in the sea-level mitigation capacity of the grounded AIS surface. This warming is however reached before 2100 by only one model in the highest-emission scenario suggesting that more work is needed to asses the confidence of this threshold, the response of the AIS to strong warming after 2100 and AIS contribution to global sea-level rise.

CHAPTER 6

Cloud phase drives differences in future surface melt over Antarctic ice shelves

Following:

Kittel, C., Amory, C., Hofer, S., Agosta, C., Jourdain, N. C., Gilbert, E., Gallée, H., Fettweis, X.: Cloud phase drives differences in future surface melt over Antarctic ice shelves, in preparation.

This chapter has been written in the form of a publication to be submitted shortly. Note to readers: the layout and formatting of the considered journal requests a change in the way scientific numbers are numbered (a comma is used to separate thousands).

Abstract Warm atmospheric conditions have damaged Antarctic Peninsula ice shelves through surface melt and hydrofracturing, and could potentially initiate collapse over other Antarctic ice shelves. The reduced buttressing capacity of these ice shelves associated with mass loss has increased the Antarctic Ice Sheet contribution to sea level rise through a speed-up in glacier flow. However, even within equivalent radiative forcing in the future, model projections suggest large differences in cumulative 21st century surface melting. So far it remains unclear whether these differences are due to variations in warming rates in individual models, or whether local surface energy budget feedbacks could also play a notable role. Here we use the polar-oriented regional climate model MAR to study the physical mechanisms that will control the future melt over the Antarctic ice shelves in high-emission scenarios RCP8.5 and ssp585. We show that clouds enhance future surface melt by increasing the atmospheric emissivity of longwave radiation towards the surface. Furthermore, we highlight that differences in meltwater production depend on cloud properties and particularly cloud phase. Clouds containing a larger amount of liquid water lead to stronger melt, also favouring the absorption of solar radiation due to the melt-albedo feedback. By driving melt differences over the ice shelves in the next decades, liquid-containing clouds could be a major source of uncertainties related to the future Antarctic contribution to sea-level rise.

6.1 Context

Clouds are key drivers of the SEB. They can have opposing effects by reflecting solar (shortwave) radiation towards space and by re-emitting trapped

energy through thermal (longwave) radiation towards the surface. The net cloud effect - the balance between these opposite contributions - is notably determined by the surface albedo (Bintanja and van den Broeke, 1996; Hofer et al., 2017), and cloud properties, i.e their temperature (Stephens, 1984), structure (Barrett et al., 2017; Gilbert et al., 2020), and water phase (ice or liquid) (Lachlan-Cope, 2010; Hines et al., 2019; Gilbert et al., 2020). The absorption and reflection properties of clouds depend on the cloud optical depth (COD), which can be partly linked to their liquid water content (Stephens, 1984; Zhang et al., 1996). Liquid-containing clouds, including both liquid-only and mixed-phase clouds, have therefore a stronger effect on the SEB (Bennartz et al., 2013; Gorodetskaya et al., 2015; Hofer et al., 2019).

Clouds currently warm the Antarctic surface (Pavolonis and Key, 2003). While the highly-reflective snow combined with scarce blue-ice areas prevent significant absorption of SWD in summer, clouds act as another source of incoming energy in the infrared spectrum. This additional energy can be used to heat and melt the snow (Bintanja and van den Broeke, 1996; Van Den Broeke et al., 2006). Abundant liquid-containing clouds associated with warm and moist air advection are responsible for intense melt events due to enhanced LWD (Nicolas et al., 2017; Scott et al., 2019; Wille et al., 2019). These liquid-containing clouds can also become a significant source of incoming energy in winter and trigger surface melt even outside of the usual summer melt season (Kuipers Munneke et al., 2018; Wille et al., 2019).

Quantifying the influence of clouds on the SEB remains challenging, particularly over the AIS where observations are scarce and expensive to maintain (Bromwich et al., 2012; Boucher et al., 2013). Furthermore, little is known about how these cloud-related uncertainties will influence the future climate and surface mass balance projections over the Antarctic ice shelves. Additionally, ESMs usually lack the necessary spatial resolution and underlying physics/processes to resolve the small floating ice shelves. Moist air can intrude further inland over the ice shelves before reaching the grounded ice-sheet slope because the steep topographic gradient at the peripheries of the grounded ice sheet is smoothed in coarse resolution ESMs. This highlights the need for a more detailed quantification of the future cloud effects with higher-resolution and polar-oriented models to evaluate uncertainties related to cloud properties on the projected AIS contribution to SLR.

To understand how the cloud radiative effect drives the differences in future melt over the Antarctic ice shelves, we force the regional climate model

MAR (Gallée and Schayes, 1994) with four ESMs from the CMIP5 (ACCESS1.3 and NorESM1-M) and CMIP6 (CNRM-CM6-1, CESM2) database using the highest greenhouse gas concentration pathways (respectively RCP8.5 and SSP585). These four models reproduce the current state of the Antarctic climate, but also maximise the diversity of projected future warming (Kittel et al., 2020). From these simulations we show that LWD increases drive projected surface melt. Furthermore, clouds, and particularly their phase, determine the differences in projected LWD increase with more liquid-containing clouds inducing stronger future melt for a same temperature anomaly. They also enhance SWD absorption by decreasing surface albedo which again strengthens melt. Since clouds are projected to control in part future surface melt rates, our study suggests that their correct representation into models could significantly influence the future Antarctic contribution to SLR.

6.2 Additional methodological aspects

6.2.1 MAR and experiments

We used the version 3.11 of MAR, with the exact same configuration and forcing than in Ch. 5 (see also Sect. 2.2.2 for the selection method). In this study, MAR is then forced by two CMIP5 models (ACCESS1.3 and NorESM-1-M) and two CMIP6 models (CNRM-CM6-1 and CESM2) using the highest concentration pathways (RCP8.5 for CMIP5 models and ssp585 for CMIP6 models). A detailed description of the model setup and physics adaptation for the AIS is given in Agosta et al. (2019); Kittel et al. (2020) and in Ch. 2. The model results when forced by the selected ESMs have been thoroughly evaluated in Appendix D.1.

6.2.2 Anomalies

The reference (present) period in this study is taken as the average from 1981 to 2010 for both MAR (melt, SEB components, cloud amount and properties, surface albedo) and ESMs (Antarctic regionnal, i.e 90°S–60°S, near-surface warming). Since most of the total annual melt occurs in summer (December-January-February, DJF), we only discussed the summer anomalies. In order to easily compare integrated melt anomalies (mass per unit of time i.e., $\mathrm{Gt\,3mo^{-1}}$) with SEB component anomalies (energy flow per unit of area per unit of time i.e.,

$\mathrm{W\,m^{-2}}$), we have converted the latter into integrated melt potential equivalent (potential induced melt mass per unit of time i.e., $\mathrm{Gt\,3mo^{-1}}$) following Hofer et al. (2017, 2019) whenever SEB component anomalies are not presented in their SI unit ($\mathrm{W\,m^{-2}}$). We performed the SEB conversion as follows:

a. computing the mean DJF values from daily outputs and calculating the anomalies compared to reference climate 1981–2010 (Units: $\mathrm{W\,m^{-2}}$);

b. summing the anomalies over the whole region (ice shelves or grounded ice) weighted by the fraction covered by ice over that pixel and its area (taken into account projection deformations) (Units: $\mathrm{Gt\,s^{-1}}$);

c. multiplying by the number of seconds during the summer (Units: $\mathrm{J\,3mo^{-1}}$) and finally dividing by the heat of fusion needed to melt 1 kg of snow/ice ($\mathrm{Hf} = 333.55\ \mathrm{kJ\,kg^{-1}}$) (Units: potential $\mathrm{kg\,3mo^{-1}}$ converted into potential $\mathrm{Gt\,3mo^{-1}}$).

Positive (negative) potential melt anomalies depict enhanced (reduced) contribution to surface melt. Although this conversion enables direct comparison between melt and (non-) radiative SEB components, it neglects some physical processes such as heating of the surface (i.e, a part of the energy might heat the surface instead of directly melting the snow), refreezing energy, and variations of the subsurface conductive heat flux. In MAR, the latter is however considered to be closed to zero and negligible when the model simulates melt. Finally, as the amount of melted water is summed for every time step while the SEB components are averaged over each day in the model outputs, the total SEB expressed in melt potential is not necessarily equivalent to the total simulated melt. We therefore discuss the potential contribution of each SEB component to melt instead of their actual contribution.

6.3 Results

6.3.1 Contributions to summer melt increase

Our simulations project a summer melt increase over the ice shelves that strongly differs depending on the forcing ESM during the 21st century (Fig. 6.1). We find a factor of ∼3.9 between the lowest and highest cumulative melt anomalies

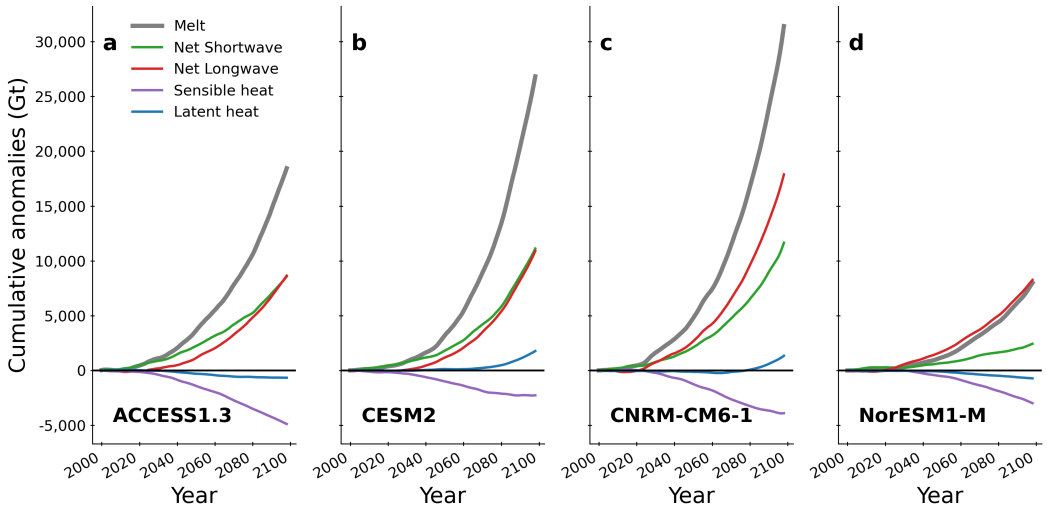

Figure 6.1: Cumulative summer melt and SEB components converted into melt potential (Gt). Cumulative summer anomalies of melt, turbulent, net shortwave, and longwave fluxes expressed as melt potential projected by MAR forced by (a) ACCESS1.3, (b) CESM2, (c) CNRM-CM6-1, (d) NorESM1-M, compared to the reference 1981-2010 summer.

over the 21st century, despite equivalent radiative forcing from greenhouse gases. MAR driven by NorESM1-M simulates a total melt increase of ∼8000 Gt during the 21st century, while the increase reaches ∼31,400 Gt when MAR is driven by CNRM-CM6-1. This spread in projected melt (while forced with an equivalent concentration pathway) is as large as differences in melt between low and high concentration pathways (Trusel et al., 2015; Kittel et al., 2020).

The main differences in ice-shelf summer melt arise from differences in LWN and SWN fluxes (Fig. 6.1). MAR projects a strong increase in LWN as the surface receives more LWD by 2100 (Fig. E.1). The cumulative LWN fluxes for the 21st century corresponds to 17,900 Gt potential melt in MAR driven by CNRM-CM6-1, i.e the higher-melt projection (see Methods for the computation of potential melt). This represents ∼57% of the projected changes, a similar potential contribution to MAR driven by ACCESS1.3 (∼47%) or CESM2 (∼41%). MAR driven by NorESM1-M produces the lowest melt increase. In this simulation, the LWN potential melt is equivalent to the cumulative melt anomalies.

Contrary to LWD, SWD fluxes decrease in all our simulations (Fig. E.1). However, the albedo decreases as melt increases, reducing shortwave reflection by the surface. This leads to positive potential melt contributions for SWN. MAR driven by CNRM-CM6, CESM2, and to a lesser extent ACCESS1.3 suggest an equivalent shortwave potential melt accumulated over the 21st century (11,600 Gt; 11,100 Gt; and 8,500 Gt), whereas MAR driven by NorESM1-M projects only a

2,400 Gt shortwave contribution to potential melt.

Longwave contributions account for most of the melt anomaly differences. Despite relatively similar turbulent and shortwave melt potential contributions with MAR driven by CESM2, the CNRM-CM6-1 experiment leads to larger accumulated melt values that result from a larger longwave contribution. This is also true to a lesser extent when compared with MAR driven by ACCESS1.3 whose accumulated shortwave contribution differs by only ∼3,100 Gt while the difference in melt with MAR driven by CNRM-CM6-1 reaches ∼12,900 Gt.

Non-radiative, turbulent fluxes play a minor role compared to the radiative fluxes (Fig. 6.1). Although other studies (Kuipers Munneke et al., 2012, 2018; Lenaerts et al., 2017a; Datta et al., 2019) have indicated that turbulent fluxes (especially SHF) can be the main drivers behind intense sporadic melt events occurring locally in peripheral regions of the ice sheet, our model results indicate that from a continent-wide perspective, they have a future potential melt contribution that is substantially lower relative to radiative fluxes over ice shelves at the end the century. Except for the NorESM1-M experiment where the melt increase remains weak, individual turbulent fluxes always have a lower (by a factor of 0.18 to 0.35) potential contribution than radiative fluxes. While latent heat fluxes undergo relatively few changes, SHF is projected to decrease inducing a slightly negative potential melt contribution that we attribute to 1) a reduced thermal inversion between the atmosphere and the surface, and 2) slower katabatic winds (See the supplementary information in Sect.E.2).

6.3.2 Factors behind the differences in LWD

The projected LWD increases due to higher temperature in the atmosphere and larger greenhouse-gas concentration. Approximating the atmosphere as a longwave-opaque and black body, we estimated the contribution of the atmosphere to the increase in LWD over 2071-2100 (see the additional element E.4). While our results project significant differences in LWD increase between the CNRM-CM6-1 and CESM2 experiments, the future atmospheric temperature in these experiments only explains 29% of modelled future LWD differences. This implies the contribution of additional significant processes.

While greenhouse gas concentrations mainly determine the emissivity of the atmosphere in clear-sky conditions, clouds also contribute to the atmospheric emissivity depending on their optical depth. The MAR experiments project more

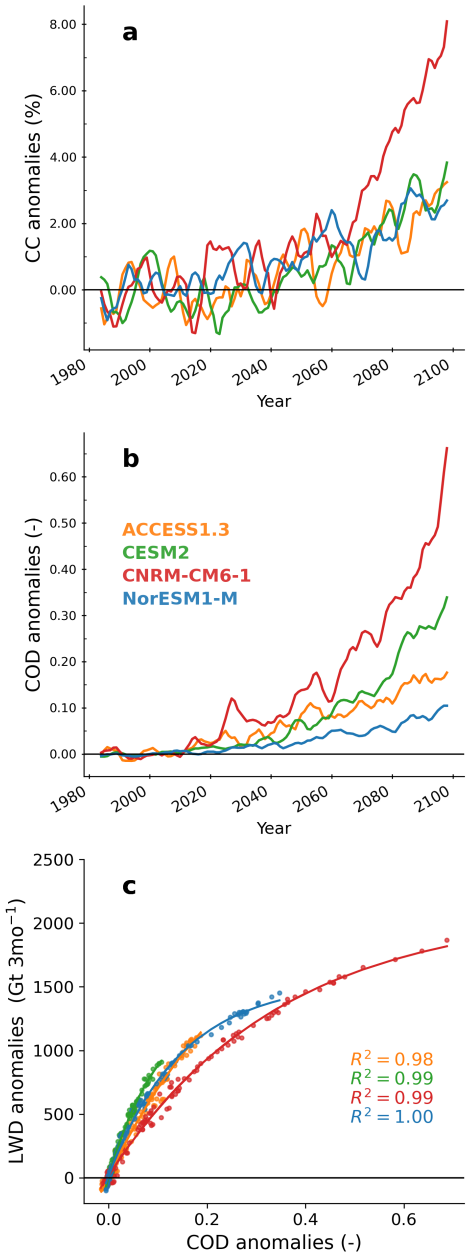

Figure 6.2: Changes in cloud cover, cloud optical depth, and association between cloud optical depth and longwave down radiations converted into melt potential (Gt). Anomalies of summer cloud cover (%) (a), cloud optical depth (-) (b), Summer longwave downwelling radiations (expressed as potential melt in Gt 3mo^{-1}) versus mean cloud optical depth anomalies during summer (-) (c) projected by MAR forced by ACCESS1.3 (orange), CESM2 (green), CNRM-CM6-1 (red), and NorESM1-M (blue), in summer compared to the present summer climate (1981–2010).

numerous and opaque clouds that enhance LWD (Fig. 6.2) and decrease SWD (Fig. E.1). The mean summer cloud cover (CC) over the ice shelves fluctuates around the mean value of the present period until 2050-2060 when it starts to increase in all our simulations. While MAR driven by ACCESS1.3, NorESM1-M, and CESM2 suggests a similar increase (between ∼3% and 4%), the CNRM-CM6-1 experiment (ie., with the strongest melt) reveals the largest cloud cover increase with 8% more frequent clouds during the southern summer. This is a factor of two compared to the other projections. While the absence or presence of clouds is a determining factor favouring longwave emission towards the surface, CC changes remain close to the present values compared to COD changes (Fig. 6.2). The mean CC in summer does not strongly change until 2050 while LWD is already projected to increase in all our simulations, as a result of higher COD values. Moreover, ACCESS1.3, CESM2 and NorESM1-M experiments project a similar increase in CC after 2050 while LWD increases differently from one model to another (Fig. E.1). This suggests that CC anomalies remain less influential compared to the large COD anomalies in our results. We will then hereafter only focus on COD which predominantly explain the differences in LWD and ultimately melt.

Although COD is projected to increase in all our simulations, MAR driven by CNRM-CM6-1 similarly suggests a stronger increase (up to ∼0.7), which corresponds to clouds twice as opaque than clouds simulated in the MAR-CESM2 experiment (i.e, the simulation with the second-largest COD increase). The higher LWD fluxes are strongly correlated with large increases in COD ($R>0.99$; Fig. 6.2). Our experiments also project an increase in the atmospheric water vapour content (Fig. E.4). However, both MAR-CNRM-CM6-1 and MAR-CESM2 experiments reveal a similar increase that does not explain LWD differences between these two projections. We therefore attribute the future differences in LWD increase to clouds.

Although the increase in LWD due to optically-thicker clouds saturates for large COD increases expressing a longwave-opaque atmosphere, our results highlight that changes in LWD and the cloud radiative effect are projected to remain highly sensitive to COD changes over the 21st century (See the supplementary Sect. E.6 and Fig. E.5). We find that COD increases with a variable rate around 2040–2060 and starts to spread afterwards. While projected COD increases with temperature, Figure E.6 demonstrates that the future changes are not only a direct consequence of the atmospheric warming as MAR driven

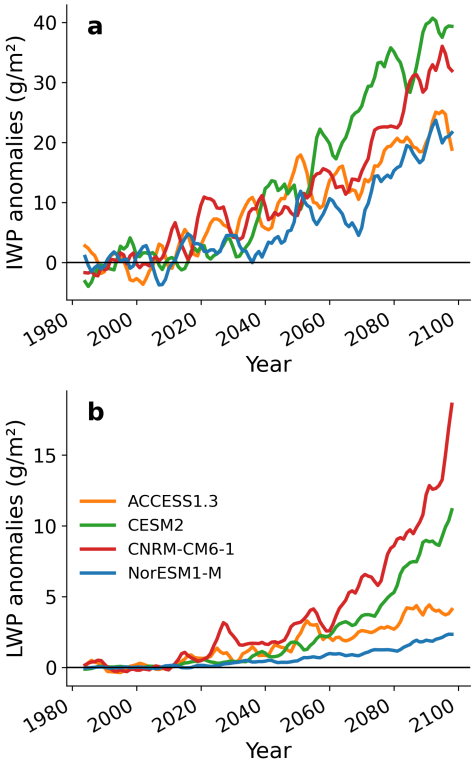

Figure 6.3: Changes in cloud phase properties. Anomalies of mean summer ice water path (IWP) summer cloud cover ($g\,m^{-2}$) (a), and mean summer liquid water path (LWP) anomalies ($g\,m^{-2}$) (b), driven by MAR forced by ACCESS1.3 (orange), CESM2 (green), CNRM-CM6-1 (red), and NorESM1-M (blue) compared to the present summer climate (1981–2010).

by CNRM-CM6-1 simulates stronger COD changes than others experiments for equivalent near-surface warmings.

MAR projects an increase in cloud particle contents and phases over the ice shelves that differ following the experiment, resulting in different optical properties (Fig. 6.3). The mean Ice Water Path (IWP, the mean total amount of ice and snow content in the atmosphere here including clear-sky value) is increasing similarly among experiments with anomalies between 19.7 $g\,m^{-2}$ and 41.8 $g\,m^{-2}$ which represents a factor of 2.1 between the lowest (ACCESS1.3) and the highest increase (CESM2). While all projections simulate a higher Liquid Water Path (LWP, equivalent of IWP for liquid content) in the future, large differences persist in the anomalies. MAR driven by CNRM-CM6-1 projects a stronger variation in LWP (19.9 $g\,m^{-2}$) that is 8.7 larger than the increase in the NorESM1-M experiment (2.3 $g\,m^{-2}$). As the emissivity of clouds strongly depends on the liquid water content, the different increases in LWP control the spread in projected LWD. While the CESM2 experiment suggests slightly larger changes in IWP than the CNRM-CM6-1 experiment, the latter projects more liquid-containing

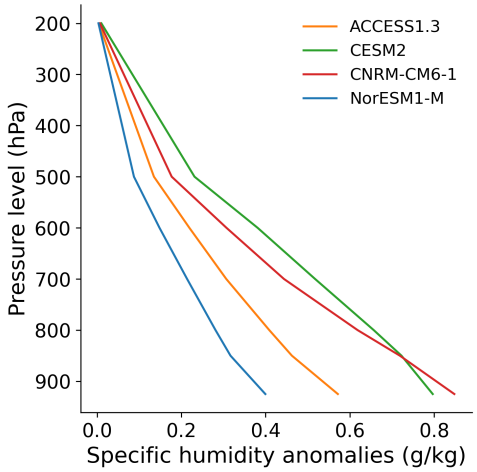

Figure 6.4: Changes in vertical specific humidity profiles. Anomalies in mean summer specific humidity ($g\,kg^{-1}$) in 2071–2100 compared to 1981–2010 projected by ACCESS1.3 (orange), CESM2 (green), CNRM-CM6-1 (red), and NorESM1-M (blue) over the ice shelves.

clouds (higher LWP) resulting in more opaque clouds (higher COD). This analysis highlights that the projected melt differences are mainly caused by differences in cloud water phase.

The projected cloud phase differences are explained by the preferential increase of either water and rain droplets or ice and snow particles. Over 2071–2100, both the vertically-averaged atmospheric changes in humidity and temperature projected by MAR driven by CESM2 and CNRM-CM6-1 are similar over the ice shelves (Tab. E.2). However, they differ in their vertical structure. MAR driven by CESM2 project stronger changes in humidity advection in the middle and high atmosphere above 800 hPa while future CNRM-CM6-1 atmosphere is characterised by stronger low-level humidity advection in the ice-shelf atmosphere below 800 hPa (Fig. 6.4). The formation of either snow and ice particles (CESM2) or water droplets (CNRM-CM6-1) when saturation is reached results in differences in IWP and LWP. This also explains why MAR driven by CNRM-CM6 simulates more liquid precipitation than when driven by CESM2 at an equivalent warming rate and conversely for solid precipitation (see Kittel et al. (2020) or Ch. 5).

6.3.3 Enhanced SWD absorption due to LWD

The surface is projected to absorb more shortwave despite decreased SWD (Fig. 6.5). The excess energy at the surface due to LWD warms and melts snow. This in turn promotes snow grain metamorphism that combined with refreezing

of liquid meltwater, lowers the albedo and favours SWD absorption. We therefore find a strong association between LWD and SWN (Fig. 6.5). The quadratic relation suggests an amplification of the increase in SWN due to LWN as a consequence of the melt albedo feedback. The low R^2 (determination coefficient) value between LWD and SWN in the NorESM1-M experiment suggests a low or absent melt-albedo feedback explained by the weak projected increase in melt. On the contrary, the albedo is projected to strongly decrease when MAR is forced by CNRM-CM6-1 leading to large anomalies in SWN. In this experiment, mean summer 2-m temperatures over the ice shelves nearly reach the 0 °C isotherm (-0.9 °C over 2095–2100). This highlights the importance of cloud radiative effect on melt and inherent surface feedbacks. The influence of clouds on absorbed SWD mainly depends on the surface albedo but also on the rate at which SWD is projected to decrease (Bintanja and van den Broeke, 1996). In warmer climates after 2100, clouds could be more reflective than the ice-covered surface (as summer albedo decreases). These warmer conditions could reverse the summer cloud radiative effect (reducing melt) similarly as over the dark ablation zone of the Greenland Ice Sheet (Hofer et al., 2017; Wang et al., 2019b) suggesting a growing importance of surface albedo in determining the future cloud radiative effect.

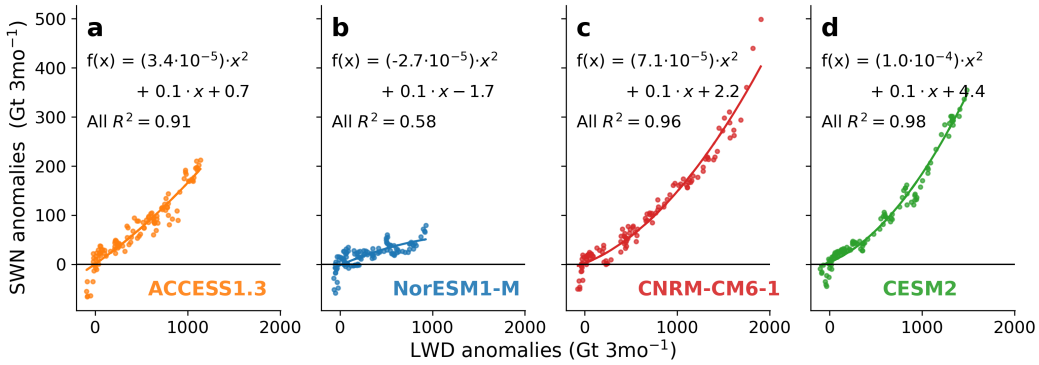

Figure 6.5: Association between summer SWN and LWD anomalies (Gt 3mo^{-1}). Summer anomalies of shortwave net radiation compared to summer longwave downwelling radiation anomalies projected by MAR forced by ACCESS1.3 (a), NorESM1-M (b), CNRM-CM6-1 (c), and CESM2 (d) over the Antarctic ice shelves based on the 1981–2010 mean values, with second order polynomial equations and R^2 values.

6.4 Chapter conclusion

In conclusion, we highlight in this study that liquid water content explains most of the differences in future melt over the Antarctic ice shelves. They induce

a stronger increase in LWD that enhances meltwater production but also favours SWD absorption (due to the melt-albedo feedback) further increasing melt.

By controlling future melt differences over the ice shelves, liquid-containing clouds could lead to different Antarctic contributions to sea-level rise. For instance, the larger melt rate projected in the CNRM-CM6-1 experiment could trigger 23% (relative augmentation, or 15.6% in absolute values) more susceptible hydrofracturing collapses than the CESM2 experiment despite a similar global warming (Gilbert and Kittel, 2020, in review). In 2100, MAR driven by CNRM-CM6-1 projects that around 47% (23.69% over 2071-2100) of the Antarctic ice shelves could be vulnerable to surface-melt disintegration which would strongly enhance ice discharge towards the ocean and the Antarctic sea-level contribution. Without the buttressing effect of these ice shelves, Antarctic glaciers accelerate their discharge towards the ocean and raise the sea level (Sun et al., 2016). This suggests that clouds are projected to have a strong effect on determining the Antarctic contribution to SLR. While models still poorly simulate clouds over the present (King et al., 2015; Gilbert et al., 2020), our study stresses the need to improve cloud representation in climate models to better constrain SLR projections.

CHAPTER 7

Parallel studies and additional discussion elements

This chapter presents additional experiments that were made in parallel with the three previous chapters of this manuscript. It also discusses several elements of perspectives covered previously such as blowing snow processes, the resolution used for our simulations and the interest of a coupling with an ocean model in Adelie Land. It does not aim to be a precise discussion on the conclusions of the previous chapters even if links between these chapters are done. Rather, this chapter seeks to generate new research questions and perspectives on the basis of (preliminary) works using MAR carried out during my thesis and which are reported here.

7.1 Drifting-snow processes

Drifting-snow processes change the local SMB. Until now, these processes have been neglected meaning that we have simplified the SMB equation (Eq. 1.1) while wind-driven snow transport contributes to redistribute snow. Snow can be eroded from the surface (surface mass loss) and be advected downwind and reposited (surface mass gain), while also sublimate during transport. Drifting-snow sublimation is often considered as an individual component of the SMB (e.g., Van de Berg et al., 2006; Lenaerts et al., 2012a; Lenaerts and Van den Broeke, 2012; Van Wessem et al., 2018; Lenaerts et al., 2019), but it is actually already included in the erosion/deposition budget (Amory et al., 2020). Drifting-snow processes (including erosion, advection, sublimation and deposition) result in a high (sub-kilometre-scale) SMB variability (e.g., Eisen et al., 2008; Agosta et al., 2012) and can locally remove all the accumulated snow leading to areas of near-zero to negative SMB (Bintanja, 1999; Scambos et al., 2012; Das et al., 2013).

In order to evaluate the influence of drifting-snow on the Antarctic SMB, we performed two simulations using MAR forced by ERA5 over 1980–2019. The first simulation corresponds to the reference configuration described in Ch. 2 and evaluated in Ch. 5 and Ch. 6 (called MAR(NDS) hereafter). In the second one, the drifting-snow scheme has been switched on (MAR(DS) hereafter). We refer to Amory et al. (2020) and Ch. 2 (Sect. 2.1.3.5) for a detailed description of how MAR accounts for drifting-snow processes.

Figure 7.1 illustrates the effect of drifting-snow on the SMB with significant

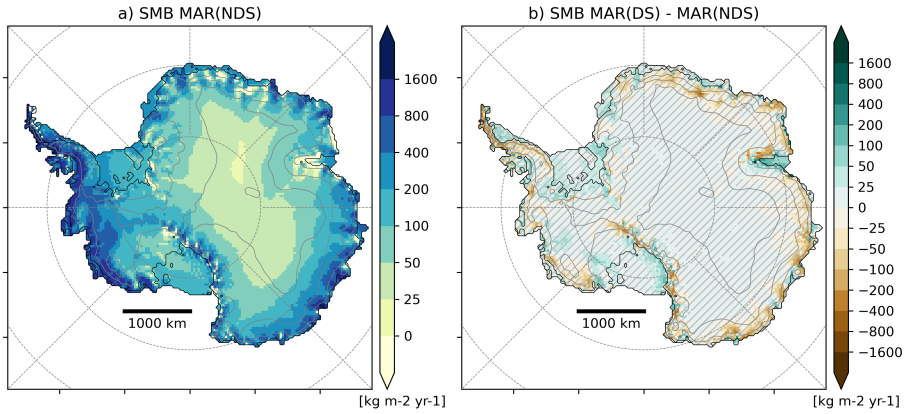

Figure 7.1: a. Mean annual SMB ($\mathrm{kg\,m^{-2}\,yr^{-1}}$) as simulated MARv3.11 forced by ERA5 without drifting snow over 1980–2019. b. SMB anomalies ($\mathrm{kg\,m^{-2}\,yr^{-1}}$) between MARv3.11 with drifting snow and MARv3.11 without drifting snow both forced by ERA5 over 1980–2019. SMB anomalies lower than the annual variability (i.e, the standard deviation) are hatched.

decreases on the margin slopes and increases on the ice shelves. As katabatic winds accelerate down the slopes, the erosion is weak on the plateau leading to a similar SMB (differences lower than the interannual variability), and increases as approaching the margins (Lenaerts and Van den Broeke, 2012). Drifting-snow particles are then advected downslope and can sublimate due to improved ventilation during transport, both preventing local redeposition when the windborne snow mass is entirely restituted to the atmosphere. As a result, SMB is decreased over the margins of the grounded ice sheet where winds accelerate in confluent topography. The flattening of the topography near the grounded line and over the ice shelves reduces the buoyancy force (or katabatic force) and then the katabatic-wind speed. This prevents strong erosion and also favours redeposition of previously eroded snow over the ice shelves. While the Antarctic integrated SMB is rather similar from one simulation to another (Tab. 7.1), the grounded SMB is reduced when accounting for drifting snow but increased over the ice shelves suggesting that drifting-snow processes mainly redistributes snow from grounded to ice-shelf areas.

Individual SMB components reflect stronger differences despite similar integrated SMB (Tab. 7.1). The stronger sublimation in the atmosphere due to the presence of enhanced snow particle content in the drifting-snow simulation tends to cool the air resulting in a weaker melt production (and runoff) but also reduce the rainfall amount reaching the surface. This likely results from the colder atmosphere freezing liquid precipitation or favouring ice/snow nucleation at the expense of droplet growth; and potentially from the formation of snow instead

Table 7.1: Mean (1981–2010) annual integrated ($Gt\,yr^{-1}$) SMB, snowfall, rainfall, runoff, net sublimation (defined as surface sublimation minus surface deposition), and melt for the grounded ice sheet, the ice shelves and the total AIS as simulated by MAR without drifting snow (MAR(NDS)) forced by ERA5, as well as the respective anomalies of the simulation with drifting snow (MAR(DS)) compared to MAR(NDS). Anomalies are larger than the present interannual variability (i.e, standard deviation) are considered as significant and highlighted in bold.

Mean ($Gt\,yr^{-1}$)	SMB	SF	RF	SU	RU	ME
Grounded ice (11.94 $10^6\,km^2$)						
MAR(NDS)	2214 ± 98	2340 ± 94	8 ± 2	118 ± 9	16 ± 5	23 ± 14
MAR(DS)	-38	/	**-8**	**-118**	**-6**	-9
Ice shelves (1.77 $10^6\,km^2$)						
MAR(NDS)	472 ± 23	556 ± 20	10 ± 2	56 ± 2	38 ± 11	123 ± 24
MAR(DS)	**+65**	/	**-10**	**-33**	**-10**	-16
Total AIS (13.71 $10^6\,km^2$)						
MAR(NDS)	2686 ± 116	2894 ± 112	19 ± 3	173 ± 11	54 ± 14	174 ± 38
MAR(DS)	+26	/	**-18**	**-151**	**-16**	-25

of graupels in case of collision between raindrops and snow/ice clouds whose occurrence is more important because of drifting snow. Low-level sublimation of drifting-snow particles reduces the humidity gradient between the surface and the atmosphere, drastically weakening or even inhibiting surface sublimation when the drifting-snow scheme is activated in MAR. However, the small differences in SMB and preliminary works on differences in the atmospheric humidity budget (Agosta et al., 2019; Le Toumelin et al., 2020) suggest that high sublimation rates at the surface in the simulations without drifting-snow processes actually compensate for missing atmospheric sublimation. Successfully representing these two sublimation terms would help to better understand variations in the atmospheric humidity budget in Antarctica and could have important consequences on the isotopic signal (Bréant et al., 2019). Note that the drifting-snow implementation in MAR does not enable the distinction between the snow directly falling from clouds and the one resulting from many cycles of local erosion-deposition, preventing the comparison of snowfall rates at the surface between the two simulations.

Drifting snow interacts with the energy and mass budgets of the atmosphere and the surface. The moisture release and latent heat consumption induced by drifting-snow sublimation influence the turbulent (sensible and latent) heat exchange between the atmosphere and the surface (e.g., Bintanja, 2001; Barral et al., 2014; Amory and Kittel, 2019; Le Toumelin et al., 2020). Furthermore, drifting-snow particles act as a near-surface cloud that can increase outgoing and downwelling longwave radiations (Yamanouchi and Kawaguchi, 1984; Gallée and Gorodetskaya, 2010; Yang et al., 2014; Le Toumelin et al., 2020). Le Toumelin

et al. (2020) suggested through numerical simulations with MAR ,that sublimation-induced cooling dominates over radiative warming.

Furthemore, Hofer et al. (in preparation) have revealed strong changes in the snow/ice cloud particle content as a consequence of the inclusion of drifting snow in the atmosphere with MAR. Since variations in cloud liquid-particle content could lead to different Antarctic contributions to sea-level rise due to their strong effect on the SEB (see Ch. 6), this stresses the need to improve our comprehension of how drifting snow affects the Antarctic SEB, climate and SMB.

Despite these potential important effects of drifting snow on the Antarctic (future) climate, drifting-snow processes are generally undocumented. Recent advances made through interpretation of model (e.g., Lenaerts and Van den Broeke, 2012) and satellite (e.g., Palm et al., 2018) products suggest a low interannual variability of the drifting-snow occurrence and transport at the continental scale, but are dependent on methodology limitations. Due to the harsh Antarctic environment, technical constraints and the inherent scarcity in measurements the observed variability of drifting-snow processes has been mostly described from a local perspective (e.g., Mann et al., 2000; Mahesh et al., 2003; Gossart et al., 2017; Amory, 2020). In this context, the recent and future variability in drifting snow remains subject to considerable uncertainty. In a warmer climate, increased melt is projected to reduce drifting-snow erosion by enhancing the cohesion of the snowpack (reflected in MAR by an increase in snow density and the inhibition of erosion if liquid water is present at the surface). Our projections also suggest a decrease in the katabatic wind speed during summer (Ch. 5) potentially also contributing to a diminution in drifting-snow erosion. Drifting-snow processes are currently considered as the main ablation component at the surface of the AIS over the recent period (e.g., Lenaerts and Van den Broeke, 2012; Van Wessem et al., 2018) while our simulations suggest that it could become of second-order importance and largely be overcomed by runoff by 2100. Forthcoming efforts should therefore focus on the future evolution of drifting snow over the ice sheet to improve our estimations of the Antarctic SMB and its contribution to sea-level rise.

7.2 Influence of horizontal resolution

The horizontal resolution is often raised as an influential factor behind differences in simulated Antarctic SMB between (both global and regional) cli-

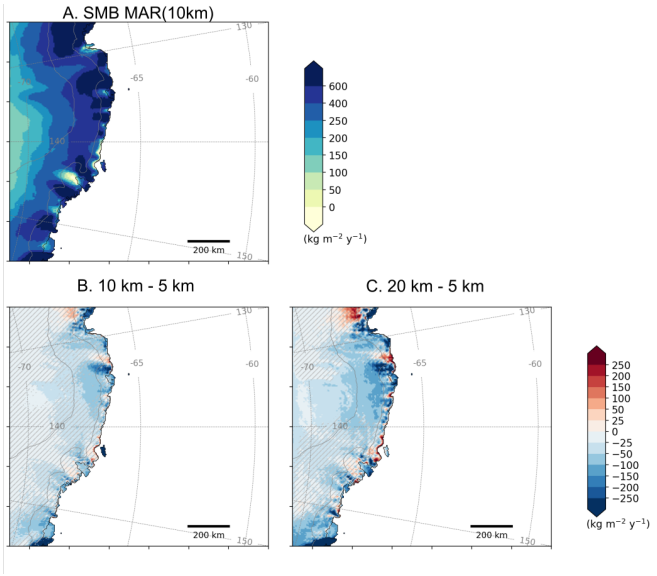

Figure 7.2: A. Mean annual SMB ($\mathrm{kg\,m^{-2}\,yr^{-1}}$) as simulated by MARv3.11 at 5 km forced by ERA5 over 2000–2015. SMB anomalies ($\mathrm{kg\,m^{-2}\,yr^{-1}}$) between MARv3.11 at 10 km (B), MARv3.11 at 20 km (C) and MARv3.11 at 5 km. SMB anomalies lower than the annual variability (i.e, the standard deviation) are hatched.

mate models (e.g., Genthon et al., 2009; Seroussi et al., 2020; Mottram et al., 2020). The horizontal resolution affects the representation of the topography and slopes which then influence snow accumulation through (mostly orographic) precipitation and erosion in peripheral Antarctica (Agosta et al., 2012; Lenaerts et al., 2012c; van Wessem et al., 2016; Van Wessem et al., 2018). Capturing the mean topographic features is therefore important over regions where topographic channelings enhance the nearly-permanent strong katabatic flows such as Adelie Land (e.g., Parish and Wendler, 1991; Wendler et al., 1993, 1997). This is all the more important because these strong katabatic winds also play a significant role over the ocean by driving polynya activities (Massom et al., 1998) and therefore contributing to the oceanic circulation and to the creation of Antarctic Bottom Water (Rintoul, 1985).

In order to evaluate the sensitivity of MAR and its modelled climate to its horizontal resolution, we further performed supplementary MAR experiments with three different resolutions (5 km, 10 km, and 20 km) using the exact same model configuration (without drifting snow) and integration domain (Fig. 7.2) over Adélie Land (East Antarctica) between 2000–2015. In addition to being an interesting region for katabatic winds, Adélie Land is a fairly well-documented region in Antarctica thanks to the permanent manned Dumont d'Urville station that provides continuous atmospheric measurements and serves as a base for

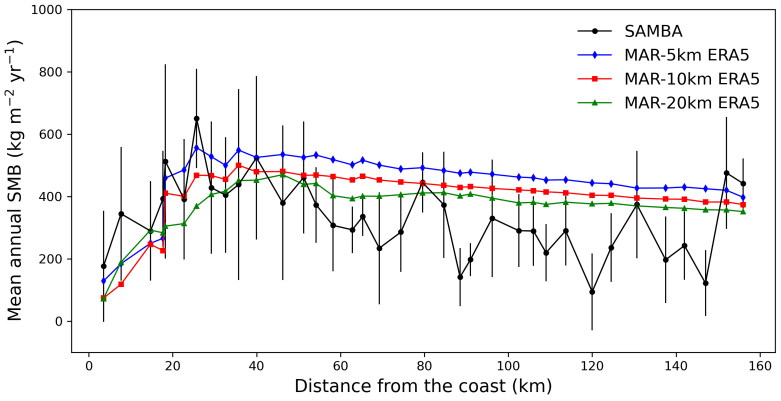

Figure 7.3: Mean annual (2004–2015) SMB ($\mathrm{kg\,m^{-2}\,yr^{-1}}$) as simulated MARv3.11 at 5 km (blue), at 10 km (red), at 20 km (green) over the GLACIOCLIM-SAMBA network (black). Coarser-resolution simulations (high-resolution observations) have been interpolated (aggregated) on the 5 km. The observed variability (standard deviation) inside a same pixel is represented by black bars.

conducting annual surveys of snow accumulation (Agosta et al., 2012) and for the deployment and maintenance of AWSs in the region (Amory, 2020).

Figure 7.3 compares the modelled mean annual SMB against the 156-km stake-line GLACIOCLIM-SAMBA network (Agosta et al., 2012) over 2004–2015. Observations contained in the same pixel of the 5 km grid were averaged while the 10 and 20 km SMB were interpolated onto the 5 km grid. Results of the 3 resolutions correctly reproduce the strong increase in SMB over the first 30 km of the transect and underestimates the slight decrease occurring further inland. The highest-resolution run (5 km) better simulates the increase but also overestimates the most the accumulation upstream of the break-in-slope some 30 km inland. On the opposite, the lowest resolution run (20 km) reveals a more smoothed pattern by underestimating the gradient and being closer to the accumulations after the first 30 km. The simulated peak is furthermore delayed by about 20 km. These differences between the two resolutions likely result from the influence of the topography on the precipitation: steeper margins enhance precipitation by triggering faster condensation.

The comparison between the mean SMB modelled by MAR (Fig. 7.2) reveals that the higher resolution favours a larger accumulation over the lee side of the crests and inland while it underestimates the accumulation over the windward side of the crests. It also simulates a stronger ablation near Dumont d'Urville around 140°E and over coastal areas in front of C-28 iceberg (Mertz broken floating ice tongue) that is explained by higher surface sublimation rates (not shown)

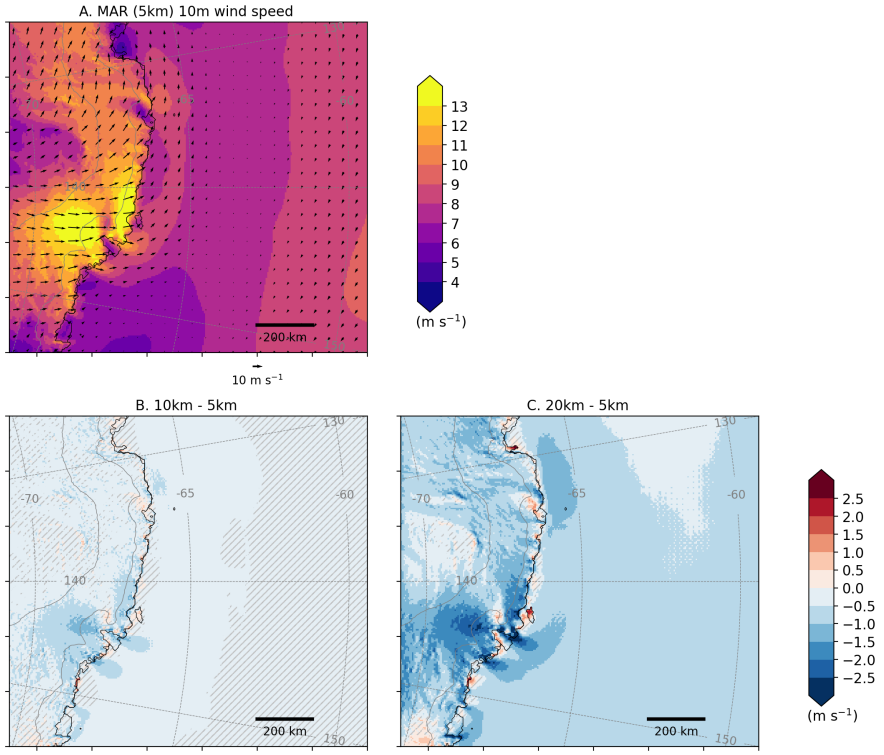

Figure 7.4: A. Mean annual 10-m wind speed ($m\,s^{-1}$) as simulated by MARv3.11 at 5 km forced by ERA5 over 2000–2015. 10-m wind-speed anomalies ($m\,s^{-1}$) between MARv3.11 at 10 km (B), MARv3.11 at 20 km (C) and MARv3.11 at 5 km. 10-m wind-speed anomalies lower than the annual variability (i.e, the standard deviation) are hatched.

due to stronger katabatic winds (Fig. 7.4). As already illustrated by Fig. 7.3, the precipitation in the higher resolution run tends to be located closer to the crests while a lower resolution favours accumulation windward of the topographic barriers. Finally the excess of accumulation inland at 5 km resolution might result from the use of the higher resolution through interactions between air masses and improved topography. However, this would be counterintuitive as we previously stated that a higher resolution favours the accumulation closer to the lee side of the crests (which was also suggested in the SMB evaluation presented in Ch. 3). Furthermore, Franco et al. (2012) demonstrated that a higher resolution prevents air masses from penetrating far inland of the Greenland Ice Sheet by increasing the topographic barrier effect. This is more likely to reflect the difficulty of maintaining consistent humidity at the domain boundaries with the use of multiple resolutions as the interpolation of the humidity from the forcing fields onto high-resolution grids under-saturates the air masses. Correcting the interpolated forcing humidity values to account for this effect likely results in artificially increased accumulation inland.

Using different resolutions with MAR lead to similar temperature statistics when evaluated with near-surface observations in Adelie Land. The higher resolutions yet better represent the real topography and inherent temperature variations (not shown). After correcting simulated temperatures to account for the difference in height between the model and the AWS (using the modelled lapse rate temperature in the vicinity of the station), Figure 7.5. also suggests a non-significant improvement for the higher resolutions over the margins but highlights that using a 5 km, 10 km, or 20 km resolution results in same mean biases, centered rmse and correlation. MAR underestimates near-coastal temperature while overestimating temperatures at higher elevations. This is also highlighted by the higher CRMSE at E-66 and D-85. This feature comes from an overestimation ranging between +2 °C and +2.6 °C in winter whatever the resolution used and is also shared with the 35 km Antarctic configuration (Ch. 3). This suggests that the direct effect of resolution on the representation of different physical processes likely to influence air temperature (in particular clouds) does not explain this bias.

For most observation locations, using a higher resolution improves the representation of near-surface wind speed (Fig. 7.6). At 5 km resolution, the mean biases, and CRMSE are reduced and the correlation increases compared to 20 km resolution for most locations. Higher resolutions better represent the ice-sheet slope over the margins yielding better modelled katabatic winds. As lower resolutions smooth the slope, increasing the resolution leads to stronger katabatic winds especially in valleys (and their left side) and downwind areas over the ocean (Fig. 7.4c). Furthermore, Huot et al. (in preparation) revealed a strong influence of the atmospheric wind resolution on the ocean by forcing the ocean and sea-ice model NEMO-LIM with the MAR simulations presented here. They showed that MAR forcings at higher resolutions, and especially stronger katabatic winds, enhance the polynya activity, the sea-ice production and the salt rejection simulated by NEMO-LIM. However, the comparison between mean 10-m winds simulated by MAR at 10 km and 5 km reveals small anomalies suggesting that the topography at 10 km is as well represented as at 5 km over Adelie Land. A transect (not shown) through 140° of longitude (and through the location of the Dumont d'Urville manned station) furthermore highlights that the 10 km resolution topography is equivalent to the original topography (1 km) from Fretwell et al. (2013) suggesting that this resolution is appropriate in this area.

The sensitivity of the SMB and near-surface climate in MAR to the horizontal resolution is similar to that of RACMO (Lenaerts et al., 2012c) while being partly

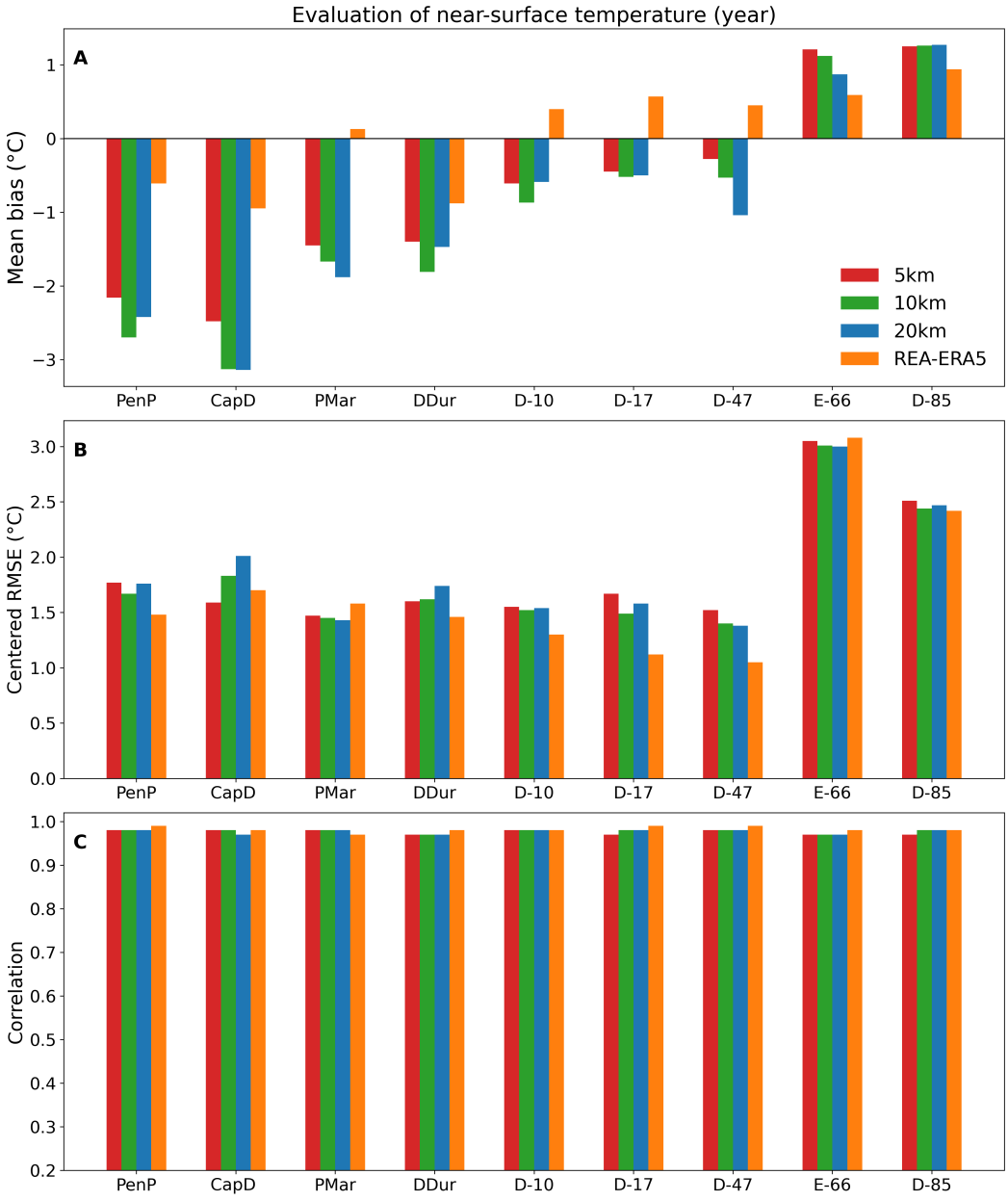

Figure 7.5: Comparison (A. mean bias, B. CRMSE, C. correlation) of the daily near-surface temperature (°C) simulated by MARv3.11 at 5 km (red), 10 km (green), 20 km (blue), and by ERA5 (orange) to AWS over Adelie Land between 2000–2015. Temperature difference due to altitude differences between the pixel and the AWS have been corrected using the modelled lapse rate temperature in the vicinity of the station.

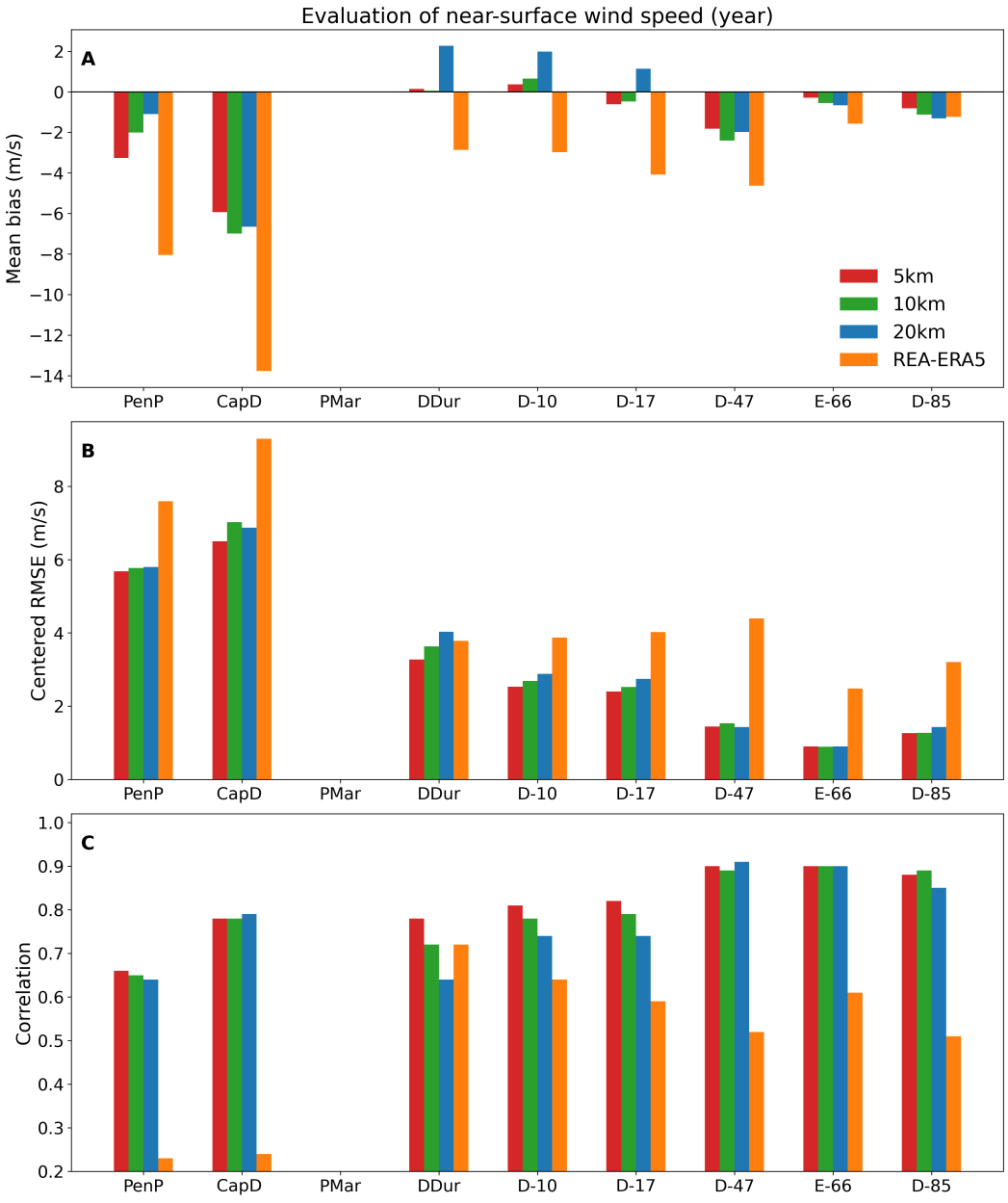

Figure 7.6: Comparison (A. mean bias, B. CRMSE, C. correlation) of the daily near-surface wind speed ($m\,s^{-1}$) simulated by MARv3.11 at 5 km (red), 10 km (green), 20 km (blue), and by ERA5 (orange) to AWS over Adelie Land between 2000–2015.

different to (polar) WRF (Vignon et al., 2019). Using a 5.5 km resolution instead of a 27 km with RACMO, Lenaerts et al. (2012c)) concluded that this higher resolution leads to stronger wind in confluence valleys while Vignon et al. (2019) found that WRF using coarser resolution overestimates the katabatic wind speeds. Using higher resolution with MAR and RACMO induces stronger katabatic wind, but higher resolutions in WRF decrease the katabatic strength and the cold air bumps over the ocean. The higher horizontal resolution used with the three models improves the local results (through a higher spatial variability) and better represents the strong gradients around the margins but does not improve the mean simulated climate and SMB. Consistently with our results, both Lenaerts et al. (2012c); Vignon et al. (2019) suggested that a resolution even coarser than 20 km might be appropriate for simulating the mean SMB and climate over Adelie Land.

MAR does not represent the mean temperature as well as its forcing ERA5 which likely results from the 1) assimilation of (near-surface) temperature observation and 2) assimilation of radiance and cloud products that improves the representation of energy fluxes in ERA5 (Delhasse et al., 2019). However, MAR better represents the mean near-surface wind speed (Fig. 7.6). Our results suggest that ERA5 underestimates wind speed for all stations in Adelie Land and despite assimilation of AWS data, atmospheric profile and scatterometer observations (Hersbach et al., 2020), it does not correctly represent the temporal evolution of wind speed (low correlation coefficient), especially at the coast. Delhasse et al. (2019) raised the same issues for the Greenland Ice Sheet. Data assimilation (AWS and airborne soundings) at the scientific base Dumont D'Urville probably explains why ERA5 is as good as MAR for this specific location only. While having a higher resolution than MAR at 20km, the wind speeds in ERA5 are less accurate than MAR, highlighting the interest of using a polar-oriented model (such as MAR) for representing the katabatic wind dynamics over Adelie Land independently from the resolution.

Despite the inherent limitations of the method (small domain, limited range of resolutions, humidity consistency), running the model at high resolution remains mainly interesting for the representation of wind speed but investigations on the model sensitivity to the resolution should be carried out over the whole AIS. Indeed, it highlights large differences over the margins, over which the strongest changes are projected by the end of the 21st century (Genthon et al., 2009; Kittel et al., 2020). Genthon et al. (2009) revealed that higher resolution ESMs project a larger precipitation increase suggesting differences in contribution of the AIS to the

sea level rise. However, models with different resolutions but also different levels of complexity and physical adaptations are compared in Genthon et al. (2009) thus leaving the sensitivity of the future SMB changes using a constant and adapted (polar-oriented) physics for future work. Furthermore, RCMs are often considered to be more accurate than ESMs as they are usually run at higher resolution (e.g., Lenaerts et al., 2019; Barthel et al., 2020; Fettweis et al., 2020; Seroussi et al., 2020). However, RCM (Mottram et al., 2020) and ESM (Gorte et al., 2020) SMB comparisons have revealed that the best SMB estimations do not come from the higher resolution models, but from those using coarser resolution suggesting that the horizontal resolution is of second order with respect to the physics of the model. Conversely, we conclude in Ch. 3 that using a 35 km resolution instead of the 50 km resolution improves the modelled SMB. This highlights the need to better determine the effect of the resolution on the SMB for selecting the most appropriate resolution as being a compromise between a sufficient level of details (reliability of results) and computation time (diversity of scenarios and better consideration of uncertainties).

Since we found small SMB differences between the different resolutions over Adelie Land, this suggests that the processes governing the SMB in our simulation (precipitation and sublimation) are not sensitive to the horizontal resolution in the range of tested values (5 to 20 km). Including drifting-snow processes will likely result in a more pronounced difference as these processes are correlated with wind speed (and inherently the topography) in a power-law fashion (e.g., Budd, 1966; Mann et al., 2000; Amory, 2020; Amory et al., 2020). Lenaerts et al. (2012c) therefore found a strong feedback between topography, wind and erosion leading to large differences in local SMB. Furthermore, frequent atmospheric rotors due to katabatic jumps (or sudden cessation of katabatic wind speed) have been documented to transport a significant amount of drifting snow (Gallée, 1996; Gallée and Pettré, 1998; Vignon et al., 2020). These rotors advect the airborne snow and humidity to higher atmospheric levels likely enabling a stronger sublimation as these higher levels are likely less saturated (Amory and Kittel, 2019). In addition to having a strong influence on the atmospheric mass and energy budgets, these rotors generate gravity waves (Vignon et al., 2020) affecting the formation of cirrus clouds (Alexander et al., 2017) and stratospheric polar clouds (Carslaw et al., 1998). Even though hydrostatic models can partly be used to study the driving mechanisms behind katabatic jumps (Gallée et al., 1996), only high-resolution (1 km) and non-hydrostatic models can represent these strong

vertical movements. This questions the representation of the katabatic layer in coarser-resolution climate models (Vignon et al., 2020). Katabatic winds also play a significant role on snowfall sublimation, thus influencing the Antarctic SMB (Grazioli et al., 2017; Agosta et al., 2019). Next studies should therefore focus on the representation of the katabatic layer, its vertical extent and sensitivity to both horizontal and vertical (although not mentioned here) resolutions as katabatic winds are determining elements of the Antarctic climate.

7.3 Supplementary insights related to sea-surface conditions

Several studies (e.g., Kittel et al., 2018; Beaumet et al., 2019b; Wang et al., 2020, and references therein) have shown that reducing SIC and/or increasing SST result in an increase in precipitation through enhanced evaporation over the open ocean. Similar results were also obtained in the Arctic (e.g., Noel et al., 2014; Lambert et al., 2019). Polynyas and leads, i.e. areas of "open" water (lower SIC) inside the sea-ice pack, are important locations with strong interactions between the atmosphere (cold katabatic wind that exerts a stress and cools the ocean surface) and the ocean (heat release) (Massom et al., 1998; Morales Maqueda et al., 2004). However, the relatively small extension of some polynyas (less or of the same order than the typical resolution of RCMs, see for instance, (Smith et al., 1990; Massom et al., 1998; Barber et al., 2001; Morales Maqueda et al., 2004) prevents an accurate representation of the interactions between the atmosphere and the ocean. SIC at the surface of the atmospheric models can then be considered as a compromise between the ice pack and polynyas resulting in overestimated SIC. Furthermore, the coarse resolution of these models induces a misrepresentation of the sea-ice pack margins. These two biases are also amplified by the coarse resolution of the reanalyses while their SSCs originally come from higher resolution datasets that have been aggregated to the resolution of the reanalyses (see for instance Dee et al. (2011) for ERA-Interim). Consequently, atmospheric models likely underestimate interactions between open-ocean and the atmosphere, influencing latent and sensible heat transferts. Since, a decrease in SIC and/or an increase in SST result(s) in more precipitation over the AIS, using appropriate forcing SSC could have a significant influence on the Antarctic SMB.

To assess the atmospheric sensibility to the polynya size and the represent-

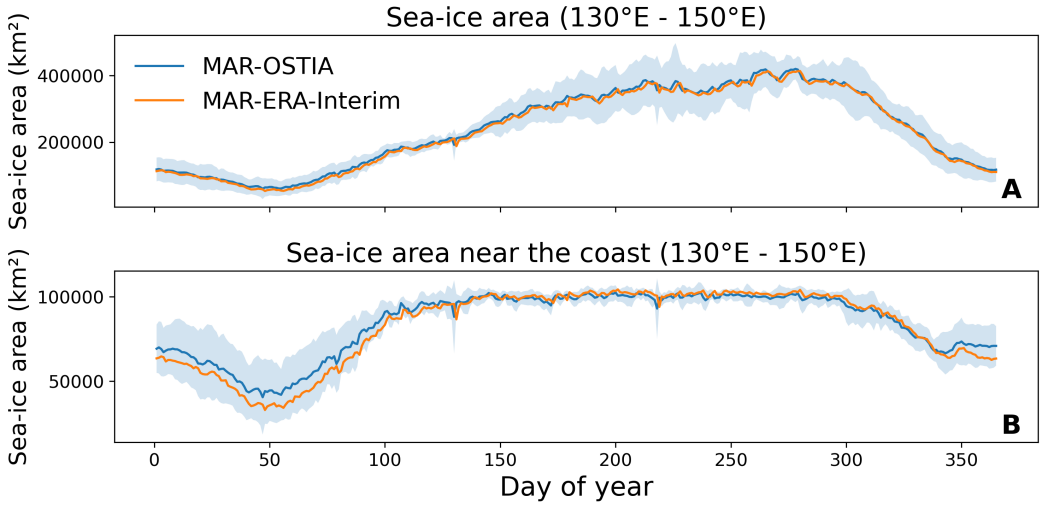

Figure 7.7: Mean (2009–2015) daily sea-ice area (km^2) between 130°E and 150°E (A) and between 130°E and 150°E but no more than 100 km away from the coast (B) for OSTIA (blue) and ERA-Interim (orange) interpolated on the MAR 10 km grid. The interannual variability (standard deviation) of sea-ice area in OSTIA is shown by the shaded area.

ation of the sea-ice pack margin, we performed simulations using MAR at 10 km resolution over the Adelie Land region where ERA-Interim SSCs were replaced by SSCs from the OSTIA reanalysis. We then compared these simulations (MAR-OSTIA) to the MAR-ERA-Interim results over 2009–2015. Although this period is relatively short, it enables a fair comparison knowing that ERA-Interim SSCs are based on the OSTIA reanalysis after 2009, i.e the ERA-Interim SSCs are an equivalent product but at a lower resolution.

The sea ice summed area barely differs between ERA-Interim and OSTIA on the 10 km MAR grid (Fig. 7.7A). The sea ice in OSTIA has a larger northern extension resulting in a higher value but this difference remains negligible. As polynyas around Antarctica are mainly maintained by katabatic winds (Massom et al., 1998), the same comparison for the regions close to the coast (less than 100 km from the coast,Fig. 7.7B) revealed a slightly larger sea-ice area in OSTIA than in ERA-Interim during summer as a result of the northward expansion of the ice pack and higher SIC near the coast (Fig. 7.8B). In winter, this effect is overcompensated by the increased presence of polynyas near the coastal margins (Fig. 7.8D) explaining why ERA-Interim has a larger sea-ice area in that season (Fig. 7.7B). Although SSCs remain quite similar in the two forcings, local significant differences in SIC can be found near the coast in summer and at the sea-ice pack margins for both seasons (Fig. 7.8).

Over the ice sheet, these anomalies in SSCs do not induce significant changes

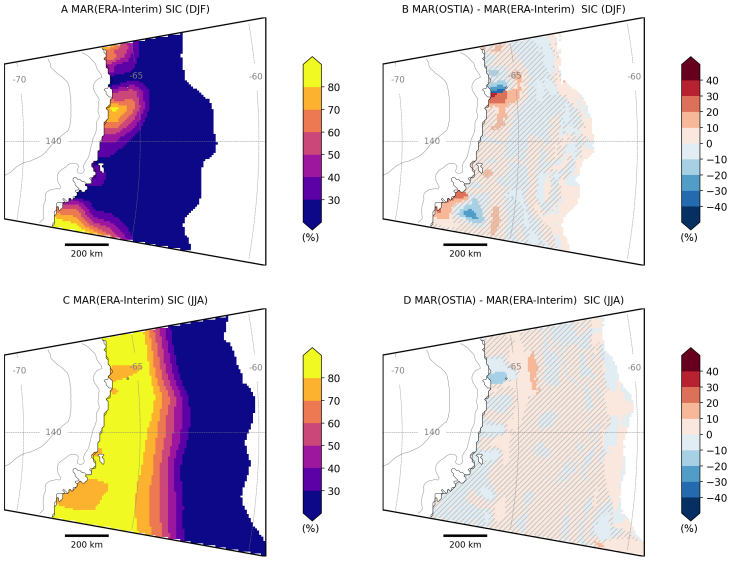

Figure 7.8: Mean (2009–2015) sea-ice concentration (%) in summer (A) and in winter (B) simulated by ERA-Interim. Differences in mean (2009–2015) sea-ice concentration (%) in summer (C) and in winter (D) simulated by OSTIA and ERA-Interim. Non-significant anomalies (smaller) than the interannual deviation are hatched.

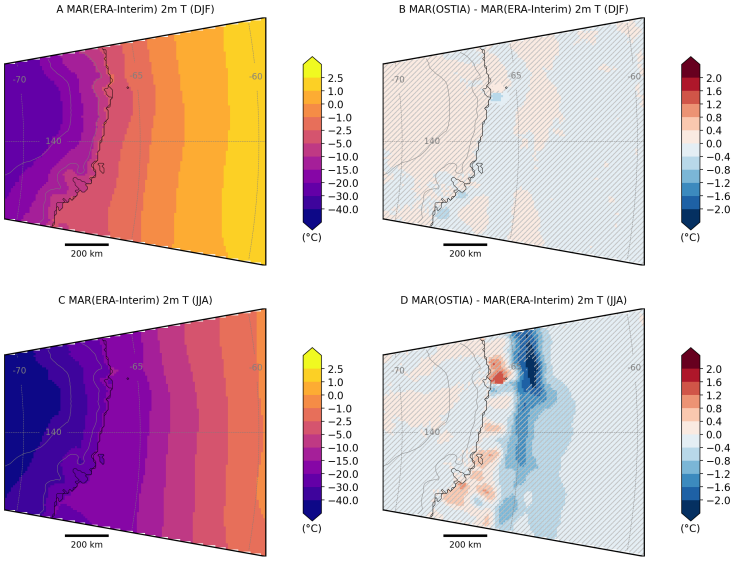

Figure 7.9: Mean (2009–2015) 2-m air temperature (°C) in summer (A) and in winter (B) simulated by MAR forced by ERA-Interim. Differences in mean (2009–2015) 2-m air temperature in summer (B) and in winter (D) simulated by MAR forced by ERA-Interim with OSTIA sea-surface conditions and forced by ERA-Interim. Non-significant anomalies (smaller) than the interannual deviation are hatched.

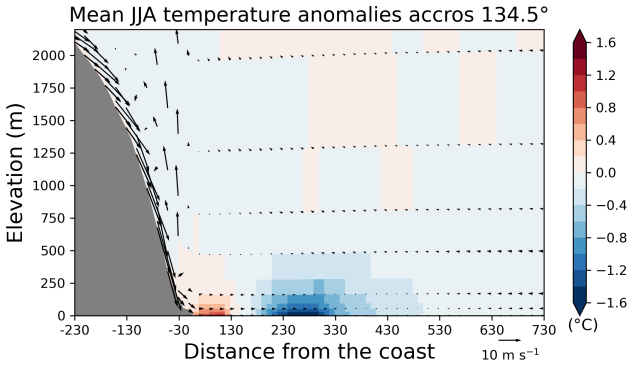

Figure 7.10: Atmospheric cross section following 134.5°W illustrating the difference in mean (2009–2015) JJA temperature simulated by MAR forced by ERA-Interim with OSTIA sea-surface conditions and forced by ERA-Interim (units: °C). Meridional and vertical components of the mean (2009–2015) JJA wind are represented by black vectors (units: $\mathrm{m\,s^{-1}}$). The transect follows the 134.5° W direction as it crosses areas with significant anomalies of near-surface air temperature in Fig. 7.9D.

neither on the SMB nor on the near-surface climate in contrast to the ocean. Comparing the 2-m air temperature and wind speed with the near-surface and accumulation observations previously used in Sect. 7.2, reveals the same statistics for both simulations (not shown) meaning that the higher SSC resolution does not yield any significant improvement. Furthermore, we found non-significant differences in the 2-m air temperature (Fig. 7.9B and D) over the ice sheet in Adelie Land and similarly (not shown) for wind speed and SMB, with for the latter differences of less than 25 $\mathrm{kg\,m^{-2}\,yr^{-1}}$. Conversely, Figures 7.9B and 7.9D suggest more significant changes occuring over the ocean particularly during winter. The larger polynyas in MAR (OSTIA) favour the warming of the air by the ocean resulting in higher 2-m air temperature close ($<$ 200 km) to the coast; while offshore higher SIC colds the near-surface atmosphere. Areas with higher (lower) 2-m air temperature coincides with locations where the wind is decreased (increased) although these changes in wind speed are also non-significant.

The large local positive and negative temperature anomalies (up to 2 °C) induced by using different SSC remain confined in the prolongation of the katabatic layer corresponding to the lowest atmospheric levels (Fig 7.10). As already discussed in Ch. 4, the mean offshore direction of these winds prevents the advection of the anomalies induced by different SSCs inland. They also advect cold air from inland regions resulting in a temperature inversion (e.g., Vignon et al., 2019) that caps most of the anomalies into the lowest atmospheric levels. Figure 7.10 also highlights that large offshore anomalies not located inside the katabatic layer tends to propagate more easily into higher atmospheric levels.

Furthermore, the development of frontal structures and strengthened mesocyclonic activities where the cold and dry katabatic flow meets the warm and wet offshore flow can propagate upwards the anomalies located at the katabatic area margins (Gallée, 1995, 1996). If the anomalies reach sufficiently high atmospheric levels where the meridional flow is directed towards the ice sheet, they then can have an influence on the ice sheet climate (Ch. 4). This means that a similar anomaly in SSCs might have a larger influence if it is located offshore than close to the ice sheet margins.

While these supplementary investigations over Adelie Land suggest a small influence of surrounding SSC on the Antarctic climate and SMB, large SSC anomalies can alter the Antarctic climate. Comparing Ch. 4 (where we assessed the sensitivity of the present Antarctic SMB to SSC) to Ch. 5 (where we assessed the sensitivity of the present Antarctic SMB to future climate changes) reveals that SSC anomalies over the present climate can lead to changes of the same order than a warmer future climate highlighting the importance of SSCs. This also questions the selection of some ESMs presenting large SST biases to refine Antarctic SMB projections as done in Gorte et al. (2020). These authors have selected GISS-E2-H among other ESMs, while in Ch. 4, we showed that this model has the largest positive SST biases over the present climate within the CMIP5 ensemble and that using GISS-E2-H SSCs leads to significant positive SMB anomalies.

Furthermore, important feedbacks between the atmosphere and the ocean are inhibited because SSCs were prescribed in all our experiments. Since differences in atmospheric conditions can exert a strong influence on the state of the surface ocean (Huot et al., in preparation), experiments in which MAR is coupled to the ocean and sea-ice model NEMO-LIM could result in more significant differences in the atmosphere and ultimately over the ice sheet. By coupling together these models over the Ross Sea sector, Jourdain et al. (2011) found however that the atmosphere seems to be less sensitive to local feedbacks than the ocean in agreement with our results while sea-ice production and deep-water formation were more affected (as in Huot et al. (in preparation) in MAR-forced NEMO experiments). Coupling MAR and NEMO-LIM could then be of higher interest for characterizing the oceanic response to atmospheric changes than the other way round. Coupling experiments will also enable to better simulate the atmospheric and ocean melt of the ice shelves that is currently poorly represented in the ESMs for both the atmospheric (Lenaerts et al., 2019) and oceanic (Jourdain et al., 2020) parts leading to better projections of the Antarctic sea-level contribution.

At the time of writing MAR and NEMO-LIM have been re-coupled on Adelie Land in a joint project between UCLouvain (P.-V. Huot under the supervision of Pr T. Fichechet) and ULiège (C. Kittel under the supervision of Dr X. Fettweis) to investigate the influence of small-scale processes on the dynamics of the coupled atmosphere-cryosphere-ocean system. As the evaluation phase is almost complete, the next steps will focus on the analysis of interactions in Adelie Land before applying this new tool over both the Antarctic and Greenland ice sheets under present and future climatic conditions.

CHAPTER 8

Conclusions

8.1 Summary of the main results

We use the regional climate model MAR to reconstruct (using ERA-Interim and ERA5 reanalyses) and project (using different GCMs from CMIP5 and CMIP6 ensemble) the SMB of the Antarctic ice sheet over 1980–2100 and to identify driving processes from different components of the climate system (from the surface of the ocean to high-level clouds). Furthermore, the climate and SMB modelled by MAR have been thoroughly evaluated with a set of available diverse observations to assess the performance of the model over the current period. The main findings are summarized below.

SSCs have a second-order influence on the regional and temporal variability of the SMB.

The initial subject of the thesis was to study small-scale interactions within the atmosphere - (sea) ice - ocean system using regional atmospheric and oceanic models. During the individual setup phase of these models, it was proposed to use the robust and evaluated configuration of MARv3.6 from Agosta et al. (2019) to evaluate the influence of SSCs over the Antarctic SMB.

To determine to what extent the ocean surrounding the AIS can exert a direct influence on the atmosphere and SMB, we performed sensitivity experiments with perturbed SSCs. Results mainly highlight the effect of stronger (weaker) evaporation associated with warmer (colder) SSCs on SMB by increasing (decreasing) precipitation. Colder SSCs decrease precipitation at the margins due to the lower moisture content of the air masses. On the opposite, warmer SSCs significantly enhance precipitation due to stronger and earlier condensation over the ice-sheet margins. Given this influence of SSC perturbations on the current Antarctic SMB, projections using models with biased SSCs (e.g., Gorte et al., 2020) over the current climate could then be highly unrobust.

Only the largest SSCs perturbations (ie., combined SST and SIC) lead to both spatial and integrated significant SMB anomalies. These perturbations enable SSC-induced anomalies to reach sufficiently high atmospheric levels where the katabatic flow no longer repels these anomalies offshore. However, the applied perturbations over the present climate can be described as extreme. The sea-ice

area was decreased by more than 28% in winter and 50% in summer (and SSTs higher by more than 3°C) compared to their mean values over 1979–2015. These reductions correspond to the middle range of projected sea-ice changes by CMIP5 models using RCP8.5 at the end of the 21cst century (Beaumet et al., 2019a).

The fact that only the largest SSC anomalies lead to significant differences also suggests that the Antarctic SMB is more sensitive to changes in the atmosphere (circulation) than over the surrounding ocean. We have therefore focused our work on the sensitivity of the SMB to projected atmospheric warmings by downscaling with MAR, two CMIP5 ESMs and two CMIP6 ESMs using their respective highest-emission scenarios (RCP8.5 and ssp585). The selected ESMs cover a large range of projected increase in temperature to evaluate the SMB sensitivity to several atmospheric warmings.

Future regional variability of the Antarctic SMB is more important than the inter-model and emission-scenario variability.

Higher temperatures lead to increased SMB on the grounded ice as a result of increasing snowfall amounts while the future SMB over the ice shelves is dominated by higher runoff values and is consequently projected to decrease. Global warming is likely to lead to significant diverging changes over the grounded ice sheet and the ice shelves regardless of the forcing ESM at the end of the 21st century. We found that future regional and integrated changes are similar for a same warming compared to the present climate independently of the scenario and ESM used as forcing This suggests that future SMB uncertainties are mainly due to differences in the timing of the projected warming by ESMs and their sensitivity to a same anthropogenic forcing.

Furthermore, the near-surface warming projected by the future ESMs around the AIS determines the future integrated SMB over large area. This enables us to reconstruct integrated SMB anomalies over the grounded ice sheet as well as over the ice shelves for the whole CMIP5 (RCP8.5) and CMIP6 (ssp126, ssp245, ssp585) database using a statistical regression. This reconstructed grounded SMB suggests a higher increase for CMIP6-ssp585 ($+447 \pm 134$ Gt yr^{-1}) than for CMIP5-RCP8.5 ($+ 353 \pm 114$ Gt yr^{-1}) over 2071–2100 compared to 1981-2010. These respectively correspond to a 2000-2100 summed sea-level contribution of -6.3 ±2.0 cm SLE and -5.1 ±1.9 cm SLE. Low (ssp126) and intermediate (ssp245) CMIP6 emission scenarios project a lower negative contribution to sea-level rise than ssp585 (-3.0 ±1.4 cm SLE using ssp126 and -4.2 ±1.6 cm SLE using ssp245).

Conversely, CMIP6-ssp585 yield a stronger SMB decrease over the ice shelves

(-119 ± 100 Gt yr^{-1}) than CMIP5-RCP8.5 (-54 ± 55 Gt yr^{-1}). This highlights that higher temperature increases lead to more accumulation on the grounded ice sheet but a stronger decrease in SMB over the ice shelves with changes between these two regions larger than those induced by different ESMs or scenarios.

Leaving aside the role of the ocean on the thinning of ice shelves, our results suggest that increasing surface melt should remain weak, limiting potential ice-shelf collapses due to hydrofracturing under the Paris Agreement. For higher warming, we found that ice-shelf SMB could strongly decrease with widespread surface melt production and runoff potentially compromising the stability of ice shelves. Even if same increases in temperature result in similar melt increases, the projected timing of the warming strongly differs between the forcing ESM leading to differences of 390% between the lowest and the highest cumulative melt anomalies over the 21st century. So far it remains unclear whether these differences are due to variations in warming rates in individual models only, or whether local surface energy budget feedbacks could also play a notable role.

The main source of inter-model variability in melting by 2100 is cloud microphysics.

We again use MAR to study the physical drivers inducing the future ice-shelf summer melt increase in high-concentration scenarios RCP8.5 and ssp585. Main differences in ice-shelf summer melt arise from differences in net longwave fluxes and to a lesser extent to shortwave fluxes while turbulent fluxes are not significantly influential. In particular, the atmospheric longwave radiations towards the surface are projected to increase. Higher greenhouse-gas concentrations and warmer free atmosphere explain the increase in LWD, but differences in LWD are mainly attributed to differences in cloud properties simulated by MAR. The projections reveal an increase in cloud cover and more importantly in cloud optical depth as a result of cloud particle contents and phase changes with more liquid-containing clouds. While rising air temperatures increase moisture content, differences in projected cloud phase are mainly related to the vertical structure of specific humidity changes. Finally, liquid clouds also increase absorbed solar radiation despite decrease in SWD due to the melt-albedo feedback. Higher melt production further lowers the albedo by promoting surface snow grain metamorphism which further strengthens absorption of solar radiation and increases melt again.

By increasing melt over the peripheral ice shelves, liquid-containing clouds could trigger more hydrofracturing and ice-shelf collapses. While recent reduction in ice-shelf buttressing already increases the Antarctic contribution to SLR,

enhanced ice discharge after future collapses could also trigger several feedbacks such as MICI that would lead to a rapid increase in SLR. This suggests that liquid-containing clouds could be a major source of uncertainties in determining the future Antarctic contribution to SLR.

To conclude, this thesis focused on the uncertainty in the estimation of the SMB related to future oceanic and atmospheric conditions. All these conclusions rely on the outputs from the regional climate model MAR developed at ULiège. Obtaining most of these results with an operational recent version of the model has required the development of a new stable configuration over Antarctica beforehand to switch from MARv3.6 to MARv3.11. This development includes bug fixations, sensitivity tests to model parameters and improvements of the model by adding, for example, the possibility of representing nunataks in Antarctica. MAR has been thoroughly evaluated against a set of gathered observations. The simulations performed during the framework of this thesis have now become new MAR reference runs over the AIS and are available in open-access notably through the CORDEX initiative. The results are already used in various exercises including model intercomparison, ice-core dating, reconstruction of the firn thickness change, evaluation of the (future) permeability of the snowpack on ice shelves or investigations between surface accumulation and meteorology in Antarctica in which I am a co-author.

8.2 Perspectives

Although Greenland and Antarctica have often been associated as the two main potential contributors to SLR in the context of global warming, the size and isolation of the Antarctic continent as well as the much more extreme conditions have long inhibited scientific investigations compared to its Arctic counterpart. Even if Antarctica is now receiving continuously growing attention, the largest ice mass on Earth still remains poorly understood while over Greenland, the consequences of global warming are already more obvious.

This thesis focused on the SMB and more specifically on the influence that the ocean surface and atmospheric warming can exert on it. A number of choices have guided the reflection on the factors influencing the SMB, but many others remain to be explored. Hereafter, we present two types of perspectives guided by the previous chapters: research questions directly inspired from our results that could directly use the MAR setup developed during this thesis and research

questions inspired by the current MAR limitations that should request new model developpements.

8.2.1 Further direct research topics

Among the points of interest envisaged but not addressed in this work are: present and future changes in atmospheric circulation, the effect of ozone depletion on the SMB, and the very fine-scale processes taking place during interactions between the atmosphere and the ocean and of course potential links between them. For instance, the SAM index has exhibited a positive trend (e.g., Marshall and Thompson, 2016) since the late 1950s resulting in a southward shift and intensification of the westerlies (Gillett and Thompson, 2003; Arblaster and Meehl, 2006; Polvani et al., 2011; Schneider et al., 2015; Waugh et al., 2015). This circulation change has been attributed to ozone depletion and greenhouse-gas concentrations (Arblaster and Meehl, 2006; Polvani et al., 2011). Although MAR does not aim to simulate large-scale circulation changes, it would be interesting to assess the effect of ozone depletion and associated circulation changes by forcing MAR over a longer period in the past. The recent availability of the ERA5 reanalysis back to 1950 could thus make it possible to analyse the evolution of the SMB over a longer period when recent climate change would be less masked by natural climate variability in Antarctica. However, this reanalysis has yet to be evaluated for its pre-1979 performances. Similarly, assessing atmospheric circulation changes due to SSCs modifications (e.g., Bromwich et al., 1998; Krinner et al., 2014) could also be done with MAR under conditions where it is less constrained at the top of its atmosphere. This would also make a coupling between MAR and an ocean model more interesting, provided that the domain is large enough to deconstrain MAR.

The grounded SMB is projected to increase with temperature as long as the increase in snowfall accumulation is larger than the increase in runoff. We found that an increase of +7.5°C near-surface warming compared to 1981–2010 could lead to a stabilisation and even a decrease in the grounded SMB. This would result in a decrease in the sea-level mitigation capacity of the grounded AIS surface. This warming is however reached before 2100 by only one model in the highest-emission scenario suggesting that more work is needed to assess the confidence in this threshold and then the response of the AIS surface to strong warming rates after 2100.

Katabatic winds have an important effect on the Antarctic SMB as they influence the (surface and atmospheric) sublimation, heat and mass exchanges within the Southern hemisphere and can also prevent anomalies caused by interactions with the ocean surface to propagate inland. Our projections suggest a decrease in summer near-surface wind speed over the ice shelves with stronger decreases associated with larger warmings. This is consistent with previous studies (e.g., van den Broeke et al., 1997; Bintanja et al., 2014) where this decrease was mainly attributed to changes in the synoptic forcing instead of a decrease in the inversion strength due to surface warming. Yet, we found a decrease in air temperature inversion over the ice shelves in summer over 2071–2100 but we did not investigate the individual contribution of each katabatic drivers. Since the future global warming is much stronger in our projections than in these previous studies and given the importance of katabatic winds for the Antarctic climate (including creation of polynyas and sea-ice production over the surrounding ocean), forthcoming studies should therefore focus on physical drivers behind future reduction of katabatic winds.

8.2.2 Further model developments

A lot of developments in MAR were performed during this PhD thesis, notably via the coupling with NEMO-LIM, the results of which remain to be studied, but generally in the reconfiguration of the different MAR versions of the Antarctic setup and the discovery of inherent bugs linked to the development of a climate model. This also enabled us over the course of the chapters to highlight the next steps in th e development of the model which could make it possible to better represent the Antarctic climate and reduce the uncertainties in our present and future estimation of the SMB. Probably the most obvious would be to perform simulations at much higher resolution with a non-hydrostatic version, but there are more specific developments for the AIS that have to be mentioned. We will then highlight several methodological and technical (specific to MAR) limits which are proposed here as perspectives to refine present and future SMB estimates using MAR.

The most interesting development concerning the AIS and its climate is the drifting snow module in MAR that has recently been redeveloped. As highlighted in the previous chapter (Ch. 7), drifting snow can have important effects on the energy and mass budgets of the atmosphere and the surface but is generally

undocumented. Even if drifting-snow could probably become minor compared to the increase in runoff in the future, drifting-snow and feedbacks with the surface could still be a major source of uncertainties in future estimations of Antarctic SMB. Forthcoming efforts should therefore focus on the recent past (thanks to the availability of ERA5 back to 1950) and future periods to determine evolution of drifting-snow processes over the ice sheet to improve our estimations of the Antarctic SMB and its contribution to sea-level rise. Finally, from a strictly MAR developer's point of view, the (re)conciliation of MARv3 assets with the version 4 of the model (developed by Hubert Gallée) including its more advanced microphysical scheme enabling to distinguish drifting-snow particles from atmospheric snowfall particles is certainly one of the most urgent developments.

Clouds are likely to become a major source of uncertainties in the Antarctic contribution to SLR by potentially triggering ice-shelf collapses and increasing ice discharge. Although MAR is particularly adapted to simulate the cloud microphysical processes of the polar regions, these processes could be improved in particular by using more recent schemes enabling to represent, in addition to the evolution of the mass of hydrometeors a second parameter such as their size distributions or their nuclei numbers. Furthermore, the drifting-snow effect on clouds is generally unknown, inducing a second source of uncertainties in cloud effect on the Antarctic SMB. We should also mention the uncertainties linked to the radiative scheme itself, which should be updated in MAR to improve the representation of the atmospheric radiative budget, notably through a better capture of the optical properties of (drifting snow) clouds in relation to their snow/ice/liquid content and the transition from a broadband to a multiband irradiance.

Beyond the uncertainties linked to the quantity of water produced at the surface, whether this water percolates and refreezes into the snowpack, or accumulates on the surface forming lakes or finally flows towards the ocean is perhaps a second large source of uncertainties about the future evolution of Antarctic ice shelves. The surface water balance in MAR is currently computed on the vertical dimension only. Water can percolate, refreeze and if the snowpack can no longer absorb liquid water, it is considered to runoff directly into the ocean without being able to flow over the ice surface as runoff streams and rivers (e.g., Bell et al., 2017). However, the hydrological behaviour of melt water according to whether it percolates, freezes, accumulates or flows can have very different consequences on the state of the ice shelves (Bell et al., 2017; Banwell et al., 2019; Arthur

et al., 2020). This highlights the interest of studying melt water on ice shelves, in particular via the coupling of MAR to a hydraulics model that would enable water to be routed above and within the snowpack.

Finally, determining whether ice shelves could collapse due to hydrofracturing or bending would require a coupling between MAR and an ice sheet model that represents these dynamical processes. It will also enable to take into account feedbacks between the ice-sheet geometry (i.e surface elevation and ice mask) with the atmosphere that are currently not represented in MAR. For instance, the melt-elevation feedback should increase melt due to the lowering of the surface elevation by atmospheric melt. Since atmospheric processes are not the only processes that modify the ice sheet geometry, coupling an atmospheric model to both ocean and ice-sheet models would be even more interesting as it will enable the representation of the full AIS dynamics and certainly better constrain the contribution of the AIS to SLR.

References

Agosta, C., Favier, V., Genthon, C., Gallée, H., Krinner, G., Lenaerts, J. T., and van den Broeke, M. R.: A 40-year accumulation dataset for Adelie Land, Antarctica and its application for model validation, Climate dynamics, 38, 75–86, 2012.

Agosta, C., Favier, V., Krinner, G., Gallée, H., Fettweis, X., and Genthon, C.: High-resolution modelling of the Antarctic surface mass balance, application for the twentieth, twenty first and twenty second centuries, Climate dynamics, 41, 3247–3260, 2013.

Agosta, C., Fettweis, X., and Datta, R.: Evaluation of the CMIP5 models in the aim of regional modelling of the Antarctic surface mass balance, The Cryosphere, 9, 2311–2321, 2015.

Agosta, C., Amory, C., Kittel, C., Orsi, A., Favier, V., Gallée, H., van den Broeke, M. R., Lenaerts, J., van Wessem, J. M., van de Berg, W. J., et al.: Estimation of the Antarctic surface mass balance using the regional climate model MAR (1979-2015) and identification of dominant processes, The Cryosphere, 13, 281–296, 2019.

Agosta, C., Kittel, C., and Amory, C.: Evaluation of CMIP6 and CMIP5 models for regional modelling of Greenland and Antarctic surface mass balance, in preparation.

Akperov, M., Rinke, A., Mokhov, I. I., Matthes, H., Semenov, V. A., Adakudlu, M., Cassano, J., Christensen, J. H., Dembitskaya, M. A., Dethloff, K., Fettweis, X., Glisan, J., Gutjahr, O., Heinemann, G., Koenigj, T., Koldunov, N., Laprise, R., Mottram, R., Nikiéma, O., Scinocca, J. F., Sein, D., Soboloswki, S., Winger, K., and Zhang, W.: Cyclone activity in the Arctic from an ensemble

of regional climate models (Arctic CORDEX), Journal of Geophysical Research: Atmospheres, 123, 2537–2554, 2018.

Alexander, P., Tedesco, M., Fettweis, X., Van De Wal, R., Smeets, C., and Van Den Broeke, M.: Assessing spatio-temporal variability and trends in modelled and measured Greenland Ice Sheet albedo (2000–2013), The Cryosphere, 8, 2293–2312, 2014.

Alexander, S., Orr, A., Webster, S., and Murphy, D.: Observations and fine-scale model simulations of gravity waves over Davis, East Antarctica (69° S, 78° E), Journal of Geophysical Research: Atmospheres, 122, 7355–7370, 2017.

Amory, C.: Drifting-snow statistics from multiple-year autonomous measurements in Adélie Land, East Antarctica, The Cryosphere, 14, 1713–1725, 2020.

Amory, C. and Kittel, C.: Brief communication: Rare ambient saturation during drifting snow occurrences at a coastal location of East Antarctica., The Cryosphere, 13, 2019.

Amory, C., Trouvillez, A., Gallée, H., Favier, V., Naaim-Bouvet, F., Genthon, C., Agosta, C., Piard, L., and Bellot, H.: Comparison between observed and simulated aeolian snow mass fluxes in Adélie Land, East Antarctica, The Cryosphere, 9, 1373–1383, 2015.

Amory, C., Naaim-Bouvet, F., Gallée, H., and Vignon, E.: Brief communication: Two well-marked cases of aerodynamic adjustment of sastrugi, The Cryosphere, 10, 743–750, 2016.

Amory, C., Gallée, H., Naaim-Bouvet, F., Favier, V., Vignon, E., Picard, G., Trouvilliez, A., Piard, L., Genthon, C., and Bellot, H.: Seasonal variations in drag coefficient over a sastrugi-covered snowfield in coastal East Antarctica, Boundary-Layer Meteorology, 164, 107–133, 2017.

Amory, C., Kittel, C., Le Toumelin, L., Agosta, C., Delhasse, A., Favier, V., and Fettweis, X.: Performance of MAR (v3. 11) in simulating the drifting-snow climate and surface mass balance of Adelie Land, East Antarctica, Geoscientific Model Development Discussions, pp. 1–35, 2020.

Andersson, E.: Data assimilation in the polar regions, ECMWF Newsletter, 112, 10–15, 2007.

Andreas, E. L.: A theory for the scalar roughness and the scalar transfer coefficients over snow and sea ice, Boundary-Layer Meteorology, 38, 159–184, 1987.

Andreas, E. L.: Time constants for the evolution of sea spray droplets, Tellus B, 42, 481–497, 1990.

Andreas, E. L.: The temperature of evaporating sea spray droplets, Journal of the atmospheric sciences, 52, 852–862, 1995.

Andreas, E. L.: A bulk air-sea flux algorithm for high-wind, spray conditions, version 2.0, in: Preprints, 13th Conference on Interactions of the Sea and Atmosphere, Portland, ME, 9–13 August 2004, 2004.

Andreas, E. L. and Decosmo, J.: The signature of sea spray in the HEXOS turbulent heat flux data, Boundary-layer meteorology, 103, 303–333, 2002.

Andreas, E. L. and Emanuel, K. A.: Effects of sea spray on tropical cyclone intensity, Journal of the atmospheric sciences, 58, 3741–3751, 2001.

Anthes, R. A., Kuo, Y.-H., Hsie, E.-Y., Low-Nam, S., and Bettge, T. W.: Estimation of skill and uncertainty in regional numerical models, Quarterly Journal of the Royal Meteorological Society, 115, 763–806, 1989.

Arakawa, A. and Lamb, V. R.: Computational design of the basic dynamical processes of the UCLA general circulation model, General circulation models of the atmosphere, 17, 173–265, 1977.

Arblaster, J. M. and Meehl, G. A.: Contributions of external forcings to southern annular mode trends, Journal of climate, 19, 2896–2905, 2006.

Armour, K. C., Marshall, J., Scott, J. R., Donohoe, A., and Newsom, E. R.: Southern Ocean warming delayed by circumpolar upwelling and equatorward transport, Nature Geoscience, 9, 549–554, 2016.

Arthur, J. F., Stokes, C., Jamieson, S. S., Carr, J. R., and Leeson, A. A.: Recent understanding of Antarctic supraglacial lakes using satellite remote sensing, Progress in Physical Geography: Earth and Environment, 2020.

Bailey, D. A. and Lynch, A. H.: Development of an Antarctic regional climate system model. Part I: Sea ice and large-scale circulation, Journal of climate, 13, 1337–1350, 2000.

Bamber, J. L., Griggs, J., Hurkmans, R., Dowdeswell, J., Gogineni, S., Howat, I., Mouginot, J., Paden, J., Palmer, S., Rignot, E., et al.: A new bed elevation dataset for Greenland, The Cryosphere, 7, 499–510, 2013.

Banwell, A. F., MacAyeal, D. R., and Sergienko, O. V.: Breakup of the Larsen B Ice Shelf triggered by chain reaction drainage of supraglacial lakes, Geophysical Research Letters, 40, 5872–5876, 2013.

Banwell, A. F., Caballero, M., Arnold, N. S., Glasser, N. F., Mac Cathles, L., and MacAYEAL, D. R.: Supraglacial lakes on the Larsen B ice shelf, Antarctica, and at Paakitsoq, West Greenland: a comparative study, Annals of Glaciology, 55, 1–8, 2014.

Banwell, A. F., Willis, I. C., Macdonald, G. J., Goodsell, B., and MacAyeal, D. R.: Direct measurements of ice-shelf flexure caused by surface meltwater ponding and drainage, Nature communications, 10, 1–10, 2019.

Barber, D., Marsden, R., Minnett, P., Ingram, G., and Fortier, L.: Physical processes within the North Water (NOW) polynya, Atmosphere-Ocean, 39, 163–166, 2001.

Barral, H., Genthon, C., Trouvilliez, A., Brun, C., and Amory, C.: Blowing snow in coastal Adélie Land, Antarctica: three atmospheric-moisture issues, The Cryosphere, 8, 1905–1919, 2014.

Barrett, A. I., Hogan, R. J., and Forbes, R. M.: Why are mixed-phase altocumulus clouds poorly predicted by large-scale models? Part 1. Physical processes, Journal of Geophysical Research: Atmospheres, 122, 9903–9926, 2017.

Barthel, A., Agosta, C., Little, C. M., Hattermann, T., Jourdain, N. N., Goelzer, H., Nowicki, S., Seroussi, H., Straneo, F., and Bracegirdle, T. T.: CMIP5 model selection for ISMIP6 ice sheet model forcing: Greenland and Antarctica, The Cryosphere, 14, 855–879, 2020.

Beaumet, J., Déqué, M., Krinner, G., Agosta, C., and Alias, A.: Effect of prescribed sea surface conditions on the modern and future Antarctic surface climate simulated by the ARPEGE atmosphere general circulation model, The Cryosphere, 13, 3023–3043, 2019a.

Beaumet, J., Krinner, G., Déqué, M., Haarsma, R., and Li, L.: Assessing bias corrections of oceanic surface conditions for atmospheric models, Geoscientific Model Development, 12, 321–342, 2019b.

Bechtold, P., Bazile, E., Guichard, F., Mascart, P., and Richard, E.: A mass-flux convection scheme for regional and global models, Quarterly Journal of the Royal Meteorological Society, 127, 869–886, 2001.

Bell, R. E., Chu, W., Kingslake, J., Das, I., Tedesco, M., Tinto, K. J., Zappa, C. J., Frezzotti, M., Boghosian, A., and Lee, W. S.: Antarctic ice shelf potentially stabilized by export of meltwater in surface river, Nature, 544, 344–348, 2017.

Bengtsson, L., Hagemann, S., and Hodges, K. I.: Can climate trends be calculated from reanalysis data?, Journal of Geophysical Research: Atmospheres, 109, 2004.

Bennartz, R., Shupe, M., Turner, D., Walden, V., Steffen, K., Cox, C., Kulie, M., Miller, N., and Pettersen, C.: July 2012 Greenland melt extent enhanced by low-level liquid clouds, Nature, 496, 83–86, 2013.

Bentsen, M., Bethke, I., Debernard, J. B., Iversen, T., Kirkevåg, A., Seland, Ø., Drange, H., Roelandt, C., Seierstad, I. A., Hoose, C., and Kristjánsson, J. E.: The Norwegian earth system model, NorESM1-M—Part 1: Description and basic evaluation of the physical climate, Geoscientific Model Development, 6, 687–720, 2013.

Bevan, S., Luckman, A., Hubbard, B., Kulessa, B., Ashmore, D., Kuipers Munneke, P., O'Leary, M., Booth, A., Sevestre, H., and McGrath, D.: Centuries of intense melt on Larsen C Ice Shelf, The Cryosphere, 11, 2743–2753, 2017.

Bi, D., Dix, M., Marsland, S. J., O'Farrell, S., Rashid, H., Uotila, P., Hirst, A. C., Kowalczyk, E., Golebiewski, M., Sullivan, A., Yan, H., Hannah, N., Franklin, C., Sun, Z., Vohralik, P., Watterson, I., Zhou, X., Fiedler, R., Collier, M., Noonan, J., Stevens, L., Uhe, P., Zhu, H., Griffies, S. M., Hill, R., Harris, C., and Puri, K.: The ACCESS coupled model: description, control climate and evaluation, Aust. Meteorol. Oceanogr. J, 63, 41–64, 2013.

Bintanja, R.: On the glaciological, meteorological, and climatological significance of Antarctic blue ice areas, Reviews of Geophysics, 37, 337–359, 1999.

Bintanja, R.: Snowdrift suspension and atmospheric turbulence. Part I: Theoretical background and model description, Boundary-layer meteorology, 95, 343–368, 2000.

Bintanja, R.: Snowdrift sublimation in a katabatic wind region of the Antarctic ice sheet, Journal of Applied Meteorology, 40, 1952–1966, 2001.

Bintanja, R. and van den Broeke, M. R.: The influence of clouds on the radiation budget of ice and snow surfaces in Antartica and Greenland in summer, International Journal of Climatology: A Journal of the Royal Meteorological Society, 16, 1281–1296, 1996.

Bintanja, R., Van Oldenborgh, G., Drijfhout, S., Wouters, B., and Katsman, C.: Important role for ocean warming and increased ice-shelf melt in Antarctic sea-ice expansion, Nature Geoscience, 6, 376–379, 2013.

Bintanja, R., Severijns, C., Haarsma, R., and Hazeleger, W.: The future of Antarctica's surface winds simulated by a high-resolution global climate model: 2. Drivers of 21st century changes, Journal of Geophysical Research: Atmospheres, 119, 7160–7178, 2014.

Bouchard, A., Rabier, F., Guidard, V., and Karbou, F.: Enhancements of satellite data assimilation over Antarctica, Monthly weather review, 138, 2149–2173, 2010.

Boucher, O., Randall, D., Artaxo, P., Bretherton, C., Feingold, G., Forster, P., Kerminen, V.-M., Kondo, Y., Liao, H., Lohmann, U., Rasch, P., Satheesh, S., Sherwood, S., Stevens, B., and Zhang, X.-Y.: Clouds and aerosols, in: Climate change 2013: the physical science basis. Contribution of Working Group I to the Fifth Assessment Report of the Intergovernmental Panel on Climate Change, pp. 571–657, Cambridge University Press, 2013.

Brasseur, O., Gallée, H., Schayes, G., Tricot, C., and De Ridder, K.: Impact of turbulence closures on diurnal temperature evolution for clear sky situations over Belgium, Boundary-layer meteorology, 87, 163–193, 1998.

Bromwich, D. H.: Snowfall in high southern latitudes, Reviews of Geophysics, 26, 149–168, 1988.

Bromwich, D. H., Chen, B., and Hines, K. M.: Global atmospheric impacts induced by year-round open water adjacent to Antarctica, Journal of Geophysical Research: Atmospheres, 103, 11 173–11 189, 1998.

Bromwich, D. H., Guo, Z., Bai, L., and Chen, Q.-s.: Modeled Antarctic precipitation. Part I: Spatial and temporal variability, Journal of Climate, 17, 427–447, 2004.

Bromwich, D. H., Fogt, R. L., Hodges, K. I., and Walsh, J. E.: A tropospheric assessment of the ERA-40, NCEP, and JRA-25 global reanalyses in the polar regions, Journal of Geophysical Research: Atmospheres, 112, 2007.

Bromwich, D. H., Nicolas, J. P., and Monaghan, A. J.: An assessment of precipitation changes over Antarctica and the Southern Ocean since 1989 in contemporary global reanalyses, Journal of Climate, 24, 4189–4209, 2011.

Bromwich, D. H., Nicolas, J. P., Hines, K. M., Kay, J. E., Key, E. L., Lazzara, M. A., Lubin, D., McFarquhar, G. M., Gorodetskaya, I. V., Grosvenor, D. P., Lachlan-Cope, T., and van Lipzig, N. P. M.: Tropospheric clouds in Antarctica, Reviews of Geophysics, 50, 2012.

Brown, I. C. and Scambos, T. A.: Satellite monitoring of blue-ice extent near Byrd Glacier, Antarctica, Annals of Glaciology, 39, 223–230, 2004.

Brun, E., Martin, E., Simon, V., Gendre, C., and Coleou, C.: An energy and mass model of snow cover suitable for operational avalanche forecasting, Journal of glaciology, 35, 333–342, 1989.

Brun, E., David, P., Sudul, M., and Brunot, G.: A numerical model to simulate snow-cover stratigraphy for operational avalanche forecasting, Journal of Glaciology, 38, 13–22, 1992.

Bréant, C., Leroy Dos Santos, C., Agosta, C., Casado, M., Fourré, E., Goursaud, S., Masson-Delmotte, V., Favier, V., Cattani, O., Prié, F., Golly, B., Orsi, A., Martinerie, P., and Landais, A.: Coastal water vapor isotopic composition driven by katabatic wind variability in summer at Dumont d'Urville, coastal East Antarctica, Earth and Planetary Science Letters, 514, 37 – 47, 2019.

Budd, W.: The drifting of non-uniform snow particles, Studies in Antarctic meteorology, 9, 59–70, 1966.

Carslaw, K. S., Wirth, M., Tsias, A., Luo, B., Dörnbrack, A., Leutbecher, M., Volkert, H., Renger, W., Bacmeister, J. T., Reimer, E., et al.: Increased stratospheric ozone depletion due to mountain-induced atmospheric waves, Nature, 391, 675–678, 1998.

Cavalieri, D. J. and Parkinson, C. L.: Arctic sea ice variability and trends, 1979-2010, The Cryosphere, 6, 881, 2012.

Christianson, K., Bushuk, M., Dutrieux, P., Parizek, B. R., Joughin, I. R., Alley, R. B., Shean, D. E., Abrahamsen, E. P., Anandakrishnan, S., Heywood, K. J., et al.: Sensitivity of Pine Island Glacier to observed ocean forcing, Geophysical Research Letters, 43, 10–817, 2016.

Clapp, R. B. and Hornberger, G. M.: Empirical equations for some soil hydraulic properties, Water resources research, 14, 601–604, 1978.

Clem, K. R., Renwick, J. A., McGregor, J., and Fogt, R. L.: The relative influence of ENSO and SAM on Antarctic Peninsula climate, Journal of Geophysical Research: Atmospheres, 121, 9324–9341, 2016.

Colbeck, S.: A theory of water percolation in snow, Journal of glaciology, 11, 369–385, 1972.

Comiso, J. C., Gersten, R. A., Stock, L. V., Turner, J., Perez, G. J., and Cho, K.: Positive trend in the Antarctic sea ice cover and associated changes in surface temperature, Journal of Climate, 30, 2251–2267, 2017.

Cook, A. J., Holland, P., Meredith, M., Murray, T., Luckman, A., and Vaughan, D. G.: Ocean forcing of glacier retreat in the western Antarctic Peninsula, Science, 353, 283–286, 2016.

Danabasoglu, G., Lamarque, J.-F., Bacmeister, J., Bailey, D., DuVivier, A., Edwards, J., Emmons, L., Fasullo, J., Garcia, R., Gettelman, A., Hannay, C., Holland, M., Large, W. G., Lauritzen, P. H., Lawrence, D. M., Lenaerts, J. T. M., Lindsay, K., Liscomb, W. H., Mills, M. J., Neale, R., Oleson, K. W., Otto-Bliesner, B., Philips, A. S., Sacks, W., Tilmes, S., van Kampenhout, L., Vertenstein, M., Bertini, A., Dennis, J., Deser, C., Fischer, C., Fox-Kemper, B., Kay, J E dand Kinnison, D., Kushner, P. J., Larson, V. E., Long, M. C., Mickelson, S., Moore, J. K., Nienhouse, E., Polvani, L., Rasch, J., and Strand, W. G.: The Community Earth System Model version 2 (CESM2), Journal of Advances in Modeling Earth Systems, 12, 2020.

Das, I., Bell, R. E., Scambos, T. A., Wolovick, M., Creyts, T. T., Studinger, M., Frearson, N., Nicolas, J. P., Lenaerts, J. T., and Van Den Broeke, M. R.: Influence of persistent wind scour on the surface mass balance of Antarctica, Nature Geoscience, 6, 367–371, 2013.

Datta, R. T., Tedesco, M., Fettweis, X., Agosta, C., Lhermitte, S., Lenaerts, J. T., and Wever, N.: The effect of Foehn-induced surface melt on firn evolution over

the northeast Antarctic peninsula, Geophysical Research Letters, 46, 3822–3831, 2019.

Davies, H.: A lateral boundary formulation for multi-level prediction models, Quarterly Journal of the Royal Meteorological Society, 102, 405–418, 1976.

Davies, H. C.: Limitations of some common lateral boundary schemes used in regional NWP models, Monthly Weather Review, 111, 1002–1012, 1983.

De Ridder, K.: Radiative transfer in the IAGL land surface model, Journal of Applied Meteorology, 36, 12–21, 1997.

De Ridder, K. and Gallée, H.: Land surface-induce regional climate change in Southern Israel, Journal of Applied Meteorology, 37, 1470–1485, 1998.

De Ridder, K. and Schayes, G.: The IAGL land surface model, Journal of applied meteorology, 36, 167–182, 1997.

DeConto, R. M. and Pollard, D.: Contribution of Antarctica to past and future sea-level rise, Nature, 531, 591–597, 2016.

Dee, D. P., Uppala, S. M., Simmons, a. J., Berrisford, P., Poli, P., Kobayashi, S., Andrae, U., Balmaseda, M. a., Balsamo, G., Bauer, P., Bechtold, P., Beljaars, a. C. M., van de Berg, L., Bidlot, J., Bormann, N., Delsol, C., Dragani, R., Fuentes, M., Geer, a. J., Haimberger, L., Healy, S. B., Hersbach, H., Hólm, E. V., Isaksen, L., Kållberg, P., Köhler, M., Matricardi, M., Mcnally, a. P., Monge-Sanz, B. M., Morcrette, J. J., Park, B. K., Peubey, C., de Rosnay, P., Tavolato, C., Thépaut, J. N., and Vitart, F.: The ERA-Interim reanalysis: Configuration and performance of the data assimilation system, Quarterly Journal of the Royal Meteorological Society, 137, 553–597, 2011.

Delhasse, A., Christoph, K., Amory, C., Hofer, S., and Fettweis, X.: Brief communication: Interest of a regional climate model against ERA5 to simulate the near-surface climate of the Greenland ice sheet, The Cryosphere Discussions, 2019.

Dell, R., Arnold, N., Willis, I., Banwell, A., Williamson, A., Pritchard, H., and Orr, A.: Lateral meltwater transfer across an Antarctic ice shelf, The Cryosphere, 14, 2313–2330, 2020.

Delobbe, L. and Gallée, H.: Simulation of marine stratocumulus: Effect of precipitation parameterization and sensitivity to droplet number concentration, Boundary-layer meteorology, 89, 75–107, 1998.

Dix, M., Vohralik, P., Bi, D., Rashid, H., Marsland, S., O'Farrell, S., Uotila, P., Hirst, T., Kowalczyk, E., Sullivan, A., Hailin, Y., Franklin, C., Sun, Z., Watterson, I., Collier, M., Noonan, J., Rotstayn, L., Steven, L., Uhe, P., and Puri, K.: The ACCESS coupled model: documentation of core CMIP5 simulations and initial results, Aust. Meteorol. Oceanogr. J, 63, 83–99, 2013.

Donat-Magnin, M., Jourdain, N. C., C., K., Agosta, C., Amory, C., Gallée, H., Krinner, G., and Chekki, M.: Future ice-sheet surface mass balance and melting in the Amundsen region, West Antarctica, The Cryosphere Discussions, 2020, 1–30, 2020a.

Donat-Magnin, M., Jourdain, N. C., Gallée, H., Amory, C., Kittel, C., Fettweis, X., Wille, J. D., Favier, V., Drira, A., and Agosta, C.: Interannual variability of summer surface mass balance and surface melting in the Amundsen sector, West Antarctica, The Cryosphere, 14, 229–249, 2020b.

Donlon, C. J., Martin, M., Stark, J., Roberts-Jones, J., Fiedler, E., and Wimmer, W.: The operational sea surface temperature and sea ice analysis (OSTIA) system, Remote Sensing of Environment, 116, 140–158, 2012.

Doutreloup, S., Christoph, K., Wyard, C., Belleflamme, A., Amory, C., Erpicum, M., and Fettweis, X.: Precipitation evolution over Belgium by 2100 and sensitivity to convective schemes using the regional climate model MAR, Atmosphere, 10, 321, 2019a.

Doutreloup, S., Wyard, C., Amory, C., Christoph, K., Erpicum, M., and Fettweis, X.: Sensitivity to convective schemes on precipitation simulated by the regional climate model MAR over Belgium (1987–2017), Atmosphere, 10, 34, 2019b.

Dufour, A., Charrondière, C., and Zolina, O.: Moisture transport in observations and reanalyses as a proxy for snow accumulation in East Antarctica., The Cryosphere, 13, 2019.

Dupont, T. and Alley, R. B.: Assessment of the importance of ice-shelf buttressing to ice-sheet flow, Geophysical Research Letters, 32, 2005.

Duynkerke, P.: Application of the E–ε turbulence closure model to the neutral and stable atmospheric boundary layer, Journal of the atmospheric sciences, 45, 865–880, 1988.

Duynkerke, P. and Driedonks, A.: A Model for the Turbulent Structure of the Stratocumulus–Topped Atmospheric Boundary Layer, Journal of the atmospheric sciences, 44, 43–64, 1987.

Duynkerke, P. G.: Radiation fog: A comparison of model simulation with detailed observations, Monthly Weather Review, 119, 324–341, 1991.

Duynkerke, P. G. and Van den Broeke, M. R.: Surface energy balance and katabatic flow over glacier and tundra during GIMEX-91, Global and Planetary Change, 9, 17–28, 1994.

Edwards, T. L., Brandon, M. A., Durand, G., Edwards, N. R., Golledge, N. R., Holden, P. B., Nias, I. J., Payne, A. J., Ritz, C., and Wernecke, A.: Revisiting Antarctic ice loss due to marine ice-cliff instability, Nature, 566, 58–64, 2019.

Eisen, O., Frezzotti, M., Genthon, C., Isaksson, E., Magand, O., van den Broeke, M. R., Dixon, D. A., Ekaykin, A., Holmlund, P., Kameda, T., Karlöf, L., Kaspari, S., Lipenkov, V. Y., Oerter, H., Takahashi, S., and Vaughan, D. G.: Ground-based measurements of spatial and temporal variability of snow accumulation in East Antarctica, Reviews of Geophysics, 46, 2008.

Ekaykin, A. A., Lipenkov, V. Y., Kuzmina, I. N., Petit, J. R., Masson-Delmotte, V., and Johnsen, S. J.: The changes in isotope composition and accumulation of snow at Vostok station, East Antarctica, over the past 200 years, Annals of Glaciology, 39, 569–575, 2004.

Emde, K. D. and Kahlig, P.: Comparison of the observed 19th July 1981, Montana thunderstorm with results of a one-dimensional cloud model using Kessler parameterized microphysics, in: Annales geophysicae. Atmospheres, hydrospheres and space sciences, vol. 7, pp. 405–414, 1989.

Eyring, V., Bony, S., Meehl, G. A., Senior, C. A., Stevens, B., Stouffer, R. J., and Taylor, K. E.: Overview of the Coupled Model Intercomparison Project Phase 6 (CMIP6) experimental design and organization, Geoscientific Model Development, 9, 1937–1958, 2016.

Fan, T., Deser, C., and Schneider, D. P.: Recent Antarctic sea ice trends in the context of Southern Ocean surface climate variations since 1950, Geophysical Research Letters, 41, 2419–2426, 2014.

Favier, V., Agosta, C., Genthon, C., Arnaud, L., Trouvillez, A., and Gallée, H.: Modeling the mass and surface heat budgets in a coastal blue ice area of Adelie Land, Antarctica, Journal of Geophysical Research: Earth Surface, 116, 2011.

Favier, V., Agosta, C., Parouty, S., Durand, G., Delaygue, G., Gallée, H., Drouet, A.-S., Trouvilliez, A., and Krinner, G.: An updated and quality controlled surface mass balance dataset for Antarctica, The Cryosphere, 7, 583–597, 2013.

Favier, V., Krinner, G., Amory, C., Gallée, H., Beaumet, J., and Agosta, C.: Antarctica-regional climate and surface mass budget, Current Climate Change Reports, 3, 303–315, 2017.

Fettweis, X., Franco, B., Tedesco, M., Van Angelen, J., Lenaerts, J. T., van den Broeke, M. R., and Gallée, H.: Estimating the Greenland ice sheet surface mass balance contribution to future sea level rise using the regional atmospheric climate model MAR, The Cryosphere, 7, 469–489, 2013.

Fettweis, X., Box, J., Agosta, C., Amory, C., Kittel, C., Lang, C., van As, D., Machguth, H., and Gallée, H.: Reconstructions of the 1900–2015 Greenland ice sheet surface mass balance using the regional climate MAR model, The Cryosphere, 11, 1015–1033, 2017.

Fettweis, X., Hofer, S., Krebs-Kanzow, U., Amory, C., Aoki, T., Berends, C. J., Born, A., Box, J. E., Delhasse, A., Fujita, K., Gierz, P., Goelzer, H., Hanna, E., Hashimoto, A., Huybrechts, P., Kapsch, M.-L., King, M. D., Kittel, C., Lang, C., Langen, P. L., Lenaerts, J. T. M., Liston, G. E., Lohmann, G., Mernild, S. H., Mikolajewicz, U., Modali, K., Mottram, R. H., Niwano, M., Noël, B., Ryan, J. C., Smith, A., Streffing, J., Tedesco, M., van de Berg, W. J., van den Broeke, M., van de Wal, R. S. W., van Kampenhout, L., Wilton, D., Wouters, B., Ziemen, F., and Zolles, T.: GrSMBMIP: intercomparison of the modelled 1980–2012 surface mass balance over the Greenland Ice Sheet, The Cryosphere, 14, 3935–3958, 2020.

Fiorino, M.: A multi-decadal daily sea surface temperature and sea ice concentration data set for the ERA-40 reanalysis, Tech. Rep. Project Report Series No. 12, 1–22, Department of Computer Science, Michigan State University, ECMWF, Reading, UK, 2004.

Fletcher, N. H.: The physics of rainclouds, Cambridge University Press, 1962.

Fogt, R. L. and Marshall, G. J.: The Southern Annular Mode: variability, trends, and climate impacts across the Southern Hemisphere, Wiley Interdisciplinary Reviews: Climate Change, pp. 1–24, 2020.

Fogt, R. L., Bromwich, D. H., and Hines, K. M.: Understanding the SAM influence on the South Pacific ENSO teleconnection, Climate Dynamics, 36, 1555–1576, 2011.

Fortuin, J. P. and Langematz, U.: Update on the global ozone climatology and on concurrent ozone and temperature trends, in: Atmospheric Sensing and Modelling, vol. 2311, pp. 207–216, International Society for Optics and Photonics, 1995.

Fouquart, Y. and Bonnel, B.: Computations of solar heating of the earth's atmosphere: A new parameterization, Beitr. Phys. Atmos., 53, 35–62, 1980.

Franco, B., Fettweis, X., Lang, C., and Erpicum, M.: Impact of spatial resolution on the modelling of the Greenland ice sheet surface mass balance between 1990–2010, using the regional climate model MAR, The Cryosphere, 6, 695–711, 2012.

Franco, B., Fettweis, X., and Erpicum, M.: Future projections of the Greenland ice sheet energy balance driving the surface melt, The Cryosphere, 7, 1–18, 2013.

Fretwell, P., Pritchard, H. D., Vaughan, D. G., Bamber, J. L., Barrand, N. E., Bell, R., Bianchi, C., Bingham, R. G., Blankenship, D. D., Casassa, G., Catania, G., Callens, D., Conway, H., Cook, A. J., Corr, H. F. J., Damaske, D., Damm, V., Ferraccioli, F., Forsberg, R., Fujita, S., Gim, Y., Gogineni, P., Griggs, J. A., Hindmarsh, R. C. A., Holmlund, P., Holt, J. W., Jacobel, R. W., Jenkins, A., Jokat, W., Jordan, T., King, E. C., Kohler, J., Krabill, W., Riger-Kusk, M., Langley, K. A., Leitchenkov, G., Leuschen, C., Luyendyk, B. P., Matsuoka, K., Mouginot, J., Nitsche, F. O., Nogi, Y., Nost, O. A., Popov, S. V., Rignot, E., Rippin, D. M., Rivera, A., Roberts, J., Ross, N., Siegert, M. J., Smith, A. M., Steinhage, D., Studinger, M., Sun, B., Tinto, B. K., Welch, B. C., Wilson, D., Young, D. A., Xiangbin, C., and Zirizzotti, A.: Bedmap2: improved ice bed, surface and thickness datasets for Antarctica, The Cryosphere, 7, 375–393, 2013.

Fréville, H., Brun, E., Picard, G., Tatarinova, N., Arnaud, L., Lanconelli, C., Reijmer, C., and Van den Broeke, M.: Using MODIS land surface temperatures

and the Crocus snow model to understand the warm bias of ERA-Interim reanalyses at the surface in Antarctica, The Cryosphere, 8, 1361–1373, 2014.

Frezzotti, M., Pourchet, M., Flora, O., Gandolfi, S., Gay, M., Urbini, S., Vincent, C., Becagli, S., Gragnani, R., Proposito, M., et al.: Spatial and temporal variability of snow accumulation in East Antarctica from traverse data, Journal of Glaciology, 51, 113–124, 2005.

Frezzotti, M., Scarchilli, C., Becagli, S., Proposito, M., and Urbini, S.: A synthesis of the Antarctic surface mass balance during the last 800 yr, The Cryosphere, 2013.

Frieler, K., Clark, P. U., He, F., Buizert, C., Reese, R., Ligtenberg, S. R., Van Den Broeke, M. R., Winkelmann, R., and Levermann, A.: Consistent evidence of increasing Antarctic accumulation with warming, Nature Climate Change, 5, 348–352, 2015.

Fu, Q.: An accurate parameterization of the solar radiative properties of cirrus clouds for climate models, Journal of Climate, 9, 2058–2082, 1996.

Fu, Q., Yang, P., and Sun, W.: An accurate parameterization of the infrared radiative properties of cirrus clouds for climate models, Journal of climate, 11, 2223–2237, 1998.

Fürst, J. J., Durand, G., Gillet-Chaulet, F., Tavard, L., Rankl, M., Braun, M., and Gagliardini, O.: The safety band of Antarctic ice shelves, Nature Climate Change, 6, 479–482, 2016.

Fyke, J., Lenaerts, J., and Wang, H.: Basin-scale heterogeneity in Antarctic precipitation and its impact on surface mass variability, The Cryosphere, 11, 2017.

Fyke, J., Sergienko, O., Löfverström, M., Price, S., and Lenaerts, J. T.: An overview of interactions and feedbacks between ice sheets and the Earth system, Reviews of Geophysics, 56, 361–408, 2018.

Gallée, H.: Simulation of the mesocyclonic activity in the Ross Sea, Antarctica, Monthly Weather Review, 123, 2051–2069, 1995.

Gallée, H.: Mesoscale atmospheric circulations over the southwestern Ross Sea sector, Antarctica, Journal of Applied Meteorology, 35, 1129–1141, 1996.

Gallée, H.: The blowing snow scheme of MAR.4, 05-05 February 2020, Third MAR workshop, LSCE-IPSL, Paris-Saclay, 2020.

Gallée, H. and Duynkerke, P. G.: Air-snow interactions and the surface energy and mass balance over the melting zone of west Greenland during the Greenland Ice Margin Experiment, Journal of Geophysical Research: Atmospheres, 102, 13 813–13 824, 1997.

Gallée, H. and Gorodetskaya, I. V.: Validation of a limited area model over Dome C, Antarctic Plateau, during winter, Climate dynamics, 34, 61, 2010.

Gallée, H. and Pettré, P.: Dynamical constraints on katabatic wind cessation in Adélie Land, Antarctica, Journal of the atmospheric sciences, 55, 1755–1770, 1998.

Gallée, H. and Schayes, G.: Development of a three-dimensional meso-γ primitive equation model: katabatic winds simulation in the area of Terra Nova Bay, Antarctica, Monthly Weather Review, 122, 671–685, 1994.

Gallée, H., Fontaine de Ghélin, O., and van den Broeke, M. R.: Simulation of atmospheric circulation during the GIMEX 91 experiment using a meso-γ primitive equations model, Journal of climate, 8, 2843–2859, 1995.

Gallée, H., Pettré, P., and Schayes, G.: Sudden cessation of katabatic winds in Adélie Land, Antarctica, Journal of Applied Meteorology and Climatology, 35, 1142–1152, 1996.

Gallée, H., Guyomarc'h, G., and Brun, E.: Impact of snow drift on the antarctic ice sheet surface mass balance: Possible sensitivity to snow-surface properties, Boundary-Layer Meteorology, 99, 1–19, 2001.

Gallée, H., Peyaud, V., and Goodwin, I.: Simulation of the net snow accumulation along the Wilkes Land transect, Antarctica, with a regional climate model, Annals of glaciology, 41, 17–22, 2005.

Gallée, H., Trouvilliez, A., Agosta, C., Genthon, C., Favier, V., and Naaim-Bouvet, F.: Transport of snow by the wind: A comparison between observations in Adélie Land, Antarctica, and simulations made with the regional climate model MAR, Boundary-layer meteorology, 146, 133–147, 2013.

Garbe, J., ALbrecht, T., Donges, J. F., and Winkelmann, R.: The hysteresis of the Antarctic Ice Sheet, Nature, 585, 538–544, 2020.

Gardner, A. S., Moholdt, G., Scambos, T., Fahnstock, M., Ligtenberg, S., Van Den Broeke, M., and Nilsson, J.: Increased West Antarctic and unchanged East Antarctic ice discharge over the last 7 years, The Cryosphere, 12, 521–547, 2018.

Garratt, J. R.: The atmospheric boundary layer, Cambridge atmospheric and space science series, Cambridge University Press, Cambridge, England, 1992.

Gelaro, R., McCarty, W., Suárez, M. J., Todling, R., Molod, A., Takacs, L., Randles, C. A., Darmenov, A., Bosilovich, M. G., Reichle, R., Wargan, K., Coy, L., Cullather, R., Draper, C., Akella, S., Buchard, V., Conaty, A., da Silva, A. M., Gu, W., Kim, G.-K., Koster, R., Lucchesi, R., Merkova, D., Nielsen, J. E., Partyka, G., Pawson, S., Putman, W., Rienecker, M., Schubert, S. D., Sienkiewicz, M., and Zhao, B.: The Modern-Era Retrospective Analysis for Research and Applications, Version 2 (MERRA-2), Journal of Climate, 30, 5419 – 5454, 2017.

Genthon, C., Lardeux, P., and Krinner, G.: The surface accumulation and ablation of a coastal blue-ice area near Cap Prudhomme, Terre Adélie, Antarctica, Journal of Glaciology, 53, 635–645, 2007.

Genthon, C., Krinner, G., and Castebrunet, H.: Antarctic precipitation and climate-change predictions: horizontal resolution and margin vs plateau issues, Annals of Glaciology, 50, 55–60, 2009.

Genthon, C., Six, D., Gallée, H., Grigioni, P., and Pellegrini, A.: Two years of atmospheric boundary layer observations on a 45-m tower at Dome C on the Antarctic plateau, Journal of Geophysical Research: Atmospheres, 118, 3218–3232, 2013.

Gilbert, E. and Kittel, C.: Surface melt and runoff on Antarctic ice shelves at 1.5°C, 2°C and 4°C of future warming, Geophysical Research Letters, 2020, in review.

Gilbert, E., Orr, A., King, J. C., Renfrew, I., Lachlan-Cope, T., Field, P., and Boutle, I.: Summertime cloud phase strongly influences surface melting on the Larsen C ice shelf, Antarctica, Quarterly Journal of the Royal Meteorological Society, 146, 1575–1589, 2020.

Gillett, N. P. and Thompson, D. W.: Simulation of recent Southern Hemisphere climate change, Science, 302, 273–275, 2003.

Glasser, N. and Scambos, T. A.: A structural glaciological analysis of the 2002 Larsen B ice-shelf collapse, Journal of Glaciology, 54, 3–16, 2008.

Glasser, N., Scambos, T., Bohlander, J., Truffer, M., Pettit, E., and Davies, B.: From ice-shelf tributary to tidewater glacier: continued rapid recession, acceleration and thinning of Röhss Glacier following the 1995 collapse of the Prince Gustav Ice Shelf, Antarctic Peninsula, Journal of Glaciology, 57, 397–406, 2011.

Golledge, N. R., Kowalewski, D. E., Naish, T. R., Levy, R. H., Fogwill, C. J., and Gasson, E. G.: The multi-millennial Antarctic commitment to future sea-level rise, Nature, 526, 421–425, 2015.

Gorodetskaya, I., Kneifel, S., Maahn, M., Van Tricht, K., Thiery, W., Schween, J., Mangold, A., Crewell, S., and Van Lipzig, N.: Cloud and precipitation properties from ground-based remote-sensing instruments in East Antarctica, The Cryosphere, 9, 285–304, 2015.

Gorte, T., Lenaerts, J., and Medley, B.: Scoring Antarctic surface mass balance in climate models to refine future projections, The Cryosphere, 14, 4719–4733, 2020.

Gossart, A., Souverijns, N., Gorodetskaya, I. V., Lhermitte, S., Lenaerts, J., Schween, J. H., and van Lipzig, N. P.: An new algorithm to detect blowing snow from ground-based remote sensing ceilometer observations in Dronning Maud Land, East Antarctica., in: EGU General Assembly Conference Abstracts, p. 13922, 2017.

Gossart, A., Helsen, S., Lenaerts, J., Broucke, S. V., van Lipzig, N., and Souverijns, N.: An evaluation of surface climatology in state-of-the-art reanalyses over the Antarctic Ice Sheet, Journal of Climate, 32, 6899–6915, 2019.

Grazioli, J., Madeleine, J.-B., Gallée, H., Forbes, R. M., Genthon, C., Krinner, G., and Berne, A.: Katabatic winds diminish precipitation contribution to the Antarctic ice mass balance, Proceedings of the National Academy of Sciences, 114, 10 858–10 863, 2017.

Greuell, W. and Konzelmann, T.: Numerical modelling of the energy balance and the englacial temperature of the Greenland Ice Sheet. Calculations for the ETH-Camp location (West Greenland, 1155 m asl), Global and Planetary change, 9, 91–114, 1994.

Gudmundsson, G. H.: Ice-shelf buttressing and the stability of marine ice sheets, The Cryosphere, 7, 647–655, 2013.

Haarsma, R. J., Roberts, M. J., Vidale, P. L., Senior, C. A., Bellucci, A., Bao, Q., Chang, P., Corti, S., Fučkar, N. S., Guemas, V., von Hardenberg, J., Hazeleger, W., Kodama, C., Koenigk, T., Leung, L. R., Lu, J., Luo, J.-J., Mao, J., Mizielinski, M. S., Mizuta, R., Nobre, P., Satoh, M., Scoccimarro, E., Semmler, T., Small, J., and von Storch, J.-S.: High Resolution Model Intercomparison Project (HighResMIP v1.0) for CMIP6, Geoscientific Model Development, 9, 4185–4208, 2016.

Hersbach, H., Bell, B., Berrisford, P., Hirahara, S., Horányi, A., Muñoz-Sabater, J., Nicolas, J., Peubey, C., Radu, R., Schepers, D., Simmons, A., Soci, C., Abdalla, S., Abellan, X., Balsamo, G., Bechtold, P., Biavati, G., Bidlot, J., Bonavita, M., De Chiara, G., Dahlgren, P., Dee, D., Diamantakis, M., Dragani, R., Flemming, J., Forbes, R., FUentes, M., Geer, A., Haimberger, L., Healy, S., Hogan, R. J., Hólm, E., Janisková, M., Keeley, S., Laloyaux, P., Lopez, P., Lupu, C., Radnoti, G., De Rosnay, P., Rorum, I., Vamborg, F., Vollaume, S., and Thépaut, J.-N.: The ERA5 global reanalysis, Quarterly Journal of the Royal Meteorological Society, 2020.

Hillebrand, F. L., Bremer, U. F., Arigony-Neto, J., da Rosa, C. N., Mendes Jr, C. W., Costi, J., de Freitas, M. W. D., and Schardong, F.: Comparison between Atmospheric Reanalysis Models ERA5 and ERA-Interim at the North Antarctic Peninsula Region, Annals of the American Association of Geographers, pp. 1–13, 2020.

Hillel, D.: The state of water in the soil, In Soil and Water. Physical principles and processes, 63, 1971.

Hines, K. M., Bromwich, D. H., Wang, S.-H., Silber, I., Verlinde, J., and Lubin, D.: Microphysics of summer clouds in central West Antarctica simulated by the Polar Weather Research and Forecasting Model (WRF) and the Antarctic Mesoscale Prediction System (AMPS)., Atmospheric Chemistry & Physics, 19, 2019.

Hoegh-Guldberg, O., Jacob, D., Taylor, M., Bindi, M., Brown, S., Camilloni, I., Diedhiou, A., DJalante, R., Ebi, K., Engelbrecht, F., Guiot, J., Hijioka, Y., Mehrotra, S., Payne, A., Seneviratne, S. I., Thomas, A., Warren, R., and Zhou, G.: Impacts of 1.5°C Global Warming on Natural and Human Systems, in:

Global Warming of 1.5°C. An IPCC Special Report on the impacts of global warming of 1.5°C above pre-industrial levels and related global greenhouse gas emission pathways, in the context of strengthening the global response to the threat of climate change, sustainable development, and efforts to eradicate poverty, edited by Masson-Delmotte, V., Zhai, P., Pörtner, H.-O., Roberts, D., Skea, J., Shukla, P., Pirani, A., Moufouma-Okia, W., Péan, C., Pidcock, R., Connors, S., Mattheaws, J., Chen, Y., Shou, X., M.I., G., Lonnoy, E., Maycock, T., Tignor, M., and Waterfield, T., 2018.

Hofer, S., Tedstone, A. J., Fettweis, X., and Bamber, J. L.: Decreasing cloud cover drives the recent mass loss on the Greenland Ice Sheet, Science Advances, 3, e1700 584, 2017.

Hofer, S., Tedstone, A. J., Fettweis, X., and Bamber, J. L.: Cloud microphysics and circulation anomalies control differences in future Greenland melt, Nature Climate Change, 9, 523–528, 2019.

Hofer, S., Lang, C., Amory, C., Kittel, C., Delhasse, A., Tedstone, A., and Fettweis, X.: Greater Greenland Ice Sheet contribution to global sea level rise in CMIP6, Nature communications, 11, 1–11, 2020.

Hofer, S., Amory, C., Kittel, C., Carlsen, C., Letoumelin, L., and Storelvmo, T.: The contribution of blowing snow to cloud properties and the atmospheric radiative budget over Antarctica, in preparation.

Holland, P. R.: The seasonality of Antarctic sea ice trends, Geophysical Research Letters, 41, 4230–4237, 2014.

Holland, P. R. and Kwok, R.: Wind-driven trends in Antarctic sea-ice drift, Nature Geoscience, 5, 872–875, 2012.

Hosking, J. S., Orr, A., Bracegirdle, T. J., and Turner, J.: Future circulation changes off West Antarctica: Sensitivity of the Amundsen Sea Low to projected anthropogenic forcing, Geophysical Research Letters, 43, 367–376, 2016.

Huai, B., Wang, Y., Ding, M., Zhang, J., and Dong, X.: An assessment of recent global atmospheric reanalyses for Antarctic near surface air temperature, Atmospheric Research, 226, 181–191, 2019.

Hubbard, B., Luckman, A., Ashmore, D. W., Bevan, S., Kulessa, B., Munneke, P. K., Philippe, M., Jansen, D., Booth, A., Sevestre, H., Rison, J.-L., O'Leary,

M., and Rutt, I.: Massive subsurface ice formed by refreezing of ice-shelf melt ponds, Nature communications, 7, 1–6, 2016.

Hui, F., Ci, T., Cheng, X., Scambo, T. A., Liu, Y., Zhang, Y., Chi, Z., Huang, H., Wang, X., Wang, F., Zhao, C., Jin, Z., and Wang, K.: Mapping blue-ice areas in Antarctica using ETM and MODIS data, Annals of Glaciology, 55, 129–137, 2014.

Huot, P.-V., Kittel, C., Fichefet, T., Jourdain, N. C., Sterlin, J., and Fettweis, X.: Effect of atmospheric forcing resolution on sea ice and polynyas off Adelie Land, in preparation.

Inoue, J., Sato, K., Rinke, A., Cassano, J. J., Fettweis, X., Heinemann, G., Matthes, H., Orr, A., Phillips, T., Seefeldt, M., Solomon, A., and Webster, S.: Clouds and Radiation Processes in Regional Climate Models Evaluated Using Observations Over the Ice-free Arctic Ocean, Journal of Geophysical Research: Atmospheres, 126, 1–25, 2021.

IPCC: Summary for policymakers, in: Global Warming of 1.5°C. An IPCC Special Report on the impacts of global warming of 1.5°C above pre-industrial levels and related global greenhouse gas emission pathways, in the context of strengthening the global response to the threat of climate change, sustainable development, and efforts to eradicate poverty, edited by Masson-Delmotte, V., Zhai, P., Pörtner, H.-O., Roberts, D., Skea, J., Shukla, P., Pirani, A., Moufouma-Okia, W., Péan, C., Pidcock, R., Connors, S., Mattheaws, J., Chen, Y., Shou, X., M.I., G., Lonnoy, E., Maycock, T., Tignor, M., and Waterfield, T., pp. 1–32, 2018.

Iversen, T., Bentsen, M., Bethke, I., Debernard, J., Kirkevåg, A., Seland, Ø., Drange, H., Kristjansson, J., Medhaug, I., Sand, M., et al.: The Norwegian earth system model, NorESM1-M-part 2: Climate response and scenario projections, Geoscientific Model Development, 6, 389, 2013.

Jakobs, C. L., Reijmer, C. H., Smeets, C. P., Trusel, L. D., Van De Berg, W. J., Van Den Broeke, M. R., and Van Wessem, J. M.: A benchmark dataset of in situ Antarctic surface melt rates and energy balance, Journal of Glaciology, 66, 291–302, 2020.

Jenkins, A., Shoosmith, D., Dutrieux, P., Jacobs, S., Kim, T. W., Lee, S. H., Ha, H. K., and Stammerjohn, S.: West Antarctic Ice Sheet retreat in the Amundsen Sea driven by decadal oceanic variability, Nature Geoscience, 11, 733–738, 2018.

Jones, J. M., Gille, S. T., Goosse, H., Abram, N. J., Canziani, P. O., Charman, D. J., Clem, K. R., Crosta, X., de Lavergne, C., Eisenman, I., England, M. H., Fogt, R. L., Frankcombe, L. M., Marshall, G. J., Masson-Delmotte, V., Morrison, A. K., Orsi, A. J., Raphael, M. N., Renwick, J. A., Schneider, D. P., Simpkins, G. R., Steig, E. J., Stenni, B., Swingedouw, D., and Vance, T. R.: Assessing recent trends in high-latitude Southern Hemisphere surface climate, Nature Climate Change, 6, 917–926, 2016.

Joseph, J. H., Wiscombe, W., and Weinman, J.: The delta-Eddington approximation for radiative flux transfer, Journal of the Atmospheric Sciences, 33, 2452–2459, 1976.

Joughin, I., Smith, B. E., and Medley, B.: Marine ice sheet collapse potentially under way for the Thwaites Glacier Basin, West Antarctica, Science, 344, 735–738, 2014.

Jourdain, N. C. and Gallée, H.: Influence of the orographic roughness of glacier valleys across the Transantarctic Mountains in an atmospheric regional model, Climate dynamics, 36, 1067–1081, 2011.

Jourdain, N. C., Mathiot, P., Gallée, H., and Barnier, B.: Influence of coupling on atmosphere, sea ice and ocean regional models in the Ross Sea sector, Antarctica, Climate dynamics, 36, 1523–1543, 2011.

Jourdain, N. C., Asay-Davis, X., Hattermann, T., Straneo, F., Seroussi, H., Little, C. M., and Nowicki, S.: A protocol for calculating basal melt rates in the ISMIP6 Antarctic ice sheet projections, The Cryosphere, 14, 3111–3134, 2020.

Kain, J. S. and Fritsch, J. M.: A one-dimensional entraining/detraining plume model and its application in convective parameterization, Journal of the Atmospheric Sciences, 47, 2784–2802, 1990.

Kessler, E.: On the distribution and continuity of water substance in atmospheric circulations, in: On the distribution and continuity of water substance in atmospheric circulations, pp. 1–84, Springer, 1969.

Kim, B.-H., Seo, K.-W., Eom, J., Chen, J., and Wilson, C. R.: Antarctic ice mass variations from 1979 to 2017 driven by anomalous precipitation accumulation, Scientific reports, 10, 1–9, 2020.

King, J., Gadian, A., Kirchgaessner, A., Kuipers Munneke, P., Lachlan-Cope, T., Orr, A., Reijmer, C., van den Broeke, M., Van Wessem, J., and Weeks, M.: Validation of the summertime surface energy budget of Larsen C Ice Shelf (Antarctica) as represented in three high-resolution atmospheric models, Journal of Geophysical Research: Atmospheres, 120, 1335–1347, 2015.

King, J. C. and Turner, J.: Antarctic meteorology and climatology, Cambridge University Press, 1997.

Kingslake, J., Ely, J. C., Das, I., and Bell, R. E.: Widespread movement of meltwater onto and across Antarctic ice shelves, Nature, 544, 349–352, 2017.

Kittel, C., Amory, C., Agosta, C., Delhasse, A., Doutreloup, S., Huot, P.-V., Wyard, C., Fichefet, T., and Fettweis, X.: Sensitivity of the current Antarctic surface mass balance to sea surface conditions using MAR, The Cryosphere, 12, 3827–3839, 2018.

Kittel, C., Amory, C., Agosta, C., Jourdain, N. C., Hofer, S., Delhasse, A., Doutreloup, S., Huot, P.-V., Lang, C., Fichefet, T., and Fettweis, X.: Diverging future surface mass balance between the Antarctic ice shelves and grounded ice sheet, The Cryosphere Discussions, pp. 1–29, 2020.

Kobayashi, S., Ota, Y., Harada, Y., Ebita, A., Moriya, M., Onoda, H., Onogi, K., Kamahori, H., Kobayashi, C., Endo, H., Miyaoka, K., and Takahasi, K.: The JRA-55 reanalysis: General specifications and basic characteristics, Journal of the Meteorological Society of Japan. Ser. II, 93, 5–48, 2015.

Konrad, H., Gilbert, L., Cornford, S. L., Payne, A., Hogg, A., Muir, A., and Shepherd, A.: Uneven onset and pace of ice-dynamical imbalance in the Amundsen Sea Embayment, West Antarctica, Geophysical Research Letters, 44, 910–918, 2017.

Krinner, G. and Flanner, M. G.: Striking stationarity of large-scale climate model bias patterns under strong climate change, Proceedings of the National Academy of Sciences, 115, 9462–9466, 2018.

Krinner, G., Magand, O., Simmonds, I., Genthon, C., and Dufresne, J.-L.: Simulated Antarctic precipitation and surface mass balance at the end of the twentieth and twenty-first centuries, Climate Dynamics, 28, 215–230, 2007.

Krinner, G., Guicherd, B., Ox, K., Genthon, C., and Magand, O.: Influence of oceanic boundary conditions in simulations of Antarctic climate and surface mass balance change during the coming century, Journal of Climate, 21, 938–962, 2008.

Krinner, G., Largeron, C., Ménégoz, M., Agosta, C., and Brutel-Vuilmet, C.: Oceanic forcing of Antarctic climate change: A study using a stretched-grid atmospheric general circulation model, Journal of Climate, 27, 5786–5800, 2014.

Kuipers Munneke, P., Picard, G., Van den Broeke, M., Lenaerts, J., and Van Meijgaard, E.: Insignificant change in Antarctic snowmelt volume since 1979, Geophysical Research Letters, 39, 2012.

Kuipers Munneke, P., Ligtenberg, S. R. M., van den Broeke, M. R., and Vaughan, D. G.: Firn air depletion as a precursor of Antarctic ice-shelf collapse, Journal of Glaciology, 60, 205–214, 2014.

Kuipers Munneke, P., Luckman, A., Bevan, S., Smeets, C., Gilbert, E., Van den Broeke, M., Wang, W., Zender, C., Hubbard, B., Ashmore, D., Orr, A., King, J., and Kulessa, B.: Intense winter surface melt on an Antarctic ice shelf, Geophysical Research Letters, 45, 7615–7623, 2018.

Lac, C., Chaboureau, P., Masson, V., Pinty, P., Tulet, P., Escobar, J., Leriche, M., Barthe, C., Aouizerats, B., Augros, C., et al.: Overview of the Meso-NH model version 5.4 and its applications, Geoscientific Model Development, 11, 1929–1969, 2018.

Lachlan-Cope, T.: Antarctic clouds, Polar Research, 29, 150–158, 2010.

Lambert, M., Kittel, C., Damseaux, A., and Fettweis, X.: Sensitivity of arctic surface temperatures to sea ice thickness changes using the regional climate model mar, BSGLg, 2019.

Latif, M., Anderson, D., Barnett, T., Cane, M., Kleeman, R., Leetmaa, A., O'Brien, J., Rosati, A., and Schneider, E.: A review of the predictability and prediction of ENSO, Journal of Geophysical Research: Oceans, 103, 14 375–14 393, 1998.

Le clec'h, S., Charbit, S., Quiquet, A., Fettweis, X., Dumas, C., Kageyama, M., Wyard, C., and Ritz, C.: Assessment of the Greenland ice sheet–atmosphere feedbacks for the next century with a regional atmospheric model coupled to an ice sheet model, The Cryosphere, 13, 2019.

Le Toumelin, L., Amory, C., Favier, V., Kittel, C., Hofer, S., Fettweis, X., Gallée, H., and Kayetha, V.: Sensitivity of the surface energy budget to drifting snow as simulated by MAR in coastal Adelie Land, Antarctica, The Cryosphere Discussions, pp. 1–27, 2020.

Lefebre, F., Gallée, H., van Ypersele, J.-P., and Greuell, W.: Modeling of snow and ice melt at ETH Camp (West Greenland): A study of surface albedo, Journal of Geophysical Research: Atmospheres, 108, 2003.

Lenaerts, J. and Van den Broeke, M.: Modeling drifting snow in Antarctica with a regional climate model: 2. Results, Journal of Geophysical Research: Atmospheres, 117, 2012.

Lenaerts, J., Lhermitte, S., Drews, R., Ligtenberg, S., Berger, S., Helm, V., Smeets, C., Van Den Broeke, M., Van De Berg, W. J., Van Meijgaard, E., Eijkelboom, M., Eisen, O., and Pattyn, F.: Meltwater produced by wind–albedo interaction stored in an East Antarctic ice shelf, Nature climate change, 7, 58–62, 2017a.

Lenaerts, J. T., Van den Broeke, M., Déry, S., Van Meijgaard, E., Van de Berg, W., Palm, S. P., and Sanz Rodrigo, J.: Modeling drifting snow in Antarctica with a regional climate model: 1. Methods and model evaluation, Journal of Geophysical Research: Atmospheres, 117, 2012a.

Lenaerts, J. T., Van den Broeke, M., Van de Berg, W., Van Meijgaard, E., and Kuipers Munneke, P.: A new, high-resolution surface mass balance map of Antarctica (1979–2010) based on regional atmospheric climate modeling, Geophysical Research Letters, 39, 2012b.

Lenaerts, J. T., Van Den Broeke, M. R., Scarchilli, C., and Agosta, C.: Impact of model resolution on simulated wind, drifting snow and surface mass balance in Terre Adélie, East Antarctica, Journal of Glaciology, 58, 821–829, 2012c.

Lenaerts, J. T., Vizcaino, M., Fyke, J., Van Kampenhout, L., and van den Broeke, M. R.: Present-day and future Antarctic ice sheet climate and surface mass balance in the Community Earth System Model, Climate Dynamics, 47, 1367–1381, 2016.

Lenaerts, J. T., Van Tricht, K., Lhermitte, S., and L'Ecuyer, T. S.: Polar clouds and radiation in satellite observations, reanalyses, and climate models, Geophysical Research Letters, 44, 3355–3364, 2017b.

Lenaerts, J. T., Medley, B., van den Broeke, M. R., and Wouters, B.: Observing and modeling ice sheet surface mass balance, Reviews of Geophysics, 57, 376–420, 2019.

Levkov, L., Rockel, B., Kapitza, H., and Raschke, E.: 3D mesoscale numerical studies of cirrus and stratus clouds by their time and space evolution, Contributions to atmospheric physics, 65, 35–58, 1992.

Lhermitte, S., Sun, S., Shuman, C., Wouters, B., Pattyn, F., Wuite, J., Berthier, E., and Nagler, T.: Damage accelerates ice shelf instability and mass loss in Amundsen Sea Embayment, Proceedings of the National Academy of Sciences, 2020.

Li, L. and Pomeroy, J. W.: Estimates of threshold wind speeds for snow transport using meteorological data, Journal of Applied Meteorology, 36, 205–213, 1997.

Ligtenberg, S., Van de Berg, W., Van den Broeke, M., Rae, J., and Van Meijgaard, E.: Future surface mass balance of the Antarctic ice sheet and its influence on sea level change, simulated by a regional atmospheric climate model, Climate dynamics, 41, 867–884, 2013.

Ligtenberg, S., Kuipers Munneke, P., and Van den Broeke, M.: Present and future variations in Antarctic firn air content, The Cryosphere, 8, 1711–1723, 2014.

Lilien, D. A., Steinhage, D., Taylor, D., Parrenin, F., Ritz, C., Mulvaney, R., Martín, C., Yan, J.-B., O'Neill, C., Frezzotti, M., Miller, H., Gogineni, P., Dahl-Jensen, D., and Eisen, O.: Brief Communication: New radar constraints support presence of ice older than 1.5 Ma at Little Dome C, The Cryosphere Discussions, 2020, 1–12, 2020.

Lin, Y.-L., Farley, R. D., and Orville, H. D.: Bulk parameterization of the snow field in a cloud model, Journal of Applied Meteorology and climatology, 22, 1065–1092, 1983.

Lindner, T. and Li, J.: Parameterization of the optical properties for water clouds in the infrared, Journal of Climate, 13, 1797–1805, 2000.

Locatelli, J. D. and Hobbs, P. V.: Fall speeds and masses of solid precipitation particles, Journal of Geophysical Research, 79, 2185–2197, 1974.

Loth, B., Graf, H.-F., and Oberhuber, J. M.: Snow cover model for global climate simulations, Journal of Geophysical Research: Atmospheres, 98, 10 451–10 464, 1993.

Ludescher, J., Yuan, N., and Bunde, A.: Detecting the statistical significance of the trends in the Antarctic sea ice extent: an indication for a turning point, Climate dynamics, 53, 237–244, 2019.

Madec, G.: NEMO ocean engine. Note du Pôle de modélisation de l'Institut Pierre-Simon Laplace 27, 2016.

Mahesh, A., Eager, R., Campbell, J. R., and Spinhirne, J. D.: Observations of blowing snow at the South Pole, Journal of Geophysical Research: Atmospheres, 108, 2003.

Mahlstein, I., Gent, P. R., and Solomon, S.: Historical Antarctic mean sea ice area, sea ice trends, and winds in CMIP5 simulations, Journal of Geophysical Research: Atmospheres, 118, 5105–5110, 2013.

Mann, G., Anderson, P., and Mobbs, S.: Profile measurements of blowing snow at Halley, Antarctica, Journal of Geophysical Research: Atmospheres, 105, 24 491–24 508, 2000.

Marbaix, P., Gallée, H., Brasseur, O., and van Ypersele, J.-P.: Lateral boundary conditions in regional climate models: a detailed study of the relaxation procedure, Monthly weather review, 131, 461–479, 2003.

Marshall, G. J.: Half-century seasonal relationships between the Southern Annular Mode and Antarctic temperatures, International Journal of Climatology: A Journal of the Royal Meteorological Society, 27, 373–383, 2007.

Marshall, G. J. and Thompson, D. W.: The signatures of large-scale patterns of atmospheric variability in Antarctic surface temperatures, Journal of Geophysical Research: Atmospheres, 121, 3276–3289, 2016.

Marshall, G. J., Thompson, D. W., and van den Broeke, M. R.: The signature of Southern Hemisphere atmospheric circulation patterns in Antarctic precipitation, Geophysical Research Letters, 44, 11–580, 2017.

Martin, G., Johnson, D., and Spice, A.: The measurement and parameterization of effective radius of droplets in warm stratocumulus clouds, Journal of the Atmospheric Sciences, 51, 1823–1842, 1994.

Massager, C., Gallée, H., and Brasseur, O.: Precipitation sensitivity to regional SST in a regional climate simulation during the West African monsoon for two dry years, Climate Dynamics, 22, 249–266, 2004.

Massom, R., Harris, P., Michael, K. J., and Potter, M.: The distribution and formative processes of latent-heat polynyas in East Antarctica, Annals of Glaciology, 27, 420–426, 1998.

Massonnet, F., Mathiot, P., Fichefet, T., Goosse, H., Beatty, C. K., Vancoppenolle, M., and Lavergne, T.: A model reconstruction of the Antarctic sea ice thickness and volume changes over 1980–2008 using data assimilation, Ocean Modelling, 64, 67–75, 2013.

Mattingly, K. S., Mote, T. L., Fettweis, X., Van As, D., Van Tricht, K., Lhermitte, S., Pettersen, C., and Fausto, R. S.: Strong summer atmospheric rivers trigger Greenland Ice Sheet melt through spatially varying surface energy balance and cloud regimes, Journal of Climate, 33, 6809–6832, 2020.

Mauritsen, T., Bader, J., Becker, T., Behrens, J., Bittner, M., Brokopf, R., Brovkin, V., Claussen, M., Crueger, T., Esch, M., Fast, I., Fiedler, S., Fläschner, D., Gayler, V., Giorgetta, M., Goll, D. S., Haak, H., Hagemann, S., Hedemann, C., Hohenegger, C., Ilyina, T., Jahns, T., Jimenéz-de-la Cuesta, D., Jungclaus, J., Kleinen, T., Kloster, S., Kracher, D., Kinne, S., Kleberg, D., Lasslop, G., Kornblueh, L., Marotzke, J., Matei, D., Meraner, K., Mikolajewicz, U., Modali, K., Möbis, B., Müller, W. A., Nabel, J. E. M. S., Nam, C. C. W., Notz, D., Nyawira, S.-S., Paulsen, H., Peters, K., Pincus, R., Pohlmann, H., Pongratz, J., Popp, M., Raddatz, T. J., Rast, S., Redler, R., Reick, C. H., Rohrschneider, T., Schemann, V., Schmidt, H., Schnur, R., Schulzweida, U., Six, K. D., Stein, L., Stemmler, I., Stevens, B., von Storch, J.-S., Tian, F., Voigt, A., Vrese, P., Wieners, K.-H., Wilkenskjeld, S., Winkler, A., and Roeckner, E.: Developments in the MPI-M Earth System Model version 1.2 (MPI-ESM1. 2) and its response to increasing CO2, Journal of Advances in Modeling Earth Systems, 11, 998–1038, 2019.

Medley, B. and Thomas, E.: Increased snowfall over the Antarctic Ice Sheet mitigated twentieth-century sea-level rise, Nature Climate Change, 9, 34–39, 2019.

Medley, B., Joughin, I., Smith, B., Das, S. B., Steig, E. J., Conway, H., Gogineni, S., Lewis, C., Criscitiello, A. S., McConnell, J. R., et al.: Constraining the

recent mass balance of Pine Island and Thwaites glaciers, West Antarctica, with airborne observations of snow accumulation, The Cryosphere, 8, 1375–1392, 2014.

Medley, B., McConnell, J. R., Neumann, T., Reijmer, C., Chellman, N., Sigl, M., and Kipfstuhl, S.: Temperature and snowfall in western Queen Maud Land increasing faster than climate model projections, Geophysical Research Letters, 45, 1472–1480, 2018.

Meehl, G. A., Arblaster, J. M., Chung, C. T., Holland, M. M., DuVivier, A., Thompson, L., Yang, D., and Bitz, C. M.: Sustained ocean changes contributed to sudden Antarctic sea ice retreat in late 2016, Nature communications, 10, 1–9, 2019.

Meehl, G. A., Senior, C. A., Eyring, V., Flato, G., Lamarque, J.-F., Stouffer, R. J., Taylor, K. E., and Schlund, M.: Context for interpreting equilibrium climate sensitivity and transient climate response from the CMIP6 Earth system models, Science Advances, 6, 1–10, 2020.

Meredith, M., Sommerkorn, M., Cassotta, S., Derksen, C., Ekaykin, A., Hollowed, A., Kofinas, G., Mackintosh, A., Melbourne-Thomas, J., Muelbert, M., Ottersen, G., Pritchard, H., and Schuur, E.: Polar Regions, in: IPCC Special Report on the Ocean and Cryosphere in a Changing Climate, edited by Portner, H.-O., Roberts, D., Masson-Delmotte, V., Zhai, P., Tignor, M., Poloczanska, E., Mintenbeck, K., Alegria, A., Nicolai, M., Okem, A., Petzold, J., Rama, B., and Weyer, N., pp. 571–657, 2019.

Meyers, M. P., DeMott, P. J., and Cotton, W. R.: New primary ice-nucleation parameterizations in an explicit cloud model, Journal of Applied Meteorology, 31, 708–721, 1992.

Mlawer, E. J., Taubman, S. J., Brown, P. D., Iacono, M. J., and Clough, S. A.: Radiative transfer for inhomogeneous atmospheres: RRTM, a validated correlated-k model for the longwave, Journal of Geophysical Research: Atmospheres, 102, 16 663–16 682, 1997.

Monaghan, A. J., Bromwich, D. H., Fogt, R. L., Wang, S.-H., Mayewski, P. A., Dixon, D. A., Ekaykin, A., Frezzotti, M., Goodwin, I., Isaksson, E., Kaspari, S. D., M. V. I., H, O., Van Ommen, T. D., Van der Veen, C., and Wen, J.: Insignificant change in Antarctic snowfall since the International Geophysical Year, Science, 313, 827–831, 2006.

Monaghan, A. J., Bromwich, D. H., and Schneider, D. P.: Twentieth century Antarctic air temperature and snowfall simulations by IPCC climate models, Geophysical Research Letters, 35, 2008.

Morales Maqueda, M., Willmott, A., and Biggs, N.: Polynya dynamics: A review of observations and modeling, Reviews of Geophysics, 42, 2004.

Morcrette, J.: Revision of the clear-sky and cloud radiative properties in the ECMWF model, ECMWF newsletter, 61, 3–14, 1993.

Morcrette, J., Barker, H. W., Cole, J., Iacono, M. J., and Pincus, R.: Impact of a new radiation package, McRad, in the ECMWF Integrated Forecasting System, Monthly weather review, 136, 4773–4798, 2008.

Morcrette, J.-J.: The Surface Downward Longwave Radiation in the ECMWF Forecast System, Journal of Climate, 15, 1875–1892, 2002.

Morcrette, J.-J.: Ozone-radiation interactions in the ECMWF forecast system, Tech. Rep. Technical Memorandum No 375, European Centre for Medium-Range Weather Forecasts, 2003.

Morcrette, J.-J. and Fouquart, Y.: The overlapping of cloud layers in shortwave radiation parameterizations, Journal of the atmospheric sciences, 43, 321–328, 1986.

Morcrette, J.-J., Clough, S. A., Mlawer, E. J., and Iacono, M. J.: Impact of a validated ratiative transfer scheme, RRTM, on the ECWF moel climate and 10-day forecasts, Tech. Rep. Technical Memorandum No 252, European Centre for Medium-Range Weather Forecasts, 2003.

Morlighem, M., Rignot, E., Binder, T., Blankenship, D., Drews, R., Eagles, G., Eisen, O., Ferraccioli, F., Forsberg, R., Fretwell, P., et al.: Deep glacial troughs and stabilizing ridges unveiled beneath the margins of the Antarctic ice sheet, Nature Geoscience, 13, 132–137, 2020.

Morrison, H. and Pinto, J.: Mesoscale modeling of springtime Arctic mixed-phase stratiform clouds using a new two-moment bulk microphysics scheme, Journal of the atmospheric sciences, 62, 3683–3704, 2005.

Morrison, H., Curry, J., and Khvorostyanov, V.: A new double-moment microphysics parameterization for application in cloud and climate models. Part I: Description, Journal of the atmospheric sciences, 62, 1665–1677, 2005.

Moss, R. H., Edmonds, J. A., Hibbard, K. A., Manning, M. R., Rose, S. K., Van Vuuren, D. P., Carter, T. R., Emori, S., Kainuma, M., Kram, T., Meehl, G. A., Mitchell, J. F. B., Nakicenovic, N., Riahi, K., SMith, S. J., Stouffer, R. J., Thompson, A. M., Weynant, J., and J., W. T.: The next generation of scenarios for climate change research and assessment, Nature, 463, 747–756, 2010.

Mottram, R., Hansen, N., Kittel, C., Wessem, M. v., Agosta, C., Amory, C., Boberg, F., Berg, W. J. v. d., Fettweis, X., Gossart, A., et al.: What is the Surface Mass Balance of Antarctica? An Intercomparison of Regional Climate Model Estimates, The Cryosphere Discussions, pp. 1–42, 2020.

Mouginot, J., Rignot, E., and Scheuchl, B.: Sustained increase in ice discharge from the Amundsen Sea Embayment, West Antarctica, from 1973 to 2013, Geophysical Research Letters, 41, 1576–1584, 2014.

Moussavi, M., Pope, A., Halberstadt, A. R. W., Trusel, L. D., Cioffi, L., and Abdalati, W.: Antarctic supraglacial lake detection using Landsat 8 and Sentinel-2 imagery: Towards continental generation of lake volumes, Remote Sensing, 12, 134, 2020.

Naithani, J., Gallée, H., and Schayes, G.: Marine air intrusion into the Adelie Land sector of East Antarctica: A study using the regional climate model (MAR), Journal of Geophysical Research: Atmospheres, 107, ACL–6, 2002.

Navarre, J.: Modele unidimensionnel d'evolution de la neige deposee, Météorologie, 4, 103–120, 1975.

Nicolas, J. P., Vogelmann, A. M., Scott, R. C., Wilson, A. B., Cadeddu, M. P., Bromwich, D. H., Verlinde, J., Lubin, D., Russell, L. M., Jenkinson, C., Powers, H. H., Ryczek, M., Stone, G., and Wille, J. D.: January 2016 extensive summer melt in West Antarctica favoured by strong El Niño, Nature Communications, 8, 15 799, 2017.

Noel, B., Fettweis, X., Van de Berg, W., Van den Broeke, M., and Erpicum, M.: Sensitivity of Greenland Ice Sheet surface mass balance to perturbations in sea surface temperature and sea ice cover: a study with the regional climate model MAR, The Cryosphere, 8, 1871–1883, 2014.

Noone, D. and Simmonds, I.: Sea ice control of water isotope transport to Antarctica and implications for ice core interpretation, Journal of Geophysical Research: Atmospheres, 109, 2004.

Nowicki, S., Goelzer, H., Seroussi, H., Payne, A. J., Lipscomb, W. H., Abe-Ouchi, A., Agosta, C., Alexander, P., Asay-Davis, X. S., Barthel, A., Bracegirdle, T. J., Cullather, R., Felikson, D., Fettweis, X., Gregory, J. M., Hattermann, T., Jourdain, N. C., Kuipers Munneke, P., Larour, E., Little, C. M., Morlighem, M., Nias, I., Shepherd, A., Simon, E., Slater, D., Smith, R. S., Straneo, F., Trusel, L. D., van den Broeke, M. R., and van de Wal, R.: Experimental protocol for sea level projections from ISMIP6 stand-alone ice sheet models, The Cryosphere, 14, 2331–2368, 2020.

Nowicki, S. M., Payne, T., Larour, E., Seroussi, H., Goelzer, H., Lipscomb, W., Gregory, J., Abe-Ouchi, A., and Shepherd, A.: Ice sheet model intercomparison project (ISMIP6) contribution to CMIP6, Geoscientific model development, 9, 4521, 2016.

O'Neill, B. C., Tebaldi, C., van Vuuren, D., Eyring, V., Friedlingstein, P., Hurtt, G., Knutti, R., Kriegler, E., Lamarque, J.-F., Lowe, J., et al.: The Scenario Model Intercomparison Project (ScenarioMIP) for CMIP6, Geoscientific Model Development, 9, 3461–3482, 2016.

Oppenheimer, M., Glavovic, B., Hinkel, J., van de Wal, R., Magnan, A., Abd-Elgawad, A., Cai, R., Cifuentes-Jara, M., DeConto, R., Ghosh, T., Hay, J., Isla, F., Marzeion, B., Meyssignac, B., and Z., S.: Sea Level Rise and Implications for Low-Lying Islands, Coasts and Communities, in: IPCC Special Report on the Ocean and Cryosphere in a Changing Climate, edited by Portner, H.-O., Roberts, D., Masson-Delmotte, V., Zhai, P., Tignor, M., Poloczanska, E., Mintenbeck, K., Alegria, A., Nicolai, M., Okem, A., Petzold, J., Rama, B., and Weyer, N., 2019.

Palerme, C., Genthon, C., Claud, C., Kay, J. E., Wood, N. B., and L'Ecuyer, T.: Evaluation of current and projected Antarctic precipitation in CMIP5 models, Climate dynamics, 48, 225–239, 2017.

Palm, S. P., Yang, Y., Spinhirne, J. D., and Marshak, A.: Satellite remote sensing of blowing snow properties over Antarctica, Journal of Geophysical Research: Atmospheres, 116, 2011.

Palm, S. P., Kayetha, V., Yang, Y., and Pauly, R.: Blowing snow sublimation and transport over Antarctica from 11 years of CALIPSO observations, The Cryosphere, 11, 2555–2569, 2017.

Palm, S. P., Kayetha, V., and Yang, Y.: Toward a Satellite-Derived Climatology of Blowing Snow Over Antarctica, Journal of Geophysical Research: Atmospheres, 123, 10–301, 2018.

Paolo, F., Padman, L., Fricker, H., Adusumilli, S., Howard, S., and Siegfried, M.: Response of Pacific-sector Antarctic ice shelves to the El Niño/Southern oscillation, Nature geoscience, 11, 121–126, 2018.

Paolo, F. S., Fricker, H. A., and Padman, L.: Volume loss from Antarctic ice shelves is accelerating, Science, 348, 327–331, 2015.

Parish, T. R. and Bromwich, D. H.: Continental-scale simulation of the Antarctic katabatic wind regime, Journal of Climate, 4, 135–146, 1991.

Parish, T. R. and Bromwich, D. H.: Reexamination of the near-surface airflow over the Antarctic continent and implications on atmospheric circulations at high southern latitudes, Monthly Weather Review, 135, 1961–1973, 2007.

Parish, T. R. and Wendler, G.: The katabatic wind regime at Adélie Land, Antarctica, International journal of climatology, 11, 97–107, 1991.

Parkinson, C. L. and Cavalieri, D. J.: Antarctic sea ice variability and trends, 1979–2010, The Cryosphere, 6, 871–880, 2012.

Pattyn, F. and Decleir, H.: Satellite monitoring of ice and snow conditions in the Sør Rondane Mountains, Antarctica, Annals of Glaciology, 17, 41–48, 1993.

Pattyn, F. and Morlighem, M.: The uncertain future of the Antarctic Ice Sheet, Science, 367, 1331–1335, 2020.

Pattyn, F., Matsuoka, K., and Berte, J.: Glacio-meteorological conditions in the vicinity of the Belgian Princess Elisabeth Station, Antarctica, Antarctic science, 22, 79, 2009.

Pattyn, F., Ritz, C., Hanna, E., Asay-Davis, X., DeConto, R., Durand, G., Favier, L., Fettweis, X., Goelzer, H., Golledge, N. R., Kuipers Munneke, P., Lenaerts, J. T. M., Nowicki, S., Payne, A. J., Robinson, A., Seroussi, H., Trusel, L. D., and van den Broeke, M.: The Greenland and Antarctic ice sheets under 1.5 C global warming, Nature Climate Change, 8, 1053–1061, 2018.

Pavolonis, M. J. and Key, J. R.: Antarctic cloud radiative forcing at the surface estimated from the AVHRR Polar Pathfinder and ISCCP D1 datasets, 1985–93, Journal of Applied Meteorology, 42, 827–840, 2003.

Peter, D. and Brower, K. R.: The melting of floating ice raises the ocean level, Geophysical Journal International, 170, 145–150, 2007.

Picard, G. and Fily, M.: Surface melting observations in Antarctica by microwave radiometers: Correcting 26-year time series from changes in acquisition hours, Remote sensing of environment, 104, 325–336, 2006.

Picard, G., Fily, M., and Gallée, H.: Surface melting derived from microwave radiometers: a climatic indicator in Antarctica, Annals of Glaciology, 46, 29–34, 2007.

Pielke, R.: Mesoscale meterorological modelling, Academic press, 1984.

Polvani, L. M., Waugh, D. W., Correa, G. J., and Son, S.-W.: Stratospheric ozone depletion: The main driver of twentieth-century atmospheric circulation changes in the Southern Hemisphere, Journal of Climate, 24, 795–812, 2011.

Pomeroy, J.: A process-based model of snow drifting, Annals of Glaciology, 13, 237–240, 1989.

Prenni, A. J., Harrington, J. Y., Tjernström, M., DeMott, P. J., Avramov, A., Long, C. N., Kreidenweis, S. M., Olsson, P. Q., and Verlinde, J.: Can ice-nucleating aerosols affect Arctic seasonal climate?, Bulletin of the American Meteorological Society, 88, 541–550, 2007.

Previdi, M. and Polvani, L. M.: Anthropogenic impact on Antarctic surface mass balance, currently masked by natural variability, to emerge by mid-century, Environmental Research Letters, 11, 094 001, 2016.

Raphael, M. N., Marshall, G., Turner, J., Fogt, R., Schneider, D., Dixon, D., Hosking, J., Jones, J., and Hobbs, W. R.: The Amundsen sea low: variability, change, and impact on Antarctic climate, Bulletin of the American Meteorological Society, 97, 111–121, 2016.

Raymond, W. H. and Garder, A.: A spatial filter for use in finite area calculations, Monthly weather review, 116, 209–222, 1988.

Rignot, E., Casassa, G., Gogineni, P., Krabill, W., Rivera, A., and Thomas, R.: Accelerated ice discharge from the Antarctic Peninsula following the collapse of Larsen B ice shelf, Geophysical research letters, 31, 2004.

Rignot, E., Mouginot, J., Scheuchl, B., van den Broeke, M., van Wessem, M. J., and Morlighem, M.: Four decades of Antarctic Ice Sheet mass balance from 1979–2017, Proceedings of the National Academy of Sciences, 116, 1095–1103, 2019.

Rintoul, S. R.: On the origin and influence of Adélie Land Bottom Water, Ocean, ice, and atmosphere: Interactions at the Antarctic continental margin, 75, 151–171, 1985.

Rintoul, S. R., Silvano, A., Pena-Molino, B., van Wijk, E., Rosenberg, M., Greenbaum, J. S., and Blankenship, D. D.: Ocean heat drives rapid basal melt of the Totten Ice Shelf, Science Advances, 2, e1601 610, 2016.

Ritz, C., Edwards, T. L., Durand, G., Payne, A. J., Peyaud, V., and Hindmarsh, R. C.: Potential sea-level rise from Antarctic ice-sheet instability constrained by observations, Nature, 528, 115–118, 2015.

Roach, L. A., Dean, S. M., and Renwick, J. A.: Consistent biases in Antarctic sea ice concentration simulated by climate models., The Cryosphere, 12, 2018.

Rott, H., Skvarca, P., and Nagler, T.: Rapid collapse of northern Larsen ice shelf, Antarctica, Science, 271, 788–792, 1996.

Rousset, C., Vancoppenolle, M., Madec, G., Fichefet, T., Flavoni, S., Barthélemy, A., Benshila, R., Chanut, J., Lévy, C., Masson, S., et al.: The Louvain-La-Neuve sea ice model LIM3. 6: global and regional capabilities, Geoscientific Model Development, 8, 2991–3005, 2015.

Sato, T., Kosugi, K., Mochizuki, S., and Nemoto, M.: Wind speed dependences of fracture and accumulation of snowflakes on snow surface, Cold Regions Science and Technology, 51, 229–239, 2008.

Scambos, T., Hulbe, C., and Fahnestock, M.: Climate-induced ice shelf disintegration in the Antarctic Peninsula, Antarctic Peninsula Climate Variability: Historical and Paleoenvironmental Perspectives, Antarct. Res. Ser, 79, 79–92, 2003.

Scambos, T., Fricker, H. A., Liu, C.-C., Bohlander, J., Fastook, J., Sargent, A., Massom, R., and Wu, A.-M.: Ice shelf disintegration by plate bending and hydro-fracture: Satellite observations and model results of the 2008 Wilkins ice shelf break-ups, Earth and Planetary Science Letters, 280, 51–60, 2009.

Scambos, T., Frezzotti, M., Haran, T., Bohlander, J., Lenaerts, J., Van Den Broeke, M., Jezek, K., Long, D., Urbini, S., Farness, K., Neumann, T., Albert, M., and Winther, J.-G.: Extent of low-accumulation 'wind glaze' areas on the East Antarctic plateau: implications for continental ice mass balance, 58, 633–647, 2012.

Scambos, T. A., Hulbe, C., Fahnestock, M., and Bohlander, J.: The link between climate warming and break-up of ice shelves in the Antarctic Peninsula, Journal of Glaciology, 46, 516–530, 2000.

Scambos, T. A., Bohlander, J., Shuman, C. A., and Skvarca, P.: Glacier acceleration and thinning after ice shelf collapse in the Larsen B embayment, Antarctica, Geophysical Research Letters, 31, 2004.

Scambos, T. A., Berthier, E., Haran, T., Shuman, C. A., Cook, A. J., Ligtenberg, S. R. M., and Bohlander, J.: Detailed ice loss pattern in the northern Antarctic Peninsula: widespread decline driven by ice front retreats, The Cryosphere, 8, 2135–2145, 2014.

Scarchilli, C., Frezzotti, M., Grigioni, P., De Silvestri, L., Agnoletto, L., and Dolci, S.: Extraordinary blowing snow transport events in East Antarctica, Climate Dynamics, 34, 1195–1206, 2010.

Schlosser, E., Manning, K. W., Powers, J. G., Duda, M. G., Birnbaum, G., and Fujita, K.: Characteristics of high-precipitation events in Dronning Maud Land, Antarctica, Journal of Geophysical Research: Atmospheres, 115, 2010.

Schmidt, G. A., Kelley, M., Nazarenko, L., Ruedy, R., Russell, G. L., Aleinov, I., Bauer, M., Bauer, S. E., Bhat, M. K., Bleck, R., Canuto, V., Chen, Y.-H., Cheng, Y., Clune, T. L., Del Genio, A., Fainchtein, R., Faluvegi, G., Hansen, J. E., Healy, R., Kiang, N. Y., Koch, D., Lacis, A. A., Legrand, A. N., Lerner, J., Lo, K. K., Mathhews, E. E., Menon, S., Miller, R. L., Oinas, V., Oloso, A. O., Perlwitz, J. P., Puma, M. J., Putman, W. M., Rind, R., Romanou, A., Sato, M., Shindel, D. T., Sun, S., Syed, R. A., Tausnev, N., Tsigaridis, K., Unger, N., Voulgarakis, A., Yao, M.-S., and Zhang, J.: Configuration and assessment

of the GISS ModelE2 contributions to the CMIP5 archive, Journal of Advances in Modeling Earth Systems, 6, 141–184, 2014.

Schmidt, R.: Vertical profiles of wind speed, snow concentration, and humidity in blowing snow, Boundary-Layer Meteorology, 23, 223–246, 1982.

Schmidtko, S., Heywood, K. J., Thompson, A. F., and Aoki, S.: Multidecadal warming of Antarctic waters, Science, 346, 1227–1231, 2014.

Schneider, D. P., Deser, C., and Fan, T.: Comparing the impacts of tropical SST variability and polar stratospheric ozone loss on the Southern Ocean westerly winds, Journal of Climate, 28, 9350–9372, 2015.

Schoof, C.: Ice sheet grounding line dynamics: Steady states, stability, and hysteresis, Journal of Geophysical Research: Earth Surface, 112, 2007.

Scott, R. C., Nicolas, J. P., Bromwich, D. H., Norris, J. R., and Lubin, D.: Meteorological drivers and large-scale climate forcing of West Antarctic surface melt, Journal of Climate, 32, 665–684, 2019.

Segal, M., Garratt, J., Pielke, R., and Ye, Z.: Scaling and numerical model evaluation of snow-cover effects on the generation and modification of daytime mesoscale circulations, Journal of the atmospheric sciences, 48, 1024–1042, 1991.

Seibert, P. and Morariu, B.: Improvements of upstream, semi-Lagrangian numerical advection schemes, Journal of Applied Meteorology, 30, 117–125, 1991.

Sellar, A. A., Jones, C. G., Mulcahy, J. P., Tang, Y., Yool, A., Wiltshire, A., O'Connor, F. M., Stringer, M., Hill, R., Palmieri, J., Woodward, S., de Mora, L., Kuhlbrodt, T., Rumbold, S. T., Kelley, D. I., Ellis, R., Johnson, C. E., Walton, J., Abraham, N. L., Andrews, M. B., Andrews, T., Archibald, A. T., Berthou, S., Burke, E., Blockley, E., Carslaw, K., Dalvi, M., Edwards, J., Folberth, G. A., Gedney, N., Griffiths, P. T., Harper, A. B., Hendry, M. A., Hewitt, A. J., Johnson, B., Jones, A., Jones, C. D., Keeble, J., Liddicoat, S., Morgenstern, O., Parker, R. J., Predoi, V., Robertson, E., Siahaan, A., Smith, R. S., Swaminathan, R., Woodhouse, M. T., Zeng, G., and Zerroukat, M.: UKESM1: Description and Evaluation of the U.K. Earth System Model, Journal of Advances in Modeling Earth Systems, 11, 4513–4558, 2019.

Seo, K.-W., Wilson, C. R., Scambos, T., Kim, B.-M., Waliser, D. E., Tian, B., Kim, B.-H., and Eom, J.: Surface mass balance contributions to acceleration

of Antarctic ice mass loss during 2003–2013, Journal of Geophysical Research: Solid Earth, 120, 3617–3627, 2015.

Seroussi, H., Nakayama, Y., Larour, E., Menemenlis, D., Morlighem, M., Rignot, E., and Khazendar, A.: Continued retreat of Thwaites Glacier, West Antarctica, controlled by bed topography and ocean circulation, Geophysical Research Letters, 44, 6191–6199, 2017.

Seroussi, H., Nowicki, S., Payne, A. J., Goelzer, H., Lipscomb, W. H., Abe Ouchi, A., Agosta, C., Albrecht, T., Asay-Davis, X., Barthel, A., et al.: ISMIP6 Antarctica: a multi-model ensemble of the Antarctic ice sheet evolution over the 21st century, The Cryosphere Discussions, 2020.

Shepherd, A., Ivins, E. R., Geruo, A., Barletta, V. R., Bentley, M. J., Bettadpur, S., Briggs, K. H., Bromwich, D. H., Forsberg, R., Galin, N., et al.: A reconciled estimate of ice-sheet mass balance, Science, 338, 1183–1189, 2012.

Shepherd, A., Ivins, E., Rignot, E., Smith, B., van den Broeke, M., Velicogna, I., Whitehouse, P., Briggs, K., Joughin, I., Krinner, G., Nowicki, S., Payne, T., Scambos, T., Schlegel, N., A, G., Agosta, C., Ahlstrøm, A., Babonis, G., Barletta, V., Blazquez, A., Bonin, J., Csatho, B., Cullather, R., Felikson, D., Fettweis, X., Forsberg, R., Gallee, H., Gardner, A., Gilbert, L., Groh, A., Gunter, B., Hanna, E., Harig, C., Helm, V., Horvath, A., Horwath, M., Khan, S., Kjeldsen, K. K., Konrad, H., Langen, P., Lecavalier, B., Loomis, B., Luthcke, S., McMillan, M., Melini, D., Mernild, S., Mohajerani, Y., Moore, P., Mouginot, J., Moyano, G., Muir, A., Nagler, T., Nield, G., Nilsson, J., Noel, B., Otosaka, I., Pattle, M. E., Peltier, W. R., Pie, N., Rietbroek, R., Rott, H., Sandberg-Sørensen, L., Sasgen, I., Save, H., Scheuchl, B., Schrama, E., Schröder, L., Seo, K.-W., Simonsen, S., Slater, T., Spada, G., Sutterley, T., Talpe, M., Tarasov, L., van de Berg, W. J., van der Wal, W., van Wessem, M., Vishwakarma, B. D., Wiese, D., Wouters, B., and team, T. I.: Mass balance of the Antarctic Ice Sheet from 1992 to 2017, Nature, 558, 219–222, 2018.

Shu, Q., Song, Z., and Qiao, F.: Assessment of sea ice simulations in the CMIP5 models., The Cryosphere, 9, 2015.

Simmonds, I. and Budd, W.: Sensitivity of the Southern Hemisphere circulation to leads in the Antarctic pack ice, Quarterly Journal of the Royal Meteorological Society, 117, 1003–1024, 1991.

Simmonds, I. and Jacka, T.: Relationships between the interannual variability of Antarctic sea ice and the Southern Oscillation, Journal of Climate, 8, 637–647, 1995.

Simmonds, I. and Wu, X.: Cyclone behaviour response to changes in winter Southern Hemisphere sea-ice concentration, Quarterly Journal of the Royal Meteorological Society, 119, 1121–1148, 1993.

Slater, T., Hogg, A. E., and Mottram, R.: Ice-sheet losses track high-end sea-level rise projections, Nature Climate Change, 10, 879–881, 2020.

Slater, T., Lawrence, I. R., Otosaka, I. N., Shepherd, A., Gourmelen, N., Jakob, L., Tepes, P., Gilbert, L., and Nienow, P.: Earth's ice imbalance, The Cryosphere, 15, 233–246, 2021.

Slingo, A.: A GCM parameterization for the shortwave radiative properties of water clouds, Journal of the Atmospheric Sciences, 46, 1419–1427, 1989.

Smith, S. D., Muench, R. D., and Pease, C. H.: Polynyas and leads: An overview of physical processes and environment, Journal of Geophysical Research: Oceans, 95, 9461–9479, 1990.

Sodemann, H. and Stohl, A.: Asymmetries in the moisture origin of Antarctic precipitation, Geophysical research letters, 36, 2009.

Souverijns, N., Gossart, A., Gorodetskaya, I. V., Lhermitte, S., Mangold, A., Laffineur, Q., Delcloo, A., and Van Lipzig, N. P.: How does the ice sheet surface mass balance relate to snowfall? Insights from a ground-based precipitation radar in East Antarctica, The Cryosphere, 12, 1987–2003, 2018.

Souverijns, N., Gossart, A., Demuzere, M., Lenaerts, J., Medley, B., Gorodetskaya, I., Vanden Broucke, S., and van Lipzig, N.: A New Regional Climate Model for POLAR-CORDEX: Evaluation of a 30-Year Hindcast with COSMO-CLM2 Over Antarctica, Journal of Geophysical Research: Atmospheres, 124, 1405–1427, 2019.

Spaulding, N. E., Spikes, V. B., Hamilton, G. S., Mayewski, P. A., Dunbar, N. W., Harvey, R. P., Schutt, J., and Kurbatov, A. V.: Ice motion and mass balance at the Allan Hills blue-ice area, Antarctica, with implications for paleoclimate reconstructions, Journal of Glaciology, 58, 399–406, 2012.

Spence, P., Griffies, S. M., England, M. H., Hogg, A. M., Saenko, O. A., and Jourdain, N. C.: Rapid subsurface warming and circulation changes of Antarctic coastal waters by poleward shifting winds, Geophysical Research Letters, 41, 4601–4610, 2014.

Spence, P., Holmes, R. M., Hogg, A. M., Griffies, S. M., Stewart, K. D., and England, M. H.: Localized rapid warming of West Antarctic subsurface waters by remote winds, Nature Climate Change, 7, 595–603, 2017.

Stark, J. D., Donlon, C. J., Martin, M. J., and McCulloch, M. E.: OSTIA: An operational, high resolution, real time, global sea surface temperature analysis system, in: Oceans 2007-Europe, pp. 1–4, IEEE, 2007.

Stephens, G. L.: The parameterization of radiation for numerical weather prediction and climate models, Monthly Weather Review, 112, 826–867, 1984.

Sun, S., Cornford, S. L., Gwyther, D. E., Gladstone, R. M., Galton-Fenzi, B. K., Zhao, L., and Moore, J. C.: Impact of ocean forcing on the Aurora Basin in the 21st and 22nd centuries, Annals of Glaciology, 57, 79–86, 2016.

Sun, Z. and Rikus, L.: Parametrization of effective sizes of cirrus-cloud particles and its verification against observations, Quarterly Journal of the Royal Meteorological Society, 125, 3037–3055, 1999.

Sundqvist, H.: Parameterization of condensation and associated clouds in models for weather prediction and general circulation simulation, in: Physically-based modelling and simulation of climate and climatic change, pp. 433–461, Springer, 1988.

Taylor, K. E., Stouffer, R. J., and Meehl, G. A.: An overview of CMIP5 and the experiment design, Bulletin of the American Meteorological Society, 93, 485–498, 2012.

Tedesco, M., Doherty, S., Fettweis, X., Alexander, P., Jeyaratnam, J., and Stroeve, J.: The darkening of the Greenland ice sheet: trends, drivers, and projections (1981–2100), The Cryosphere, 10, 477–496, 2016.

Tegen, I., Hollrig, P., Chin, M., Fung, I., Jacob, D., and Penner, J.: Contribution of different aerosol species to the global aerosol extinction optical thickness: Estimates from model results, Journal of Geophysical Research: Atmospheres, 102, 23 895–23 915, 1997.

Termonia, P., Van Schaeybroeck, B., De Cruz, L., De Troch, R., Caluwaerts, S., Giot, O., Hamdi, R., Vannitsem, S., Duchêne, F., Willems, P., Tabari, H., Van Uyten, E., Hosseinzadehtalaei, P., Van Lipzig, N., Wouters, H., Vanden Broucke, S., van Ypersele, J.-P., Marbaix, P., Villanueva-Birriel, C., Fettweis, X., Wyard, C., Scholzen, C., Doutreloup, S., De Ridder, K., Gobin, A., Lauwaet, D., Stavrakou, T., Bauwen, M., Müller, J.-F., Luyten, P., Ponsar, S., Van den Eynde, D., and Pottiaux, E.: The CORDEX. be initiative as a foundation for climate services in Belgium, Climate Services, 11, 49–61, 2018.

Thiery, W., Gorodetskaya, I., Bintanja, R., Van Lipzig, N., Van den Broeke, M., Reijmer, C., and Kuipers Munneke, P.: Surface and snowdrift sublimation at Princess Elisabeth station, East Antarctica, The Cryosphere, 6, 841–857, 2012.

Thomas, E. R., van Wessem, J. M., Roberts, J., Isaksson, E., Schlosser, E., Fudge, T. J., Vallelonga, P., Medley, B., Lenaerts, J., Bertler, N., van den Broeke, M. R., Dixon, D. A., Frezzotti, M., Stenni, B., Curran, M., and Ekaykin, A. A.: Regional Antarctic snow accumulation over the past 1000 years, Climate of the Past, 13, 1491–1513, 2017.

Thompson, D. W. and Wallace, J. M.: Annular modes in the extratropical circulation. Part I: Month-to-month variability, Journal of climate, 13, 1000–1016, 2000.

Traversi, R., Becagli, S., Castellano, E., Cerri, O., Morganti, A., Severi, M., and Udisti, R.: Study of Dome C site (East Antartica) variability by comparing chemical stratigraphies, Microchemical Journal, 92, 7–14, 2009.

Trusel, L., Frey, K. E., and Das, S. B.: Antarctic surface melting dynamics: Enhanced perspectives from radar scatterometer data, Journal of Geophysical Research: Earth Surface, 117, 2012.

Trusel, L. D., Frey, K. E., Das, S. B., Munneke, P. K., and Van Den Broeke, M. R.: Satellite-based estimates of Antarctic surface meltwater fluxes, Geophysical Research Letters, 40, 6148–6153, 2013.

Trusel, L. D., Frey, K. E., Das, S. B., Karnauskas, K. B., Munneke, P. K., Van Meijgaard, E., and Van Den Broeke, M. R.: Divergent trajectories of Antarctic surface melt under two twenty-first-century climate scenarios, Nature Geoscience, 8, 927–932, 2015.

Tuckett, P. A., Ely, J. C., Sole, A. J., Livingstone, S. J., Davison, B. J., van Wessem, J. M., and Howard, J.: Rapid accelerations of Antarctic Peninsula outlet glaciers driven by surface melt, Nature communications, 10, 1–8, 2019.

Turner, J.: The el nino–southern oscillation and antarctica, International Journal of Climatology: A Journal of the Royal Meteorological Society, 24, 1–31, 2004.

Turner, J., Colwell, S. R., Marshall, G. J., Lachlan-Cope, T. A., Carleton, A. M., Jones, P. D., Lagun, V., Reid, P. A., and Iagovkina, S.: The SCAR READER project: Toward a high-quality database of mean Antarctic meteorological observations, Journal of Climate, 17, 2890–2898, 2004.

Turner, J., Bracegirdle, T. J., Phillips, T., Marshall, G. J., and Hosking, J. S.: An initial assessment of Antarctic sea ice extent in the CMIP5 models, Journal of Climate, 26, 1473–1484, 2013a.

Turner, J., Phillips, T., Hosking, J. S., Marshall, G. J., and Orr, A.: The amundsen sea low, International Journal of Climatology, 33, 1818–1829, 2013b.

Turner, J., Hosking, J. S., Marshall, G. J., Phillips, T., and Bracegirdle, T. J.: Antarctic sea ice increase consistent with intrinsic variability of the Amundsen Sea Low, Climate Dynamics, 46, 2391–2402, 2016.

Turner, J., Phillips, T., Thamban, M., Rahaman, W., Marshall, G. J., Wille, J. D., Favier, V., Winton, V. H. L., Thomas, E., Wang, Z., van den Broeke, M., Hosking, J. S., and Lachlan-Cope, T.: The Dominant Role of Extreme Precipitation Events in Antarctic Snowfall Variability, Geophysical Research Letters, 46, 3502–3511, 2019.

Uppala, S. M., Kållberg, P., Simmons, A., Andrae, U., Bechtold, V. D. C., Fiorino, M., Gibson, J., Haseler, J., Hernandez, A., Kelly, G., Li, X., Onogo, K., Saarinen, S., Sokka, N., Allan, R. P., Andersson, E., Arpe, K., Balmaseda, M. A., Beljaars, A. C. M., Berg, L. V. D., Bidlot, J., Bormann, N., Caires, S., Chevallier, F., Dethof, A., Dragosavac, M., Fisher, M., Fuentes, M., Hagemann, S., Hólm, E., Hoskins, B. J., Isaksen, L., Janssen, P. A., Jenne, R., Mcnally, A. P., Mahfouf, J. F., Morcrette, J.-J., Rayner, N. A., Saunders, R. W., Simon, P., Sterl, A., Trenberth, K. E., Untch, A., Vasiljevic, D., Viterbo, P., and Woolen, J.: The ERA-40 re-analysis, Quarterly Journal of the Royal Meteorological Society: A journal of the atmospheric sciences, applied meteorology and physical oceanography, 131, 2961–3012, 2005.

van Dalum, C. T., van de Berg, W. J., and van den Broeke, M. R.: Impact of updated radiative transfer scheme in RACMO2. 3p3 on the surface mass and energy budget of the Greenland ice sheet, The Cryosphere Discussions, pp. 1–30, 2020.

Van de Berg, W., Van den Broeke, M., Reijmer, C., and Van Meijgaard, E.: Reassessment of the Antarctic surface mass balance using calibrated output of a regional atmospheric climate model, Journal of Geophysical Research: Atmospheres, 111, 2006.

van de Berg, W. J. and Medley, B.: Brief Communication: Upper-air relaxation in RACMO2 significantly improves modelled interannual surface mass balance variability in Antarctica, The Cryosphere, 10, 459–463, 2016.

van den Broeke, M.: Strong surface melting preceded collapse of Antarctic Peninsula ice shelf, Geophysical Research Letters, 32, 2005.

van den Broeke, M., van As, D., Reijmer, C., and van de Wal, R.: Assessing and improving the quality of unattended radiation observations in Antarctica, Journal of Atmospheric and Oceanic Technology, 21, 1417–1431, 2004.

Van Den Broeke, M., Reijmer, C., Van As, D., and Boot, W.: Daily cycle of the surface energy balance in Antarctica and the influence of clouds, International Journal of Climatology: A Journal of the Royal Meteorological Society, 26, 1587–1605, 2006.

van den Broeke, M. R., van de Wal, R. S., and Wild, M.: Representation of Antarctic katabatic winds in a high-resolution GCM and a note on their climate sensitivity, Journal of Climate, 10, 3111–3130, 1997.

van Lipzig, N. P., van Meijgaard, E., and Oerlemans, J.: Temperature sensitivity of the Antarctic surface mass balance in a regional atmospheric climate model, Journal of climate, 15, 2758–2774, 2002.

Van Wessem, J., Reijmer, C., Lenaerts, J., Van de Berg, W., Van den Broeke, M., and Van Meijgaard, E.: Updated cloud physics in a regional atmospheric climate model improves the modelled surface energy balance of Antarctica, The Cryosphere, 8, 125–135, 2014a.

Van Wessem, J., Reijmer, C., Morlighem, M., Mouginot, J., Rignot, E., Medley, B., Joughin, I., Wouters, B., Depoorter, M., Bamber, J., Leneaerts, J., Van de Berg,

W., and van den Broeke, M.: Improved representation of East Antarctic surface mass balance in a regional atmospheric climate model, Journal of Glaciology, 60, 761–770, 2014b.

Van Wessem, J. M., Jan Van De Berg, W., Noël, B. P., Van Meijgaard, E., Amory, C., Birnbaum, G., Jakobs, C. L., Krüger, K., Lenaerts, J., Lhermitte, S., Ligtenberg, S. R. M., Medley, B., Reijmer, C. H., van Tricht, K., Trusel, L. D., van Ulft, L. H., Wouter, B., Wuite, J., and van den Broeke, M. R.: Modelling the climate and surface mass balance of polar ice sheets using racmo2: Part 2: Antarctica (1979-2016), The Cryosphere, 12, 1479–1498, 2018.

van Wessem, J. M., Ligtenberg, S. R. M., Reijmer, C. H., van de Berg, W. J., van den Broeke, M. R., Barrand, N. E., Thomas, E. R., Turner, J., Wuite, J., Scambos, T. A., and van Meijgaard, E.: The modelled surface mass balance of the Antarctic Peninsula at 5.5 km horizontal resolution, The Cryosphere, 10, 271–285, 2016.

Velicogna, I., Sutterley, T., and Van Den Broeke, M.: Regional acceleration in ice mass loss from Greenland and Antarctica using GRACE time-variable gravity data, Geophysical Research Letters, 41, 8130–8137, 2014.

Vieli, A., Payne, A. J., Shepherd, A., and Du, Z.: Causes of pre-collapse changes of the Larsen B ice shelf: Numerical modelling and assimilation of satellite observations, Earth and Planetary Science Letters, 259, 297–306, 2007.

Vignon, E., van de Wiel, B. J., van Hooijdonk, I. G., Genthon, C., van der Linden, S. J., van Hooft, J. A., Baas, P., Maurel, W., Traullé, O., and Casasanta, G.: Stable boundary-layer regimes at Dome C, Antarctica: observation and analysis, Quarterly Journal of the Royal Meteorological Society, 143, 1241–1253, 2017.

Vignon, É., Traullé, O., and Berne, A.: On the fine vertical structure of the low troposphere over the coastal margins of East Antarctica, Atmospheric Chemistry and Physics, 19, 4659–4683, 2019.

Vignon, É., Picard, G., Durán-Alarcón, C., Alexander, S. P., Gallée, H., and Berne, A.: Gravity wave excitation during the coastal transition of an extreme katabatic flow in Antarctica, Journal of the Atmospheric Sciences, 77, 1295–1312, 2020.

Vionnet, V., Guyomarc'h, G., Bouvet, F. N., Martin, E., Durand, Y., Bellot, H., Bel, C., and Puglièse, P.: Occurrence of blowing snow events at an alpine site

over a 10-year period: observations and modelling, Advances in water resources, 55, 53–63, 2013.

Voldoire, A., Saint-Martin, D., Sénési, S., Decharme, B., Alias, A., Chevallier, M., Colin, J., Guérémy, J.-F., Michou, M., Moine, M.-P., Nabat, P., Roehrig, R., Salas y Mélia, D., Séférian, R., Valcke, S., Beau, I., Belamari, S., Berthet, S., Cassou, C., Cattiaux, J., Deshayes, J., Douville, H., Ethé, C., Franchistéguy, L., Geoffroy, O., Lévy, C., Madec, G., Meurdesoif, Y., Msadek, R., Ribes, A., Sanchez-Gomez, E., Terray, L., and Waldman, R.: Evaluation of CMIP6 deck experiments with CNRM-CM6-1, Journal of Advances in Modeling Earth Systems, 11, 2177–2213, 2019.

Walden, V. P., Warren, S. G., and Tuttle, E.: Atmospheric ice crystals over the Antarctic Plateau in winter, Journal of Applied Meteorology, 42, 1391–1405, 2003.

Wang, C., Deser, C., Yu, J.-Y., DiNezio, P., and Clement, A.: El Niño and southern oscillation (ENSO): a review, in: Coral reefs of the eastern tropical Pacific, pp. 85–106, Springer, 2017.

Wang, G., Hendon, H. H., Arblaster, J. M., Lim, E.-P., Abhik, S., and van Rensch, P.: Compounding tropical and stratospheric forcing of the record low Antarctic sea-ice in 2016, Nature communications, 10, 1–9, 2019a.

Wang, H., Fyke, J. G., Lenaerts, J., Nusbaumer, J. M., Singh, H., Noone, D., Rasch, P. J., and Zhang, R.: Influence of sea-ice anomalies on Antarctic precipitation using source attribution in the Community Earth System Model, The Cryosphere, 14, 429–444, 2020.

Wang, W., Zender, C. S., van As, D., and Miller, N. B.: Spatial distribution of melt season cloud radiative effects over Greenland: Evaluating satellite observations, reanalyses, and model simulations against in situ measurements, Journal of Geophysical Research: Atmospheres, 124, 57–71, 2019b.

Wang, Y.: An explicit simulation of tropical cyclones with a triply nested movable mesh primitive equation model: TCM3. Part I: Model description and control experiment, Monthly weather review, 129, 1370–1394, 2001.

Wang, Y., Ding, M., Van Wessem, J., Schlosser, E., Altnau, S., van den Broeke, M. R., Lenaerts, J. T., Thomas, E. R., Isaksson, E., Wang, J., et al.: A comparison of Antarctic Ice Sheet surface mass balance from atmospheric

climate models and in situ observations, Journal of Climate, 29, 5317–5337, 2016.

Waugh, D. W., Garfinkel, C. I., and Polvani, L. M.: Drivers of the recent tropical expansion in the Southern Hemisphere: Changing SSTs or ozone depletion?, Journal of Climate, 28, 6581–6586, 2015.

Weatherly, J. W.: Sensitivity of Antarctic precipitation to sea ice concentrations in a general circulation model, Journal of climate, 17, 3214–3223, 2004.

Weertman, J.: Stability of the junction of an ice sheet and an ice shelf, Journal of Glaciology, 13, 3–11, 1974.

Wendler, G., André, J. C., Pettré, P., Gosink, J., and Parish, T.: Katabatic Winds in Adélie Coast, pp. 23–46, American Geophysical Union (AGU), 1993.

Wendler, G., Stearns, C., Weidner, G., Dargaud, G., and Parish, T.: On the extraordinary katabatic winds of Adélie Land, Journal of Geophysical Research: Atmospheres, 102, 4463–4474, 1997.

Wille, J. D., Favier, V., Dufour, A., Gorodetskaya, I. V., Turner, J., Agosta, C., and Codron, F.: West Antarctic surface melt triggered by atmospheric rivers, Nature Geoscience, 12, 911–916, 2019.

Wu, X., Simmonds, I., and Budd, W.: Southern hemisphere climate system recovery from 'instantaneous' sea-ice removal, Quarterly Journal of the Royal Meteorological Society, 122, 1501–1520, 1996.

Wyard, C., Doutreloup, S., Belleflamme, A., Wild, M., and Fettweis, X.: Global radiative flux and cloudiness variability for the Period 1959–2010 in Belgium: a comparison between reanalyses and the regional climate model MAR, Atmosphere, 9, 262, 2018.

Wyser, K., Noije, T. v., Yang, S., Hardenberg, J. v., O'Donnell, D., and Döscher, R.: On the increased climate sensitivity in the EC-Earth model from CMIP5 to CMIP6, Geoscientific Model Development, 13, 3465–3474, 2020.

Yamanouchi, T. and Kawaguchi, S.: Longwave radiation balance under a strong surface inversion in the katabatic wind zone, Antarctica, Journal of Geophysical Research: Atmospheres, 89, 11 771–11 778, 1984.

Yan, H. and Anthes, R. A.: The effect of latitude on the sea breeze, Monthly weather review, 115, 936–956, 1987.

Yang, Y., Palm, S. P., Marshak, A., Wu, D. L., Yu, H., and Fu, Q.: First satellite-detected perturbations of outgoing longwave radiation associated with blowing snow events over Antarctica, Geophysical Research Letters, 41, 730–735, 2014.

Yen, Y.-C.: Review of thermal properties of snow, ice, and sea ice, vol. 81, US Army, Corps of Engineers, Cold Regions Research and Engineering Laboratory, 1981.

Zelinka, M. D., Myers, T. A., McCoy, D. T., Po-Chedley, S., Caldwell, P. M., Ceppi, P., Klein, S. A., and Taylor, K. E.: Causes of higher climate sensitivity in CMIP6 models, Geophysical Research Letters, 47, 1–12, 2020.

Zhang, T., Stamnes, K., and Bowling, S.: Impact of clouds on surface radiative fluxes and snowmelt in the Arctic and subarctic, Journal of Climate, 9, 2110–2123, 1996.

Zhu, J., Poulsen, C. J., and Otto-Bliesner, B. L.: High climate sensitivity in CMIP6 model not supported by paleoclimate, Nature Climate Change, 10, 378–379, 2020.

Zuo, Z. and Oerlemans, J.: Modelling albedo and specific balance of the Greenland ice sheet: calculations for the Søndre Strømfjord transect, Journal of Glaciology, 42, 305–317, 1996.

Appendix

A Additional elements for Chapter 2

Table A.1: Discarded Automatic Weather Stations from the comparison database and justification

AWS name	Justification
	AWS database
A028 a	Time lag (one day?) in 1989
Briscoe Island	Drift in pressure 2003–2004 suggesting a movement of the station
Baldrick	Temperature sensor (hmp45) caped at -39 °C in winter
Dome A	Wind speed captor malfunction
Dome F	Wind speed captor malfunction
Eagle	Wind speed captor malfunction
Elaine	Pressure captor malfunction
Emilia	3 negative drifts in pressure in 2004
Eneide	Pressure captor malfunction
Erin	4 distinct pressure periods suggesting displacement (e.g., -40 hPa jump) in 2013
GC41	Inconsistent temperature cycles from 2002 onwards
GF08	Probable time lag
GF08 a	Inconsistent pressure values after 2007
Giulia	Inconsistent pressure values, pressure captor malfunction in 2006
Joinville Island	Positive pressure drift
Larsen Ice Shelf	Inconsistent temperatures (+20 °C in 1989, pressure captor malfunction in 2012
Laurie	Temperature captor malfunction in 1984 (-70 °C
Law Dome Summit South	Pressure captor malfunction
LGB00	Pressure captor malfunction
Lola	Pressure captor malfunction
Linda	Too low pressure values in 1998 and 2003 suggesting displacement
Pine Island Glacier	Jump in pressures suggesting displacement in 2008 and 2011
Sofia	Pressure captor malfunction in 2002
Rita	Pressure captor malfunction in 1993
Russkaya	Pressure captor malfunction
Schwerdfteger	Pressure and temperature jump in 1993 and 1993
Sky-Blu	Pressure captor malfunction in 2012 and 2013
Siple Dome	Pressure trend between 2000 and 2010 suggesting displacement
Thiel Mountain	Pressure captor malfunction in 2013, 2014 and 2016
Union Glacier	Pressure captor malfunction in 2008, 2009 and 2014
White Island	Jump in pressure (100 hPa) in 1999
White Out	Insufficient number of measures (40 days)
Zoraida	Jump in pressure in 2007
	Polenet network
Cape Framnes	Temperature captor malfunction
Mount Carbone	Discontinuous time series notably in 2012
	Manned Station
Byrd	Discontinuous time series and inconsistent values (eg., 1987)

Note that all the original wind-speed unit measured by LGB$*$ AWSs was indicated to be in knots but was actually m s^{-1}.

Table A.2: Automatic Weather Stations contained in the new database with their name, coordinates (°), elevation (masl) and measurement period

Name	Latitude (°)	Longitude (°)	Elevation (masl)	Start year	Start month	Start julian day	End year	End month	End julian day	Number of days
A028 b *	-68,40	112,22	1622	1998	11	6	2005	7	30	2459
A028 *	-68,40	112,22	1622	1985	4	12	1986	2	15	310
AGO A81 *	-81,50	3,74	2410	1993	1	8	1994	1	16	374
AGO A84 *	-84,36	-23,86	2103	1996	1	9	1998	11	1	1028
AGO Site *	-77,52	-23,74	1545	1991	1	26	1992	12	31	706
Alessandra *	-73,58	166,62	160	1987	1	1	2007	11	14	7623
Allison *	-89,88	-60,00	2835	1986	1	28	1987	7	31	550
AM01 *	-69,43	71,42	65	2002	2	12	2006	12	6	1759
AM02 *	-69,70	72,63	47	2001	1	10	2007	12	23	2539
AmeryG3 *	-70,88	69,87	84	1999	2	4	2011	12	31	4714
Apfel *	-66,33	100,80	150	2000	1	5	2001	7	17	560
Arelis	-76,70	162,97	150	1990	1	1	2007	11	18	6531
Asgard *	-77,60	161,07	1750	1980	2	5	1982	12	31	1061
Bonaparte Point *	-64,70	-64,07	8	1992	1	5	2017	4	26	9244
Bowers *	-85,20	163,40	2090	1986	1	11	1986	8	25	227
Brianna *	-83,89	-134,15	525	1994	11	30	2015	12	8	7679
Buckle Island	-66,87	163,24	520	1987	1	6	1988	7	31	573
Butler Island *	-72,20	-60,17	115	1986	3	1	2018	11	22	11955
Byrd *	-80,00	-119,40	1530	1980	2	5	2018	9	30	14118
Cape Adams *	-75,01	-62,53	25	1989	1	29	1992	9	22	1333
Cape Bird *	-77,22	166,44	38	1999	1	28	2018	8	22	7147
Cape Denison	-67,01	142,66	31	1990	1	20	2011	4	6	7747
Cape Spencer *	-77,97	167,53	23	1999	1	11	2004	5	15	1952
Cape Webb *	-67,94	146,81	37	1994	12	28	1997	3	16	810
Carolyn *	-79,95	175,86	52	2005	2	2	2014	11	21	3580
Clamp1 *	-75,88	-25,49	43	1996	1	9	1997	11	29	691
Clamp2 *	-75,96	-25,41	400	1996	1	11	2003	12	12	2893
Clamp3 *	-76,70	-25,53	1400	1996	1	14	2003	12	17	2895
Clamp4 *	-76,81	-25,5	1650	1997	12	7	2003	12	17	2202
Clean Air *	-90,00	0,00	2835	1986	1	29	2005	1	24	6936
Concordia *	-75,10	123,40	-999	2005	1	27	2008	5	30	1220
D 10 *	-66,72	139,84	243	1980	1	8	2018	9	30	14146
D 57 *	-68,20	137,54	2105	1981	1	16	2000	1	18	6942
D 80 *	-70,04	134,88	2500	1983	1	14	1996	3	25	4820
D 85 *	-70,43	134,15	2682	2008	1	1	2015	12	31	2922
Dismal Island *	-68,09	-68,82	10	2001	5	22	2018	9	30	6341
Dolleman Island *	-70,58	-60,92	396	1986	2	20	1988	12	27	1042
Dome C *	-74,50	123,00	3280	1980	2	5	1996	1	3	5812
Dome Fuji *	-77,31	39,70	3810	1995	2	8	2018	9	30	8636
Doug *	-82,32	-113,24	1433	1994	11	29	2001	10	8	2506
E 66 *	-68,91	134,65	2485	2008	1	1	2011	12	31	1461
Eder Island *	-66,95	143,93	52	1999	8	9	2000	10	19	438
Elizabeth *	-82,62	-137,08	519	1996	2	15	2018	9	30	8264
Eric *	-81,50	163,94	45	2005	1	29	2014	9	27	3529
Evans Knoll *	-74,85	-100,41	108	2011	1	1	2017	12	31	2557
Ferrell *	-77,90	170,82	46	1980	12	10	2018	9	30	13809
Fogle *	-77,90	166,72	200	1984	1	25	1985	1	5	347
Fossil Bluff *	-71,32	-68,28	66	2006	12	9	2018	11	22	4367
GC46 *	-74,13	109,83	3096	1994	6	2	1999	4	20	1784
Gill *	-79,98	-178,60	54	1985	1	19	2018	9	30	12308
Gomez Nunatak	-75,88	-63,53	1417	2010	1	8	2012	1	9	732
Halley Bay *	-75,50	-26,65	52	1990	4	1	1990	11	6	220
Harry *	-83,00	-121,39	945	1994	11	29	2018	9	30	8707
Henry *	-89,00	-1,017	2755	1993	1	26	2017	7	8	8930
Herbie Alley *	-78,10	166,67	30	1999	1	11	2004	2	3	1850
Hutton Mountains *	-74,07	-61,72	949	2010	1	5	2012	3	17	803
Irene *	-71,65	148,65	-999	2001	11	22	2007	12	31	2231
Janet *	-77,17	-123,39	2085	2011	1	1	2017	12	31	2557
J C *	-85,07	-135,52	549	1994	11	29	1997	7	31	976
Jennica	-74,68	164,08	-999	1999	12	30	2003	10	20	1391
Jensen Nunatak *	-73,07	-66,10	1365	2009	12	30	2012	5	30	883
Jimmy *	-77,87	166,81	202	1981	12	2	1990	4	12	3054
Kelly *	-89,00	-179,61	2950	1993	1	27	1994	1	22	361
King George Island	-62,08	-58,40	267	2000	2	2	2003	12	04	1402
Kirkwood Island	-68,34	-69,01	30	2001	05	21	2004	03	31	1046
Kominko Slade *	-79,47	-112,09	1833	2007	4	1	2018	9	30	4201
Lanyon a *	-66,27	110,78	390	1998	10	19	2008	4	24	3476
Lanyon *	-66,27	110,78	390	1991	2	22	1998	11	24	2833
Laurie II *	-77,52	170,80	37	2000	2	1	2018	9	30	6817
Law Dome Summit *	-66,73	112,83	1368	1986	4	17	1998	7	1	4459
Lettau *	-82,52	-174,45	38	1986	1	29	2018	9	30	11933
LGB00 a *	-68,65	61,10	1830	1987	12	5	1993	1	1	1855
LGB00 b *	-68,65	61,10	1830	1993	11	13	1995	2	13	458
LGB00 c *	-68,65	61,10	1830	1995	2	15	2009	8	7	5288
LGB10 a *	-71,28	59,20	2620	1993	11	22	2006	5	8	4551
LGB10 *	-71,28	59,20	2620	1990	1	1	1994	10	24	1758
LGB20 *	-73,82	55,67	2741	1991	1	18	2004	9	1	4976
LGB35 *	-76,03	65,00	2342	1993	12	21	2008	7	1	5307
LGB46 *	-75,85	71,48	2352	1994	1	7	1997	5	6	1216
LGB59 *	-73,45	76,78	2537	1994	1	25	2004	6	28	3808
LGB69 a *	-70,83	77,07	1854	2007	2	2	2008	8	20	566
LGB69 *	-70,83	77,07	1854	2002	1	22	2007	2	2	1838
Lindsay *	-89,00	-89,85	2815	1993	1	26	1994	1	22	362
Lorne *	-78,25	170,00	46	2007	1	13	2017	3	23	3723
Lynn *	-74,21	160,41	1772	1988	1	19	1998	1	4	3639
Manning *	-78,75	166,85	66	1980	12	1	1986	1	15	1872
Manuela *	-74,95	163,68	78	1984	1	5	2018	9	30	12688
Marble Point	-77,43	163,75	108	1980	2	5	2018	9	30	14118
Maria *	-74,62	164,00	-999	1997	11	1	2007	11	2	3654
Marilyn *	-79,95	165,12	64	1987	1	10	2018	9	30	11587
Martha 2 *	-78,38	-173,42	18	1987	1	21	1992	2	13	1850
Martha I *	-78,31	-172,50	42	1984	1	27	1987	12	31	1435
Mary *	-79,31	162,99	58	2005	2	1	2012	1	20	2545
Meeley *	-78,52	170,18	49	1980	12	4	1985	12	31	1854
Minna Bluff	-78,55	166,65	895	1991	1	22	2018	8	31	10084
Mizuho *	-70,70	44,29	2260	2000	10	7	2018	9	30	6568
Modesta *	-73,63	160,63	-999	1989	1	1	2007	11	23	6901
Mount Howe *	-87,32	-149,55	2400	1992	1	11	1993	11	11	671
Mount McKibben *	-75,27	-65,60	1155	2010	1	6	2010	4	25	110
Mount Siple *	-73,20	-127,05	230	1992	2	20	2018	1	25	9472
MtBrown a *	-69,12	85,98	2064	2003	2	24	2011	10	9	3150
MtBrown *	-69,12	85,98	2064	1998	12	23	2000	7	17	573
Mt Erebus	-77,53	167,13	3700	1989	12	1	1990	10	16	320
Mt Fleming *	-77,53	160,27	1950	2008	1	1	2011	1	7	1103
Mulock *	-78,92	159,00	1000	2006	10	25	2011	1	27	1556
Nico *	-89,00	89,67	2935	1993	1	26	2017	10	18	9032
Noel *	-79,33	-111,08	1833	2000	1	19	2000	7	19	183
Paola *	-72,77	159,03	-999	2003	2	8	2007	11	16	1743
Pat *	-74,88	163,10	30	1988	12	26	1991	1	1	737
Patrick *	-89,88	45,00	2835	1986	1	28	1987	6	26	515
Patriot Hills *	-80,30	-81,33	905	2008	1	4	2010	1	25	753
Pegasus *	-78,00	166,64	10	1989	1	19	1989	11	10	296
Pegasus North *	-77,95	166,50	8	1990	1	23	2017	12	14	10188
Pegasus South *	-77,99	166,57	5	1991	1	12	2009	1	7	6571
Penguin Point *	-67,62	146,18	30	1992	12	24	2002	7	4	3480
Possession Island	-71,88	171,2	30	1992	12	29	2018	9	30	9407
Racer Rock *	-64,07	-61,61	17	1989	10	15	2003	2	28	4885
Ranvik	-68,85	78,03	339	2000	2	4	2002	1	18	715
Recovery Glacier *	-80,82	-22,26	1220	1994	1	18	1995	12	30	712
Relay Station *	-74,02	43,05	3353	1995	2	1	2018	9	30	8643
Rumdoodle *	-67,70	62,80	430	2000	2	1	2001	12	26	695
Sandra *	-74,49	160,49	1525	1988	1	19	1995	8	25	2776
Santa Claus Island	-64,96	-65,67	25	1994	12	10	2000	10	29	2151
Scott Island	-67,37	-179,97	30	1988	1	1	1999	3	23	4100
Shristi *	-74,70	161,57	1200	1988	1	1	1992	9	30	1735
Silvia *	-73,52	169,73	550	1990	12	1	2007	12	5	6214
Siple *	-75,90	-83,92	1054	1982	1	1	1992	4	21	3764
Ski Hi *	-74,98	-70,77	1395	1994	2	21	1998	11	25	1739
Sofiab *	-75,60	158,58	1720	2002	11	28	2007	11	12	1811
Sushila *	-74,41	161,31	1441	1988	1	20	1991	9	15	1335
Sutton *	-67,08	141,37	871	1994	12	26	2000	12	18	2185
Swithinbank *	-81,20	-126,18	959	1997	1	18	2011	1	16	5112
Theresa *	-84,60	-115,81	1463	1994	11	29	2018	9	30	8707
Tiffany *	-77,95	166,17	25	1984	1	24	1985	12	31	708
Traverse Mountains *	-69,98	-67,55	1047	2009	12	22	2013	1	6	1112
Uranus Glacier *	-71,36	-68,80	753	1986	3	4	2003	2	28	6206
Vito *	-78,50	177,75	50	2004	2	3	2018	9	30	5354
Welch Mountains *	-70,71	-63,81	1526	2010	1	10	2010	7	15	187
Whitlock	-76,14	168,39	206	1982	1	23	2018	9	30	13400
Willie Field *	-77,87	166,98	14	1992	1	25	2018	8	31	13095
Windless Bight *	-77,72	167,69	40	1983	1	23	2018	8	31	13095
Young Island	-66,23	162,28	30	1991	1	1	1997	12	6	2532

Table A.3: Automatic Weather Stations from the POLENET program contained in the new database with their name, coordinates (°), elevation (masl) and measurement period

Name	Latitude (°)	Longitude (°)	Elevation (masl)	Start year	Start month	Start julian day	End year	End month	End julian day	Number of days
Backer Island *	-74,43	-102,48	64	2011	12	27	2016	12	19	1820
Bean Peaks *	-75,96	-69,30	-999	2010	1	7	2010	7	28	203
Bear Peninsula *	-74,55	-111,88	342	2011	1	11	2018	11	5	2856
Bennett Nunatak *	-84,79	-116,46	1441	2010	12	15	2018	1	4	2578
Brimstone Peak *	-75,80	158,47	2138	2008	12	10	2018	2	6	3346
Bumstead Nunatak *	-85,96	174,50	2648,9	2014	1	28	2018	11	5	1743
Butcher Ridge *	-79,15	155,89	2030	2008	12	9	2018	11	5	3619
Clarke Mountains *	-77,34	-141,87	1025	2010	1	4	2018	11	5	3228
Cordiner Peak *	-82,86	-53,20	963	2010	1	14	2014	8	26	1686
Deverall Island *	-81,48	161,98	95	2008	12	5	2018	2	11	3356
Duthiers Point	-64.80	-62.82	78	2009	4	3	2014	11	1	2039
Fallone Nunataks *	-85,31	-143,63	291	2009	12	22	2018	11	5	3241
Flask Glacier *	-65,75	-62,88	591	2010	2	6	2014	7	12	1618
Foyn Point *	-65,24	-61,65	123	2010	2	7	2015	7	31	2001
Franklin Island	-76,14	168,42	181	2011	1	28	2015	2	8	1473
Gomez Nunatak *	-73,88	-68,54	-999	2010	1	8	2010	12	31	358
Haag Nunatak *	-77,04	-78,29	1197	2010	1	16	2018	11	5	3216
Howard Nunatak *	-77,53	-86,77	1502	2010	1	15	2018	11	5	3217
Hugo Island	-64,96	-65,67	46	2009	4	2	2018	11	5	3505
Hutton Mountains *	-74,08	-61,73	-999	2010	1	5	2010	6	4	151
Inman Nunatak *	-74,82	-98,88	678	2013	1	8	2018	11	5	2128
Jensen Nunatak *	-73,08	-66,10	-999	2009	12	30	2010	12	31	367
Kohler Glacier *	-76,15	-120,73	1929	2010	1	24	2018	3	10	2968
Lepley Nunatak *	-73,11	-90,30	159	2011	12	14	2018	11	5	2519
Leppard Glacier *	-65,95	-62,88	612	2010	2	13	2013	5	22	1195
Lonewolf Nunatak *	-81,34	152,73	1554	2008	12	4	2018	2	7	3353
Lower Thwaites Glacier *	-76,44	-107,77	999	2009	12	12	2018	11	5	3251
Lyon Nunatak *	-74,83	-73,90	-999	2009	12	31	2014	12	31	1827
Mount Bruce	-70.60	162.52	1513	2014	12	21	2018	11	05	1416
Monte Cassino *	-72,27	163,73	1954	2014	12	17	2018	11	2	1417
Mount Howe *	-87,42	-149,43	2611	2010	12	18	2018	11	5	2880
Mount Paterson *	-78,03	-155,023	538	2008	12	26	2017	12	2	3264
Mount Sidley *	-77,13	-125,97	2123	2010	1	8	2018	11	5	3224
Mount Suggs *	-75,28	-72,18	1122	2010	1	18	2018	11	5	3214
Mount Walcott *	-85,40	-87,39	1849	2014	1	3	2018	11	5	1768
Prospect Point	-66.01	-65.34	44	2014	5	4	2018	11	5	1647
Pecora Escarpment *	-85,61	-68,55	1524	2010	1	14	2018	10	30	3212
Pirrot Hills *	-81,10	-85,14	1263	2013	12	30	2018	11	5	1772
Rambo Nunatak *	-83,87	-66,39	784	2014	1	6	2018	11	5	1765
Recovery Lakes 1 *	-82,81	18,90	2694	2009	1	10	2011	6	3	875
Recovery Lakes 2 *	-81,71	8,58	2473	2009	1	27	2012	3	19	1148
Robertson Island *	-65,25	-59,44	85	2010	2	6	2018	4	24	3000
South Georgia 1	-54,87	-36,04	85	2014	10	5	2017	5	4	943
South Georgia 2	-54,00	-38,05	205	2014	10	8	2015	4	3	178
South Georgia 3	-54,49	-37,04	53	2014	10	13	2018	11	5	1485
Spring Point	-64.29	-61.05	15	2013	3	22	2017	8	22	1615
Steward Hills *	-84,19	-86,25	1582	2014	1	8	2018	11	5	1763
Thurston Island *	-72,53	-97,56	245	2011	1	19	2018	11	5	2848
Tombstone Hill *	-72,45	169,72	620	2014	12	7	2018	11	5	1430
Toney Mountain *	-75,80	-114,66	1197	2012	12	3	2018	11	5	2164
Traverse Mountains *	-69,99	-67,55	-999	2009	12	22	2010	7	24	215
Up Thwaites Glacier *	-77,58	-109,03	1314	2010	1	15	2018	11	5	3217
Vernadsky Station	-65.25	-64.25	46	2009	4	1	2017	02	18	2881
Welch Mountains *	-70,73	-63,82	-999	2010	1	10	2014	12	31	1817
Westhaven Nunatak *	-79,84	154,22	2216	2008	12	9	2017	1	15	2960
Whichaway Nunatak *	-81,58	-28,40	1195,4	2014	1	17	2018	11	5	1754
Whitmore Mountains *	-82,68	-104,39	2374	2010	1	19	2018	11	5	3213
Wilson Nunatak *	-80,04	-80,56	692	2010	1	12	2018	11	5	3220

Table A.4: Permanent manned Weather Stations contained in the new database with their name, coordinates (°), elevation (masl) and measurement period

Name	Latitude (°)	Longitude (°)	Elevation (masl)	Start year	Start month	Start julian day	End year	End month	End julian day	Number of days
Adelaide	-67,80	-68,90	26	1962	5	1	1976	1	1	4994
Arturo Prat	-62,5	-59,68	5	1983	1	01	2003	12	31	7670
Asuka *	-71,50	24,10	931	1987	2	1	1991	12	1	1765
Belgrano I	-78,00	-38,80	50	1957	2	1	1979	10	1	8278
Belgrano II *	-77,87	-34,62	256	1980	4	1	2016	4	29	13178
Bellingshausen	-62,18	-58,88	16	1968	3	1	2017	2	1	17870
Campbell	-52,55	169,13	19	1961	4	1	1999	6	15	13955
Casey *	-66,27	110,52	42	1989	1	1	2016	4	30	9982
Casey old *	-66,27	110,52	42	1969	2	21	1990	1	31	7650
Davis	-68,57	77,97	13	1957	2	10	2016	4	30	21630
Deception	-63,00	-60,70	8	1959	1	1	1967	12	1	3257
Dumont Durville *	-66,65	140,00	43	1956	4	1	2017	8	11	22413
Esperanza *	-63,40	-56,98	13	1957	1	1	2016	4	29	21669
Faraday	-65,25	-64,27	11	1947	1	1	1995	12	31	17897
Ferraz	-62,08	-58,38	20	1985	12	2	2005	10	31	7274
Fossil Bluff *	-71,32	-68,28	250	1961	3	9	2005	3	5	16068
Great Wall	-62,22	-58,97	10	1985	01	01	2016	04	30	11443
Grytviken	-54,28	-36,48	3	1959	1	1	1981	12	31	8401
Jubany	-62,23	-58,63	4	1985	5	1	2016	5	1	11324
King Sejong	-62,22	-58,75	11	1988	5	1	2001	1	1	4629
Leningradskaja *	-69,50	159,38	304	1971	2	28	1991	2	28	7306
Macquarie Island	-54,48	158,93	8	1948	3	31	1999	7	5	18724
Marambio *	-64,23	-56,72	198	1971	1	1	2016	5	1	16558
Mario Zucchelli *	-74,68	164,08	92	1987	1	1	1999	12	31	4748
Marsh	-62,18	-58,98	10	1970	1	1	2009	12	31	14610
Mawson	-67,6	62,87	16	1954	2	23	2016	4	30	22713
McMurdo *	-77,85	166,67	24	1956	3	9	2015	12	31	21847
Mirny	-66,55	93	30	1956	2	1	2006	10	31	18536
Molodeznaja *	-67,65	45,85	40	1963	3	1	1999	6	30	13271
Novolazarevskaya *	-70,77	11,82	119	1961	2	1	2009	9	30	17774
O Higgins *	-63,37	-56,68	10	1987	11	17	2001	3	16	4869
Orcadas	-60,73	-44,73	6	1956	1	1	2016	5	1	22037
Rothera *	-67,57	-68,12	32	1976	3	8	2018	11	22	15600
San Martin	-68,12	-67,13	4	1977	1	1	2016	1	1	14245
Signy	-60,7	-45,6	6	1956	1	1	2000	3	31	16162
Syowa	-69	39,57	21	1957	2	9	2016	12	31	21876
Vernadsky	-65,25	-64,27	11	1996	1	1	2018	8	31	8279
Vostok *	-78,45	106,85	3490	1958	1	1	2017	2	28	21609
Wilkes	-66,26	110,52	42	1959	1	31	1969	2	21	3675
Zhongshan	-69,37	76,37	18	1989	3	1	2016	4	30	9923

Table A.5: Automatic Weather Stations from the IMAU, AWI, IPEV/IGE programs contained in the new database with their name, coordinates (°), elevation (masl) and measurement period. In addition to measuring (near-)surface pressure, temperature and wind speed, these stations contain reliable data on radiative fluxes and relative humidity.

Name	Latitude (°)	Longitude (°)	Elevation (masl)	Start year	Start month	Start julian day	End year	End month	End julian day	Number of days
AWS1 NARE9697 site A *	-71,90	3,08	1420	1997	1	1	2000	12	12	1442
AWS2 NARE9697 site C *	-72,25	2,88	2400	1997	2	12	2000	12	13	1401
AWS3 NARE9697 site M *	-74,98	15,00	3450	1997	1	28	2001	1	14	1448
AWS4 SWEDARP9798 Rampen *	-72,75	-15,48	35	1997	12	19	2002	12	29	1837
AWS5 SWEDARP9798 Wasa-Aboa *	-73,10	-13,17	360	1998	2	3	2014	2	7	5849
AWS6 SWEDARP9798 Svea *	-74,47	-11,52	1160	1998	1	14	2009	2	16	4052
AWS8 SWEDARP9798 Camp Victoria *	-76,00	-8,05	2400	1998	1	13	2003	1	7	1821
AWS9 DML05-Kohnen *	-75,00	0,00	2900	1997	12	30	2001	1	18	7690
AWS10 Berkner Island *	-79,57	-45,78	890	1995	2	12	2005	7	18	3810
AWS11 Halvfarryggen *	-71,17	-6,80	690	2007	1	18	2019	1	17	4381
AWS12 Plateau Station B *	-78,65	35,63	3620	2007	12	15	2016	3	11	3010
AWS13 Pole of inaccessibility *	-82,12	55,03	3730	2008	1	2	2016	3	11	2992
AWS14 Larsen C North *	-67,02	-61,50	50	2009	1	21	2017	1	4	2906
AWS15 Larsen C South *	-67,57	-62,15	50	2009	1	22	2014	5	6	1931
AWS16 Princess Elisabeth station *	-71,95	23,33	1300	2009	2	3	2019	1	17	3636
AWS17 Scar Inlet Larsen B *	-65,93	-61,85	50	2011	2	20	2016	3	10	1846
AWS18 Larsen C West *	-66,40	-63,37	70	2014	11	26	2019	1	17	1514
AWS19 King Baudoin Ice Shelf *	-70,95	26,27	50	2014	12	11	2016	2	2	419
D17 *	-66,7	139,9	450	2010	1	1	2019	1	1	3288
D 47 *	-67,4	138,73	1560	1983	1	24	2018	9	30	13034
Dome C II *	-75,12	123,37	3250	1995	12	10	2018	9	30	8331
Halley *	-75,43	-26,22	30	1957	1	1	2018	2	26	22337
Amundsen Scott *	-90,00	0,00	2835	1957	1	9	2018	11	1	22577
Neumayer *	-70,67	-8,25	50	1981	1	28	2016	3	31	12847
Panda-1 *	-74,65	77,00	2737	2011	1	1	2011	12	31	365
Sorasen	-71,36	-10,03	574	2017	1	1	2019	12	31	1095
Filchner2	-80,44	44,43	103,7	2019	1	1	2019	12	31	365

B Additional elements for Chapter 3

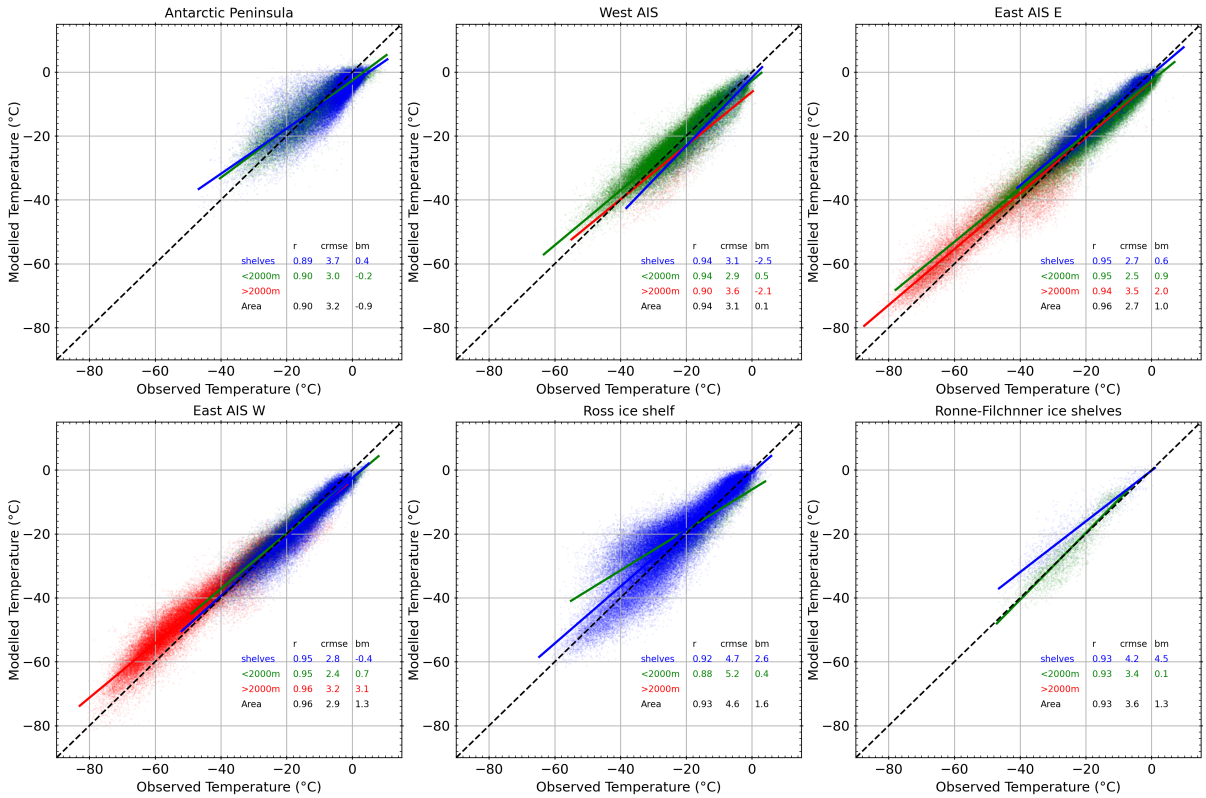

Figure B.1: Daily comparisons between MARv3.11 forced by ERA5 and near-surface temperature (°C) over different sectors (the Antarctic Peninsula, the West AIS, the East AIS (part East), the East AIS (part West), the Ross Ice Shelf, and the Ronne and Filchnner ice shelves) for grounded locations above 2000 masl (red) and below 2000 masl (green) as well as for location over the ice shelves (blue). The mean sector correlation, centered root mean square errors (CRMSE, unit:°C), and mean biases (bm, unit:°C), correlation are also given. These mean statistic indicators are weighted by the day number of each AWS. The sectors are illustrated in Fig. B.3

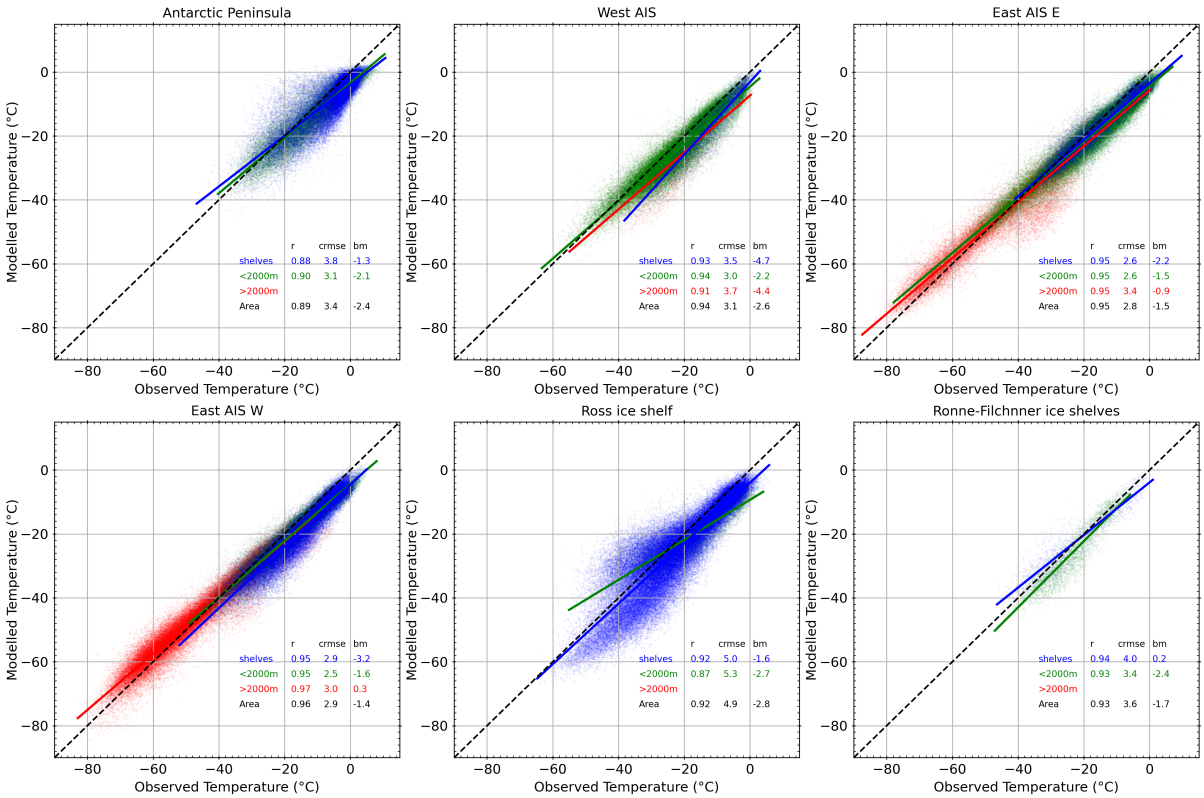

Figure B.2: Daily comparisons between MARv3.6 forced by ERA5 and near-surface temperature (°C) over different sectors (the Antarctic Peninsula, the West AIS, the East AIS (part East), the East AIS (part West), the Ross Ice Shelf, and the Ronne and Filchnner ice shelves) for grounded locations above 2000 masl (red) and below 2000 masl (green) as well as for location over the ice shelves (blue). The mean sector correlation, centered root mean square errors (CRMSE, unit:°C), and mean biases (bm, unit:°C), correlation are also given. These mean statistic indicators are weighted by the day number of each AWS. The sectors are illustrated in Fig. B.3

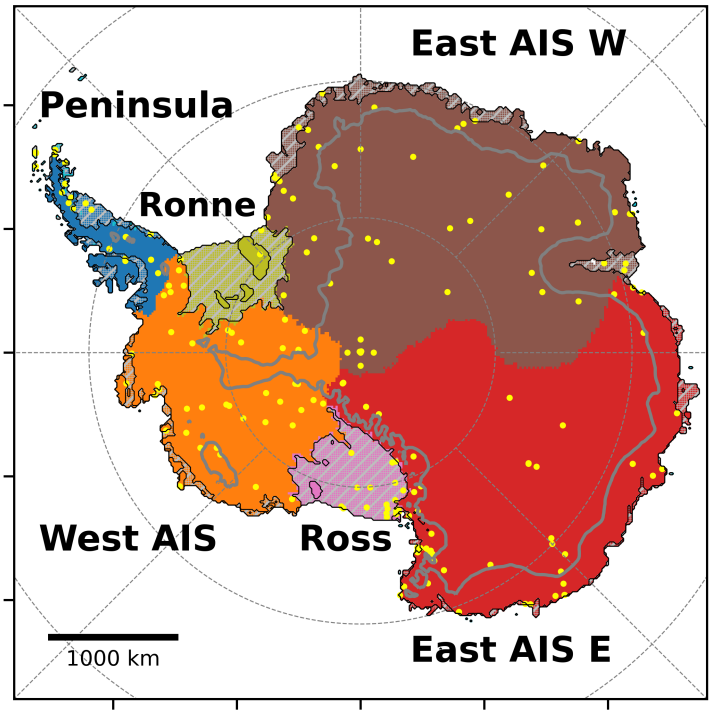

Figure B.3: Sectors used for the comparisons between MAR and the observations.

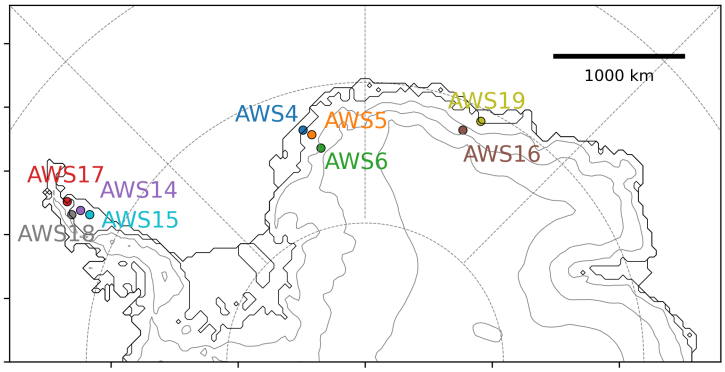

Figure B.4: Locations of AWS-forced melt estimates from Jakobs et al. (2020) used in this evaluation

C Additional elements for Chapter 4

C.1 Sensitivity of SMB components to SSCs

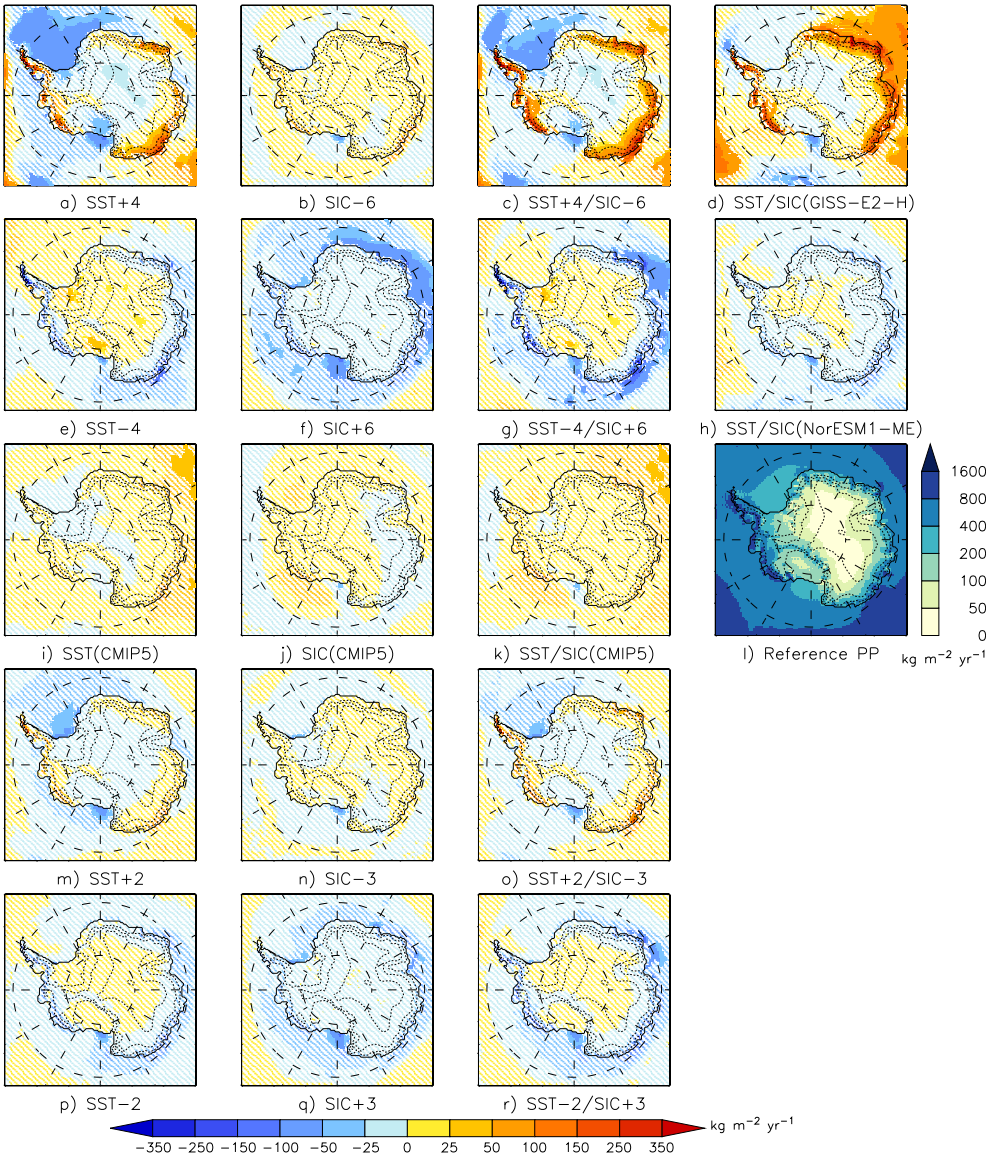

Figure C.1: Difference in mean annual total precipitation (rainfall + snowfall) (kg m^{-2} yr^{-1}) between the reference simulation and (a) SST+4, (b) SIC-6, (c) SST+4/SIC-6, (d) SST/SIC(GISS-E2-H), (e) SST-4, (f) SIC+6, (g) SST-4/SIC+6, (h) SST/SIC(NorESM1-ME), (i) SST(CMIP5), (j) SIC(CMIP5), (k) SST/SIC(CMIP5), (m) SST+2, (n) SIC-3, (o) SST+2/SIC-3, (p) SST-2, (q) SIC+3, (r) SST-2/SIC+2 experiments. Differences less than the interannual variability are considered as non-significant and are dashed. l) Mean annual SMB (kg m^{-2} yr^{-1}) simulated by MAR forced by ERA-Interim over 1979 – 2015.

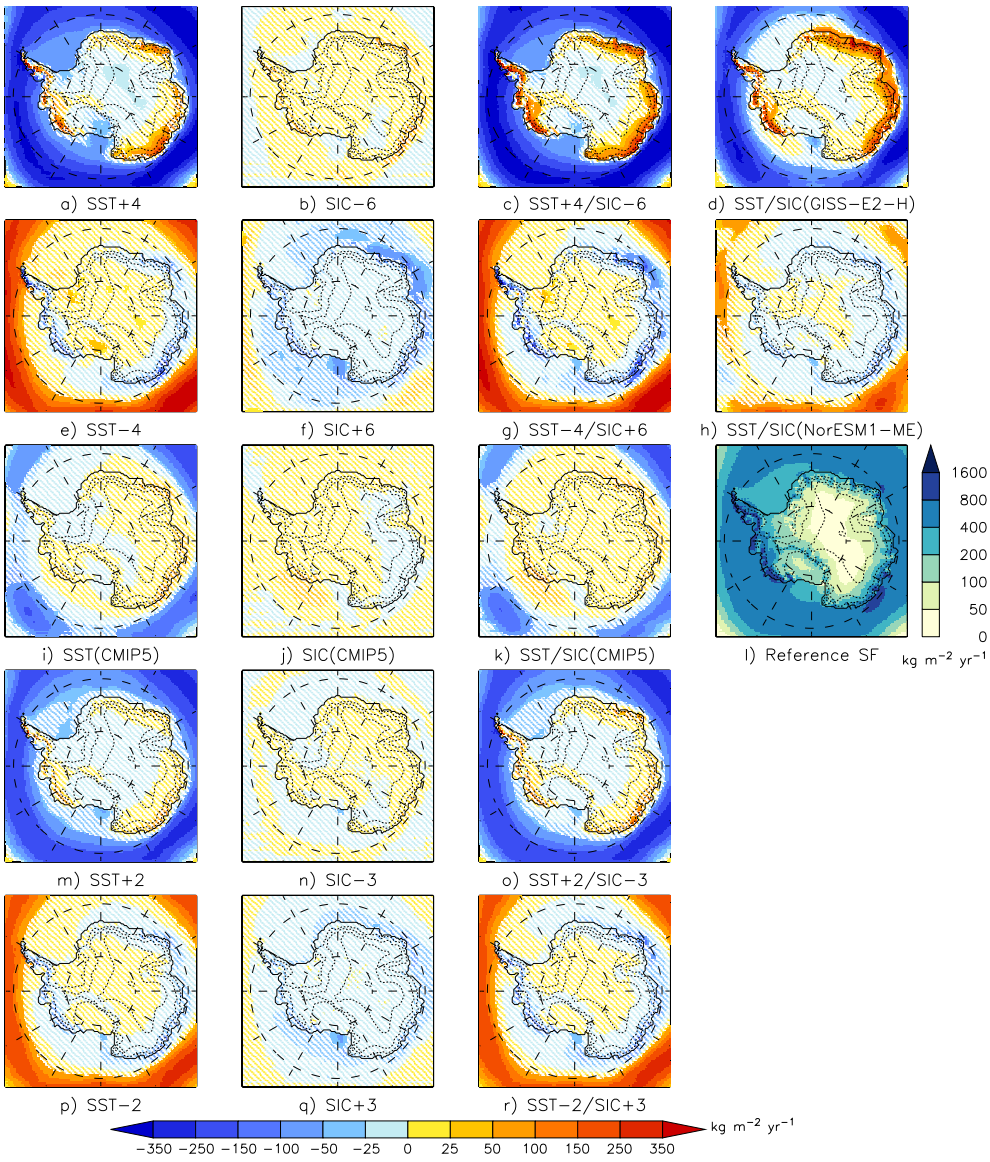

Figure C.2: Same as Fig. C.1 but for snowfall over the ice sheet and the surrounding ocean.

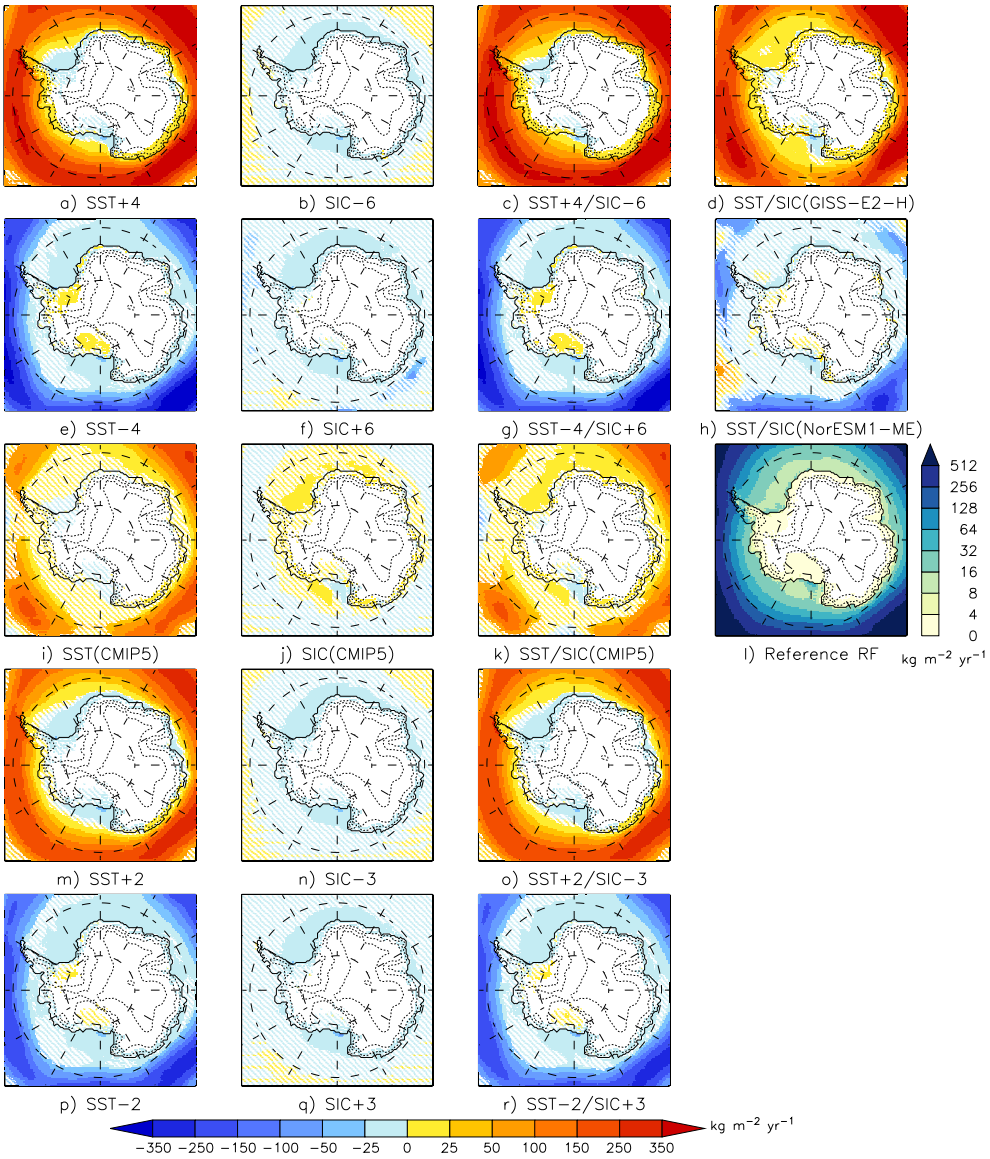

Figure C.3: Same as Fig. C.1 but for rainfall over the ice sheet and the surrounding ocean. White areas over the ice sheet indicate that there is no rainfall.

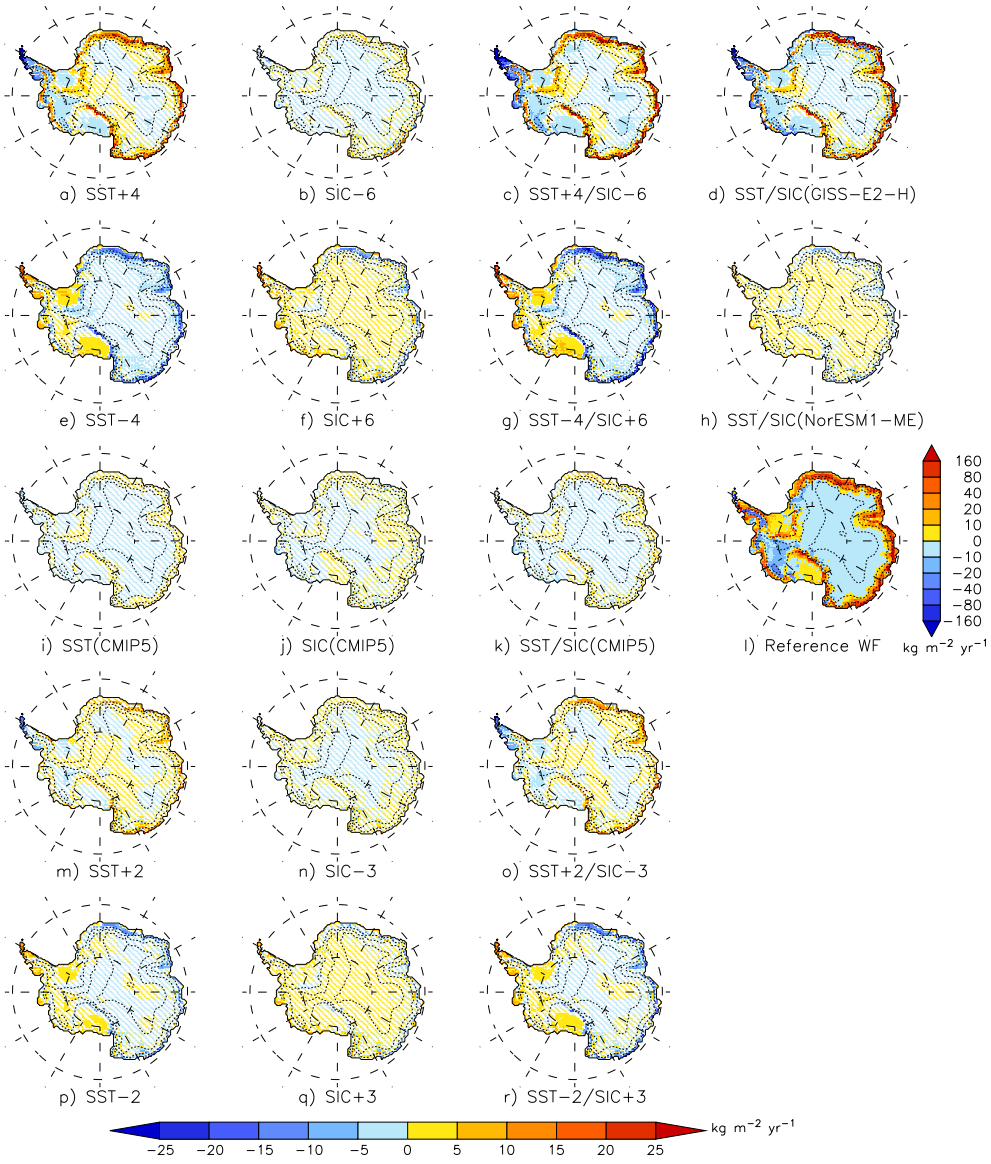

Figure C.4: Same as Fig. C.1 but for water fluxes (sublimation minus deposition) at the ice sheet surface. Positive fluxes indicate sublimation while negative fluxes are representative of deposition processes.

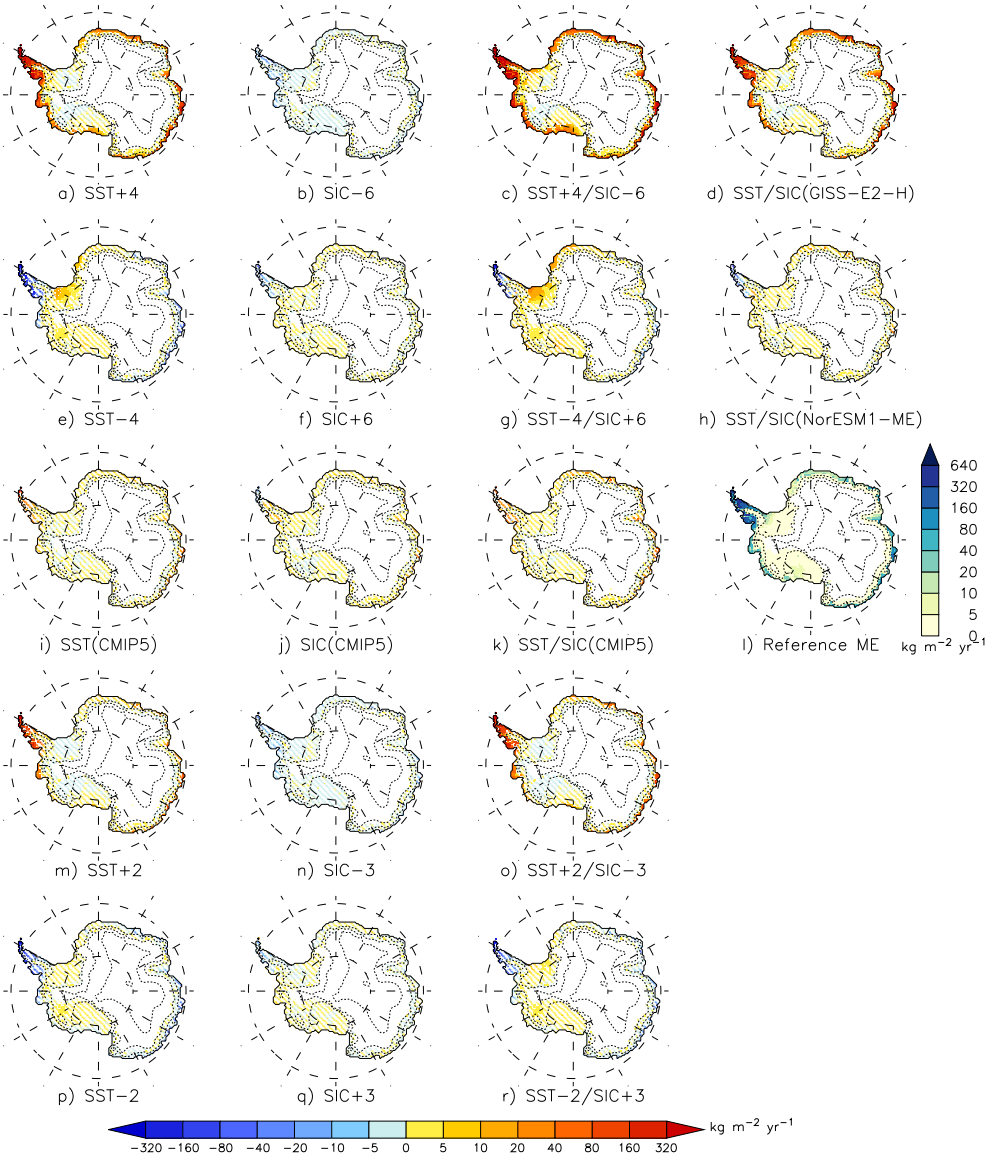

Figure C.5: Same as Fig. C.1 but for meltwater production at the surface. White areas over the ice sheet indicate that melt never occurs.

Table C.1: Top: Annual mean integrated (Gt yr^{-1}) and standard deviation (Gt yr^{-1}) total precipitation (rainfall and snowfall), snowfall and rainfall ver the whole AIS (including grounded and not grounded ice) for the reference simulation (1979–2015). Bottom: Difference of annual mean total precipitation (rainfall and snowfall), snowfall and rainfall (Gt yr^{-1} and %) between each sensitivity test and the reference simulation (1979–2015). Anomalies larger than the inter-annual variability are considered as significant and are displayed in bold.

Mean (Gt y^{-1})	Total precipitation	Snowfall	Rainfall
Reference	2678 ± 110	2658 ± 109	20± 3
Anomaly (Gt y^{-1})	Total precipitation	Snowfall	Rainfall
SST-4	-64	-61	**-3**
SST-2	-89	-85	**-4**
SST+2	+50	+45	**+5**
SST+4	**+162**	**+137**	**+25**
SIC+6	**-170**	**-166**	**-4**
SIC+3	-107	-104	**-3**
SIC-3	+25	+28	**-3**
SIC-6	+91	+93	-2
SST-4/SIC+6	**-136**	**-133**	**-3**
SST-2/SIC+3	**-129**	**-125**	**-4**
SST+2/SIC-3	**+133**	**+126**	**+7**
SST+4/SIC-6	**+344**	**+304**	**+40**
SST/SIC(NorESM1-ME)	-105	-102	**-3**
SIC(CMIP5)	+36	+35	+1
SST(CMIP5)	+80	+79	+1
SST/SIC(CMIP5)	+105	+104	+1
SST/SIC(GISS-E2-H)	**+368**	**+353**	**+15**

C.2 Locations of cited coastal areas

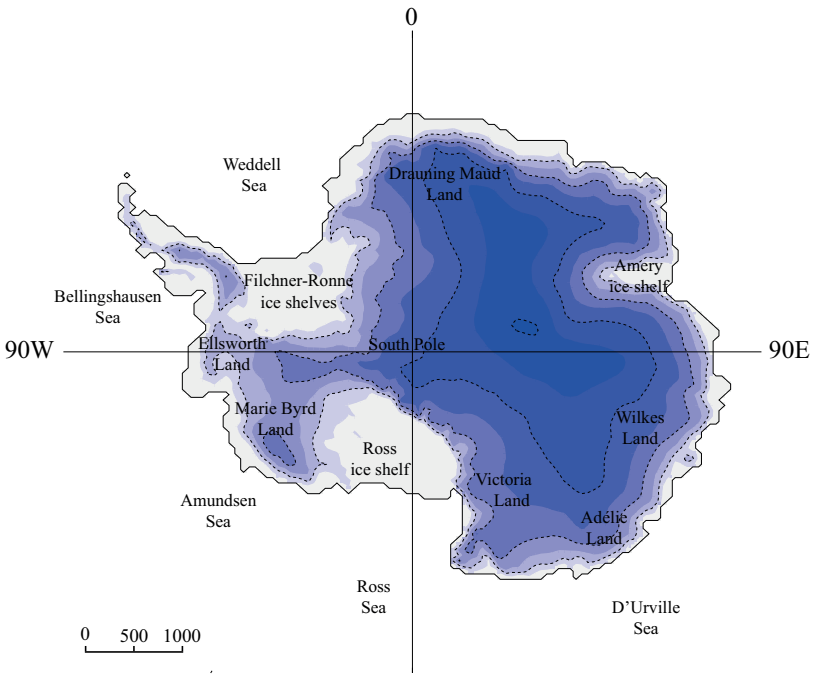

Figure C.6: The Antarctic Ice Sheet and surrounding seas. Elevation contours are shown every 1000 m.

C.3 Temperature and specific humidity anomalies

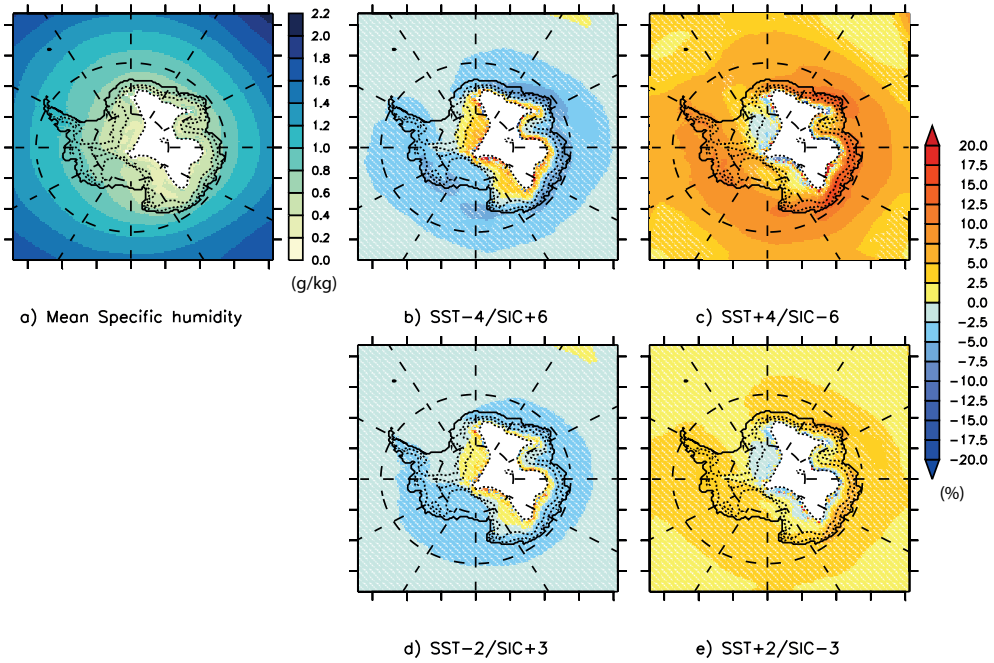

Figure C.7: a: Mean specific humidity modelled by MAR over 1979–2015 at 700 hPa (Units: g/kg). Difference in mean specific humidity (%) between the reference simulation and (b) SST-4/SIC+6, (c) SST+4/SIC-6, (d) SST-2/SIC+3, (e) SST+2/SIC-3 experiments. Differences lower than the interannual variability are considered as non-significant and are dashed.

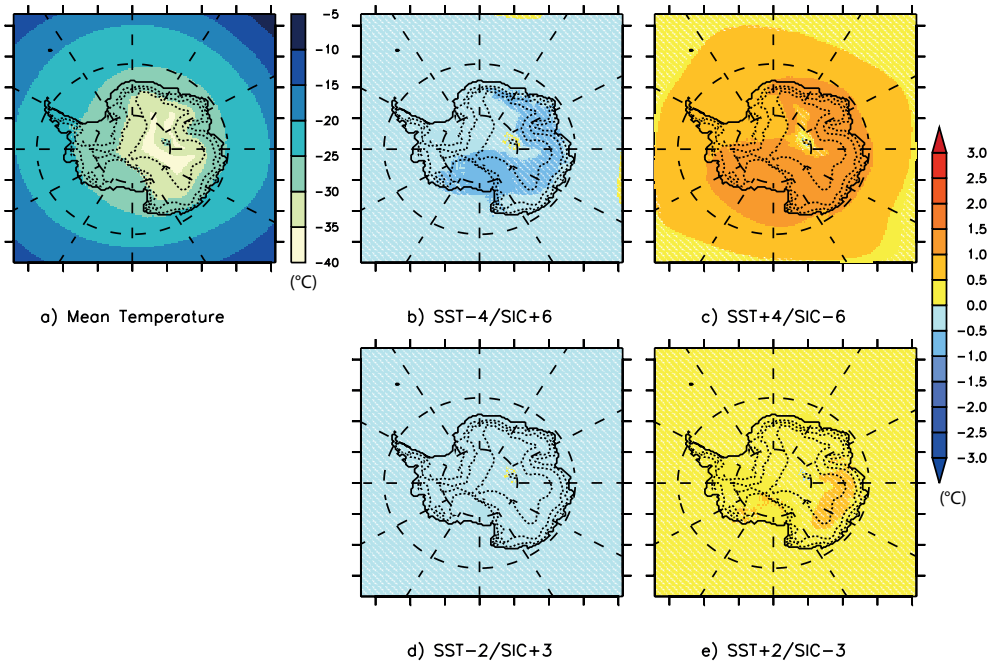

Figure C.8: a: Mean air temperature modelled by MAR over 1979–2015 at 600 hPa (Units: °C). Difference in mean air temperature (°C) between the reference simulation and (b) SST-4/SIC+6, (c) SST+4/SIC-6, (d) SST-2/SIC+3, (e) SST+2/SIC-3 experiments. Differences lower than the interannual variability are considered as non-significant and are dashed.

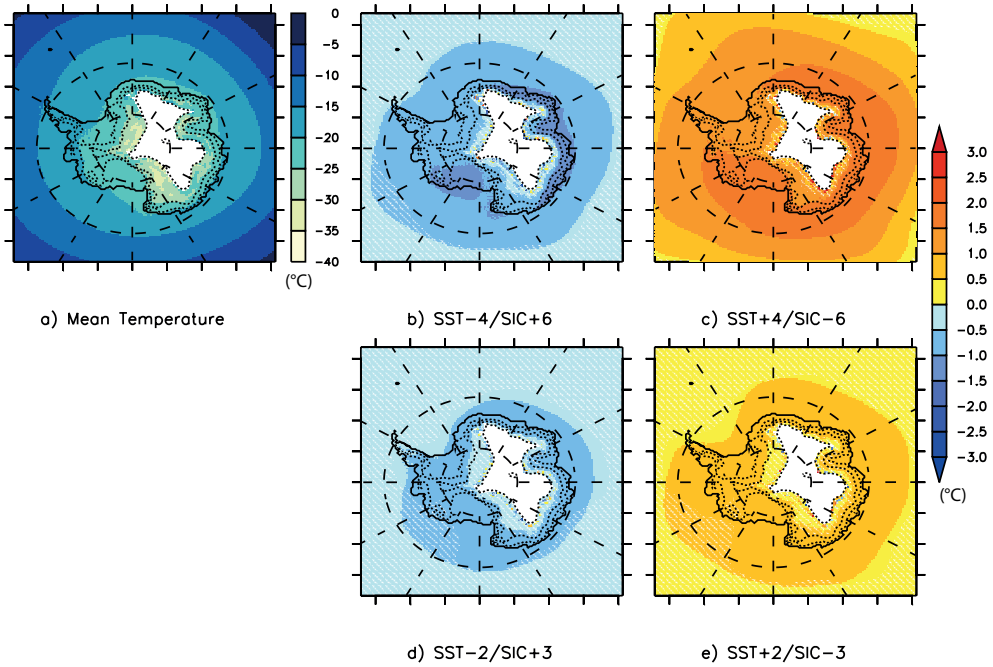

Figure C.9: Same as Fig. C.8 but at 700 hPa.

C.4 Near-surface wind anomalies

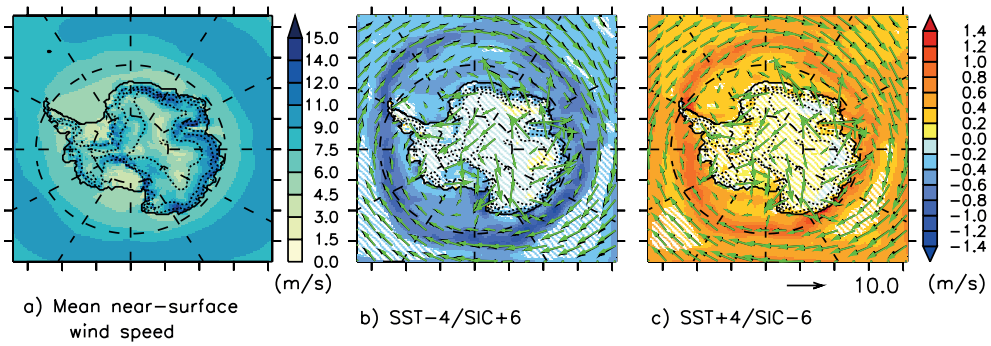

Figure C.10: a: Mean 2m wind-speed modelled by MAR over 1979–2015 (Units: m s^{-1}). Difference in Mean 2m wind-speed (m s^{-1}) between the reference simulation and (b) SST-4/SIC+6, (c) SST+4/SIC-6. Differences lower than the interannual variability are considered as non-significant and are dashed.

D Additional elements for Chapter 5

D.1 Evaluation of MAR(ESM) simulations over present

Present biases might have a significant influence on the projections results and remain in the future (Fettweis et al., 2013; Agosta et al., 2015; Krinner and Flanner, 2018), highlighting the need for a thorough evaluation over the present climate. Since ESMs only simulate meteorological conditions representative of a certain climate, evaluating MAR ESM-forced simulations cannot be done using the observations directly. We then compared these simulations to MAR(ERA5) hereafter considered as a reference and evaluated in Ch. 3.

MAR(ACCESS1.3) is the experiment that best compare with the reference MAR(ERA5) over the present climate. It displays the lowest integrated-SMB anomaly (Table D.1) and spatial RMSE and bias (Fig. D.1). MAR(ACCESS1.3) underestimates SMB over Wilkes Land, Queen Mary Land and the Amundsen sector while it overestimates SMB over Queen Maud Land and the lee side of the Antarctic Peninsula. These negative anomalies are associated with the small underestimation of the summer and winter precipitable water in ACCESS1.3 (Agosta et al., 2015). This experiments also reveals mostly non-significant temperature biases in summer (Fig. D.2), except for a small negative bias over Ross and Rhone ice shelves, yielding very similar melt integrated values.

MAR(NorESM1-M) presents mostly non-significant anomalies compared to MAR(ERA5) but overestimates the mean annual SMB as a consequence of an overestimation of the snowfall, while simulating a lower surface ablation (Table D.1). Higher snowfall values are modelled over Marie Byrd Land, the Peninsula, and the Brunt Ice Shelf whiler lower values compensate this overestimation over Queen Mary Land, Wilkes Land and the Amery ice shelf (Fig. D.3), which are strongly linked with the humidity anomalies in the forcing ESM (Agosta et al., 2015). NorESM1-M being too cold (with lower air summer and ocean temperatures and higher sea ice concentration), MAR(NorESM1-M) displays a negative temperature anomaly up to 3 °C over the plateau despite reducing the negative anomaly over half of the AIS to non-significant differences in summer (Fig. D.2). This however leads to reduced surface melting (-72 $\mathrm{Gt\,yr^{-1}}$).

MAR(CNRM-CM6-1) simulates nearly the same snowfall amount as the reference run but has a higher SMB RMSE due to a less accurate spatial representation of the precipitation. This results from an overestimation of the

Table D.1: Top: annual mean and standard deviation of, snowfall, rainfall, net sublimation (sublimation - deposition), runoff and meltwater ($Gt\,yr^{-1}$) integrated over the whole AIS for MAR(ERA5) over 1981–2010. Bottom: Difference of annual mean integrated SMB, snowfall, rainfall, net sublimation (sublimation - deposition), runoff and meltwater ($Gt\,yr^{-1}$) between each MAR(ESM) experiment and MAR(ERA5) over 1981–2010

Mean ($Gt\,yr^{-1}$)	SMB	SF	RF	SU	RU	ME
MAR(ERA5)	2686 ± 116	2894 ± 112	19 ± 3	173 ± 11	54 ± 14	174 ± 38
Anomaly ($Gt\,yr^{-1}$)	SMB	SF	RF	SU	RU	ME
MAR(ACCESS1.3)	-3	-22	11	-8	0	0
MAR(NorESM1-M)	94	38	1	-22	-31	-72
MAR(CNRM-CM6-1)	60	8	11	-10	-31	-48
MAR(CESM2)	-25	-58	-5	-4	-33	-71

precipitable water combined to a higher mean sea level pressure in CNRM-CM6-1 potentially reducing cyclonic activity. MAR(CNRM-CM6-1) underestimates the SMB over the Ellsworth Land and the windward side of the Peninsula but overestimates it over Marie Bird Land, Queen Maud Land and Victoria Land (Fig. D.1). Agosta et al. (in preparation) revealed a strong negative temperature anomaly surrounding the ice sheet, yielding lower temperature in MAR(CNRM-CM6-1) compared to MAR(ERA5) over the plateau. However, these differences are non significant over the margins, the Ronne ice shelf excepted (Fig. D.2).

As it simulates lower snowfall amounts, MAR(CESM2) slightly underestimates the mean integrated SMB. However, MAR(CESM2) represents a stronger accumulation over the area between the Peninsula, Queen Maud Land and Enderby Land (Fig. D.1). This results from the significant overestimation of the precipitable water and the sea level pressure in CESM2 over this area. On the contrary, MAR(CESM2) simulates a lower accumulation over Wilkes Land and the Amundsen sector. CESM2 is colder than ERA5 but the difference is reduced in summer (Agosta et al., in preparation), leading to mostly non significant temperature anomalies (Fig. D.2) and lower melt in MAR(CESM2).

In general, the SMB downcalled by MAR forced by the 4 ESMs is close to MAR(ERA5). The anomalies of the annual mean SMB are lower than the interannual variability of the SMB over the historical period. It is also important to note that the spatial and integrated anomalies are close to (or even lower than) the differences between several RCMs all forced by ERA-Interim(Mottram et al., 2020). This suggests a good ability of the different simulations to closely reproduce the SMB over the present climate and gives some confidence in results of the projections.

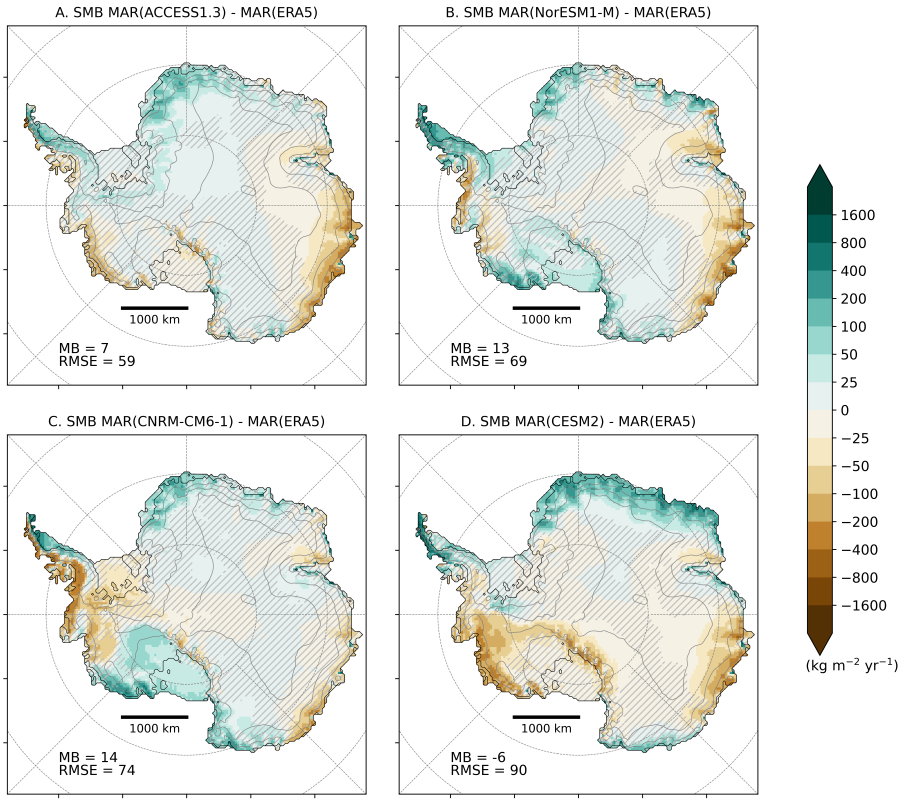

Figure D.1: Comparison between the annual mean SMB simulated by MAR forced by ACCESS1.3 (A), NorESM1-M (B), CNRM-CM6-1 (C), CESM2 (D) and the annual mean SMB simulated by MAR(ERA5) ($\mathrm{kg\,m^{-2}\,yr^{-1}}$) over 1981–2010. Locations where anomalies are smaller than the (natural) interannual variability of the present climate (interannual standard deviation) are hatched.

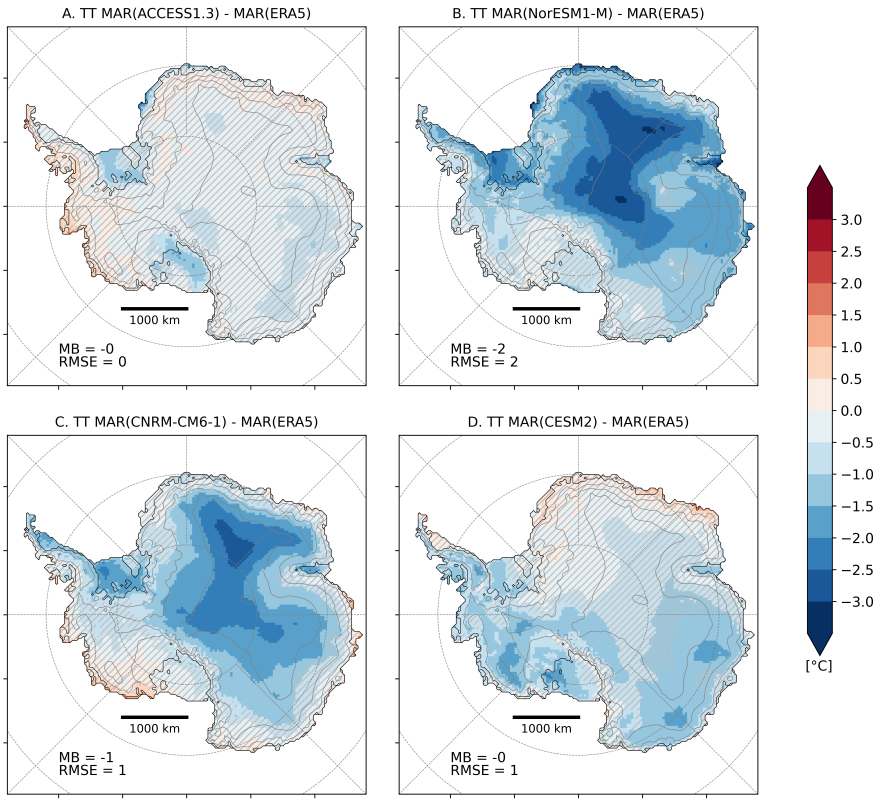

Figure D.2: Comparison between the mean summer near-surface temperature simulated by MAR forced by ACCESS1.3 (A), NorESM1-M (B), CNRM-CM6-1 (C), CESM2 (D) and the mean summer near-surface temperature simulated by MAR(ERA5) (°C) over 1981–2010. Locations where anomalies are smaller than the (natural) interannual variability of the present climate (interannual standard deviation) are hatched. Spatial Root Mean Square Error (RMSE) and mean bias (MB) of the experiment compared to MAR(ERA5) are also indicated.

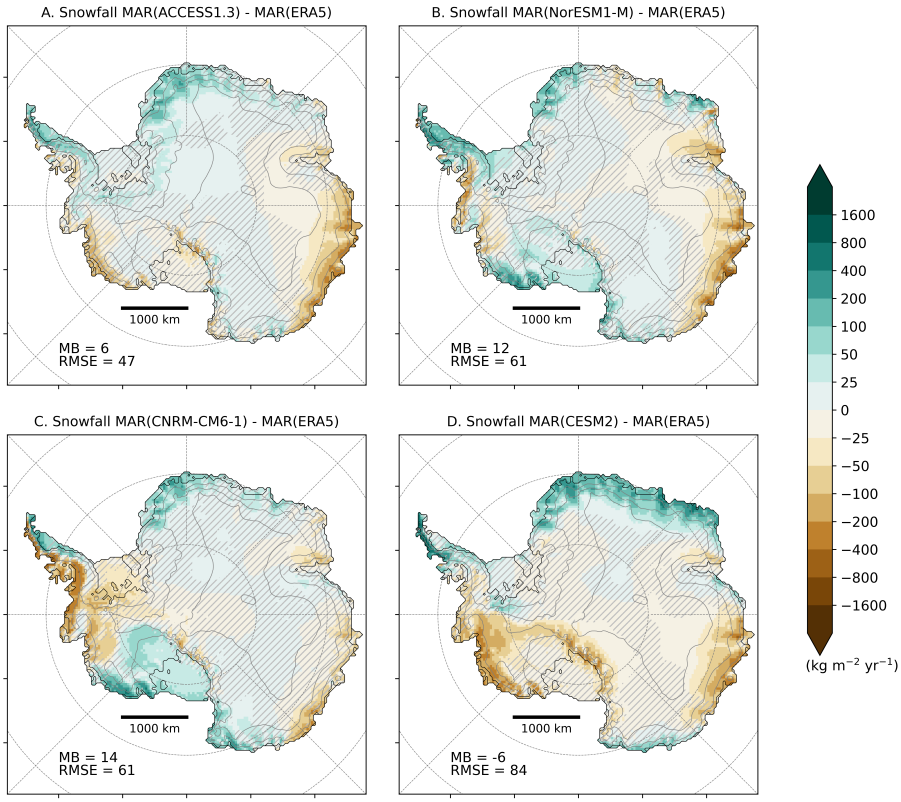

Figure D.3: Comparison between the mean annual SF simulated by MAR forced by ACCESS1.3 (A), NorESM1-M (B), CNRM-CM6-1 (C), CESM2 (D) and the mean annual SF simulated by MAR(ERA5) ($\mathrm{kg\,m^{-2}\,yr^{-1}}$) over 1981–2010. Locations where anomalies are smaller than the (natural) interannual variability of the present climate (interannual standard deviation) are hatched. Spatial Root Mean Square Error (RMSE) and mean bias (MB) of the experiment compared to MAR(ERA5) are also indicated.

D.2 Evolution of the integrated annual Antarctic

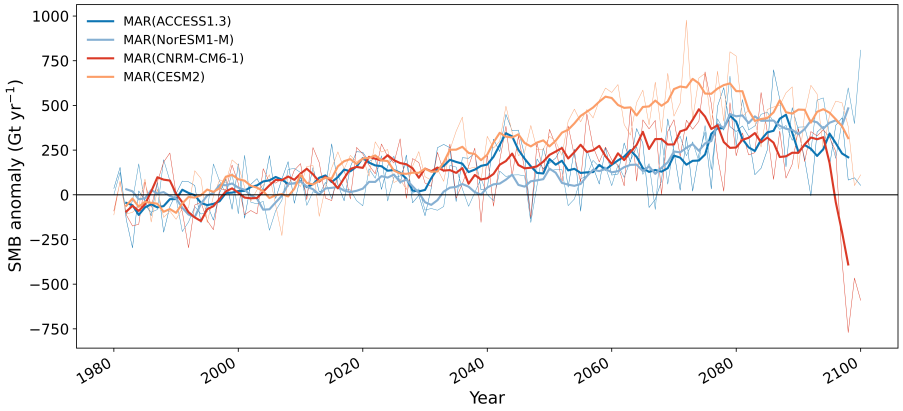

Figure D.4: Time series of the integrated annual Antarctic (ice shelves included) SMB anomaly (Gt yr^{-1}) from 1980 to 2100 in the high-emission scenarios (RCP8.5 and ssp585) simulated by MAR forced by ACCESS1-3 (blue), NorESM1-M (light blue), CNRM-CM6 (red), and CESM2 (orange) compared to the 1981–2010 reference period. A running average of 5 years was applied to the original values, while the original annual anomalies are shown as thinner lines in the background.

D.3 Locations discussed in Chapter 5

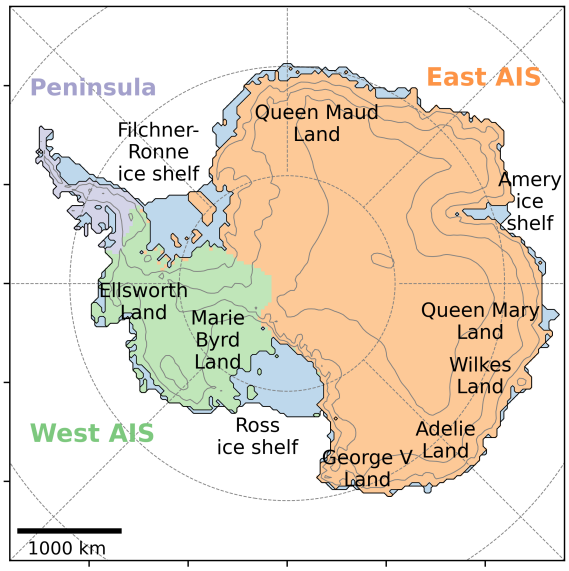

Figure D.5: The Antarctic regions and sub-regions discussed in the manuscript with elevations contours every 1000m. The ice shelves are represented in light blue.

D.4 Surface pressure changes

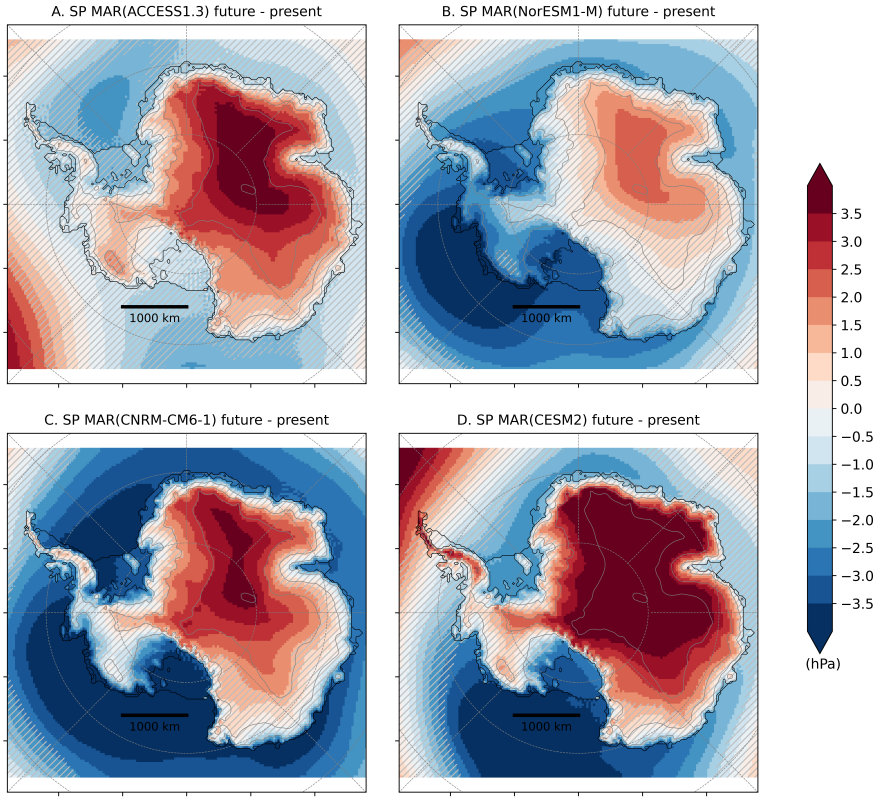

Figure D.6: Surface pressure changes (hPa) between 2071–2100 and 1981–2010 as modelled by MAR forced by ACCESS1-3 (A), NorESM1-M (B), CNRM-CM6-1 (C), and CESM2 (D). Locations where changes are smaller than the (natural) interannual variability of the present climate (interannual standard deviation) are hatched.

D.5 Evolution of SMB and its components

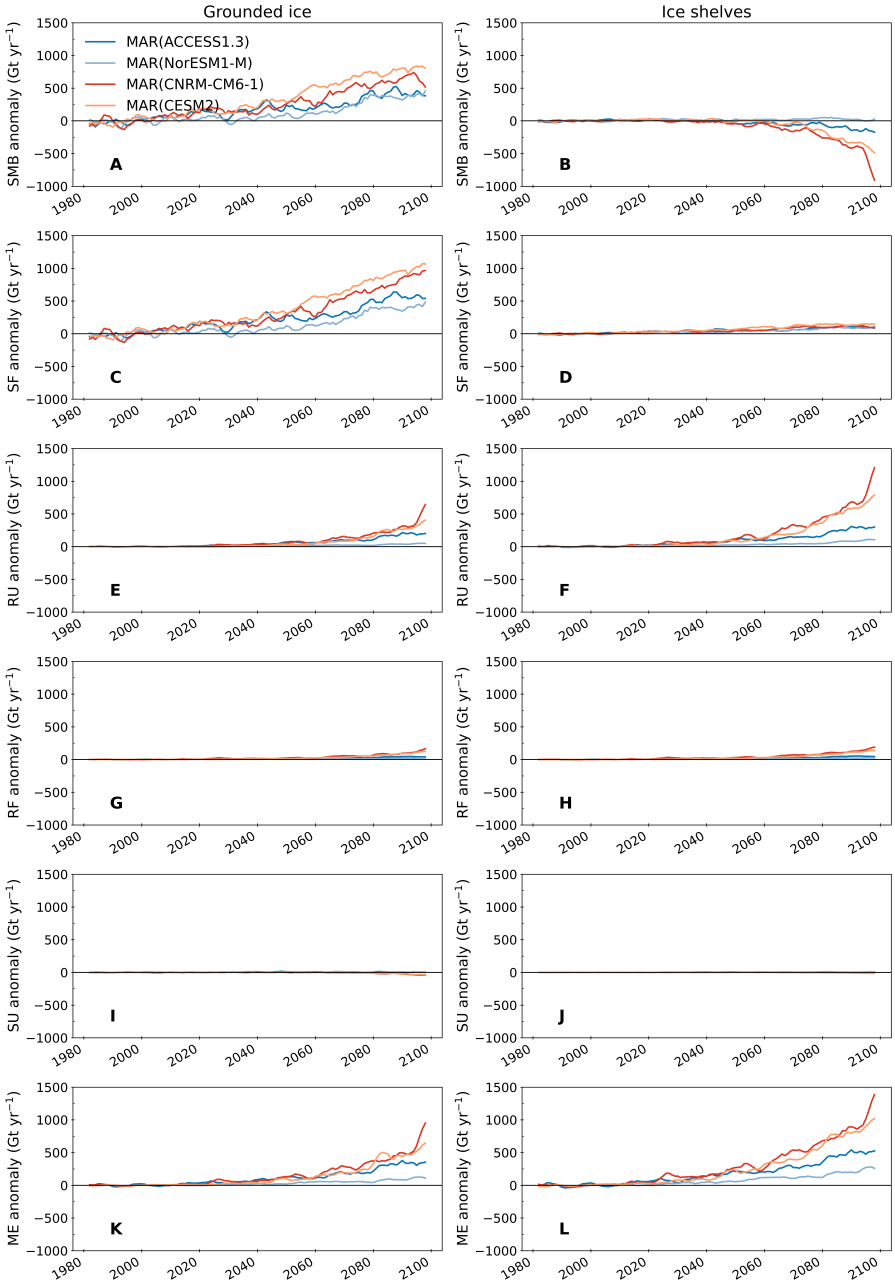

Figure D.7: Time series of the integrated annual SMB (A, B), snowfall (C, D), runoff (E, F), rainfall (G, H), net sublimation (I, J) and melt (K, L) anomalies ($\mathrm{Gt\,yr^{-1}}$) over the Antarctic grounded ice (A, C, E, G, I, K) and the Antarctic ice shelves (B, D, F, H, J, L) from 1980 to 2100 simulated by MAR forced by ACCESS1-3 (blue), NorESM1-M (light blue), CNRM-CM6 (red), and CESM2 (orange) compared to the 1981–2010 reference period. Sublimation changes are weak and do not contribute to variations in SMB. Melt anomalies follow a similar pattern than runoff anomalies suggesting than a almost all of the melt water is lost for the ice sheet as runoff.

D.6 SMB anomalies for a +2.5°C warmer climate

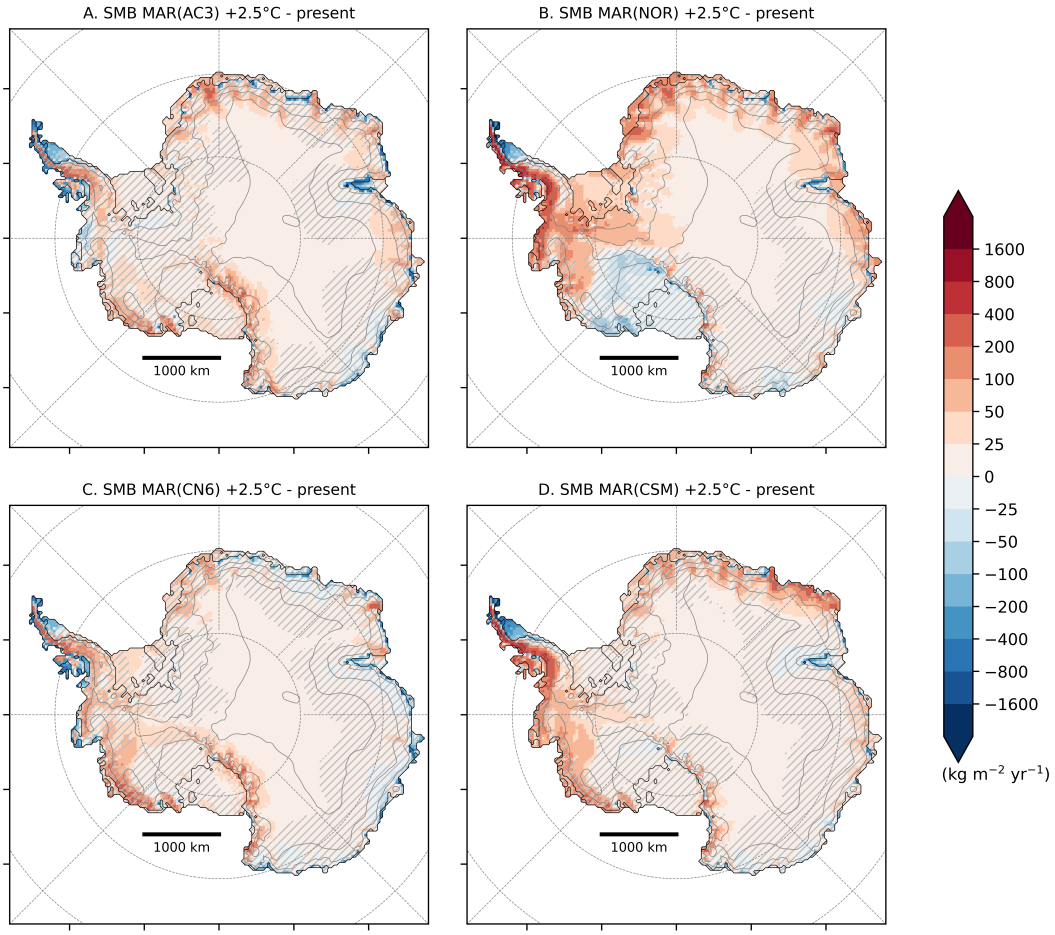

Figure D.8: SMB changes (kg m^{-2} yr^{-1}) between a +2.5°C warmer climate and the historical period by MAR forced by ACCESS1-3 (A), NorESM1-M (B), CNRM-CM6-1 (C), and CESM2 (D). Locations where changes are smaller than the (natural) interannual variability of the present climate (interannual standard deviation) are hatched.

Table D.2: The 30-year periods corresponding to an increase in Antarctic (90°S–60°S) near-surface temperature of +2.5 °C for the four selected ESMs. Exact near-surface warming is also indicated

ESM	30-year period	Near-surface temperature increase (°C)
ACCESS1.3	2041–2070	2.45
NorESM1-M	2071–2100	2.54
CNRM-CM6-1	2031–2060	2.44
CESM2	2031–2060	2.44

D.7 SMB anomalies compared to temperature anomalies

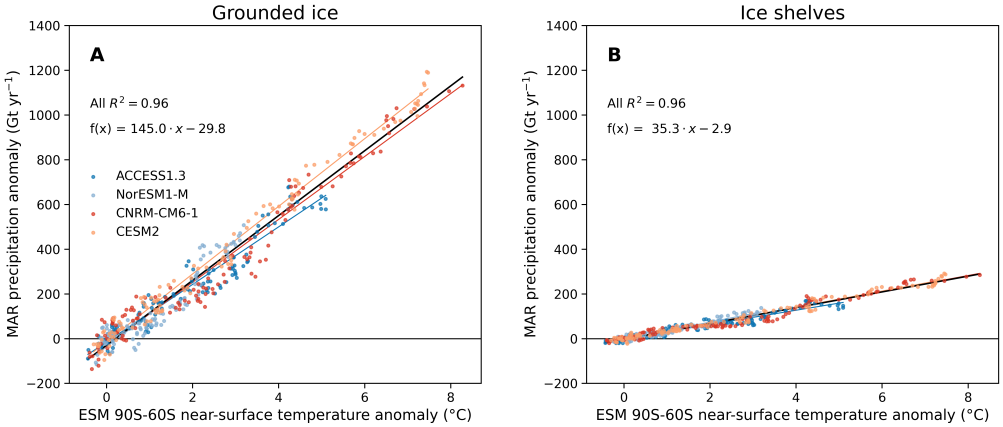

Figure D.9: MAR total (snowfall + rainfall) precipitations anomalies (Gt yr^{-1}) over the grounded ice (A) and ice shelves (B) compared to the annual near-surface temperature anomaly from the forcing ESMs between 90°S-60°S (°C). The black regression was computed using all the MAR-ESM anomalies while individual regression are also represented (coloured lines). The regression equation and determination coefficient are mentioned for each scatter plot.

Figure D.10 compares the modelled MAR SMB anomalies to the ESM reconstructed SMB anomalies. The reconstruction based on the temperature anomaly accurately reconstructs the modeled SMB over the grounded ice (RMSE = 68 Gt yr^{-1} , i.e lower by 99 Gt yr^{-1} than the present interannual grounded-SMB variabily in our MAR(ERA5) reference simulations), but is slightly less precise over the ice shelves (RMSE = 38 Gt yr^{-1}, i.e larger by 22 Gt yr^{-1} than the present interannual ice-shelf SMB variability). This is mainly due to the large decrease in SMB for MAR(CNRM-CM6-1) that is not fully represented by the regression (also valid for the grounded fit). The projected changes with the strongest warming are however much larger than the error of the regression. Moreover, among all CMIP5 and CMIP6 models, CNRM-CM6-1 projects the strongest warming in 2100, thus allowing us to use our regression to reconstruct the SMB for all CMIP5 and CMIP6 models. Note that using a similar method based on the link between individual SMB components (snowfall, rainfall and ablation) and ESM near-surface anomalies also yields a similar reconstruction. This demonstrates that the future response of the surface of both ice shelves and grounded ice can be mainly determined using the temperature warming until the end of the 21st century.

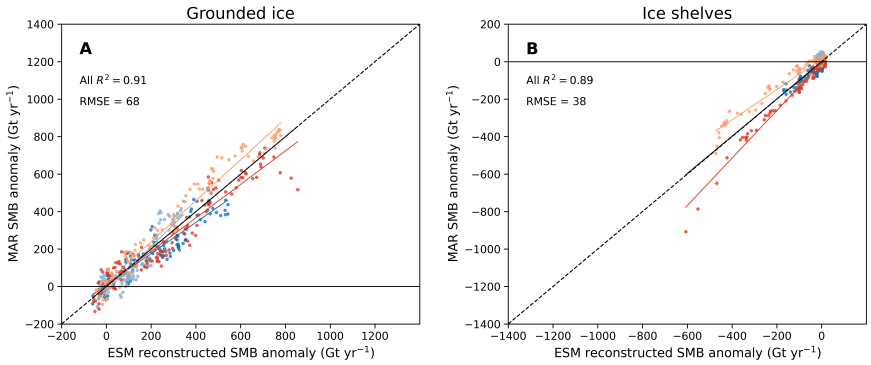

Figure D.10: Comparison of the MAR SMB anomaly ($\mathrm{Gt\,yr^{-1}}$) with the corresponding-ESM reconstructed-SMB anomaly ($\mathrm{Gt\,yr^{-1}}$) based on the regression between SMB and ESM near-surface temperature over the grounded ice (A) and over the ice shelves (B). The evaluation of the regression is done by indicating the Root Mean Square Error (RMSE,$\mathrm{Gt\,yr^{-1}}$) and determination coefficient

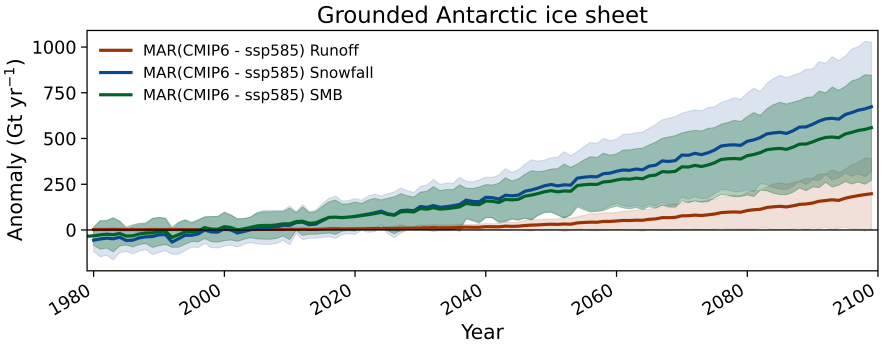

Figure D.11: Reconstructed snowfall (blue), runoff (red) and SMB (green) anomaly $\mathrm{Gt\,yr^{-1}}$ using CMIP6 (ssp585) models over the Antarctic grounded ice. Projections are shown using the multi-model mean (solid lines) and the 5 to 95% range, corresponding to ± 1.64 standard deviation, across the distribution of individual models (shading).

D.8 MAR anomalies compared to ISMIP6 anomalies

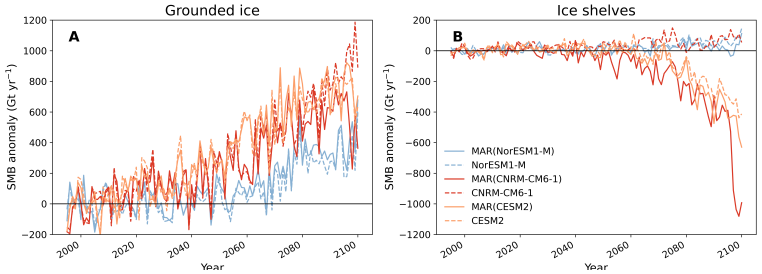

Figure D.12: Evolution of SMB anomalies (Gt yr^{-1}) projected by MAR forced by NorESM-1, CNRM-CM6-1, CESM2 (solid lines) and by the respective forcing ESMs (dashed lines) over the grounded ice (A) and the ice shelves (B)

E Additional elements for Chapter 6

E.1 Shortwave and longwave radiation contributions

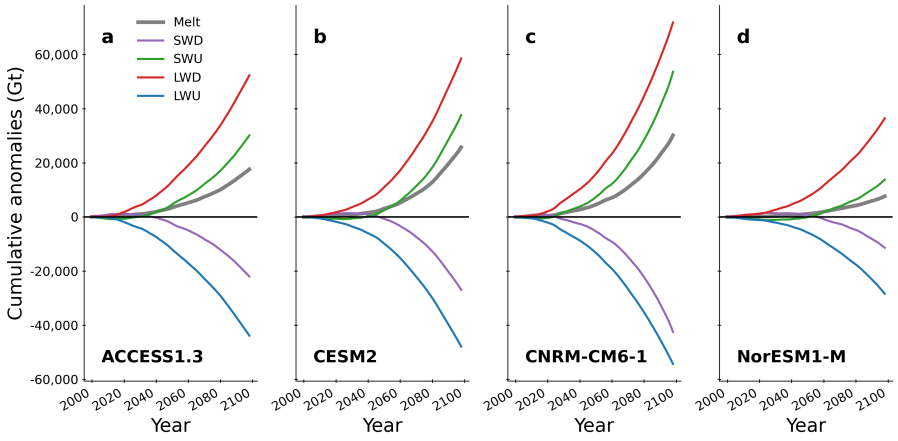

Figure E.1: Cumulative summer melt and SEB radiation components converted into melt potential (Gt). Cumulative summer anomalies of melt, shortwave downwelling (SWD), shortwave net (SWN), longwave downwelling (LWD), and longwave upwelling (LWU) fluxes expressed as melt potential (Gt) projected by MAR driven by (a) ACCESS1.3, (b) NorESM1-M, (c) CNRM-CM6-1, (d) CESM2, compared to the reference 1981–2010 summer.

E.2 Turbulent flux contributions

Both turbulent flux contributions firstly mitigate melt changes until 2070–2080 when latent heat exchanges tend to weakly increase melt only in MAR driven by CNRM-CM6 and CESM2 (Fig. 6.1). While the absolute SHF remains positive and then warms the surface in all our simulations during the 21st century, we find that SHF exchanges between the atmosphere and the surface are projected to weaken leading to a potential negative melt contribution. This effect is specific to the colder conditions in Antarctica as SHF should enhance melt over the Greenland ice sheet as a consequence of stronger barrier winds (Franco et al., 2013).

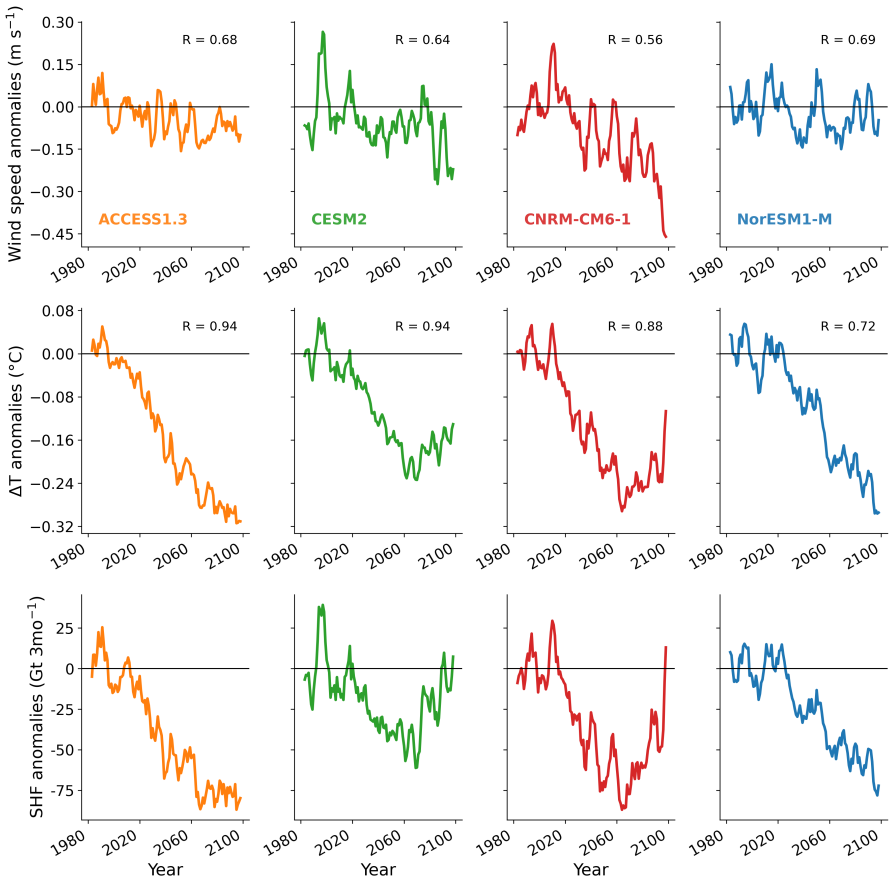

Figure E.2: Summer changes in summer near-surface wind speed, temperature gradient and SHF over the ice shelves. Summer near-surface wind-speed anomalies ($m\,s^{-1}$) (first row), temperature gradient between the first atmospheric level and the surface (°C) (second row), and sensible heat fluxes (expressed in melt potential $Gt\,3mo^{-1}$) (third row) for MAR forced by ACESS1.3 (orange), NorESM1-M (blue), CNRM-CM6-1 (red), and CESM2 (green) compared to their summer mean value over 1981–2010. The correlation coefficients (R) between near-surface wind-speed and temperature gradient anomalies with SHF anomalies are also presented (p«0.01)

SHF varies according to vertical temperature gradient between the surface

and the near-surface atmospheric layer, and wind that mixes this near-surface layer (Fig. E.2). The summer mean near-surface wind speed over ice shelves is stationary in MAR driven by NorESM1, while it tends to decrease in the other experiments ($p<0.05$). The trends remain however weak compared to the present variability except when MAR is driven by CNRM-CM6-1. By absorbing radiative energy, the surface is projected to warm faster than the above near atmosphere reducing the temperature gradient until 2060. After 2060, our results suggest that it could either still decrease in the relatively-colder projections (ACCESS1.3 and NorESM1-M) or increase in the warmer projections (CNRM-CM6-1, CESM2). SHF anomalies follow this pattern with decreasing potential melt contribution in all our experiments before diverging after 2060. We found a stronger association between SHF and the temperature gradient than with near-surface wind speed (see r values on Fig. E.2)). This suggests that the primary effect explaining SHF anomalies is the variation in the thermal inversion that can be modulated by wind shear changes. Furthermore, the more frequent presence of liquid water at the surface around the freezing point can reduce the temperature inversion or even warm the cold air advected by katabatic winds leading to negative SHF anomalies as already observed over the ice sheet (Kuipers Munneke et al., 2012; Van Wessem et al., 2014a).

The averaged values over all the Antarctic ice shelves however hide diverging local signals (Fig. E.3). SHF are projected to decrease over most of the AIS, the peninsula excepted where SHF could significantly increase. Recent studies (Kuipers Munneke et al., 2012; Van Wessem et al., 2014a; Kuipers Munneke et al., 2018; Datta et al., 2019) have suggested that warm air advections (notably during Foehn events) are an important source of energy over the Peninsula producing strong melt. Our results suggest an enhancement of the Foehn effect due to warmer and moister air advections inducing higher precipitation (Kittel et al., 2020) but also larger melt rates. Since the snow/ice-covered surface cannot warm higher than the melting temperature, warmer air advections also increase the thermal inversion and then increase SHF. The positive SHF anomalies over the Peninsula become dominant for strong warmings projected to occur after 2060 when MAR is forced by CNRM-CM6 and CESM2 explaining the inversion of SHF anomalies in these two projections.

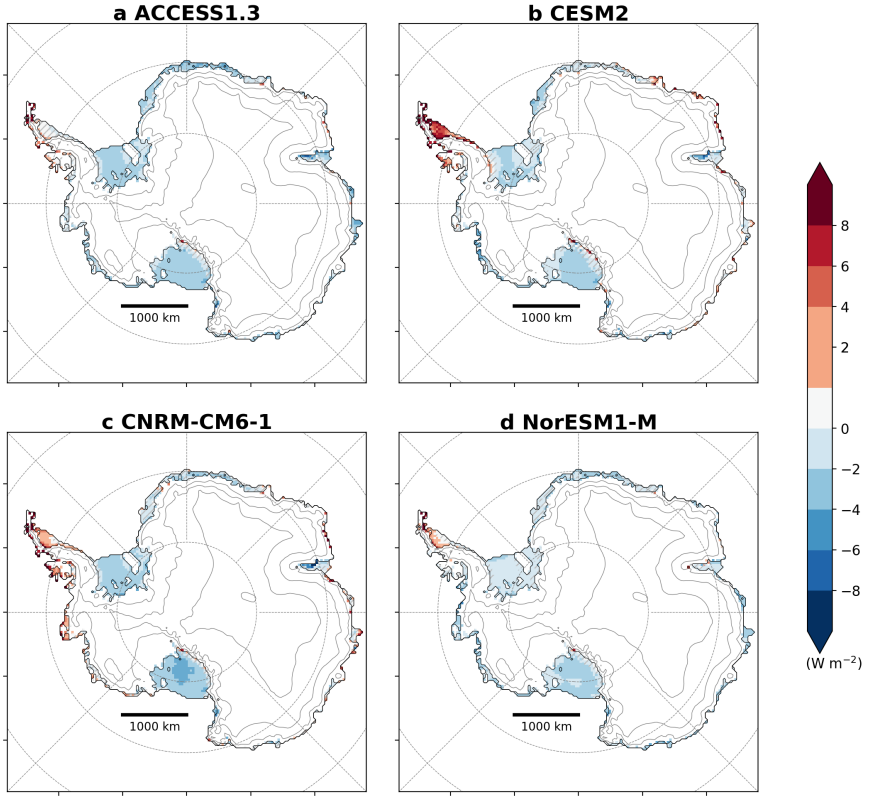

Figure E.3: Summer changes in SHF. Summer SHF anomalies ($\mathrm{W\,m^{-2}}$) in 2071–2100 compared to 1981–2010 as projected by MAR driven by ACCESS1.3 (a), NorESM1-M(b), CNRM-CM6-1 (c), and CESM2 (d). Anomalies lower than the present variability (standard deviation) are hatched.

E.3 Increase in Water Vapour Path

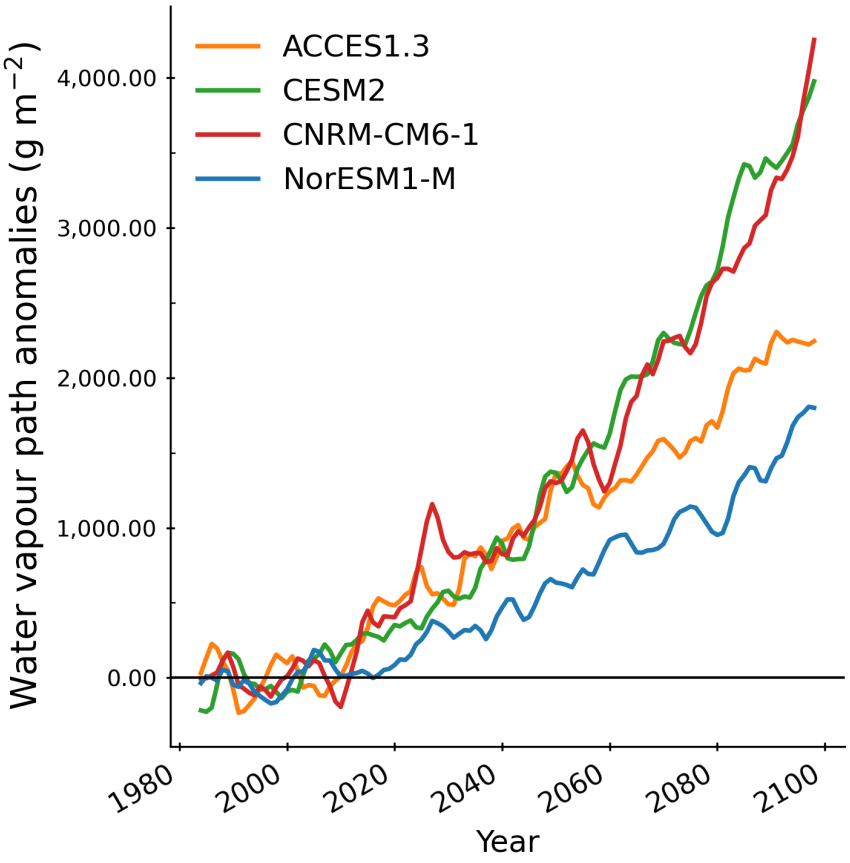

Figure E.4: Summer changes in Water Vapour Path (WVP). Evolution of the summer mean WVP anomalies (g m^{-2}) compared to 1981–2010 as projected by MAR driven by ACCESS1.3 (orange), CESM2 (green), CNRM-CM6-1 (red), and NorESM1-M (blue).

E.4 Increase in LWD due to warmer atmosphere

Assuming an opaque atmosphere ($\varepsilon = 1$) in Eq. 1, we compute the LWD which would be entirely due to the summer temperature of the atmosphere (LWDT) over the present (1981–2010) and the end of the 21st century (2071-2100) in Table E.1. The differences in LWDT anomalies between the CNRM-CM6-1 and CESM2 experiment (1.5 $\mathrm{W\,m^{-2}}$) is compared to the differences in LWD simulated by MAR for these two experiments (5.1 $\mathrm{W\,m^{-2}}$) to evaluate how much the atmosphere temperature differences explains the LWD anomalies.

$$LWDT = \varepsilon \times \sigma \times T^4, \tag{1}$$

Table E.1: Near-surface summer mean temperature (TT) over the present and at the end of the 21st century, increased in LWD explained by the temperature and simulated by MAR. Near-surface summer mean temperature over 1981-2010 °C (first row), over 2071–2100 (°C) (second row), increase in longwave downwelling radiations attributed to the increase in near-surface temperature ($\mathrm{W\,m^{-2}}$) (third row) and simulated (fourth row) by MAR driven by ACCESS1.3, CESM2, CNRM-CM6-1, NorESM1-M in 2071-2100 compared to 1981–2010.

ESM	$TT_{1981-2010}$ (°C)	$TT_{2071--2100}$ (°C)	$\Delta LWDT$ ($\mathrm{W\,m^{-2}}$)	ΔLWD ($\mathrm{W\,m^{-2}}$)
ACCESS1.3	-8.1	-4.0	+17.7	+23.2
CESM2	-8.1	-3.0	+22.4	+29.2
CNRM-CM6-1	-8.2	-2.7	+23.9	+34.3
NorESM1-M	-8.8	-5.8	+12.8	+17.3

E.5 Future mean (vertical) changes in 2071–2100

Table E.2: Mean changes in near-surface temperature, atmospheric specific humidity and temperature. Anomalies of summer near-surface air temperature (°C), atmospheric specific humidity between 925hPa and 200 hPa (g/kg), and atmospheric temperature (°C) in 2071-2100 compared to 1981-2010 as projected by MAR driven by ACCESS1.3, CESM2, CNRM-CM6-1, NorESM1-M.

ESM	$\Delta Near-Surface\,air\,Temperature$ (°C)	$\Delta Specific\,Humidity$ ($g\,kg^{-1}$)	$\Delta Air\,Temperature$ (°C)
ACCESS1.3	+4.1	+0.30	+2.4
CESM2	+5.1	+0.47	+3.8
CNRM-CM6-1	+5.5	+0.44	+3.5
NorESM1-M	+3.0	+0.21	+1.7

E.6 Association between LWD, COD and CC

We find a strong association between increases in LWD and COD (Fig. E.5) as suggested by the high R^2 scores (R^2 >=0.98; p«0.01) for each experiment. However the association between longwave cloud emissivity and COD induces a saturation for large COD increases. This situation is representative of an opaque atmosphere to longwave radiation due to clouds. We extrapolate our projections to find that increase in LWD associated to increase in COD could stop when COD equals 1.22 (ACCESS1.3; +0.96), 1.10 (NorESM1-M; +0.96), 1.78 (CNRM-CM6-1; +0.91), 1.2 (CESM2; +0.89). Since these values are not reached before 2100, future LWD increase is supposed to remain sensitive to COD during the whole 21st century.

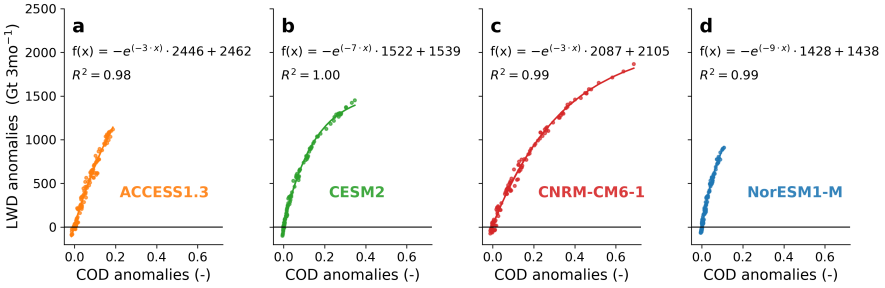

Figure E.5: Relation between LWD summer anomalies and COD summer anomalies. Summer longwave downwelling radiations (expressed as potential melt in Gt $3mo^{-1}$) versus mean cloud optical depth anomalies during summer (-) projected by MAR driven by ACCESS1.3 (a), CESM2 (b), CNRM-CM6-1 (c), and NorESM1-M (d) compared to the summer reference period (1981–2010). The exponential regression as well as corresponding determination coefficient (R^2, p «0.01) is indicated for each experiment. A 5-year running mean has been applied on the anomalies.

E.7 Near-surface temperature anomalies compared to COD

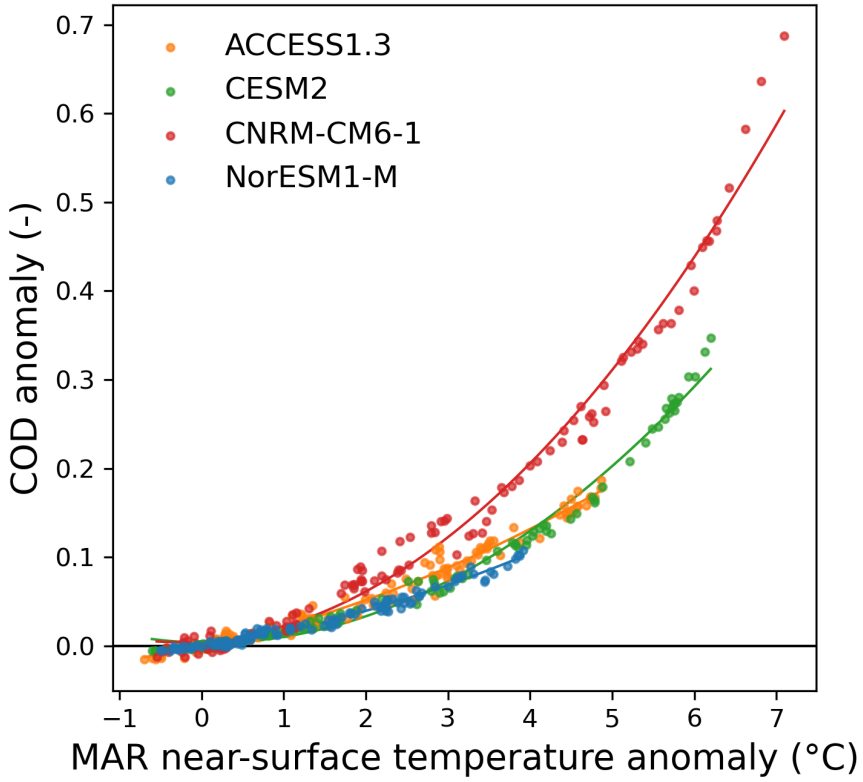

Figure E.6: Relation between summer near-surface temperature anomalies and COD summer anomalies. Mean near-surface temperature anomalies °C compared to mean COD anomalies in summer (-) projected by MAR driven by ACCESS1.3 (orange), CESM2 (green), CNRM-CM6-1 (red), and NorESM1-M (blue) compared to the summer reference period (1981–2010).